Synthesis and Performance Characterization of Polymer Semiconductors for Organic Thin Film Transistors

by

Chang Guo

A thesis

presented to the University of Waterloo

in fulfillment of the

thesis requirement for the degree of

Doctor of Philosophy

in

Chemical Engineering

Waterloo, Ontario, Canada, 2015

Author's Declaration

This thesis consists of material all of which I authored or co-authored: see Statement of Contributions included in the thesis. This is a true copy of the thesis, including any required final revisions, as accepted by my examiners.

I understand that my thesis may be made electronically available to the public.

Statement of Contribution

This thesis contains materials from several published or submitted papers, some of which resulted from collaboration with my colleagues in the group.

The content in Chapter 1 has been partially published in Reviews in Advanced Sciences and Engineering (2012), Guo, C.; Hong, W.; Aziz, H.; Li, Y.,**1**(3): 200-224.

The content in Chapter 2 has been partially published in Journal of Materials Chemistry C (2014), Guo, C.; Sun, B.; Quinn, J.; Yan, Z.; Li, Y., **2**(21): 4289-4296.

The content in Chapter 3 has been partially published in Journal of Materials Chemistry C (2015), Guo, C.; Quinn, J.; Sun, B.; Li, Y., **3**: 5226-5232.

The content in Chapter 4 has been partially published in Polymer Chemistry (2015), Guo, C.; Quinn, J.; Sun, B.; Li, Y., **DOI**: 10.1039/C5PY00821B.

The content in Chapter 5 is partially quoted from a manuscript submitted to Polymer Chemistry (2015), Guo, C.; Sun, B.; Quinn, J.; Li, Y..

The content in Chapter 6 has been partially published in Polymer Chemistry (2014), Guo, C.; Sun, B.; Li, Y., **5**: 5247-5254.

Abstract

As the most promising semiconductor candidates for organic thin film transistors (OTFTs), donor-acceptor (D-A) type π-conjugated polymers have received much attention in the recent years. Their excellent printability, light weight, mechanical robustness and flexibility are desirable characteristics for low cost and portable electronics. Some issues of polymer semiconductors as such relatively low charge carrier mobility compared to that of silicon as well as the poor stability during manufacturing and device operation in an ambient environment still remain. Although extensive efforts have been made to develop electron acceptor building blocks, which are considered to be critical for achieving high mobility, very few electron acceptors for constructing novel high performance D-A polymers are available. Nowadays most D-A polymers were synthesized using traditional Suzuki or Stille coupling, which use boron- or tin-containing monomers that require extra synthetic steps and are highly toxic in some cases (such as organotin monomers). As an alternative method, the direct (hetero)arylation polymerization (DHAP), provides a new approach to constructing D-A polymers in a cost-effective and environment friendly manner. Certain polymers synthesized by DHAP have demonstrated similar or even better performance compared to the polymers made by other methods. However side reactions and limitations on the types of monomers for DHAP have been reported. To bring the OTFT performance of polymer semiconductors to the next level, new acceptor building blocks and a further study of DHAP need to be exploded.

In the first part of this thesis (Chapters 2-4), a novel electron acceptor building block, indigo is chosen, considering its electron deficiency property, highly coplanar geometry and ease of synthesis. Furthermore, indigo and its small molecule derivatives have been demonstrated to be promising semiconductors in OTFTs. However, indigo-containing polymer semiconductors have not been reported yet. In this study, we used 6,6'-indigo as an electron acceptor to successfully develop several n-type electron transport semiconductors. Surprisingly, when 5,5'-indigo was

used, the opposite p-type hole transport performance was observed. To the best of our knowledge, this is the first observation that the charge transport polarity could be controlled or switched through different regiochemical connections of a building block. The second part of this thesis (Chapters 5 and 6) focuses on the optimization and development of dipyrrolopyrrole (DPP) based polymers. In Chapter 5, DHAP is used to construct a novel high performance pyrrolo[3,4-*c*]pyrrole-1,4(2*H*,5*H*)-dione (1,4-DPP)-thiazole based polymer. Two synthetic routes are compared and discussed, and the polymer synthesized under optimized DHAP conditions showed better performance than that of a similar polymer obtained by Stille coupling. In Chapter 6, pyrrolo[3,4-*c*]pyrrole-1,3(2*H*,5*H*)-dione (1,3-DPP), an isomer of 1,4-DPP, is developed for constructing polymer semiconductors with promising performance in OTFTs.

Systematic studies on the synthesis of these new acceptor building blocks as well as the exploration of DHAP have provided insights into the structure-property relationships of novel D-A polymers and may lead to the discovery of the next generation high mobility polymer semiconductors.

Acknowledgements

First and foremost, I would like to express my sincerest appreciation to my supervisor, Dr. Yuning Li, for his guidance, encouragement, and trust on me. His commitment to my education and seemingly endless enthusiasm to help me in all my endeavors will forever be appreciated. What I have learned from Dr. Li in these years is not only about science but also personal attitude toward work and life.

I will always be grateful for the support I have received from my current and former group members, Dr. Wei Hong, Bin Sun, Jesse Quinn, Yinghui He, Zhuangqing Yan, Mylène Le Borgne, Dr. Yunfeng Deng and Leanne Murphy. Without them, this work would not be done on so smoothly. I especially want to thank Dr. Wei Hong and Bin Sun for their help and advice on research and life even prior to my arrival in Canada. I would like to acknowledge Jesse Quinn, my coauthor on several publications, for his invaluable research contributions on DFT calculations. I also thank to my friends working together in the cleanroom, Qi Wang, Dr. Graeme Williams, Yingjie Zhang, Baolin Tian and Dr. Jian Zhang for their kind support during working.

I would like to express my heartfelt thanks to my parents for their advice, encouragement, and unconditional love through these years. Without their support, I would not be able to pursue my academic goal without any concern. At the end, I would like to express my special appreciation to my girlfriend, Shuai Leng, for her patience, selfless support and the happiness she brings to everyday of my life.

Table of Contents

List of Figures

List of Schemes

List of Tables

List of Abbreviations

AFM	Atomic Force Microscopy
CV	Cyclic Voltammetry
D-A	Donor-Acceptor
DFT	Density Functional Theory
DHAP	Direct (Hetero)arylation Polymerization
DI	Deionized
DMF	*N*,*N*-Dimethylformamide
DMAP	4-(Dimethylamino)pyridine
DSC	Differential Scanning Calorimetry
GPC	Gel Permeation Chromatography
HOMO	Highest Occupied Molecular Orbital
LUMO	Lowest Unoccupied Molecular Orbital
M_n	Number-average molecular weight
M_w	Weight-average molecular weight
MIM	Metal-insulator-metal
NBS	*N*-Bromosuccinimide
OTFTs	Organic Thin Film Transistors
TCE	1,1,2,2-Tetrachloroethane
TGA	Thermogravimetric Analysis
THF	Tetrahydrofuran
UV-Vis	Ultraviolet-Visible
XRD	X-ray Diffraction

Other abbreviations and symbols are defined in the text.

Chapter 1 Introduction

(This chapter is partially published in Reviews in Advanced Sciences and Engineering (2012), Guo, C.; Hong, W.; Aziz, H.; Li, Y.,**1**(3): 200-224.)

Organic electronics is a fast growing research area, which has shown great potential to produce cost-effective large area electronic devices such as thin film transistors (TFTs), solar-cells, light emitting diodes (LED) and photo-detectors (Figure 1-1). Quite different from the conventional silicon based electronics, organic electronics are light weight, low cost, high throughput and exhibit excellent flexibility, thus may lead to a whole new range of products such as conformable and rollable electronic displays, solar energy harvesting, identification tags and convenient medical diagnostics. Particularly OTFTs have been widely explored in a number of organic electronics including displays, radio-frequency identification (RFID) tags, memory devices, and chemo-/bio-sensors.[1–9]

Figure 1-1 Applications based on organic electronics

OTFTs operate with organic semiconductors as the active layer to control the electrical current flow.[10] Based on the molecular weight of organic semiconductors they can be classified into two groups: small molecule semiconductors (with a molecular weight less than 1000) and polymer semiconductors (with a molecular weight greater than 1000).[11] Small molecule

semiconductors generally have high purity, high crystallinity and good molecular ordering in the solid state, which are beneficial to charge-carrier transport. However, small molecules are difficult to form uniform, robust thin films by solution processing. On the other hand, various printing technologies such as screen, inkjet or gravure could be applied to polymer semiconductors to achieve low-cost manufacturing of large-area and flexible electronics.[12,13] As the carrier mobility of polymer semiconductors has improved rapidly in the recent years, the development of enabling polymer semiconductors for OTFTs has been one of the most important research topics in the field of printed organic electronics. [7,14–21]

In this chapter, a brief introduction will be given in four parts: I) Polymer semiconductors (especially donor-acceptor (D-A) polymers) and polymerization techniques; II) Charge transport in organic semiconductors; III) About organic thin film transistors (OTFTs); and IV) Operation of OTFTs. The work of this thesis will be described at the end of the chapter.

1.1 Polymer Semiconductors

Research into organic electronics is largely driven by the potential of fabricating electronics using cost-saving printing technologies.[3,22–29] Polymer semiconductors are undoubtedly the best choice as semiconductor components for organic electronics due to their excellent printability. Equally important are their mechanical robustness, light weight, and flexibility. Therefore polymer semiconductors for organic electronic applications have been attracting tremendous attention since the 1970's.[6–9,17,18,21,30–37]

One of the main concerns associated with the organic electronics is the stability of organic electronic devices during manufacturing or operation towards the ambient environment that contains elements such as oxygen, UV light, and moisture that are, in most cases, detrimental to organic semiconductors. Over the years, sufficiently photo-oxidatively stable organic/polymer semiconductors have been designed and synthesized by fine-tuning the energy levels, i.e., the

highest occupied molecular orbital (HOMO) level to be below ~-5 eV for hole transport, [16,26,38] and the lowest unoccupied molecular orbital (LUMO) to be below ~-3.7 eV for electron transport.[29,38–40] This can be done through either judicious side chain engineering or a proper selection of main chain building blocks. However the biggest challenge for polymer semiconductors as OTFT materials so far has been their rather low charge carrier mobility. For the majority of applications such as display backplane drivers and RFID tags, a mobility value on par with that of amorphous silicon (a-Si) semiconductors, i.e., 0.1-1 $cm^2V^{-1}s^{-1}$, is required. Mobility of the first reported polymer-based OTFT in 1986 was ~10^{-5} $cm^2V^{-1}s^{-1}$.[25] Owing to the extensive and combined research efforts of materials scientists and device engineers, a number of polymer semiconductors showing mobility values over 0.5 $cm^2V^{-1}s^{-1}$ even 10 $cm^2V^{-1}s^{-1}$ have been developed in the laboratories in the last few years. [31,41–51] Design and optimization of polymer structures have contributed most significantly to the recent improvements in mobility for polymer semiconductors.

Almost all the high mobility semiconductors reported to date can be classified into two categories: i) fused aromatic ring containing polymers and ii) donor-acceptor (D-A) containing polymers. The fused ring aromatic structures have a strong tendency to form π-π stacks with a large overlapping area that is preferable for charge carrier transport through intermolecular hopping, and to induce a higher order molecular organization.[52,53] D-A copolymers, which consist of an alternating arrangement of electron-donating (D) and electron-accepting (A) units, have shorter interchain distances due to the strong intermolecular D-A interaction in the solid state (Figure 1-2).[31,41,54] Partial intermolecular charge transfer (ICT) between D and A moieties within these polymers can readily manipulate their electronic structures (HOMO/LUMO levels), as well as electronic and optoelectronic properties.[55] The strength of ICT can be tuned through careful design and selection of D and A building blocks, allowing D-A copolymers to exhibit small band gaps, broad optical absorption bands, short distances between the polymer chains and high charge transport mobilities. Thiophene, alkylthiophene, bithiophene, thienothiophene,

cyclopentadithiophene, biselenophene and arylene vinylene are the typical donor blocks, whereas benzothiadiazole (BTZ), thiazole (including bithiazole and thiazolothiazole), pyrrolo[3,4-*c*]pyrrole-1,4(2*H*,5*H*)-dione (1,4-DPP) and benzo (thieno) imide are known electron acceptor blocks. Although the electron donor units play an important role for achieving high mobility values, the electron acceptor building blocks are considered to be the determining factor. The majority of the high mobility polymers are based only on a few types of electron acceptors such as isoindigo (IID)[56–59] and 1,4-DPP.[31,41–45,47,48]

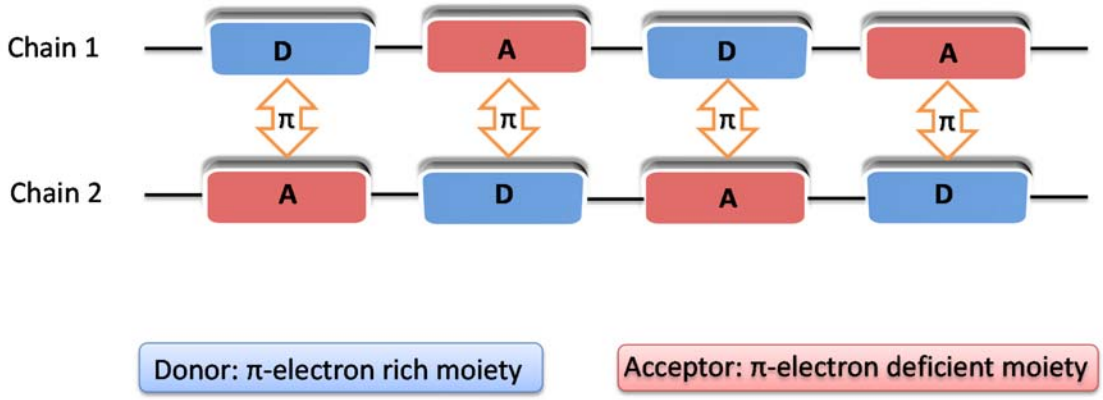

Figure 1-2 The interaction between donors and acceptors

Lei *et al.* reported several D-A copolymers with the isoindigo (IID) unit as an acceptor unit, including **IIDBT** (Figure 1-3),[56,58,59] which exhibited high hole mobility up to 0.79 $cm^2V^{-1}s^{-1}$. Later, Mei *et al.* introduced a novel siloxane-terminated solubilizing group as side chains into **IIDBT**.[57] The resultant polymer showed a maximum mobility up to 2.48 $cm^2V^{-1}s^{-1}$. However, the IID unit suffers from an intrinsic steric effect since the repulsion between the oxygen atom of the carboxyl group and the hydrogen atom of the neighboring benzene ring causes serious twisting, which may hinder close π–π stacking and thus negatively affects the charge transport. To overcome this defect, researchers replaced the benzene rings in IID with thiophene rings, and copolymerized the optimized unit with naphthalene comonomer to obtain a p-type semiconducting polymer PTIIG-Np with an ultrahigh mobility of 14.4 $cm^2V^{-1}s^{-1}$ (**PTIIG-NP**,

Figure 1-3).[60] Li's group developed a novel large acceptor building block by incorporating an electron deficient benzo[1,2-*b*:4,5-*b'*]-difuran-2,6-dione (IBDF) moiety into IID unit to strengthen its electron accepting capability.[39] With the assistance of side chain engineering, the electron mobility of **BDOPV-2T** based on IBDF has reached up to 1.74 $cm^2V^{-1}s^{-1}$.[61] All these indicate that the IID unit and its derivatives are promising structures to be further developed into novel acceptor building blocks.

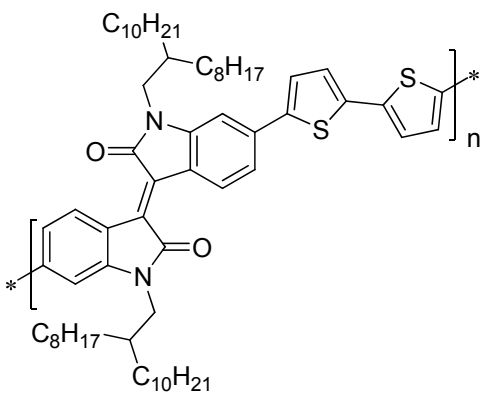

IIDBT

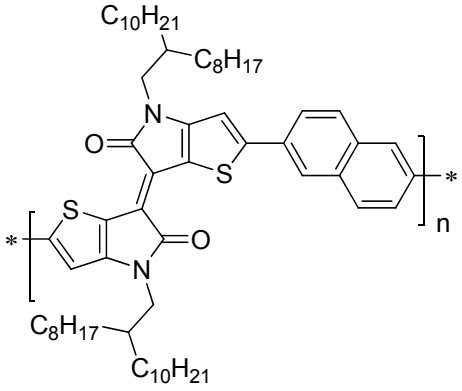

PTIIG-Np

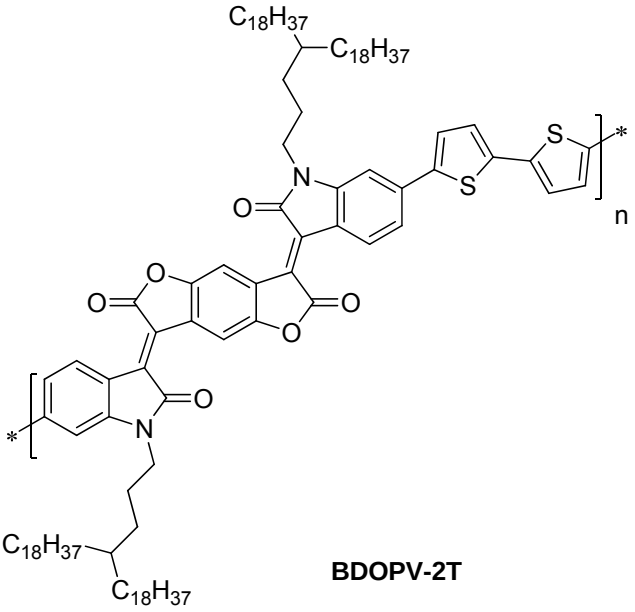

BDOPV-2T

Figure 1-3 Structures of IID and derivatives based polymers

1,4-DPP is the most intensively studied electron acceptor unit in recent years. Incorporation of 1,4-DPP into D-A copolymers leads to very narrow band-gap polymers with large intermolecular overlap through π-π stacking, and thus promising performances in organic electronics. Since the first application of 1,4-DPP in D-A polymers in 2008, the mobility of 1,4-DPP-based polymer with optimized donors and side chains in OTFTs have been improved up to 12 $cm^2V^{-1}s^{-1}$.[62] The majority of the 1,4-DPP-based polymers reported in the literature were synthesized using either Suzuki or Stille coupling polymerization (Figure 1-4), which requires extra steps to synthesize the organoboron or organotin monomers. Many organotin compounds are known to be highly toxic and are environmental hazards. Besides, according to the recent study from Li's group, Stille coupling polymerization introduced structural defects into 1,4-DPP-quaterthiophene copolymers because of homocoupling side reactions.[63] Recently, an alternative method, the direct (hetero)arylation polymerization (DHAP), has been explored to construct conjugated polymers for organic electronics. [64–71] Since DHAP involves the C–C coupling between a C–H group in one conjugated monomer (an arene or heteroarene) and a C–Br group in another, this new method is much more environmentally friendly and economical. During the past few years, several organic semiconductors including 1,4-DPP based polymers have been synthesized by DHAP, which show comparable or even better semiconducting performance than those obtained by conventional coupling methods. However some side reactions during polymerization process have been frequently observed, which result in the formation of insoluble polymers. The detailed mechanism is still not well understood and strategies to avoid these side reactions are not readily available yet. Therefore a further study on the synthesis of the 1,4-DPP based polymers by this new polymerization method DHAP is necessary although a few 1,4-DPP polymers synthesized by DHAP have been reported very recently. [70,72]

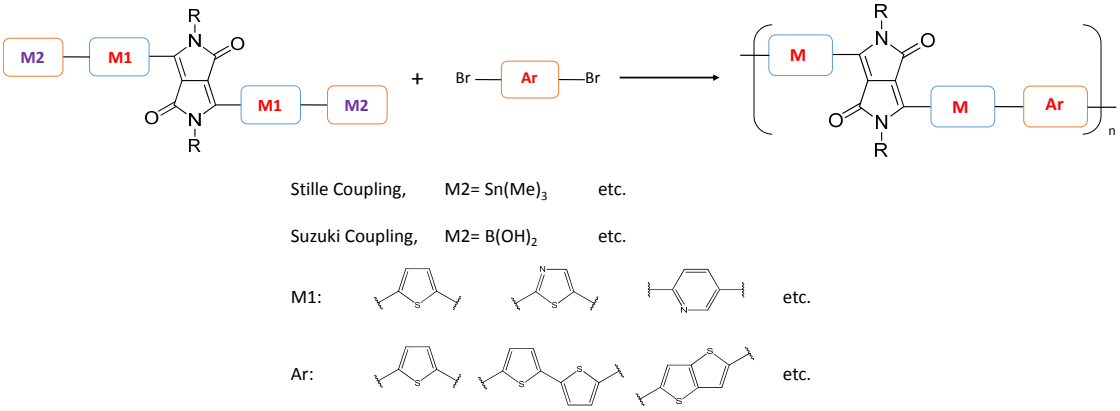

Figure 1-4 Typical 1,4-DPP based polymers obtained by Stille or Suzuki coupling. R is an alkyl chain.

Inspired by the remarkable achievements on 1,4-DPP based polymers, researchers have developed several polymers based on 1,4-DPP derivatives (Figure 1-5). Pyrrolo[3,2-*b*]pyrrole-2,5(1*H*,4*H*)-dione (2,5-DPP, Figure 1-5), an isomer of 1,4-DPP isomer, was recently investigated, whose polymers showed promising mobility up to 0.03 $cm^2V^{-1}s^{-1}$ in OTFTs and power conversion efficiency up to 5.1 % in OPVs.[73] Its derivatives, benzo[1,2-*b*:4,5-*b'*]-dipyrrole-2,6-dione (BDP)[74–76] and dipyrrolo[2,3-*b*:2',3'-*e*]-pyrazine-2,6(1H,5H)-dione (PzDP)[77], which could be viewed as extensions of 2,5-DPP by inserting a para quinoid or dihydropyrazine ring, have been used as electron acceptor building blocks for D-A polymers.

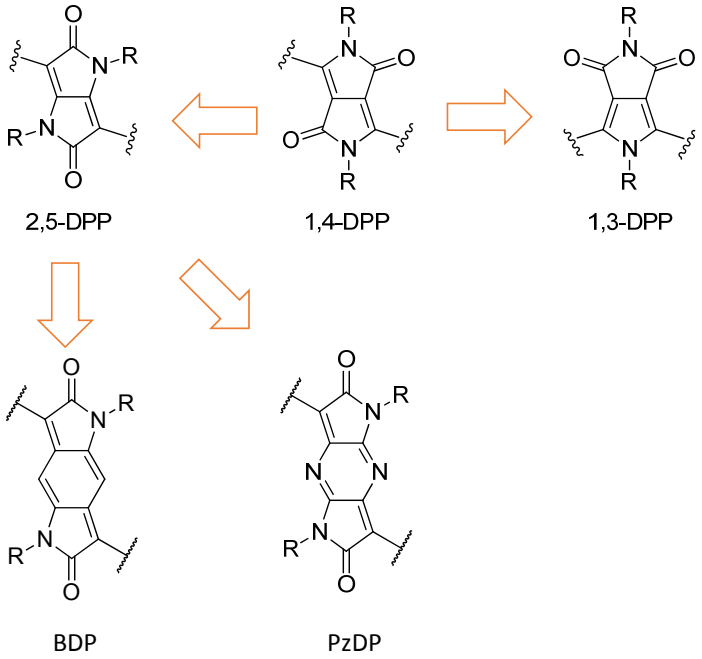

Figure 1-5 Chemical structures of DPP derivatives: pyrrolo[3,4-*c*]pyrrole-1,4(2*H*,5*H*)dione (1,4-DPP), pyrrolo[3,2-*b*]pyrrole-2,5(1*H*,4*H*)-dione (2,5-DPP), pyrrolo[3,4-*c*]pyrrole-1,3(2*H*,5*H*)-dione (1,3-DPP), benzo[1,2-*b*:4,5-*b'*]- dipyrrole-2,6-dione (BDP) and dipyrrolo[2,3-*b*:2',3'-*e*]-pyrazine-2,6(1*H*,5*H*)-dione (PzDP).

1.2 Charge Transport in Polymer Semiconductors

In 1977, MacDiarmid, Heeger, and Shirakawa discovered that doping π-conjugated polymers could convert them into conductors,[78] which is against the common notion that polymers are electrically insulators. Unlike the backbone of non-conjugated polymers, which relies on the connection of sp^3 hybridized carbon atoms, conjugated polymers comprise alternating single and double (or triple) bonds. The resultant conjugated π bonds lead to a relatively small energy gap, which is usually in the range of 1~3 eV, greatly facilitating electron delocalization from HOMOs to LUMOs.[79] Similar to the band transport in inorganic materials like silicon, these delocalized π-electrons may move along the polymer chains as charge carriers, resulting in intramolecular transport. A highly coplanar polymer backbone can provide an extended π-electron delocalization

pathway for efficient charge carrier transport, while a twisted chain usually interrupts the intramolecular charge transport.[19,39,77,80–82]

Due to the weak intermolecular interaction (Van der Waals forces or London forces), intermolecular transport becomes the bottle neck of charge transport in organic semiconductors. The intermolecular distance in organic materials is usually around 4 Å, which means that electrons have to jump from one molecule to the next by overcoming the energy barrier induced by intermolecular separation and self-induced polaronic effect. Thus, this kind of "hopping transport" is strongly field-dependent. This is also the starting point for the idea to synthesize D-A polymers with a shorter π-π distance in order to improve the charge carrier hopping.

Charge carrier transport in polymer semiconductors can be viewed at three levels: i) intramolecular (or intrachain), ii) intermolecular (or interchain), and iii) interdomain (or intergranular).[3,83] The intramolecular charge transport is mainly determined by the effective π-conjugation length along the polymer backbone. For aromatic ring systems, a highly coplanar polymer backbone can provide an extended π-electron delocalization pathway for efficient charge carrier transport. A proper choice of building blocks that can minimize main chain twisting is the key for achieving high intramolecular charge transport performance. One exception is for π-conjugated polymers having triple bound linkages, such as —C≡C—, where delocalization of π-electrons along the polymer backbone can still be maintained even if the polymer main chain is twisted. On the other hand, the intermolecular charge transport is governed by the intermolecular distances as well as the intermolecular π-π overlapping area. The charge transport between polymer chains is highly anisotropic. The most favored direction is along the π-π stacks, which usually has the shortest interchain distance among all directions and beneficial for charge hopping between chains. Charge carrier transport along the π-π stacking direction is not as fast as intramolecular charge transport, but it can still be quite efficient if a short π-π distance and a large π-overlap area are achieved. In an OTFT device, an edge-on chain orientation, where the π-π

stacking direction is parallel to the dielectric surface, is highly desirable.[71,80,84–86] Unlike most inorganic materials and small organic molecules, single crystals of polymer semiconductors are extremely difficult, if not impossible, to obtain due to their long and polydisperse chains. Consequently, polymer semiconductors inevitably compose of a significant fraction of amorphous phase. Polymer chains in the amorphous regions are twisted, randomly oriented, and loosely contacted, leading to very poor intramolecular and intermolecular charge transport properties. In a semicrystalline polymer thin film, the charge transport between crystalline domains, i.e., the interdomain charge transport, is determined by the size and the packing density of the amorphous region between the crystalline domains. To design polymers with intrinsically high charge transport performance at the intramolecular, intermolecular, and interdomain levels is a challenging task for polymer chemists, while to obtain highly crystalline, highly molecularly oriented polymer semiconductor thin films requires collective efforts from polymer physicists and device engineers.

1.3 About Organic Thin Film Transistors (OTFTs)

Transistors are often used as electronic switches that control the electrical current between the source and drain electrodes via an applied input voltage on the third terminal (known as the "gate"). The transistor effect was first observed in 1947 by John Bardeen and Walter Brattain in Bell Labs, and was further studied by William Shockley.[87] 13 years later, Kahng and Atalla developed the first metal-oxide-semiconductor field effect transistor (MOSFET) based on silicon.[88] Transistors replaced vacuum tubes in a very short period of time, and became the basic components of integrated circuits. Today, most transistors are still made of silicon. However, the costly silicon and a complicated fabrication process for MOSFETs limit this technology in certain applications. In 1983, Nara and coworkers reported the first organic thin film transistor (OTFT).[89]

Since then, OTFTs have received tremendous attention and are expected to be the key elements for next generation flexible electronics.

The operation mechanism of OTFTs is similar to that of MOSFETs. However, fabrication of OTFTs does not require high vacuum and high temperatures. Instead, OTFTs can be fabricated using low-cost solution processing techniques such as spin coating, inkjet printing, etc., at ambient conditions. In general, bottom-contact bottom-gate (BCBG) or bottom-contact top-gate (BCTG) structures (Figure 1-6) are the two most commonly adopted configurations of OTFTs. OTFTs are becoming more attractive since they not only can meet the requirements for large area coverage and flexibility, but also have achieved the high charge carrier mobility necessary to compete with silicon based transistors.

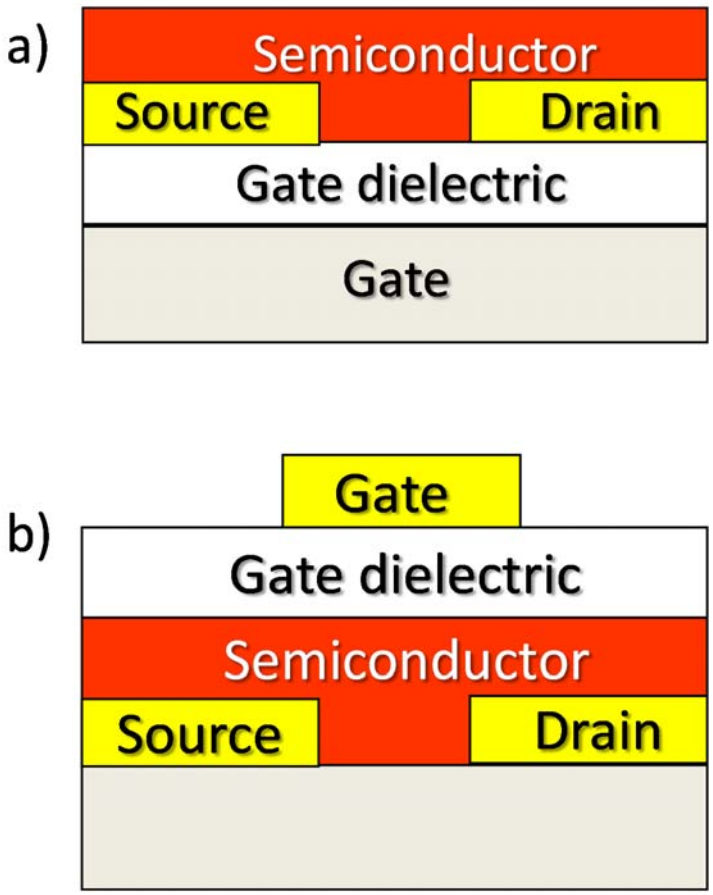

Figure 1-6 OTFTs device configurations: (a) A bottom-contact, bottom-gate (BCBG) OTFT and (b) A bottom-contact, top-gate (BCTG) OTFT.

1.4 Operation of OTFTs

As mentioned above, the operation mechanism of OTFTs is actually a derivative of MOSFETs. However due to the absence of depletion layers, most OTFTs can only operate in an accumulation regime.[90] For an OTFT with a p-type semiconductor, if a negative voltage is applied on the gate, a large concentration of holes close to the semiconductor/insulator interface will be induced to form a conducting channel (*on* state). If the gate voltage is biased positively, the holes in the channel region will be depleted (*off* state). For an OTFT with an n-type semiconductor, the voltage of the gate electrode is reversed and the majority carriers will be electrons instead of holes.

Charge carrier mobility is the most important parameter for OTFTs. For commercial applications, the maximum operation frequency of a device mainly depends on its mobility, as higher mobility would decrease the response time of the field effect transistors.[18] When the conducting channel just begins to form between the source and drain electrodes under a drain voltage (V_D), the value of the gate voltage is defined as the threshold voltage (V_{th}). The threshold voltage (V_{th}) is strongly affected by built-in dipoles, impurities, interface states and charge traps, which depend on the organic semiconductor and the insulator. I_{on} / I_{off} stands for the on-to-off current ratio. Usually an adequately large I_{on} / I_{off} is required for the transistor to be a qualified switch. The drain current I_D in the linear regime may be determined from Equation (1).

$$I_D = \left(\frac{WC_i}{L}\right)\mu_{FET}\left(V_G - V_T - \frac{V_D}{2}\right)V_D \qquad (1)$$

where μ_{FET} is the charge carrier mobility, C_i is the capacitance per unit area of the insulator, V_G is the gate voltage, W is the channel width and L is the channel length as shown in in Figure 1-7.

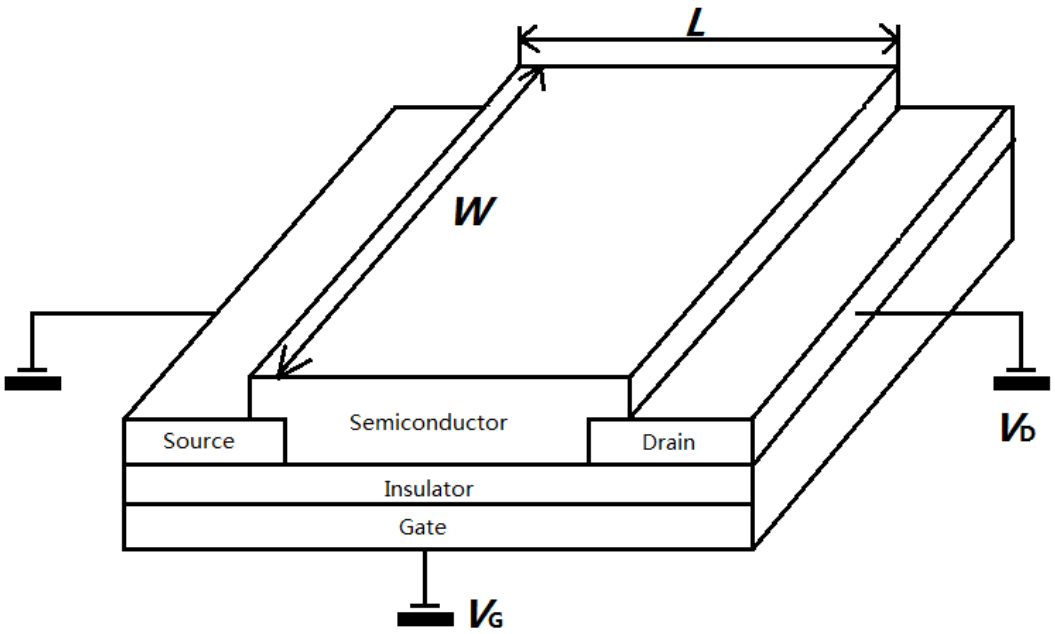

Figure 1-7 A 3-D structure of bottom contact, bottom gate OTFT device.

The current I_D tends to saturate (saturation regime) with the increment of drain voltage, and is modeled by Equation (2):

$$I_D = \left(\frac{WC_i}{2L}\right)\mu_{FET}(V_G - V_T)^2 \qquad (2)$$

In the saturation regime, μ_{FET} is proportional to the slope of the plot of $\sqrt{I_D}$ versus V_G, and the threshold voltage value can be estimated by the intercept.

It is important to note that the width to length ratio (W / L) must be equal or greater than 10 in order to minimize the effect of the fringe current flowing outside the channel. Otherwise the mobility will be overestimated.[3] Several other factors must be taken into account when using the above equations. The mobility obtained by the method above may not be accurate, since Equations (1) and (2) are only valid when the mobility is constant, while the mobility in OTFTs may depend on the gate voltage. In addition, the mismatch between the work function of metal electrodes and energy levels of the organic semiconductor would lead to the existence of contact resistance, which would affect the mobility value.

Obvious gate leakage currents are often observed. A gate leakage current originates from two contributions. The first contribution comes from the current flowing from the drain to the gate through the dielectric layer due to the gate-drain voltage difference, which exists in all transistor operation conditions (on and off). This portion of the gate leakage current is insignificant and can be ignored if an excellent dielectric such as thermal silicon dioxide is used.[91] The second contribution only exists when a gate voltage is applied. If the organic semiconductor is p-type, holes would be induced to form a conductive layer with the influence of gate voltage (Figure 1-8), which would act as an electrode to conduct current, causing a shift of the onset current on the output plots. This part of leakage current could be reduced by patterning the semiconducting material or isolating the individual devices to reduce the outside area of the organic semiconductor layer (Figure 1-9).[92]

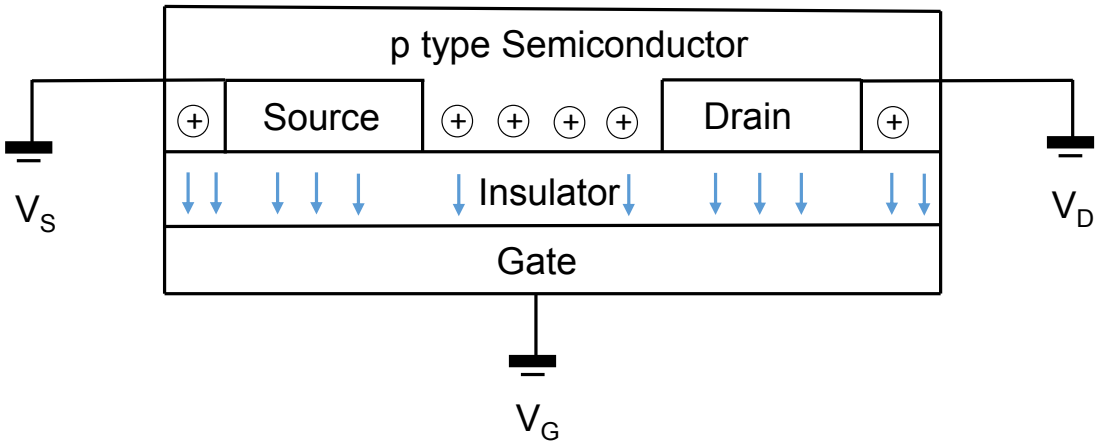

Figure 1-8 Leakage current from drain electrode and conductive organic layer to gate electrode.

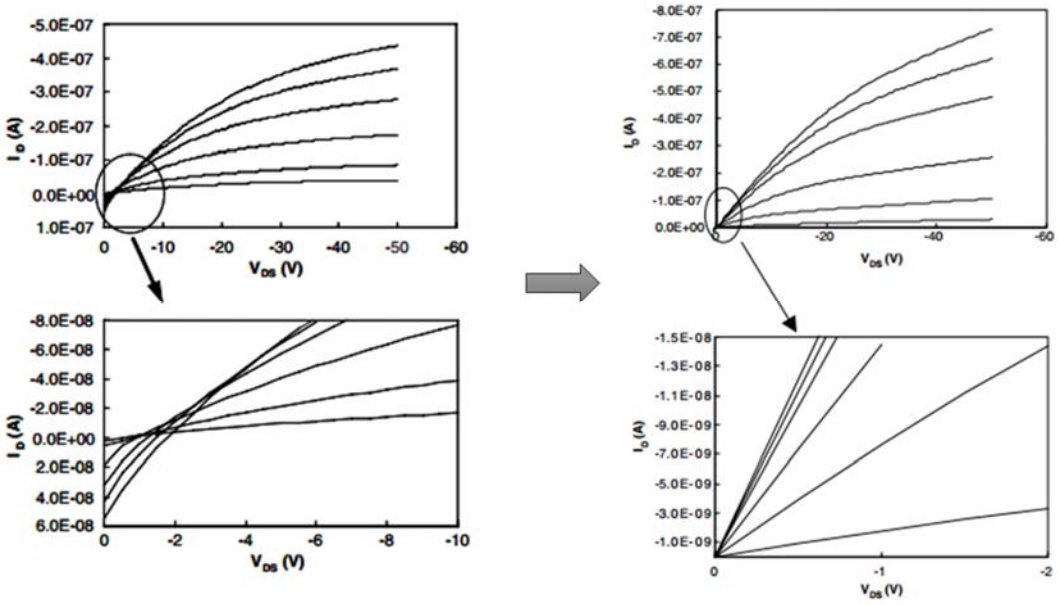

Figure 1-9 The leakage current in a **P3HT** device before and after patterning. (Reprinted with permission from H. Jia et al. (2006), Organic Electronics **7**(1): 16-21.[92])

1.5 Objectives of This Work

Despite the fact that some D-A polymers have achieved the mobility of amorphous silicon, higher mobility close to that of polycrystalline silicon (> 10 $cm^2V^{-1}s^{-1}$) is needed for a wider range of applications such as OLED displays and high frequency RFID tags. To further improve the charge carrier transport performance of polymer semiconductors, new building blocks, especially new electron acceptors, need to be developed. Inspired by the good performance of isoindigo small molecules and DPP based polymers, development of novel conjugated polymer semiconductors based on these two acceptors is the main objective of this work. The newly developed DHAP method is also explored to synthesize novel DPP-based polymers. New knowledge and findings acquired through this work may be useful for the discovery of the next generation high performance polymer semiconductors for printed electronics.

In this thesis, several novel semiconducting polymers are studied. Chapters 2, 3 and 4 discuss the synthesis, characterization and OTFT performance of novel indigo based conjugated

polymers, as well as the study on polymer structure optimization and charge transport polarity change by regioisomeric control. Chapter 5 describes the synthesis and characterization of pyrrolo[3,4-*c*]pyrrole-1,4(2*H*,5*H*)dione (1,4-DPP)-thiazole copolymer via direct (hetero)arylation polymerization. In Chapter 6, a novel pyrrolo[3,4-*c*]pyrrole-1,3-dione (1,3-DPP) building block is reported, the chemical, physical, and electrical properties of the resulted polymers are characterized. Details for the instrumentation, chemical synthesis, and device fabrication and characterization are included in the Appendix.

Chapter 2 Indigo Based Donor-Acceptor Conjugated Polymers

(This chapter is partially published in Journal of Materials Chemistry C (2014), Guo, C.; Sun, B.; Quinn, J.; Yan, Z.; Li, Y., **2**(21): 4289-4296.)

2.1 Introduction

A structural isomer of isoindigo, indigo (ID), has been widely used as a dye since 1600 BC (Figure 2-1).[93,94] The non-substituted indigo can form intramolecular hydrogen bonding between the oxygen and the hydrogen atoms of the two 1*H*-indol-3-one units, resulting in a highly coplanar geometry of the indigo molecule.[95–98] Indigo shows a much longer wavelength of absorption maximum (λ_{max} = 600-610 nm)[99,100] than that of isoindigo (λ_{max} = 520-540 nm)[101–104] in solutions, indicating the more effective conjugation of the former. Recently, indigo and its derivative, Tyrian Purple (6,6'-dibromoindigo), were used as semiconducting channel materials in OTFTs.[105–108] Devices based on these compounds have shown ambipolar charge transport characteristics with hole mobility of up to 0.40 $cm^2V^{-1}s^{-1}$. According to a recent report,[109] the hole and electron mobilities of indigo and Tyrian Purple calculated based on the Marcus's method[110] are very similar to those of isoindigo. The high mobility values both experimentally achieved and theoretically predicted for indigo and its derivatives suggest that indigo might be another promising electron acceptor building block for D-A polymers for organic electronics. In this chapter, the synthesis and properties of two polymers comprising indigo (acceptor) and bithiophene (donor) are reported, which are, to the best of our knowledge, the first D-A polymers based on indigo.

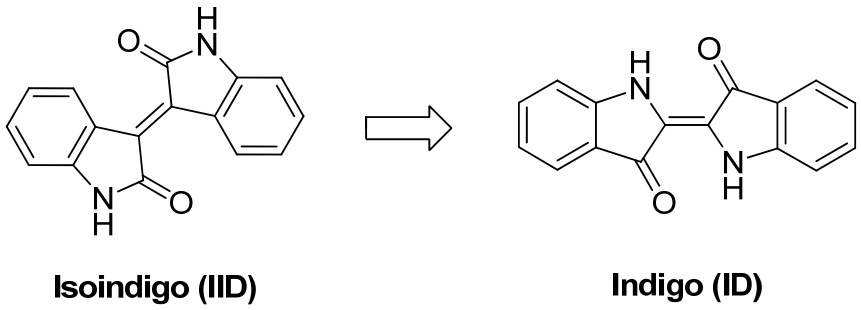

Isoindigo (IID) **Indigo (ID)**

Figure 2-1 Structures of isoindigo (IID) and indigo (ID).

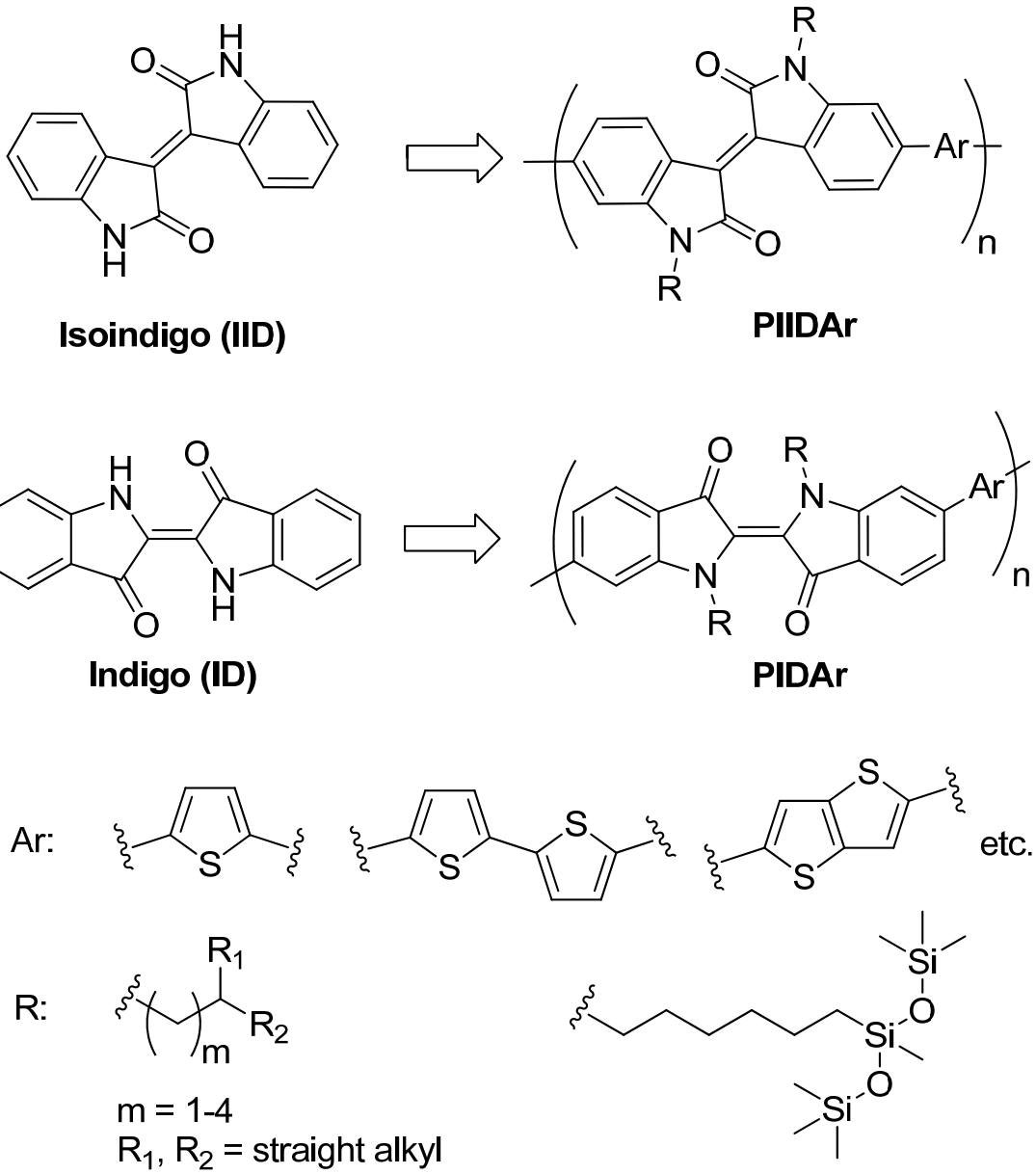

Figure 2-2 Structures of isoindigo (IID) and indigo (ID) and their polymers.

2.2 Results & Discussion

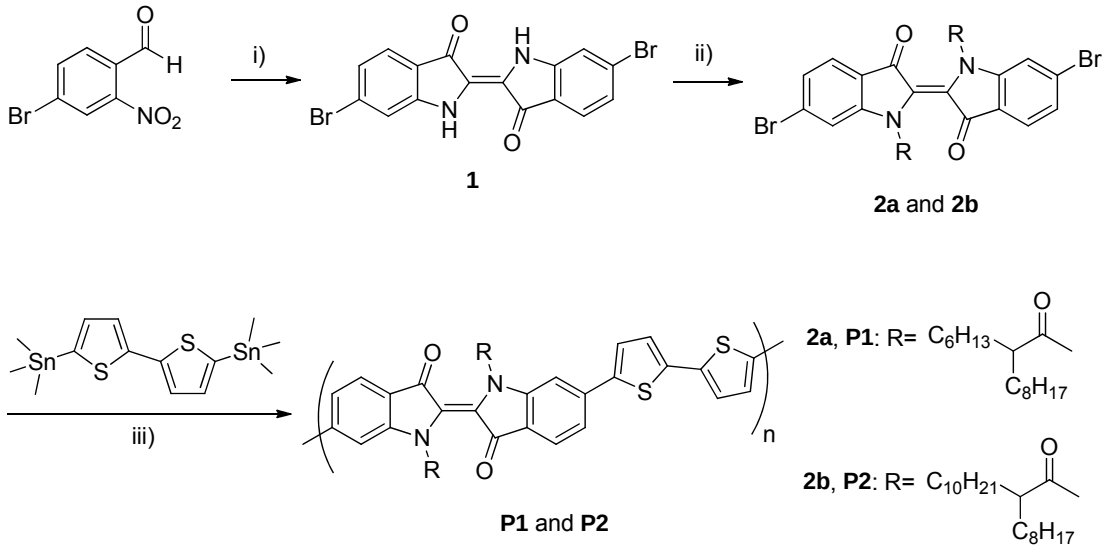

Scheme 2-1 Synthetic route to indigo monomers **2a** and **2b** and polymers **P1** and **P2**: i) NaOH/acetone/r.t.; ii) a) NaH/NMP/r.t, b) RCOCl/r.t.; iii) $Pd_2(dba)_3$/P(*o*-tolyl)$_3$/chlorobenzene/90 °C.

D-A polymers based on 6,6'-isoindigo and bithiophene, PIIDBT (Ar = bithiophene in Figure 2-2) were reported to show very high charge transport performance in OTFTs with hole mobility of up to 3.62 $cm^2V^{-1}s^{-1}$.[59] The closest structural analogue of their indigo based polymers would be PIDBT (Ar = bithiophene) as shown in Figure 2-2, where the indigo unit is connected at the 6 and 6' positions with the neighboring thiophene units. In this study, 6,6'-dibromoindigo or Tyrian Purple (**1**) was chosen, as the starting material to construct PIDBT polymers. Compound **1** was readily prepared in ~70% yield in one step by using a literature method (Scheme 2-1).[111] Substitution at the nitrogen atoms with suitable side chains such as alkyl group can improve the solubility of the resultant substituted indigo molecules and the final polymers. However, all the attempts to substitute compound **1** using an alkyl bromide such as 2-octadodecyl bromide in the presence of a base (e.g., K_2CO_3 and NaH) only led to the mono-alkylated products. Similar observations were also reported for the substitution of indigo.[112] Finally it was confirmed that the nitrogen atoms of **1** could be readily substituted with acyl groups by using the chemistry for

DPP.[113] Because most D-A polymers have very strong intermolecular interactions, they generally have poor solubility in organic solvents. Therefore, long branched side chains, 2-hexldecanoyl and 2-octyldodecanoyl groups, were used to substitute the nitrogen atoms of compound **1**, resulting in **2a** and **2b** in 34 % and 39 % yields, respectively (Scheme 2-1). It was reported that acyl substituted indigo compounds undergo photoisomerization from the stable *trans*-isomers to the less stable *cis*-isomers.[114,115] ^{1}H NMR spectra of **2a** and **2b** (Appendix A) indeed indicated the presence of ~85% of the trans-isomer and ~15% of the *cis*-isomer when the solutions were prepared under ambient light. Two PIDBT polymers, **P1** and **P2**, were synthesized via Stille coupling polymerizations of **2a** and **2b**, respectively, with 2,5'-bis(trimethyl)stannylbithiophene using $Pd_2(dba)_3$ / P(*o*-toyl)$_3$ as a catalyst system in chlorobenzene at 90 °C. Polymers were purified by Sohxlet extraction using sequentially acetone, hexane and chloroform, and then the remaining solid was heated in 1,1,2,2-tetrachloroethane (TCE) at 130 °C in a flask. Acetone and hexane were used to remove the catalyst residues and oligomers, respectively, chloroform and TCE were used to dissolve the higher molecular weight polymer fraction. **P1** showed poor solubility, which is essentially insoluble in chloroform and only 15% of the polymer was dissolved by hot TCE. The very poor solubility of **P1** indicates the very strong intermolecular D-A interactions of this polymer. **P2** with longer 2-octyldodecyl side chains showed improved solubility with 13% dissolved in chloroform and 59% dissolved in TCE, but ~28% of the polymer still remained insoluble. The molecular weights of these two polymers were determined by using GPC with chlorobenzene as an eluent and polystyrene as standards at a column temperature of 40 °C. The number average molecular weight (M_n) of **P1** dissolved with TCE was 13.5 kDa with a polydispersity index (PDI) of 3.50. The fraction of **P2** extracted with chloroform has a slightly lower M_n of 12.4 kDa. However, the weight average molecular weight (M_w) of **P2** was 131.4 kDa, which is much higher than that of **P1** (47.3 kDa), resulting in a very broad PDI of 10.6. The molecular weights of **P2** dissolved with TCE could not be measured because of its very poor

solubility in chlorobenzene used for the GPC measurements at 40 °C. However, we can reasonably assume that the molecular weight of **P2** from the TCE fraction should be higher than that of **P1**. The results used for the following discussions were obtained using fractions of **P1** and **P2** dissolved with TCE.

The thermal properties of polymers were characterized by thermogravimetric analysis (TGA) and differential scanning calarimetry (DSC). **P1** and **P2** showed the 5 % weight losses at 160 °C and 220 °C, indicating that these polymers are quite thermally labile (Figure 2-3). DSC diagrams clearly showed an exothermic peak at 258 °C in the first heating scan for both polymers (Figure 2-4, Figure 2-5). These results are reminiscent of the behavior of a DPP based polymer that also has acyl (2-dodecanoyl) substituents at the nitrogen atoms, where the 2-dodecanoyl substituents were found to be thermally unstable and the polymer started to lose side chains at ~180 °C.[113] Therefore the thermal instability observed for **P1** and **P2** is most likely caused by the thermally labile acyl groups.

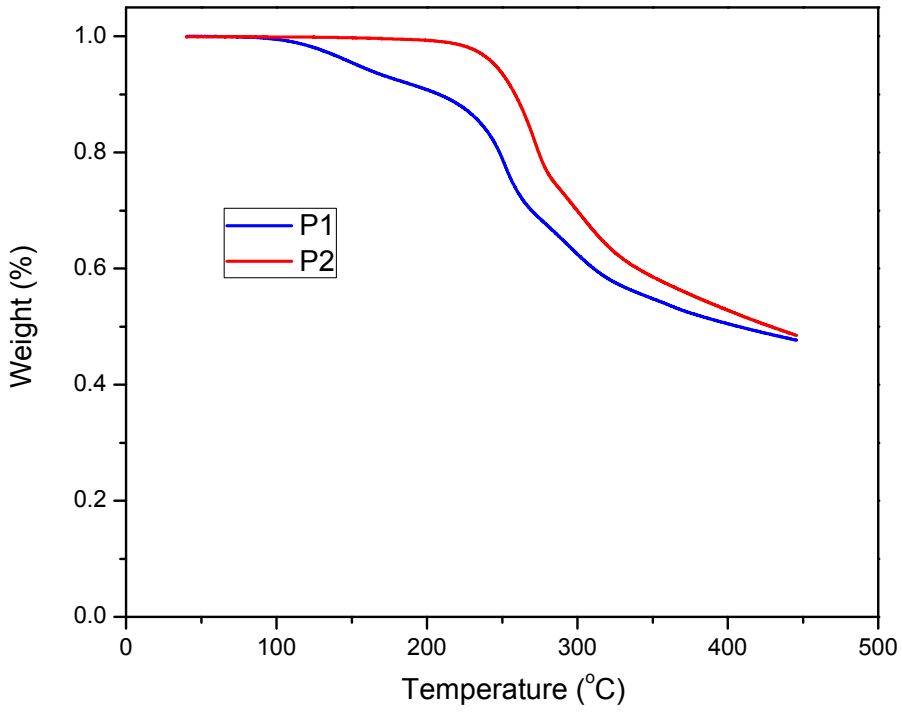

Figure 2-3 TGA curves of **P1** and **P2** with a heating rate of 10 °C·min^{-1} under N_2.

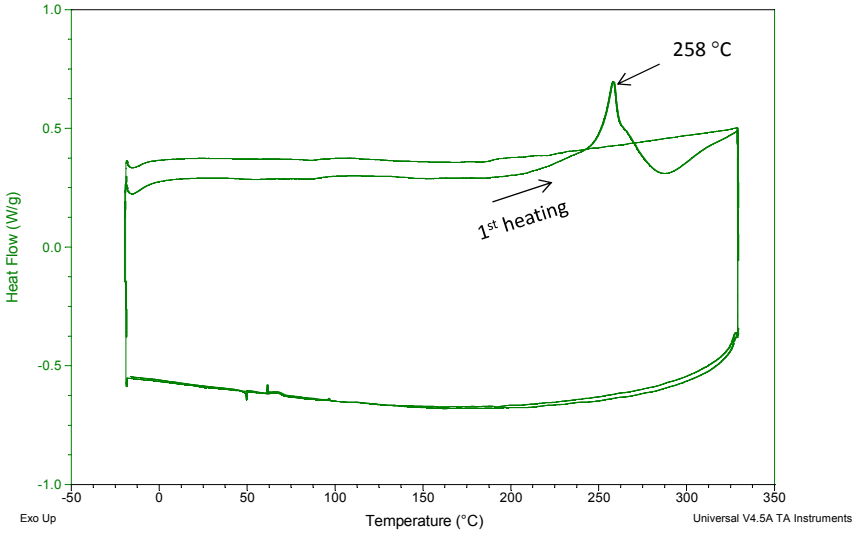

Figure 2-4 DSC curves of **P1** with a heating rate of 10 °C·min^{-1} under N_2.

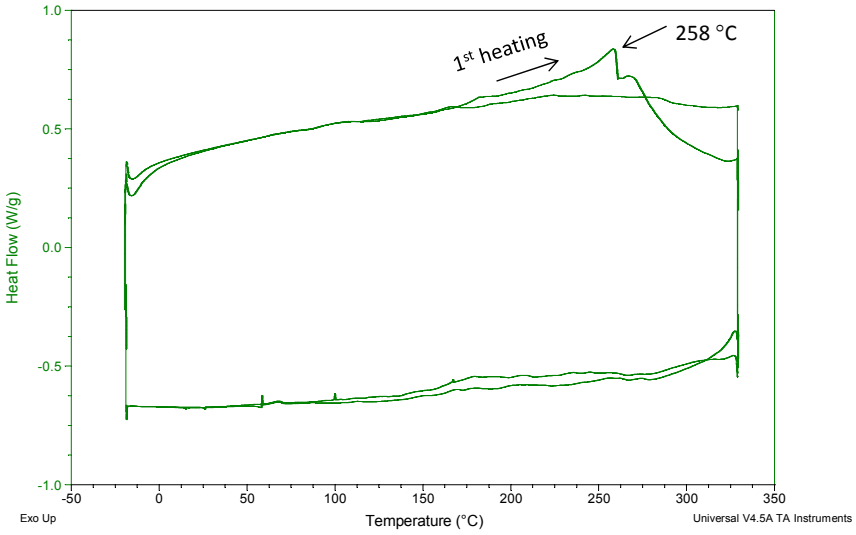

Figure 2-5 DSC curves of **P2** with a heating rate of 10 °C·min^{-1} under N_2.

Unlike the substituted isoindigo, where the substituents at the nitrogen atoms are distant from their neighbouring indol-2-one rings, substitution of indigo at the nitrogen atoms might cause twisting of the indigo moiety because the acyl side chains are very close to the C=O groups of the neighboring indol-3-one rings. An acetyl-substituted dimer compound, IDCOMe-BT-IDCOMe-BT, was simulated by performing density functional theory (DFT)

calculations using Gaussian 09W[116,117] to determine the influence of acyl substitution on the coplanarity of the indigo moiety. As shown in Figure 2-6, the dihedral angle between the two indole-3-one moieties in the acetyl-substituted indigo unit (φ_1) is ~23°. On the other hand, the dihedral angle between the two indole-2-one moieties in the methyl-substituted IID unit (φ_1) of an analogous dimer, IIDMe-BT-IIDMe-BT, is only ~11° (similar results were reported using the same simulation protocols).[20,118] We also simulated the methyl-substituted indigo dimer, IDMe-BT-IDMe-BT, the dihedral angle φ_1 increased further to 29°.(Figure 2-7) Additionally, the dihedral angles between the indigo and thiophene (φ_2 = 24°) and between two thiophene units (φ_3 = 15°) are also greater than the respective dihedral angles of its isoindigo dimer (Figure 2-7) (φ_2 = 20°; φ_3 = 5°). (Table 2-1) These results indicate that the acyl-substituted PIDBT (**P1** or **P2**) has a more twisted backbone than that of the alkyl-substituted PIIDBT.

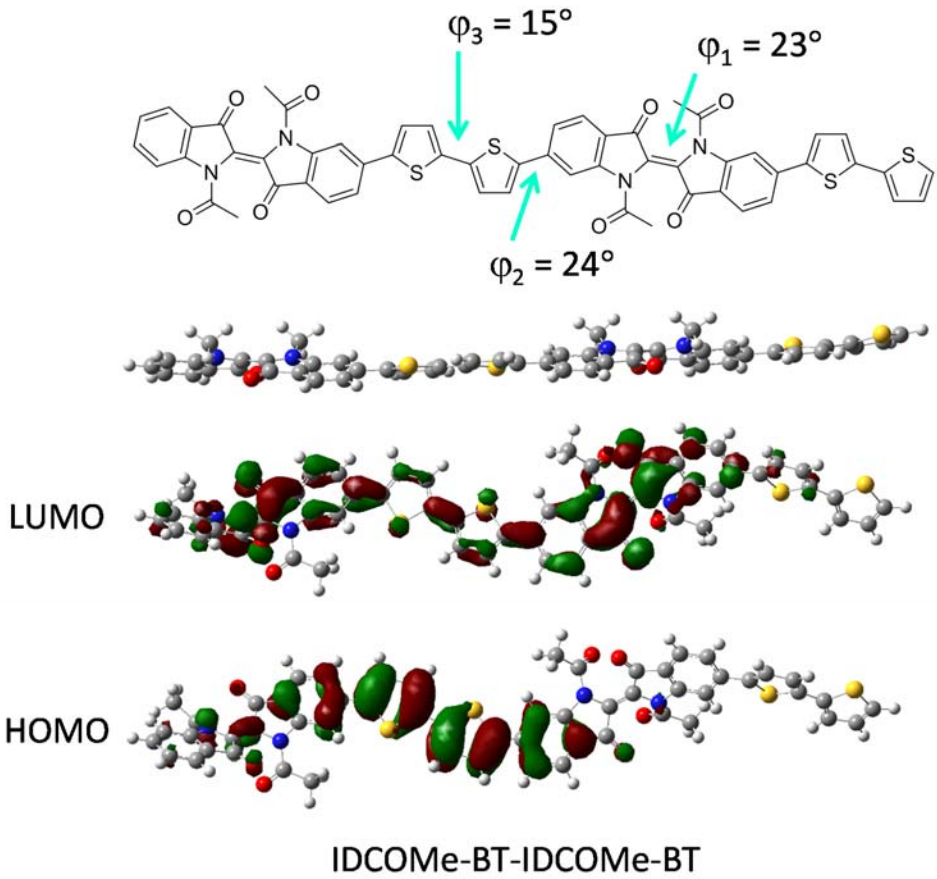

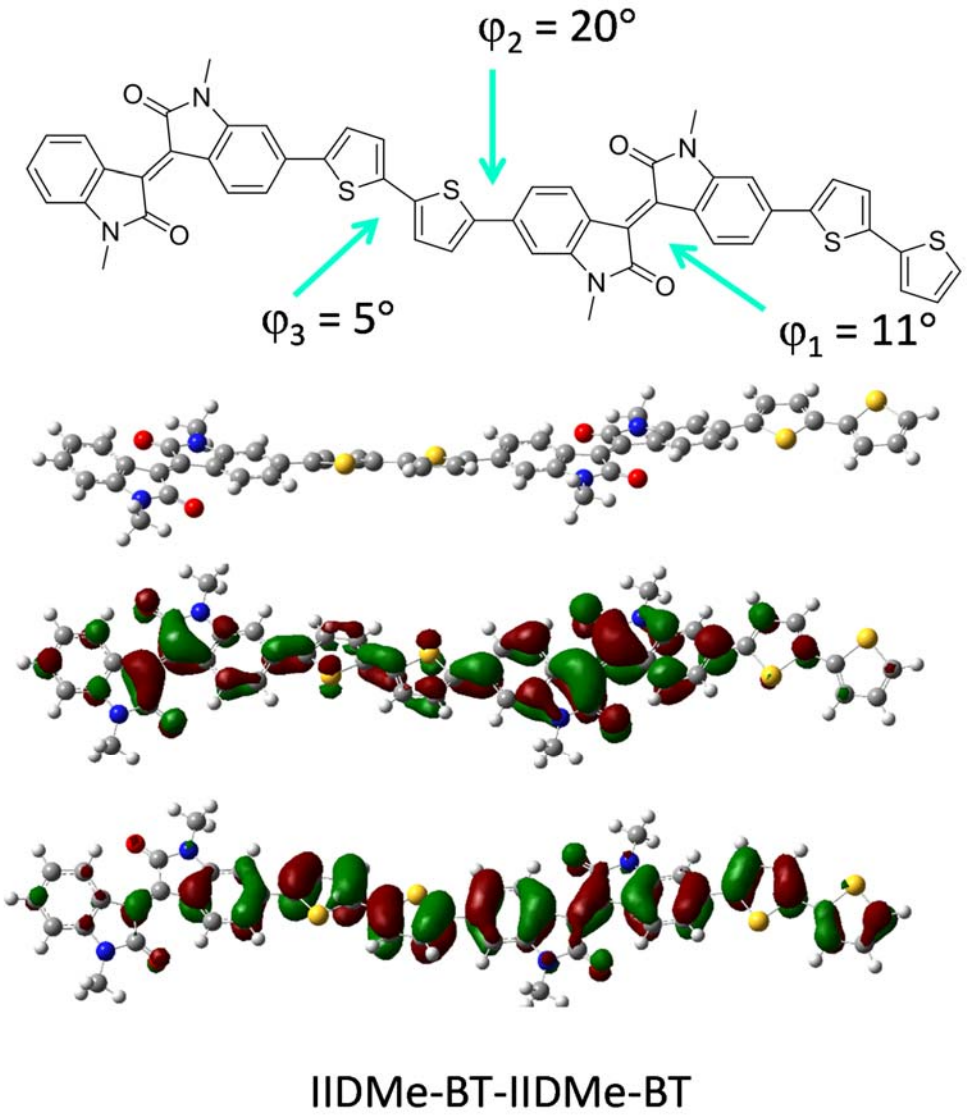

Figure 2-6 The chemical structure, geometry, LUMO orbital, and HOMO orbital of two model dimers IDCOMe-BT-IDCOMe-BT and IIDMe-BT-IIDMe-BT, which correspond to acyl-substituted PIDBT (**P1** or **P2**) and alkyl-substituted PIIDBT, respectively, obtained by performing density functional theory (DFT) calculations with B3LYP 6-31G* basis set.

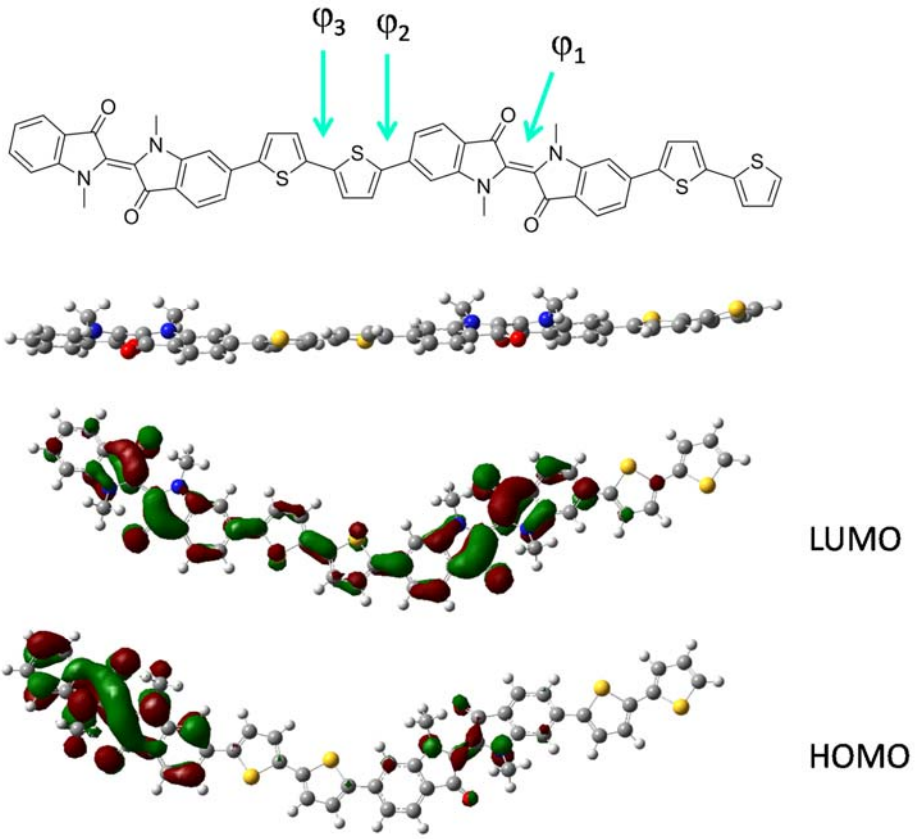

IDMe-BT-IDMe-BT

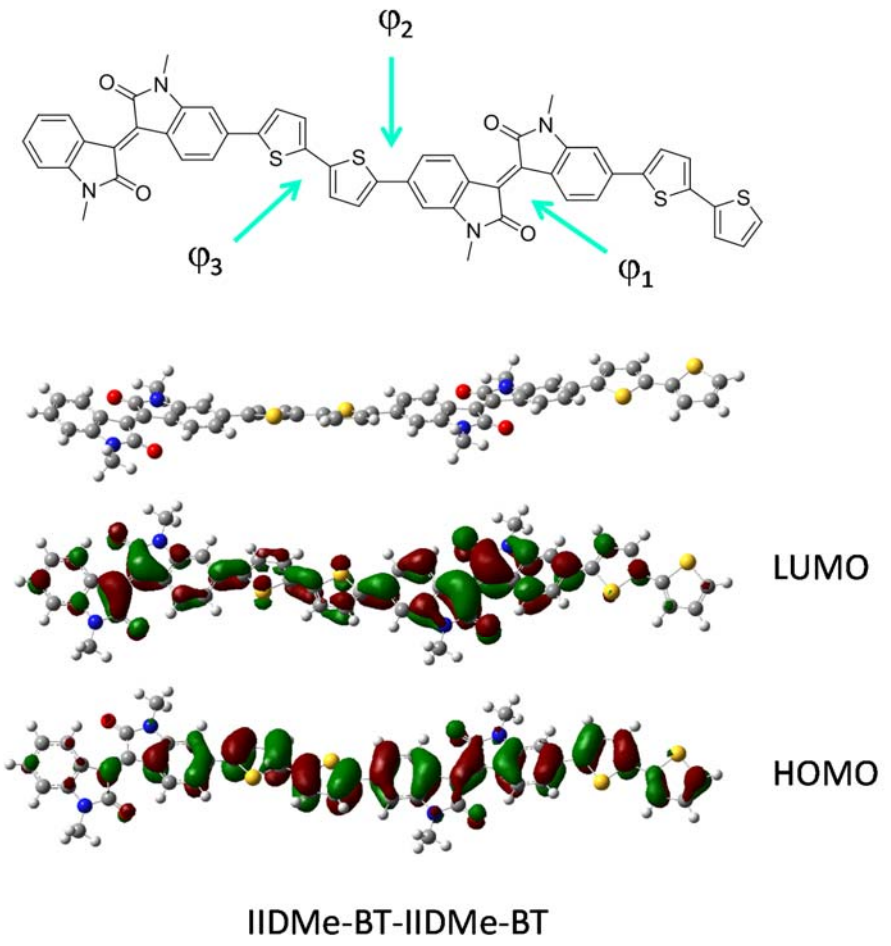

Figure 2-7 The chemical structure, geometry, LUMO orbital, and HOMO orbital of a model dimer IDMe-BT-IDMe-BT and IIDMe-BT-IDMe-BT obtained by performing density functional theory (DFT) calculations with B3LYP 6-31G*.

Table 2-1 Summary of computer simulation results of model compounds.

Entry	Model compounds	$\varphi_{1,}$ °	$\varphi_{2,}$ °	$\varphi_{3,}$ °	E_{HOMO}, eV	E_{LUMO}, eV	E_g, eV
1	IDMe-BT-IDMe-BT	29	24	1	-5.13	-2.80	2.33
2	IDCOMe-BT-IDCOMe-BT	23	24	15	-5.60	-3.00	2.60
3	IIDMe-BT-IIDMe-BT	11	20	5	-5.03	-2.89	2.14
4	IIDCOMe-BT-IIDCOMe-BT	17	22	14	-5.32	-3.30	2.02

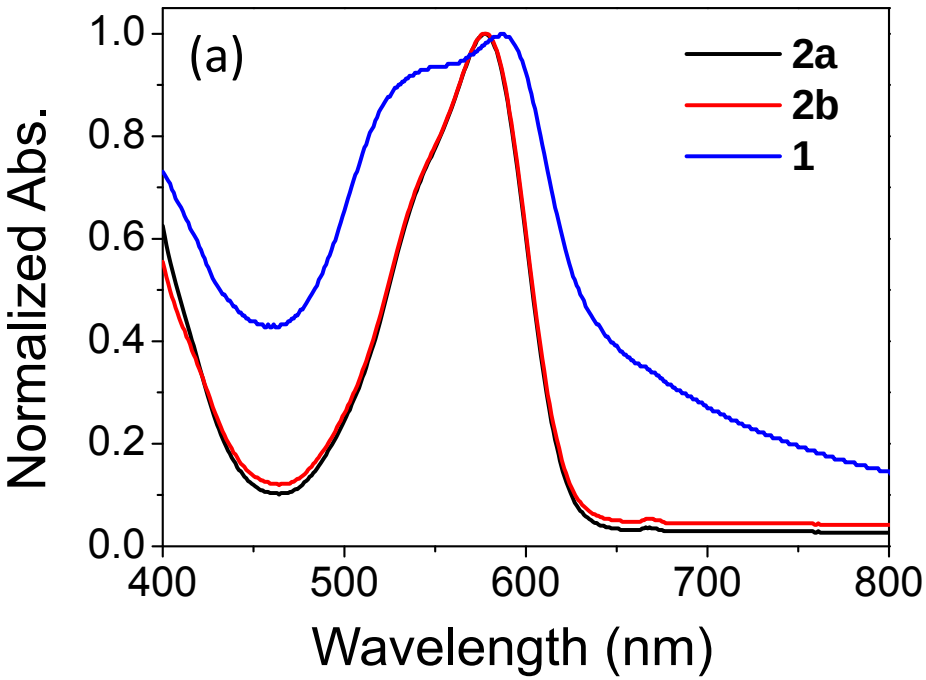
(a)
2a
2b
1
Normalized Abs.
Wavelength (nm)
1.0
0.8
0.6
0.4
0.2
0.0
400
500
600
700
800

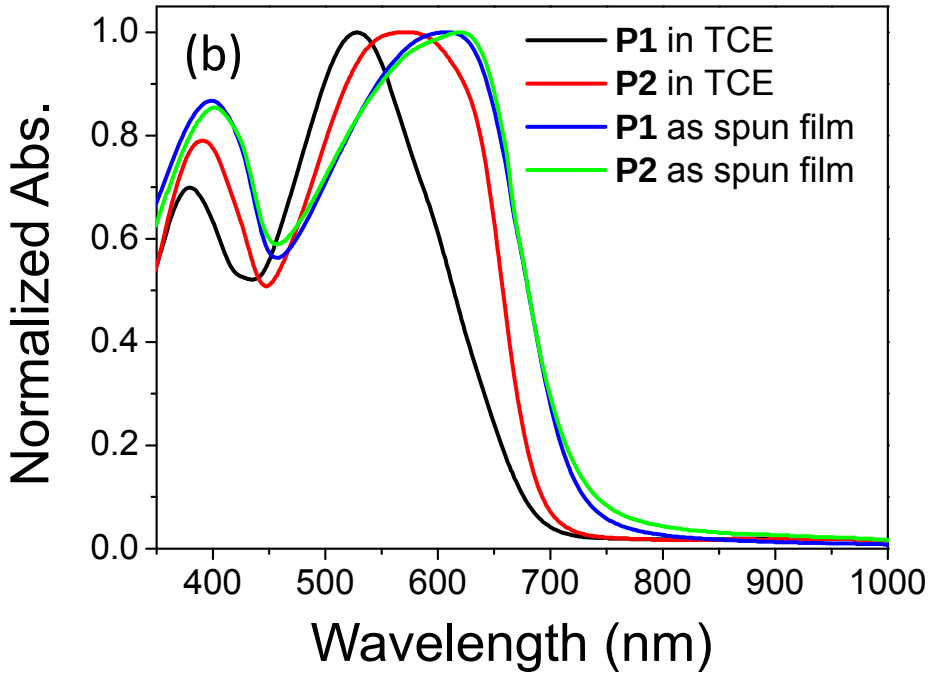
(b)
P1 in TCE
P2 in TCE
P1 as spun film
P2 as spun film
Normalized Abs.
Wavelength (nm)
1.0
0.8
0.6
0.4
0.2
0.0
400
500
600
700
800
900
1000

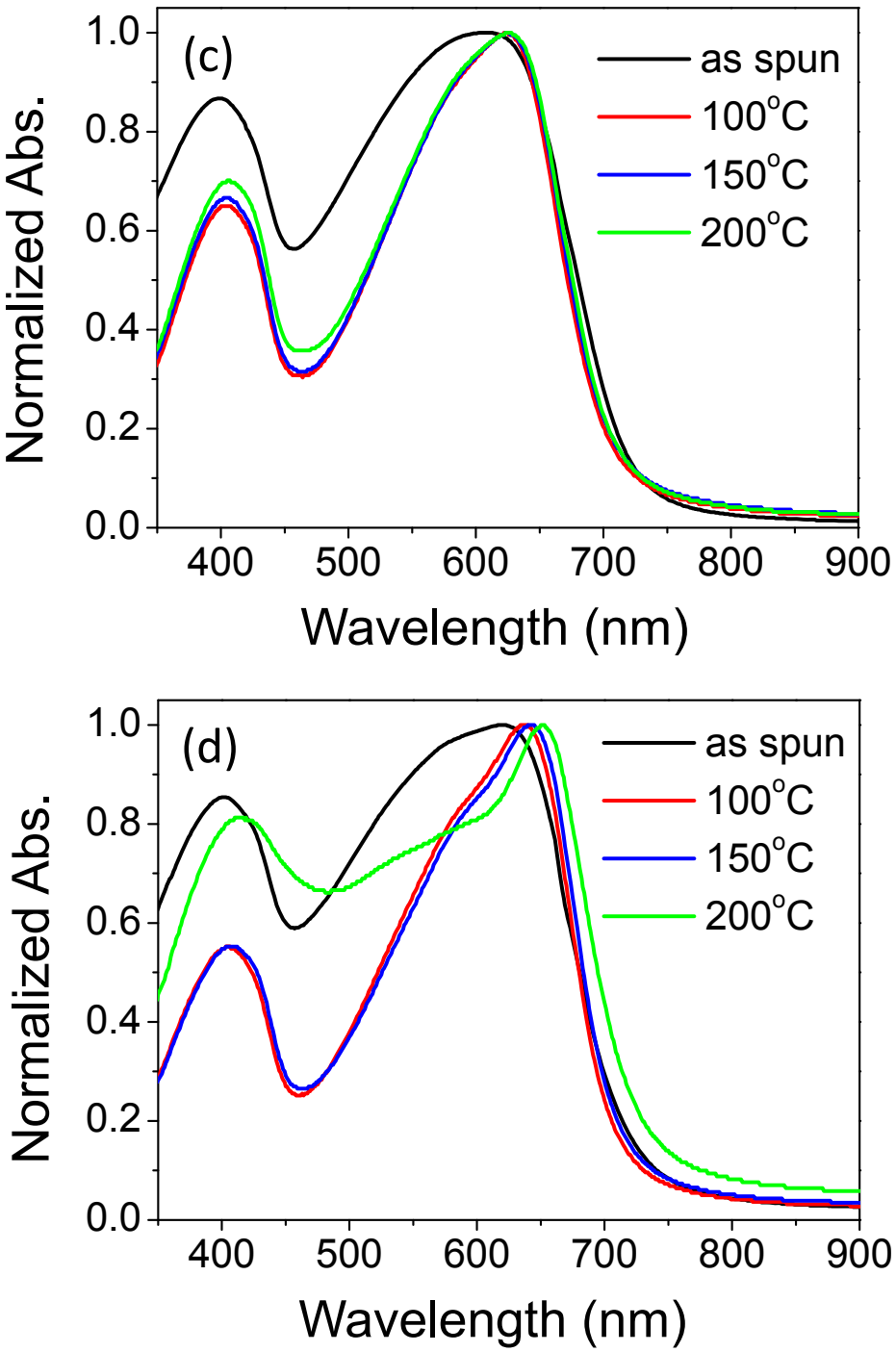

Figure 2-8 UV-vis absorption spectra of (a) **1**, **2a** and **2b** in TCE solutions; (b) **P1**and **P2** in TCE solutions and in thin films; (c) **P1** and (d) **P2** thin films on glass substrates annealed at different temperatures.

Compound **1** showed λ_{max} at 586 nm in TCE (Figure 2-8a), which agrees with the reported value of 585 nm.[119] The acyl-substituted **2a** and **2b** showed the λ_{max} at 576 nm in TCE solutions. The blue shift of ~10 nm in λ_{max} for **2a** and **2b** with respect to compound **1** is likely the result of the twisted indigo moiety caused by the acyl groups. Polymers **P1** and **P2** showed the λ_{max}'s at 527 nm and 572 nm in TCE solutions, and 607 nm and 620 nm in the solid state (as-spun films), respectively (Figure 2-8 b). The longer absorption wavelengths of **P2** than those of **P1** are considered due to the higher molecular weight and thus a longer effective conjugation length of **P2**. By comparing **P2** with its isoindigo analogue, PIIDBT-20 (Ar = bithiophene and R = 2-octyldodecyl in Figure 2-2), which showed the λ_{max}'s at 706 nm in solution and 701 nm in film,[59] the λ_{max}'s of **P2** both in solution and in the solid state blue shifted notably. This suggests that **P2** has a shorter main chain conjugation length than that of PIIDBT-20. As noted earlier, small molecular indigoids show longer absorption wavelengths and are structurally more conjugated than their isoindigo counterparts. The observed reduction in conjugation for **P2** compared with PIIDBT-20 might be accounted for by the substitution of indigo at the nitrogen atoms with the acyl groups, leading to a more twisted polymer backbone and reduced main chain conjugation. Another possible reason might be due to the presence of some *cis*-indigo units on the polymer backbone that might also cause serious twisting and less ordered packing of the polymer chains in the solid state, resulting in disrupted π-conjugation. It was reported that the λ_{max} of *cis*-IDCOMe is 438 nm (in benzene), which is significantly blue shifted compared with that of *trans*-IDCOMe (562 nm).[114]

When the thin films were thermally annealed, both polymers showed apparent red shifts in their UV-Vis spectra (Figure 2-8 c, d). The λ_{max} of the 100 °C-annealed **P1** thin film red shifted to 626 nm, indicating the improved coplanarity of the polymer backbone and more ordered chain packing. Further increasing the annealing temperature to 150 and 200 °C did not change the λ_{max} of **P1** thin films. For **P2** thin films, the λ_{max} red shifted progressively to 639 and 643 nm as the

annealing temperature increased to 100 and 150 °C, respectively. Thermal annealing would increase the chain ordering as manifested by the XRD results and might also transform the *cis*-indigo to the *trans*-indigo,[120] both would lead to more extended π-conjugation of the polymer backbone. The 200 °C-annealed **P2** sample showed a dramatically different absorption profile and a further red-shifted λ_{max} at 651 nm. This is most likely due to the removal of acyl side chains at such a high annealing temperature, which is indicated by the TGA data. The indigo units without substitution at the nitrogen atoms are almost coplanar.

The energy levels of the two polymers were determined by cyclic voltammetry (CV) in the solid thin film state using ferrocene as the standard that has a HOMO level of -4.8 eV.[121] **P2** showed reversible oxidative and reductive cycles (Figure 2-9). The HOMO / LUMO levels of **P2** were calculated by using the onset oxidative / reductive potentials to be -5.78 eV and -4.02 eV, respectively. The band gap of 1.68 eV determined by CV is close to the optical band gap of 1.74 eV calculated from the onset absorption wavelength of the as-spun film. The HOMO / LUMO levels of **P2** obtained by CV are slightly lower than those of PIIDBT-20 (E_{HOMO} = -5.70 eV; E_{LUMO} = -3.70 eV relative to the ferrocene standard).[59] The HOMO and LUMO levels of the as-spun **P1** film were determined to be -5.69 eV and -4.00 eV, respectively.

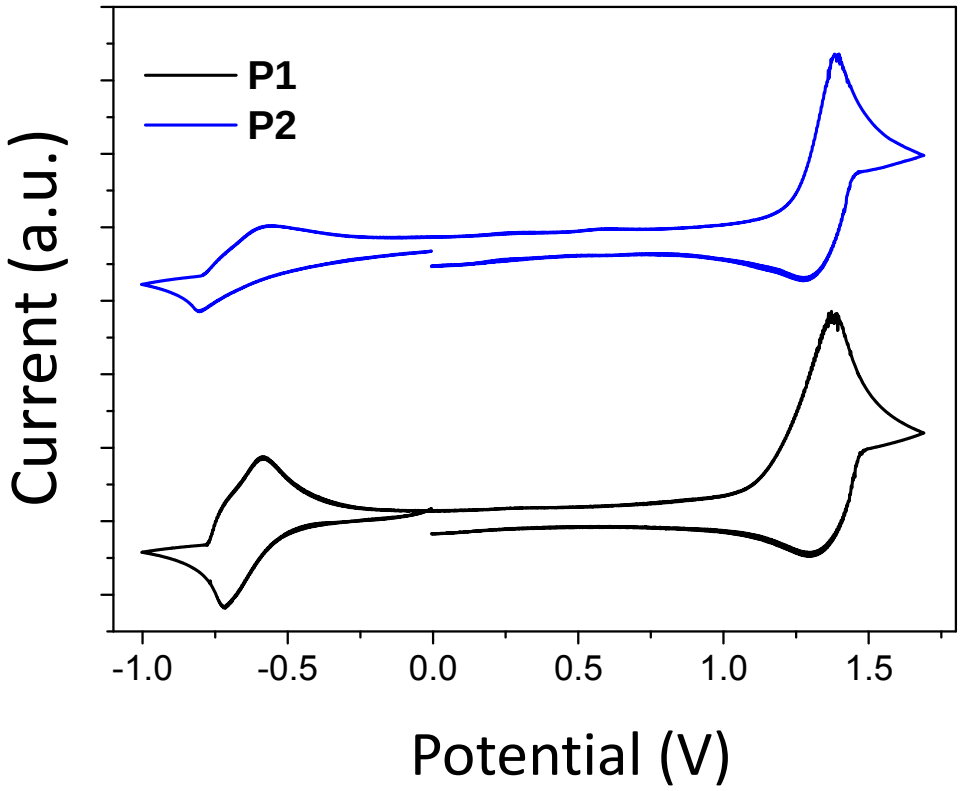

Figure 2-9 Cyclic voltammograms of as-spun **P1** and **P2** thin films measured in anhydrous CH_3CN solution using Bu_4NPF_6 as the electrolyte.

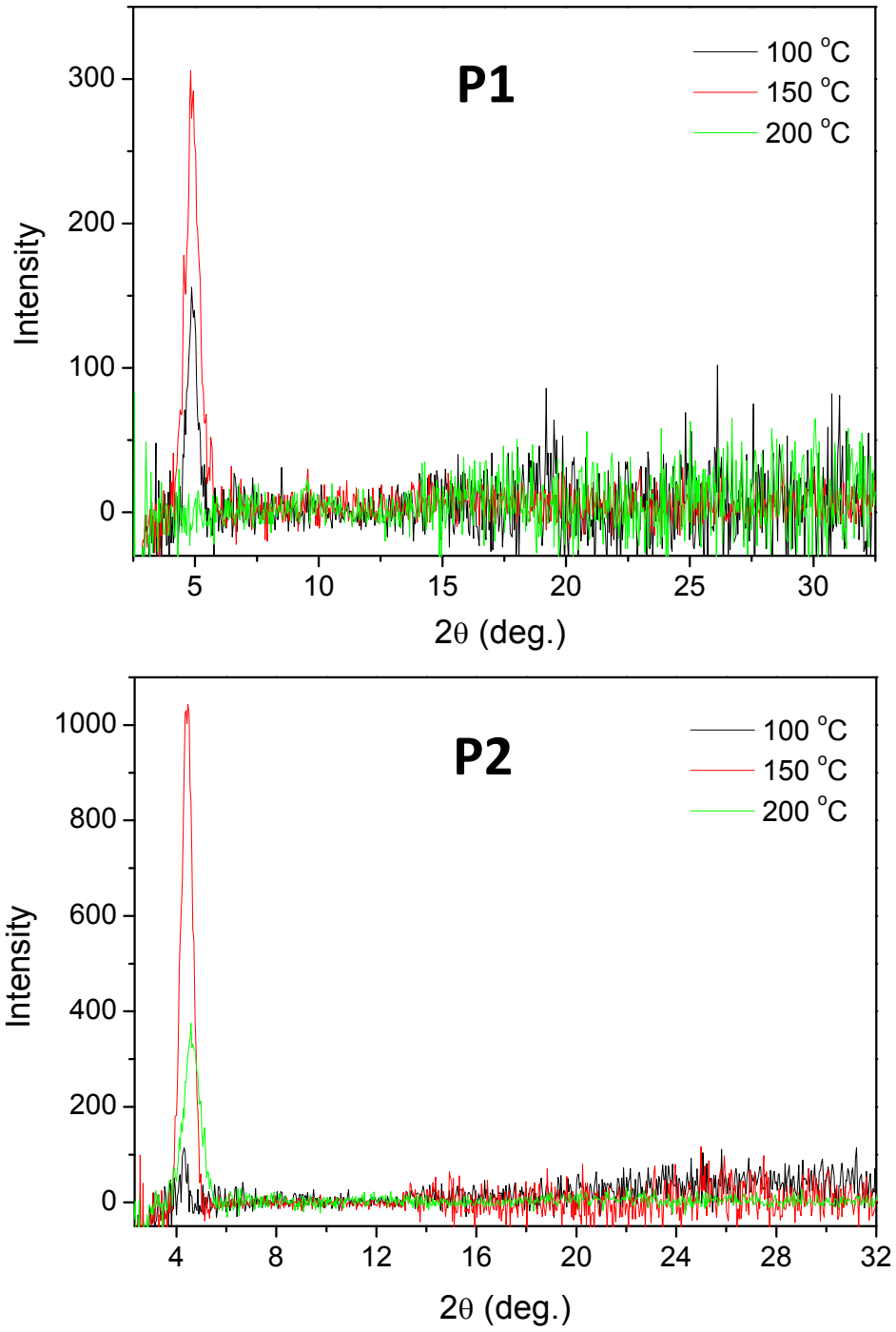

Figure 2-10 XRD diagrams obtained from spin-coated **P1** and **P2** thin film on silicon substrates annealed at 100, 150 and 200 °C.

The crystallinity of polymers was studied by using X-ray diffractometry (XRD) on polymer thin films spin coated on SiO_2 / Si substrates. The **P1** film annealed at 100 °C exhibited a weak primary at 2θ = 4.86°, which corresponds to a *d*-spacing distance of 1.82 nm (Figure 2-10). When the annealing temperature was increased to 150 °C, the primary peak shifted slightly to 2θ = 4.81° (*d*-spacing = 1.84 nm). Once the annealing temperature was raised to 200 °C, the primary peak disappeared. This is due to the loss of side chains at such a high temperature as corroborated by the thermal analysis data. The 100 °C-annealed **P2** film showed a very weak primary peak at 2θ = 4.30°, corresponding to a *d*-spacing distance of 2.05 nm. Increasing the annealing temperature to 150 °C improved the crystallinity of the **P2** film significantly, manifested by the much intensified peak at 2θ = 4.38° (*d*-spacing = 2.02 nm). Further increasing the annealing temperature to 200 °C, the intensity of the primary peak decreased and the d-spacing further decreased to 1.92 nm (2θ = 4.58°), again due to the loss of the side chains. Since the XRD diagrams of the crystalline polymer thin films only showed the primary peaks, the polymer chains of **P1** and **P2** most likely adopted a layer-by-layer lamellar packing motif,[84] a commonly observed crystal structure for most π-conjugated polymers in thin films.[17,20,31] Atomic force microscopic (AFM) images of the 100 °C- and 150 °C-annealed **P1** thin films contain large grains (Figure 2-11). The 200 °C-annealed **P1** thin film became more uniform, probably due to the removal of the side chains. On the other hand, all of the **P2** thin films are very smooth and the surface morphology was not much influenced by thermal annealing.

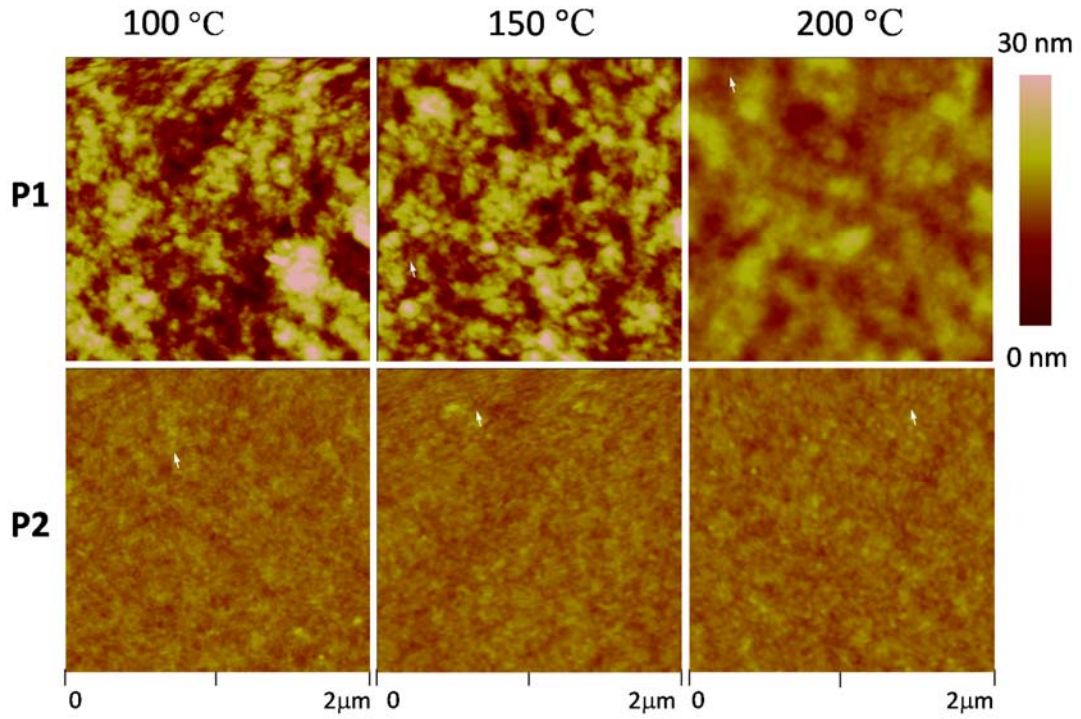

Figure 2-11 AFM images (2 μm × 2 μm) of **P1** and **P2** thin films (~50-60 nm) spin coated on silicon substrate annealed at 100, 150 and 200 °C under nitrogen.

P1 and **P2** were tested as channel semiconductors in top-gate, bottom-contact OTFTs. Heavily n-doped Si / SiO_2 wafer patterned with source and drain electrode pairs (with a channel length of 30 μm and a channel width of 1 mm) was used as the substrate. A polymer solution in TCE was spin coated on the substrate to form a polymer thin film (~30-50 nm), which was annealed at 100, 150, or 200 °C on a hot plate, followed by spin coating a CYTOP layer (~570 nm) as gate dielectric in a glove box under nitrogen. The capacitance per unit (C_i) of the dielectric layer (3.2 $nF \cdot cm^{-2}$) was determined from a metal-insulator-metal (MIM) structure. The devices were characterized in ambient conditions in the absence of light. Devices with **P1** or **P2** thin films annealed at 100 °C showed no field effect performance. Devices based on **P1** thin films annealed at 150 °C showed characteristic electron transport behavior with mobility as high as 6.6×10^{-4} $cm^2V^{-1}s^{-1}$ (current on-to-off ratios of ~10^4) (Figure 2-12 a,b). Devices based on **P2** thin films

annealed at 150 °C also exhibited electron transport performance with improved mobility of up to 1.1×10^{-3} $cm^2V^{-1}s^{-1}$ (on-to-off ratios of ~10^4) (Figure 2-12 c,d). No hole transport was observed for both polymers, which is presumably due to the large hole injection barrier between their low-lying HOMO levels and the work function of gold (~4.7-5.1 eV).[118,119] The much lower mobility values observed for **P1** and **P2** in comparison to its isoindigo counterpart, **PIIDBT-20**, and small molecular indigoids is considered originating from its poor main chain conjugation caused by the backbone twisting as discussed previously. The significantly poorer crystallinity of **P1** and **P2**, which originates from the main chain twisting and possible existence of *cis*-isomers, also accounts for their low mobility values. Further increasing the annealing temperature to 200 °C resulted in the absence of field effect performance for both polymers, due to the poor molecular ordering caused by thermal decomposition of side chains. Substitution of the indigo units with more desirable side chains to minimize the steric effect and eliminate the *cis*-isomers are expected to improve the backbone coplanarity and molecular organization for more efficient charge transport of the indigo based polymers. Notice that there is a shift of the onset current on the output plots caused by the leakage current, which origins were discussed in Chapter 1.4. Since TGBC structure was used in this case, it is very difficult to pattern the semiconductor layer or isolate individual devices to reduce the leakage current. However the leakage current is negligible compared to the on current, and would decrease with the increase of V_G. Therefore the leakage current would have little influence on the calculation of mobility.

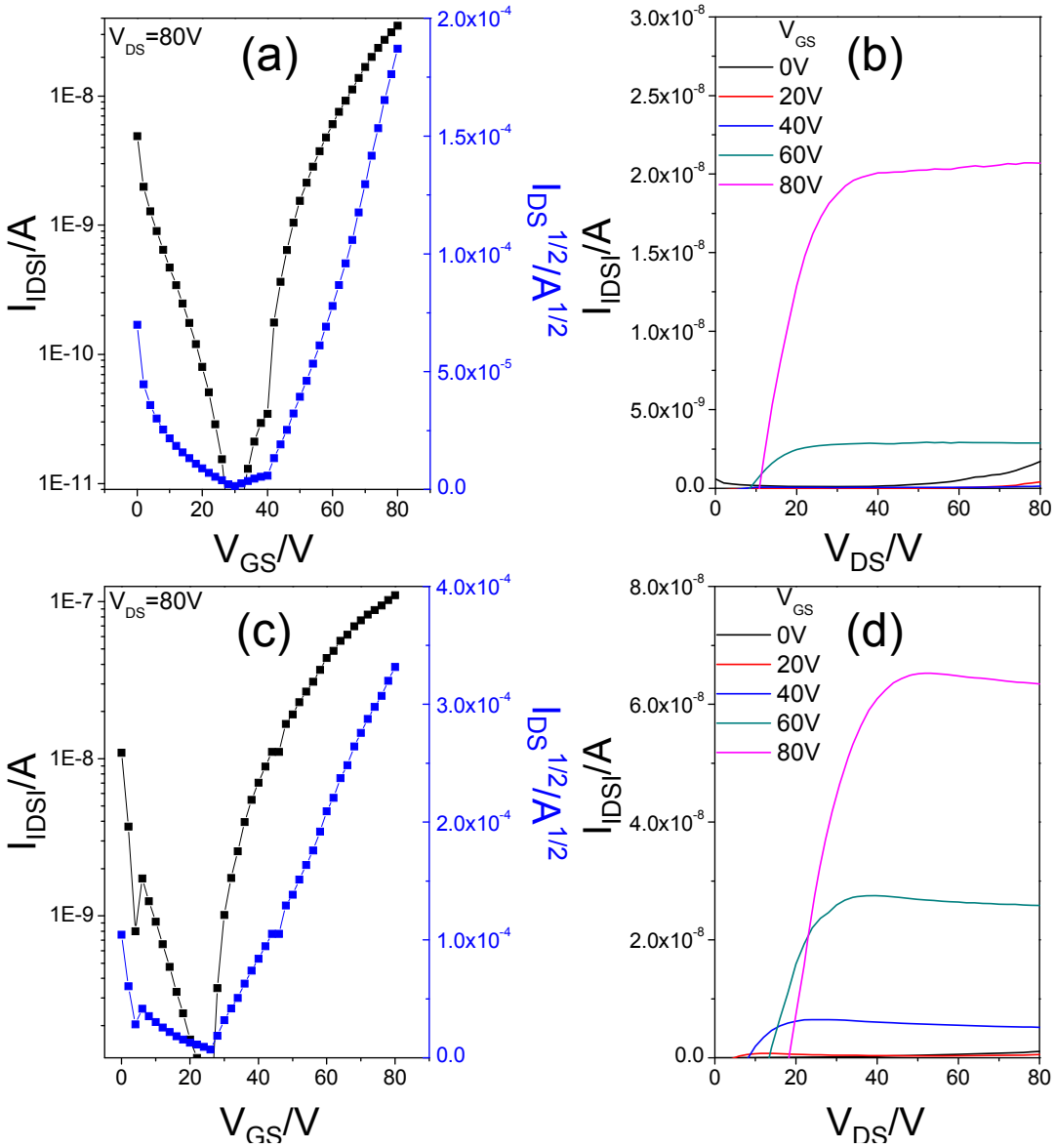

Figure 2-12 Transfer and output curves of OTFT devices with **P1** (a and b) and **P2** (c and d) thin films annealed at 150 °C for 20 min. Device dimensions: channel width (W) = 1 mm; channel length (L) = 30 μm.

2.3 Conclusion

Two new donor-acceptor polymers using indigo as the electron acceptor and bithiophene as the electron donor were reported. Acyl groups, 2-hexyldecanoyl (for polymer **P1**) and 2-octyldodecanoyl (for polymer **P2**), were used as the side chains to render these polymers

soluble in organic solvents. The strong electron-withdrawing capability of the indigo moiety was manifested with the low-lying HOMO / LUMO levels, -5.69 eV / -4.00 eV for **P1** and -5.78 eV / -4.02 eV for **P2**. Due to the strong intramolecular D-A charge transfer, rather low band gaps (~1.7 eV) were observed for both polymers. The acyl side chains were found to cause serious twisting of the polymer backbone. These side chains are thermally labile and start to decompose at 160 °C for **P1** and 220 °C for **P2**. Thermal annealing led to significant red shifts of the absorption spectra, which originated from the formation of more coplanar backbone structures. **P1** and **P2** showed characteristic electron transport performance in OTFTs with electron mobilities of up to 6.6×10^{-4} $cm^2V^{-1}s^{-1}$ and 1.1×10^{-3} $cm^2V^{-1}s^{-1}$, respectively. The lower than expected field effect performance of these polymers in comparison to their counterpart isoindigo polymers was considered due to the backbone twisting and the presence of *cis*-indigo units that are undesirable for extended delocalization of electrons. Work on minimizing the backbone twisting to improve the charge transport performance of this new class of polymers is introduced in Chapter 3.

Chapter 3 Indigo Based Conjugated Polymer Bearing Thermocleavable Side Chains

(This chapter is partially published in Journal of Materials Chemistry C (2015), Guo, C.; Quinn, J.; Sun, B.; Li, Y., **3**: 5226-5232.)

3.1 Introduction

We have shown that indigo is a promising building block for D-A conjugated polymers in the previous chapter. In this chapter, the goal is to minimize the backbone twisting by eliminating the side chain effect and the presence of the unwanted *cis*-indigo isomeric units.

As discussed in Chapter 2, Indigo derivatives, which are known as commercial dyes,[93,94] have recently attracted attention as semiconductors since they demonstrated good semiconductor performance in OTFTs.[105–108,122–124] Previously Tyrian purple, a naturally occurring indigo dye, was successfully used as an acceptor and bithiophene as a donor to construct D–A polymers **P1** and **P2**.[122] The nitrogen atoms in Tyrian purple are suitable for substitution with acyl side chains to render the resultant polymers soluble. However, the *N*-substitution led to a large dihedral angle between two lactam units, causing serious twisting of the polymer backbone. In addition, *cis*-indigo units might exist due to the steric effect of the side chains. Consequently, zigzagged and twisted polymer main chain conformations would form, which limits electron delocalization. Therefore, if the solubilizing side chains on indigo could be removed after the deposition of polymer thin films, the charge transport performance of indigo-based polymers is expected to improve.

Recently, Sariciftci *et al*. introduced a thermally labile protection group, *tert*-butoxy carbonyl (*t*-Boc) to indigo derivatives.[123] Upon thermal annealing at a moderately high temperature (>150 °C), *t*-Boc groups were removed to regenerate the planar unsubstituted indigo moiety. Although this strategy is successful for solubilizing small indigo molecules, the solubility of the

t-Boc substituted indigo-*co*-bithiophene polymer, poly(DTI), is very poor. Nonetheless, they used a potentiodynamic electropolymerization technique to form poly(DTI) films and observed a photoconduction effect of this polymer in diodes. In this study, we substituted Tyrian purple with *t*-Boc, and copolymerized it with another monomer unit, benzo[1,2-*b*:4,5-*b'*]dithiophene that bears bulky alkoxy side chains as a donor. The resultant polymer **PIDBDT** (**P3**) is readily solution processable. Upon thermal removal of the *t*-Boc groups, the indigo units of the resultant polymer become highly coplanar, affording promising electron transport performance in OTFTs (Figure 3-1).

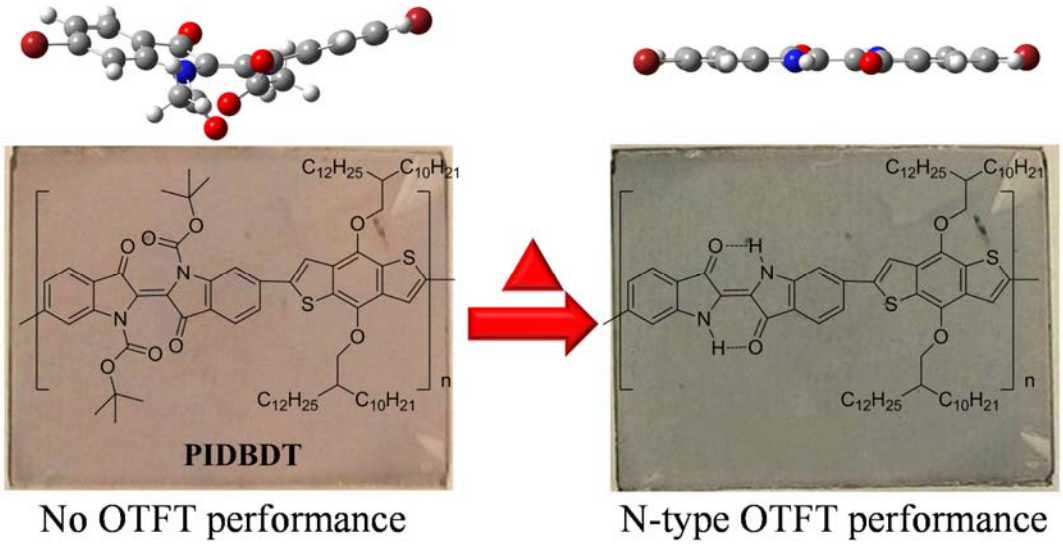

Figure 3-1 A new n-type semiconducting polymer based on indigo with thermocleavable *tert*-butoxycarbonyl (*t*-Boc) groups **PIDBDT** (**P3**) synthesized and used as an active layer in organic thin film transistors.

3.2 Results & Discussion

Tyrian purple which has two functional bromo groups at the 6 and 6' positions, can potentially be used as a monomer for constructing polymers. Nevertheless, Tyrian purple shows extremely poor solubility in common organic solvents. Substitution at the nitrogen atoms of Tyrian purple with acyl groups could improve the solubility of the substituted Tyrian purple

derivatives.[122] However, computer simulations of Tyrian purple (*trans*-IDBr) and the acetyl substituted Tyrian purple (*trans*-IDBrAc) by density functional theory (DFT) calculations with Gaussian 09W[116,117] indicated that the acyl substitution would cause serious twisting of the substituted Tyrian purple molecule (Figure 3-2 and Table 3-1). Such a large deviation from coplanarity would be destructive for a long range delocalization of π-electrons along the polymer main chain, deteriorating the charge transport performance of the polymer. Therefore, it would be desirable if the side chains on the indigo units could be removed after the polymer film is solution processed to retrieve the highly coplanar geometry of the unsubstituted indigo units.

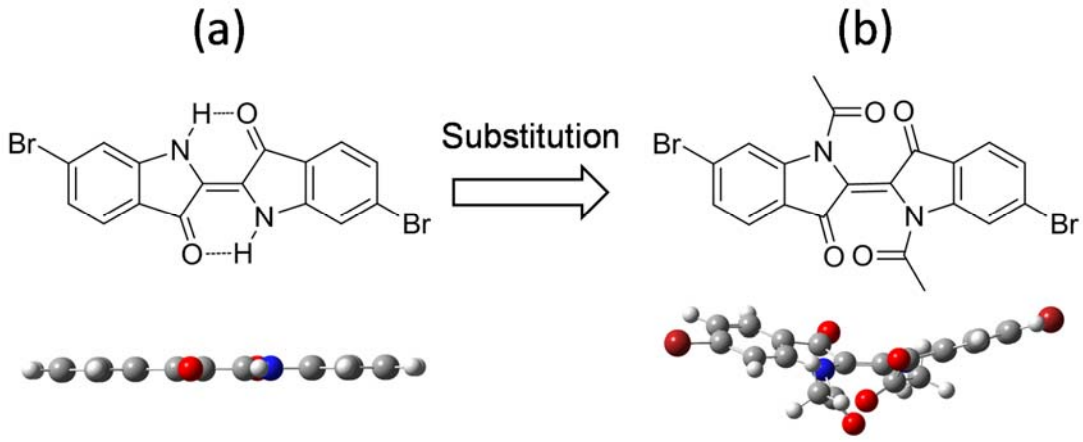

Figure 3-2 The chemical structures and geometries of model compounds (a) Tyrian purple, (*E*)-6,6'-dibromo-[2,2'-biindolinylidene]-3,3'-dione (*trans*-IDBr), and (b) the acetyl substituted Tyrian purple, (*E*)-1,1'-diacetyl-6,6'-dibromo-[2,2'-biindolinylidene]-3,3'-dione (*trans*-IDBrAc). The molecular geometries were obtained by density functional theory (DFT) calculations.

Table 3-1 Summary of computer simulation results of model compounds, *trans*-IDBr and *trans*-IDBrAc.

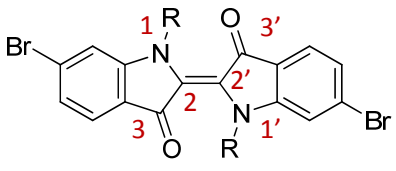

R = H (*trans*-IDBr), 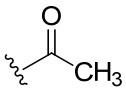 (*trans*-IDBrAc)

Model compound	Dihedral angle, °		
	N(1)-C(2)-C(2')-N(1')	N(1)-C(2)-C(2')-C(3')	C(3)-C(2)-C(2')-C(3')
trans-IDBr	180	0	180
trans-IDBrAc	173.3	22.6/24.5	139.5

t-Boc is a well-known thermally removable functional group, which was recently used as a thermocleavable functionality for small molecule and polymer semiconductors.[123,125] We designed and synthesized a D-A polymer, **P3**, whose repeat unit is comprised of a *t*-Boc-substituted indigo (ID) unit and a benzo[1,2-*b*:4,5-*b'*]dithiophene (BDT) unit (Scheme 3-1). The long branched 2-decyltetradecyloxy group on the BDT unit was used to provide addtional solubilizing ability to render **P3** soluble. After thermal removal of *t*-Boc groups, the high coplanarity of the indigo units would be recovered. The starting material, compound **1** (Tyrian purple), was synthesized as indicated in charpter **2**,[111] which was substituted with the *t*-Boc groups using di-*tert*-butyl 3,3'-dioxo-[2,2'-biindolinylidene]-1,1'-dicarboxylate in 82.7 % yield following a literature method.[126] With *t*-Boc substitution, compound **3** could be easily dissolved and purified by recrystallization. The Stille coupling polymerization between **3** and (4,8-bis((2-decyltetradecyl)oxy)benzo[1,2-*b*:4,5-*b'*]dithiophene-2,6-diyl)bis(trimethylstannane) (**5**) in the presence of tris(dibenzylideneacetone)-dipalladium (Pd_2dba_3)/tri(*o*-tolyl)phosphine (P(*o*-tolyl)$_3$) as a catalyst was carried out in chlorobenzene at 110 °C for 60 h. The obtained crude polymer product was subjected to consecutive Soxhlet extraction with acetone, hexane, and chloroform. The yield of the polymer extracted with chloroform was 62.8 % after removing the oligomers by acetone and hexane. GPC with chlorobenzene as an eluent and polystyrene as standards at 40 °C was used to determine the molecular weight of **P3**. The number average molecular weight (M_n) of the polymer fraction extracted with chloroform is 42.1 kDa with a polydispersity index (PDI) of 2.74.

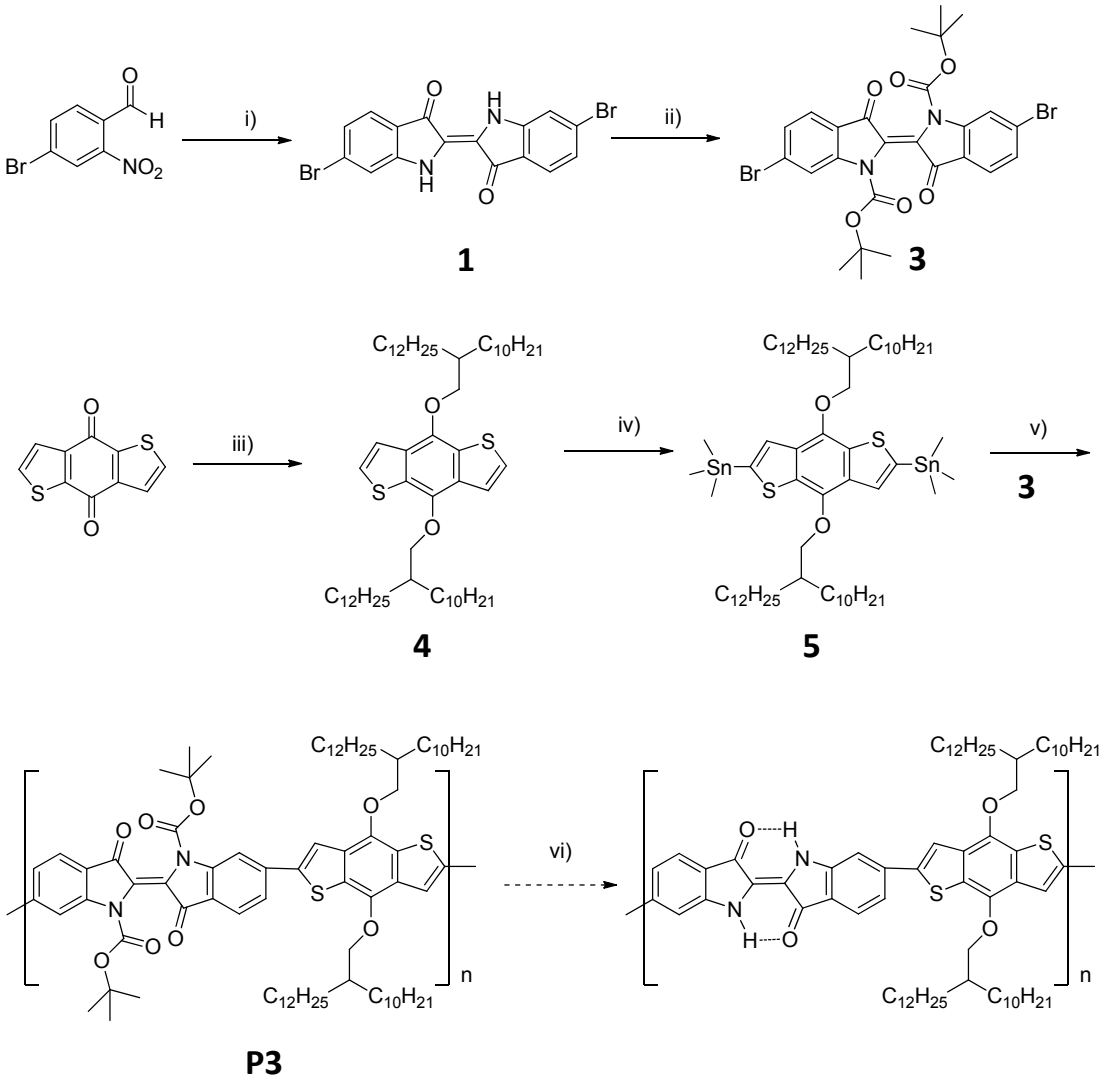

Scheme 3-1 The synthetic route to **P3**. Reagents and conditions: i) NaOH/aceton/r.t.; ii) 4-dimethylaminopyridine/di-*tert*-butyldicarbonate/DMF/0 °C to r.t.; iii) NaOH/Zn/H_2O/11-(bromomethyl)tricosane/tetrabutylammonium bromide/reflux; iv) *n*-butyllithium/trimethyltin chloride/THF/-78 °C to r.t.; v) Pd_2dba_3/ P(*o*-tolyl)$_3$/110 °C; vi) heating at ≥170 °C.

The thermocleavable behaviour of the *t*-Boc groups in **P3** was examined by TGA at 10 °C min^{-1} under nitrogen. As shown in Figure 3-3, the polymer started to lose weight at ~170 °C and the thermogram reached a flat region with a weight loss of ~15 % at ~240 °C. This weight loss coincided with the calculated mass of the *t*-Boc groups (~15 %) in **P3**, indicating almost all the

t-Boc groups were removed. At a higher temperature above ~290 °C, the polymer began to undergo a second abrupt weight loss. Since the indigo moiety is quite thermally stable (the melting point of indigo is 390-392 °C),[127] the second decomposition step was probably due to the decomposition of the alkoxy-substituted BDT units.[128–130]

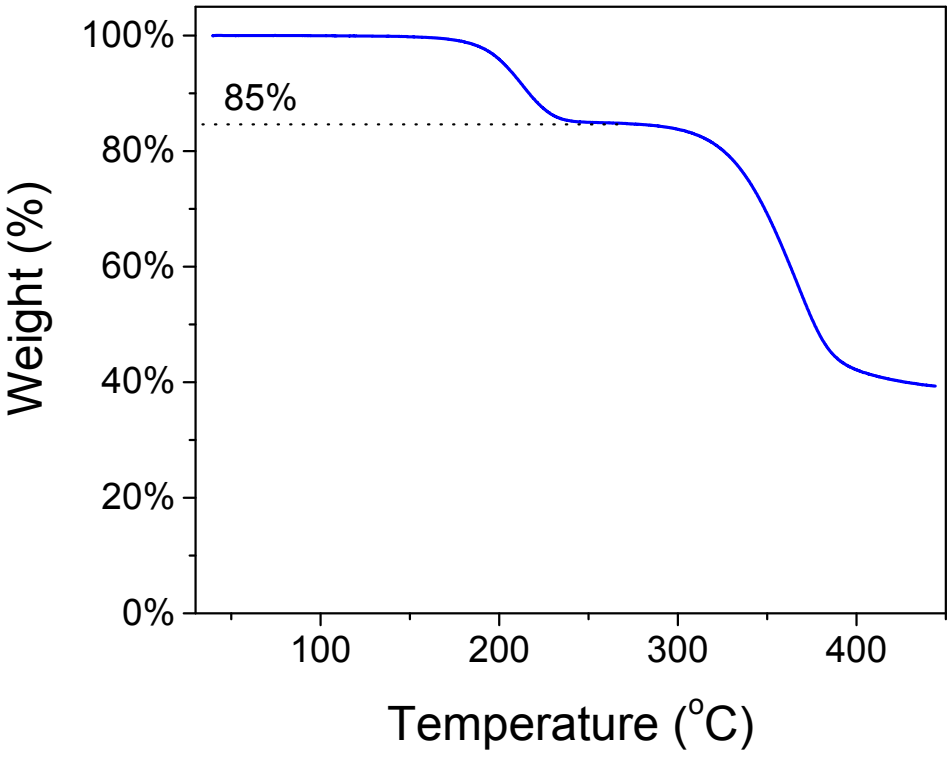

Figure 3-3 TGA curves of **P3** at a heating rate of 10 °C min^{-1} under nitrogen.

Figure 3-4 shows the X-ray diffractometry (XRD) measurements of the **P3** films annealed at 100, 150, 200 and 250 °C for 1 h, respectively. No obvious diffraction peak was observed for the film annealed at 100 °C. As the annealing temperature increased to 150 °C, a strong primary diffraction peak at 2θ = 3.95°(corresponding to a *d*-spacing distance of 2.24 nm), indicating the significantly improved crystallinity of the polymer film. When the annealing temperature further increased to 200 °C, the primary peak intensified significantly. The *d*-spacing increased to 2.37

nm (2θ = 3.73°), which is likely a result of the backbone planarization. After being annealed at 250 °C, the *d*-spacing increased further to 2.49 nm (2θ = 3.55°), but the intensity of the primary peak decreased probably due to partial decomposition of the polymer. It is reasonable to consider that the indigo units recovered high coplanarity once the *t*-Boc groups were removed, which facilitated the formation of more ordered molecular packing. The observation of only the primary peaks in the XRD diagrams suggests that upon removal of the *t*-Boc groups the polymer chains adopted a layer-by-layer lamellar packing motif in thin films as observed for many other π-conjugated polymers. [20,84] The primary peak represents the inter-lamellar distance.

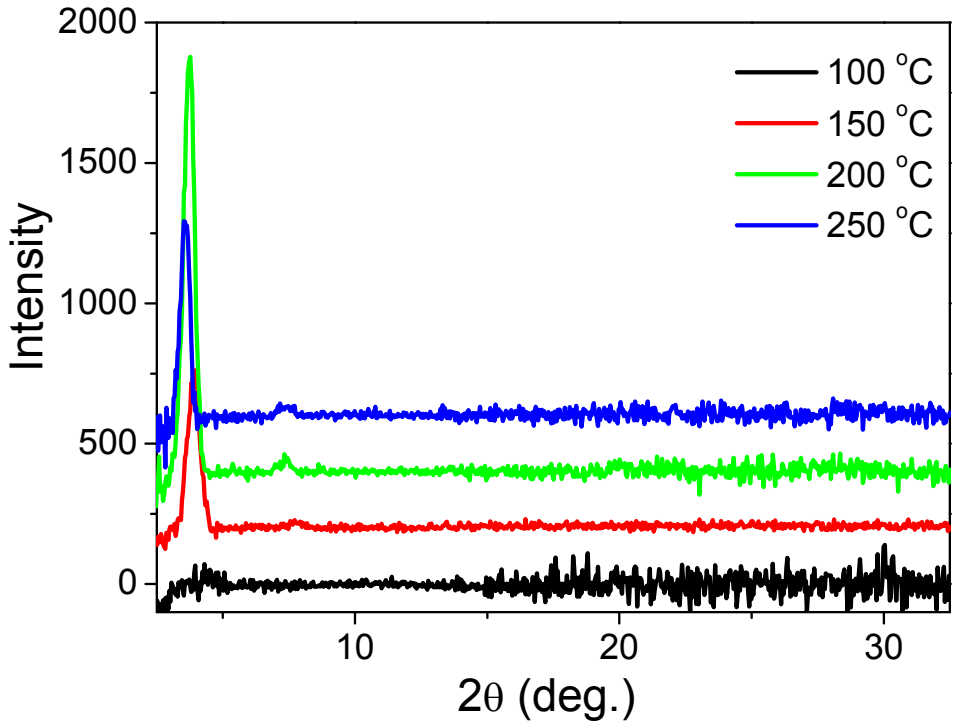

Figure 3-4 XRD diagrams obtained from spin-coating **P3** thin film on DDTS modified SiO_2 substrates annealed at 100, 150, 200 and 250 °C.

The atomic force microscopic (AFM) measurement of the **P3** films revealed the changes in the surface morphology with increasing annealing temperature (Figure 3-5). A very smooth surface (with a root-mean square (RMS) roughness of ~0.5 nm) with fine grains was observed for

the film annealed at 100 °C. As the annealing temperature increased to 150 °C, small grains appeared and the surface roughness increased slightly (RMS roughness: ~1.5 nm). When the film was annealed at 200 °C, the grains grew further and aggregated, forming fibre-like patterns. The RMS roughness increased to 3.2 nm. At a higher annealing temperature of 250 °C, more distinct grains can be observed and the RMS roughness decreased to 2.2 nm.

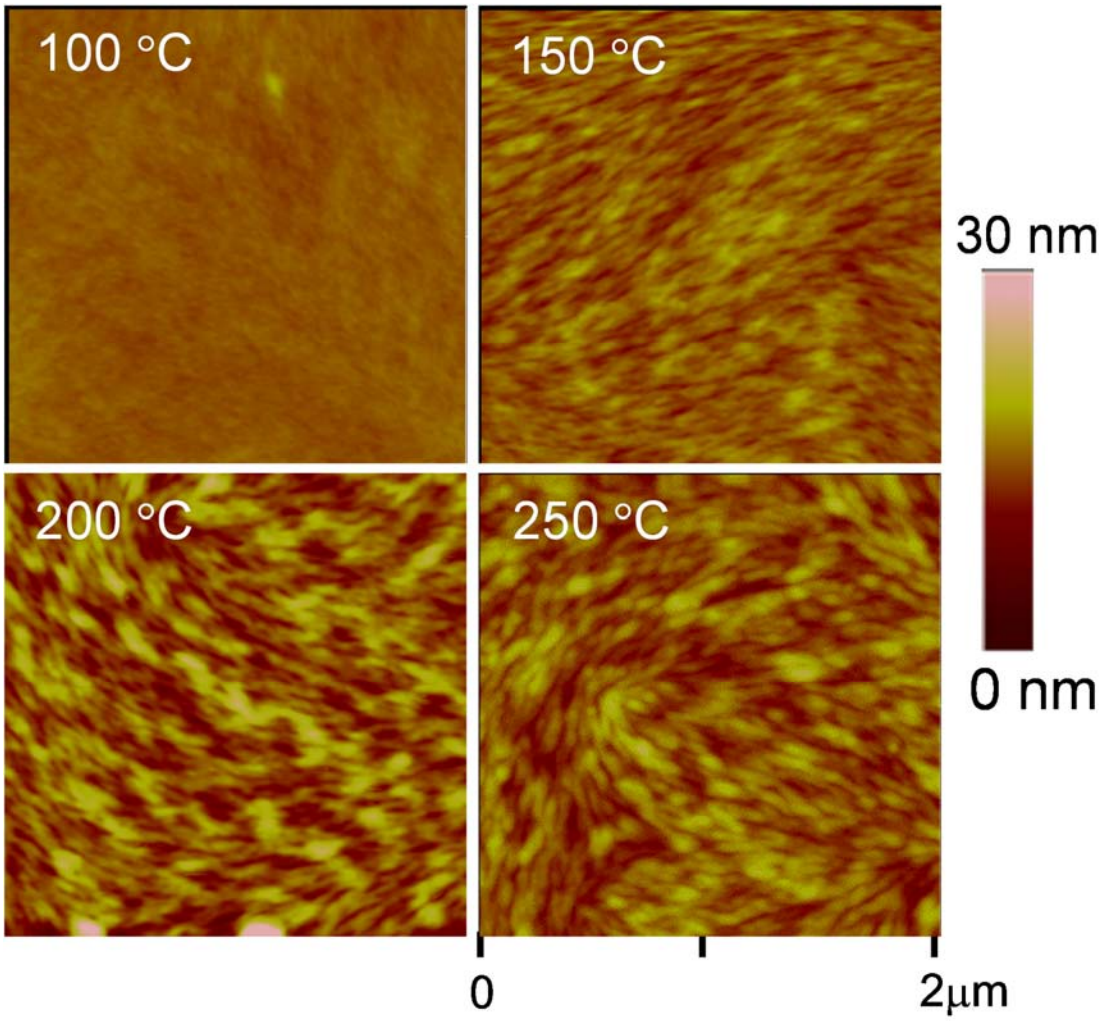

Figure 3-5 AFM images (2 μm × 2 μm) of **P3** thin films (~70 nm) on dodecyltrichlorosilane (DDTS) modified SiO_2 substrates annealed at 100, 150, 200 and 250 °C.

The UV-vis absorption spectra of compounds **1** and **3** in dilute 1,1,2,2-tetrachloroethane (TCE) solutions are shown in Figure 3-6a. The λ_{max} of compound **1** is 586 nm, which is in good

agreement with the value of 585 nm reported in literature.[131] The λ_{max} of **3** is at 545 nm, which blue-shifted by 40 nm. This is due to the twisting of this molecule caused by the *t*-Boc substitution as indicated by the simulation results discussed above. Figure 3-6b shows the UV spectra of **P3** in dilute 1,2,4-trichlorobenzene before and after heating at 200 °C for 1 h (and cooled to room temperature before the measurement). The large red shift (55 nm) in λ_{max} strongly indicated that the *t*-Boc groups were removed at 200 °C, resulting in a more coplanar conformation of the polymer main chains in solution. Spectral changes of the polymer thin films on glass substrates annealed at different temperatures are shown in Figure 3-6c. The spectrum of the 150 °C-annealed film became obviously broader and red-shifted compared with the non-annealed and the 100 °C-annealed films, indicating that the *t*-Boc groups are partially removed. For the 200 °C-annealed film, a strong new peak at 658 nm appeared, suggesting the more extended π-conjugation realized by retrieving the high coplanarity of the unsubstituted indigo units upon removal of the *t*-Boc groups. Further increasing the annealing temperature to 250 °C resulted in a decrease in intensity of the 658 nm peak, which might be caused by partial decomposition of the polymer main chain under such harsh conditions (250 °C for 1 h). The color changes of the polymer films can be clearly visualized as shown in Figure 3-7. The optical band gap calculated from the onset absorption wavelength decreased from 1.85 eV for the non-annealed film to 1.68 eV for the 200 °C-annealed film, manifesting planarization of the polymer backbone due to thermal removal of the *t*-Boc groups. The energy levels of **P3** were determined by cyclic voltammetry (CV) on polymer films spin coated on conductive indium tin oxide (ITO) substrates. The non-annealed **P3** film exhibited HOMO/LUMO levels of -5.6 eV/-3.9 eV (Figure 3-6d), respectively, using ferrocene as a reference (-4.8 eV).[120] The CV curves of the polymer film annealed at 200 °C for 1 h changed dramatically. The HOMO/LUMO levels were lowered to -5.8 eV and -4.2 eV, respectively. This suggests that the retrieved non-substituted indigo unit is a very strong electron acceptor building block. The band gap of ~1.7 eV determined

from the CV curve of the 200 °C-annealed polymer film agrees with the value of 1.68 eV calculated from the onset absorption wavelength of the annealed film in the UV spectrum.

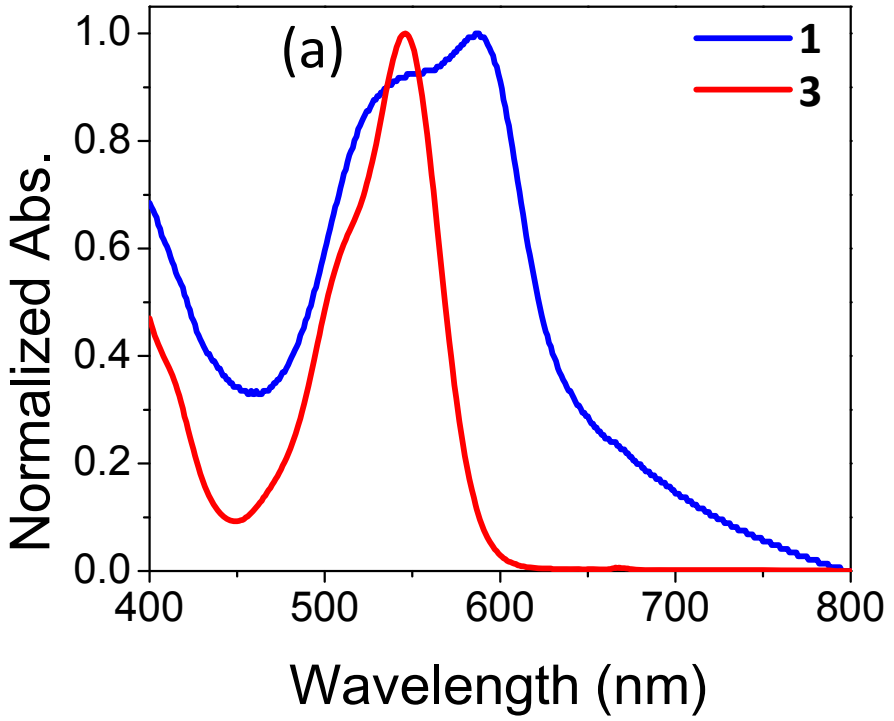
(a)
1
3
Normalized Abs.
1.0
0.8
0.6
0.4
0.2
0.0
400
500
600
700
800
Wavelength (nm)

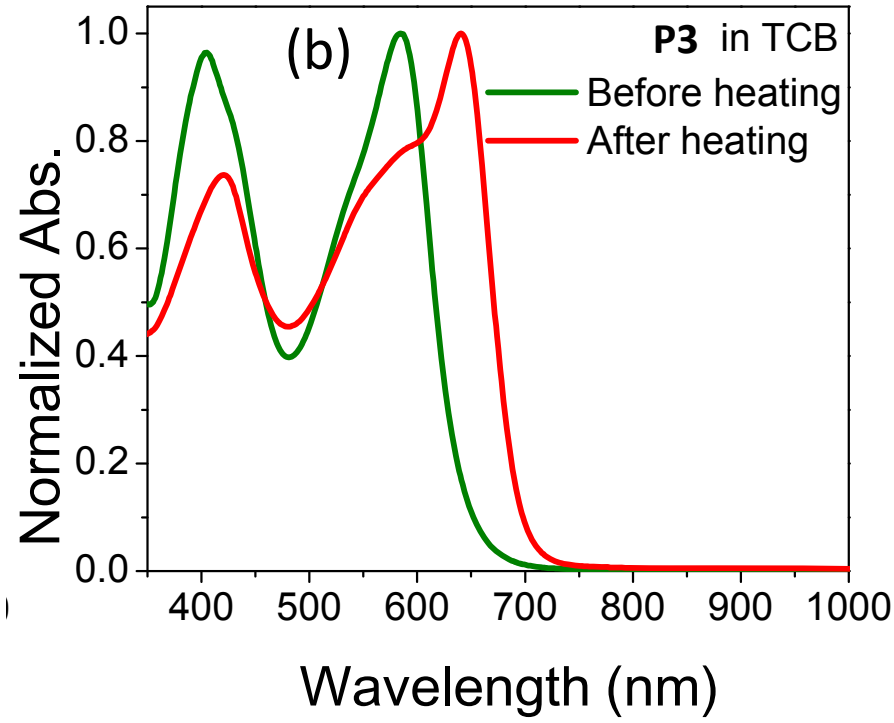
(b)
P3 in TCB
Before heating
After heating
Normalized Abs.
1.0
0.8
0.6
0.4
0.2
0.0
400
500
600
700
800
900
1000
Wavelength (nm)

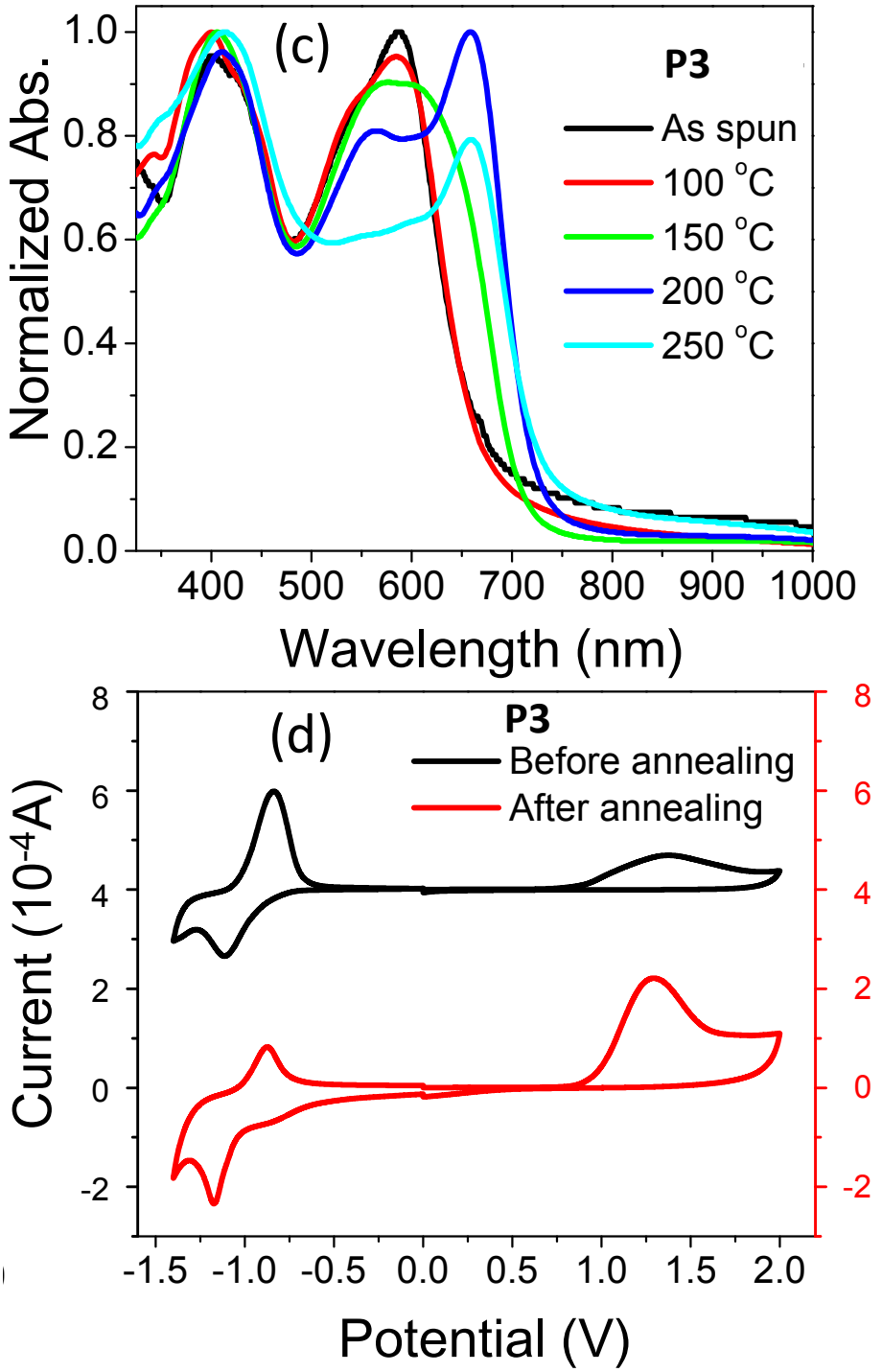

Figure 3-6 UV-vis absorption spectra of (a) **1**, and **3** in TCE solutions, (b) a solution of **P3** in 1,2,4-trichlorobenzene (TCB) before and after heating at 200 °C for 1 h, and (c) **P3** films on glass substrates annealed at different temperatures for 1 h. (d) shows the cyclic voltammograms of as-spun and 200 °C-annealed **P3** thin films measured in anhydrous CH_3CN solution using Bu_4NPF_6 as the electrolyte.

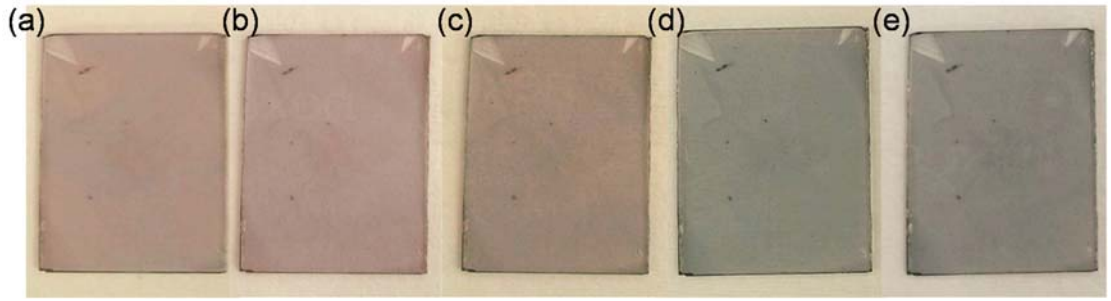

Figure 3-7 P3 films coated glass substrates before (a) and after annealing at (b) 100, (c) 150, (d) 200 and (e) 250 °C.

Bottom gate, bottom contact transistors with **P3** as a channel semiconductor were fabricated by spin-coating a **P3** solution in chloroform (5 mg mL^{-1}) on to a heavily n-doped Si/SiO_2 wafer patterned with gold source/drain electrodes (having a channel length of 30 μm and a channel width of 1 mm). Devices were annealed at 100, 150, 200 and 250 °C on a hot plate in a glove box filled with nitrogen. No field effect transistor performance was observed for the polymer films annealed at 100 and 150 °C mostly due to the highly twisted polymer backbone (with poor π-conjugation) and the disordered molecular packing of the polymer films. Devices with polymer films annealed at 200 °C for 1 h exhibited distinct n-channel electron transport behavior, reaching a highest electron mobility of 5.7×10^{-3} $cm^2V^{-1}s^{-1}$ with current on-to-off ratios of $\sim10^3$ (Figure 3-8 and Table 3-2). Apparently the charge transport of the 200 °C-annealed films was enabled by thermal removal of the *t*-Boc groups. The retrieved high coplanarity of polymer backbone and improved crystallinity of the films facilitated charge transport. Extremely weak hole transport characteristics (with negligible on current of $\sim10^{-9}$ A) were observed in the hole accumulation mode. The exhibition of electron transport performance is due to the low-lying LUMO level (-4.2 eV) of the 200 °C-annealed polymer films. We found that the UV-vis spectra of the polymer films are similar after being annealed for longer than 30 min at 200 °C (Figure 3-9 UV-vis absorption spectra of **P3** films on glass substrates annealed at 200 °C for different periods of time.). However, the film annealed for 30 min showed slightly lower mobilities (3.1×10^{-3}

$cm^2V^{-1}s^{-1}$ in average), while a longer annealing time (h) did not further improve the mobilities (Table 3-2). The average electron mobility of the device annealed at 250 °C for 1 h dropped to 2.5×10^{-3} $cm^2V^{-1}s^{-1}$ probably due to partial decomposition of the polymer at such a high temperature as observed in its XRD and UV-vis spectra.

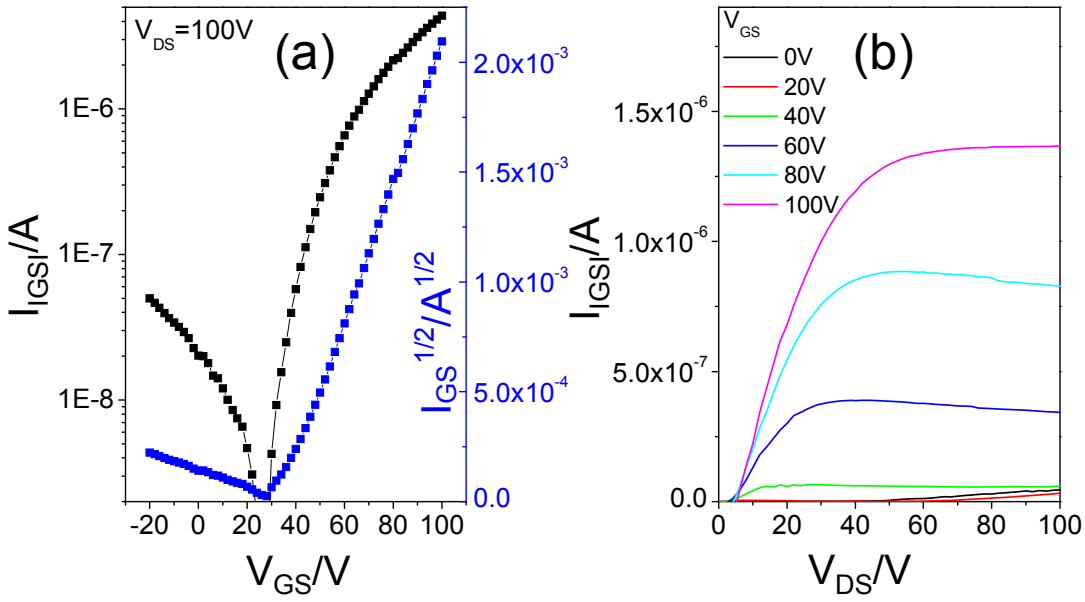

Figure 3-8 Transfer and output curves of OTFT devices with **P3** thin films annealed at 200 °C for 1 h. Device dimensions: channel width (W) = 1 mm; channel length (L) = 30 μm.

Table 3-2 Performance of OTFT devices using **P3** annealed at 200 or 250 °C.[a]

Annealing temperature / time	Average electron mobility, μ_e ($cm^2V^{-1}s^{-1}$)	Maximum electron mobility, μ_e ($cm^2V^{-1}s^{-1}$)	Standard deviation ($cm^2V^{-1}s^{-1}$)	Threshold voltage, V_{th} (V)	Current on-to-off ratio, I_{on}/I_{off}	Drain voltage, V_{DS} (V)
200 °C / 0.5 h	3.1×10^{-3}	3.9×10^{-3}	4.5×10^{-4}	39.7-55.3	$\sim10^3$	100
200 °C / 1 h	4.9×10^{-3}	5.7×10^{-3}	4.7×10^{-4}	32.2-57.5	$\sim10^3$	100
200 °C / 3 h	4.1×10^{-3}	4.9×10^{-3}	4.2×10^{-4}	35.7-56.7	$\sim10^3$	100
250 °C / 1 h	2.5×10^{-3}	3.1×10^{-3}	4.4×10^{-4}	42.2-57.6	$\sim10^3$	100

[a] Data were collected from at least five devices for each condition.

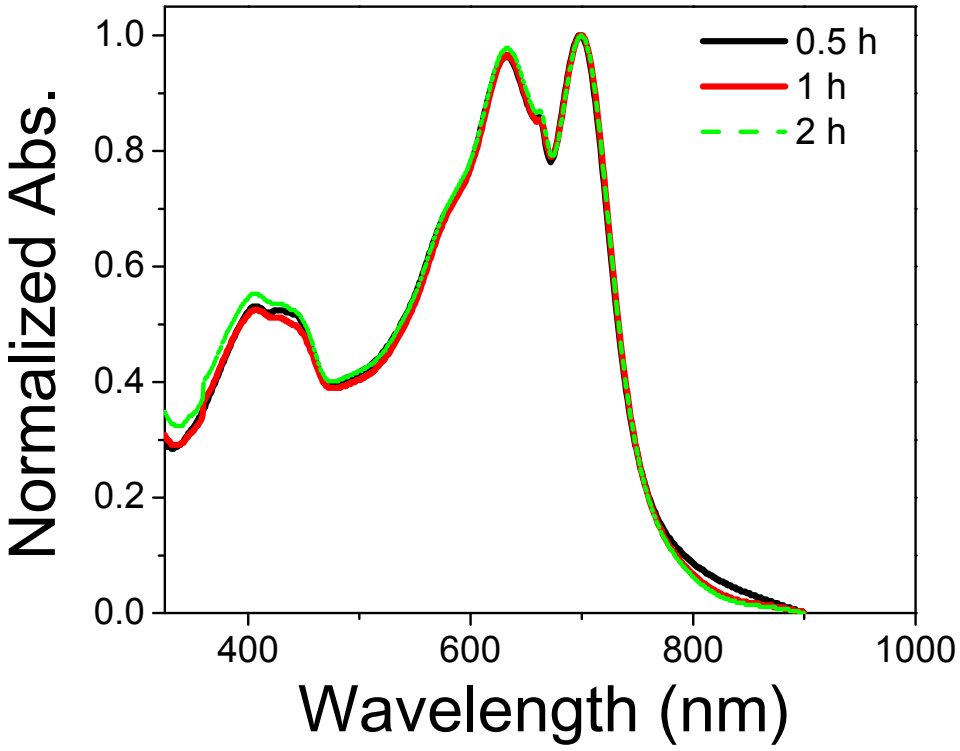

Figure 3-9 UV-vis absorption spectra of **P3** films on glass substrates annealed at 200 °C for different periods of time.

3.3 Conclusion

A novel indigo based polymer **P3** bearing thermocleavable *t*-Boc groups has been demonstrated to be a promising n-type semiconductor for organic thin film transistors. TGA confirmed the cleavage and removal of the *t*-Boc groups at >170 °C. The resultant side chain-free indigo units could retrieve a highly coplanar geometry, which was substantiated by the UV-vis and XRD results. After thermal removal of the *t*-Boc groups, the resultant polymer showed a deep-lying LUMO level of -4.2 eV, indicating the very strong electron accepting ability of the unsubstituted indigo building block. As a result, stable electron transport with electron mobility as high as 5.7×10^{-3} $cm^2V^{-1}s^{-1}$ was achieved. A more appropriate donor might improve the charge transport performance of this novel class of indigo-based polymers.

Chapter 4 Regioisomeric Control of Charge Transport Polarity for Indigo-based Polymers

(This chapter is partially published from in Polymer Chemistry (2015), Guo, C.; Quinn, J.; Sun, B.; Li, Y., **DOI**: 10.1039/C5PY00821B.)

4.1 Introduction

Based on the type of charge carriers, polymer semiconductors can be classified into p-type and n-type, where positively charged holes are the carriers in the former, while negatively charged electrons are the carriers in the latter. The polarity (p-type or n-type) of a polymer semiconductor in an OTFT device is determined by the barriers of the frontier orbital energy levels, i.e., the highest occupied molecular orbital **(**HOMO) and the lowest unoccupied molecular orbital (LUMO), with respect to the Fermi energy level (E_F) of the source electrode material. [31,132,133] For a p-type semiconductor, a higher HOMO is preferred for hole injection and transport, while for an n-type polymer, a lower LUMO is desirable for electron injection and transport. Additionally, the HOMO and LUMO levels need to be sufficiently low for realization of hole or electron transport in the presence of water, hydroxyl groups, or oxygen. Experimentally, a HOMO level below ~-5.0 eV [16,26,38] and a LUMO level below ~-3.7 eV [29,38–40] are required for stable hole and electron transport, respectively. So far, the most widely used strategy to control the polarity of polymer semiconductors is to tune the HOMO and LUMO energy levels by using various electron donor and acceptor building blocks. Alternatively, the polarity can be changed by varying the work function (or Fermi energy) of the source conductor material through surface modification. [50,134,135]

In this chapter, we report a new approach to changing the charge transport polarity by choosing regioisomerically different building blocks in the polymer semiconductors. Compared to the previously presented n-type polymer **P3**, another indigo-based polymers **P4** with the exactly

same chemical compositions but different regioisomeric connections was found to show opposite polarity. (Figure 4-1)

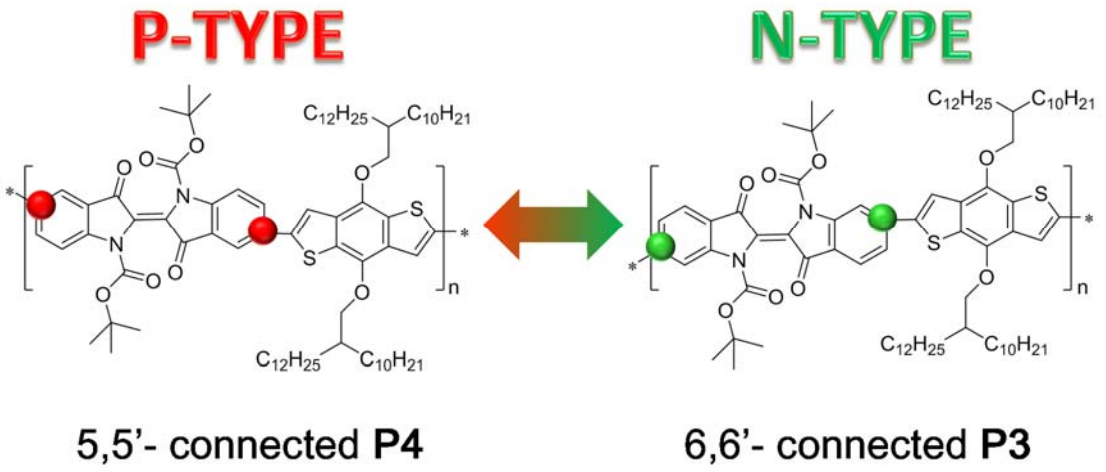

Figure 4-1 Two regioisomeric conjugated polymers containing indigo units connected at 5,5'-connected **P4** and 6,6'-connedted **P3** exhibit opposite charge transport polarity.

4.2 Results & Discussion

Previously we used a naturally occurring indigo dye, Tyrian purple (6,6'-dibromoindigo), as a starting material to construct polymer semiconductors, **P1/P2** (Chapter 2) and **P3** (Chapter 3) (Figure 4-2), as channel materials for OTFTs. N-type electron transport performance was observed for these polymers. We carried out density functional theory (DFT) calculations on indigo (ID) and found that electrons are distributed on the 6- and 6'-positions of ID in the LUMO but not in the HOMO (Figure 4-3). Therefore when the ID unit is connected with another conjugated comonomer unit through the 6- and 6'-positions, the resultant polymer would allow extended π-electron delocalization in the LUMO along the polymer backbone but prohibit the π-electron delocalization in the HOMO. This might explain the n-type electron transport behavior of **P1/P2** and **P3**, which have ID units connected through the 6 and 6' positions. Interestingly, we noticed that electrons are distributed in the HOMO but not in the LUMO at the 5- and

5’-positions, which is opposite to the case of the 6- and 6’-positions. Accordingly, we expected that polymers containing ID units connected through the 5- and 5’-positions might exhibit p-type hole transport behavior instead of n-type electron transport behavior.

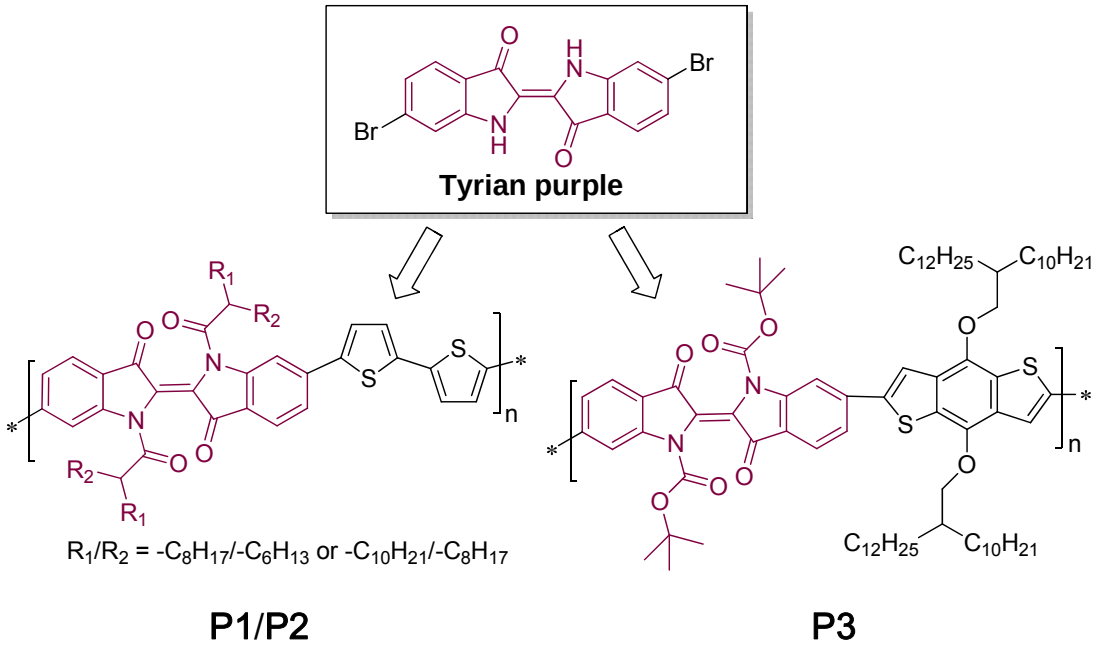

Figure 4-2 Chemical structures of Tyrian purple (6,6’-dibromoindigo) and polymers, **P1/P2** and **P3**, prepared from Tyrian purple.

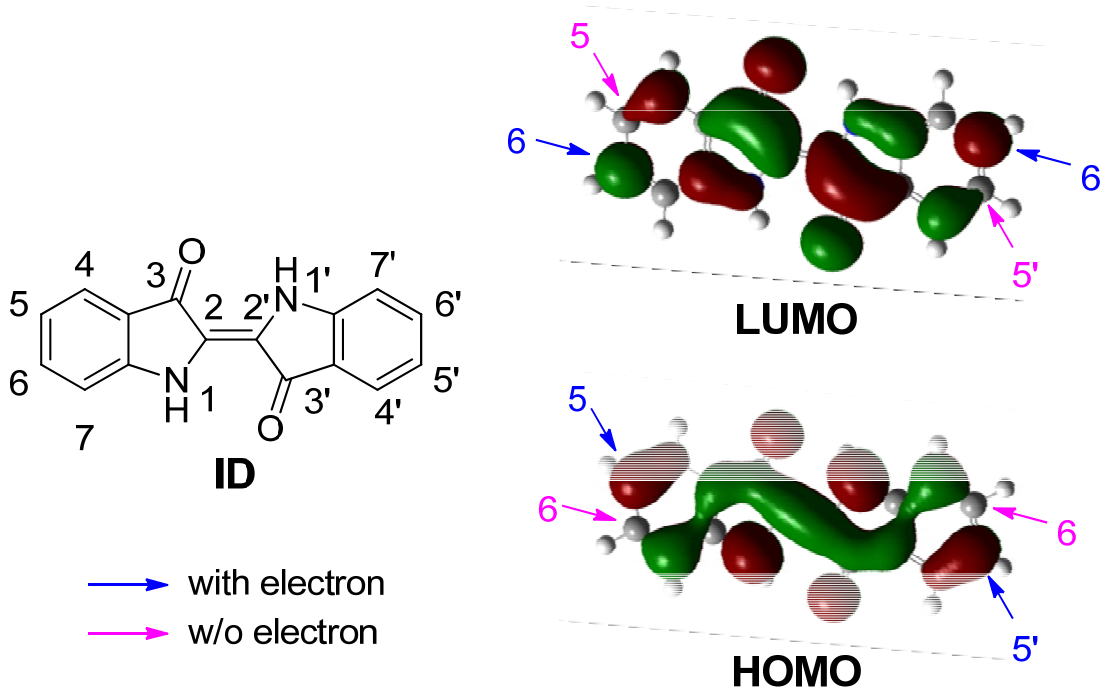

Figure 4-3 Indigo (ID) and its wave functions of the highest occupied molecular orbital (HOMO) and the lowest unoccupied molecular orbital (LUMO) obtained by density functional theory (DFT) calculations.

P3, which has thermally labile *tert*-butoxy carbonyl (*t*-Boc) group, was previously found to be able to retrieve the highly coplanar geometry of the ID units after thermal removal of the *t*-Boc groups, leading to much higher mobility than that of **P1/P2**. Therefore in this study we designed its regioisomer, **P4** (Scheme 4-1), where each *t*-Boc-substituted ID unit is connected through the 5- and 5'-positions with two neighboring benzo[1,2-*b*:4,5-*b'*]dithiophene (BDT) units. By using DFT calculations with Gaussian 09W [116,117] at the B3LYP/6-31G (d) level, we simulated two dimer compounds, 5,5'-ID-BDT-ID-BDT and 6,6'-ID-BDT-ID-BDT of **P4** and **P3** after removal of the *t*-Boc groups, respectively (Figure 4-4 and Table 4-1). Similar to the HOMO and LUMO wave functions of ID (Figure 4-3), in both dimers, the 5- and 5'-positions of the ID unit are occupied by electrons in the HOMO but empty in the LUMO. Conversely the 6- and 6'-positions of the ID unit are empty in the HOMO but occupied in the LUMO. The calculated HOMO and LUMO levels are -5.03 eV and -2.96 eV, respectively, for 5,5'-ID-BDT-ID-BDT,

and -5.30 eV and -2.96 eV, respectively, for 6,6'-ID-BDT-ID-BDT, indicating that the HOMO level of **P4** is raised compared to **P3** due to the more effective hybridization of π-electrons in the HOMO along the polymer chain of the former polymer.

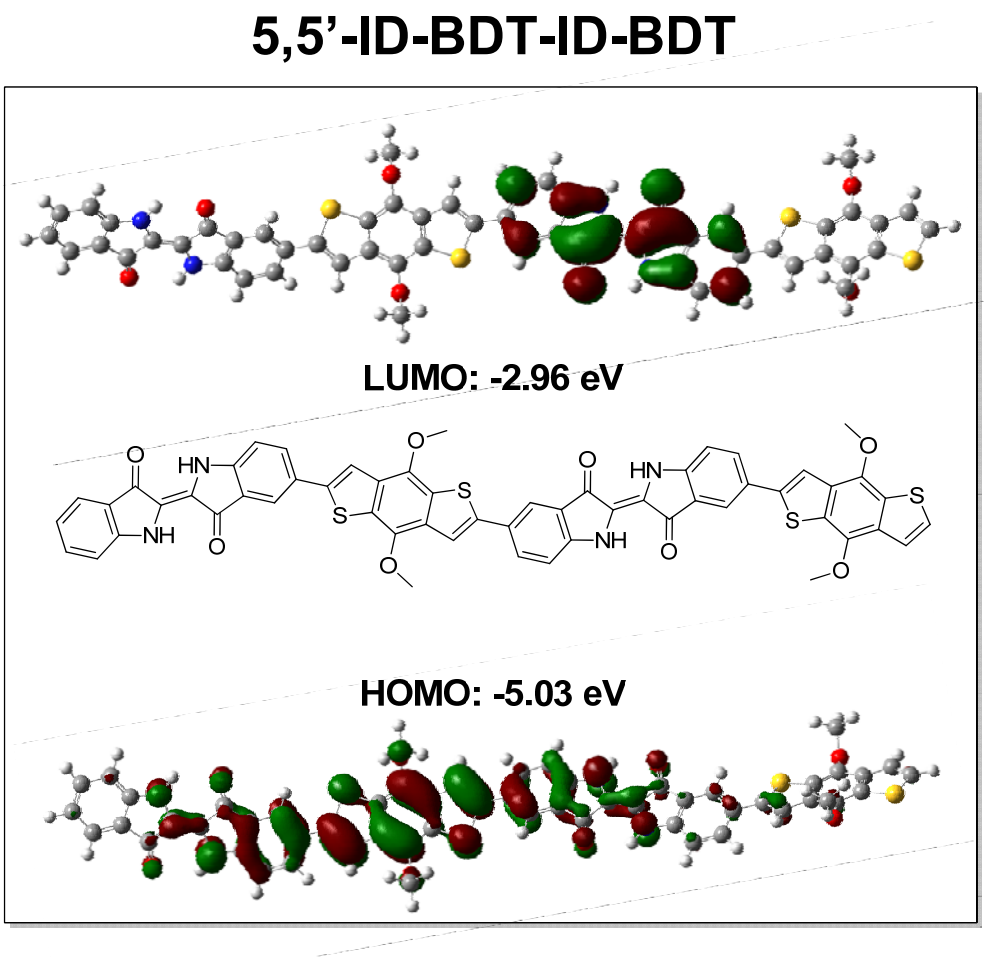

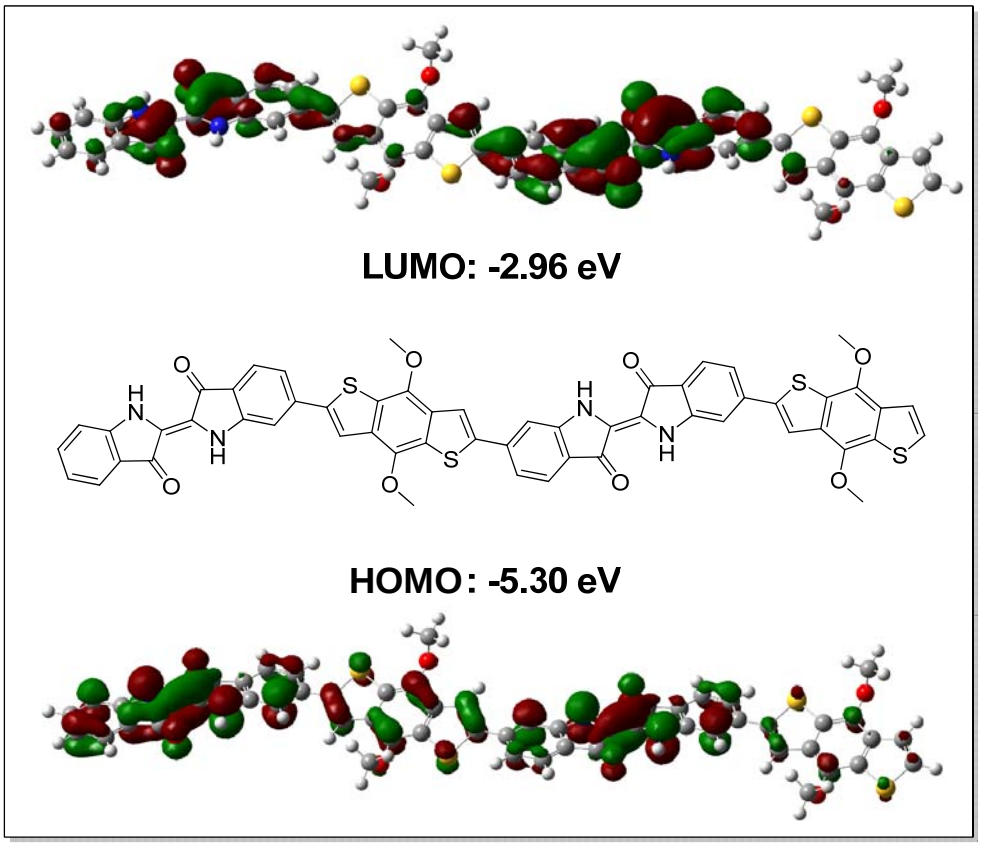

Figure 4-4 HOMO and LUMO electron distributions and energy levels of 5,5'-ID-BDT-ID-BDT and 6,6'-ID-BDT-ID-BDT obtained by density functional theory (DFT) calculations.

Table 4-1 Summary of computer simulation results of model compounds, 5,5'-ID-BDT-ID-BDT and 6,6'-ID-BDT-ID-BDT.

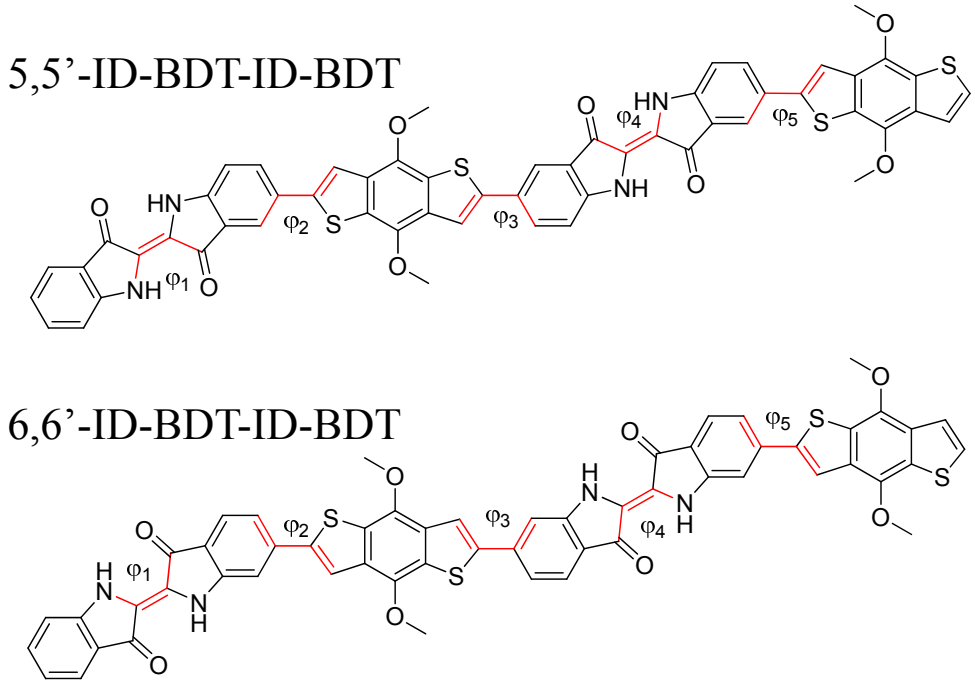

Model compound	Dihedral angle (°)				
	φ1	φ2	φ3	φ4	φ5
5,5'-ID-BDT-ID-BDT	0	24.8	26.4	0	24.8
6,6'-ID-BDT-ID-BDT	0	25.5	25.6	0	25.3

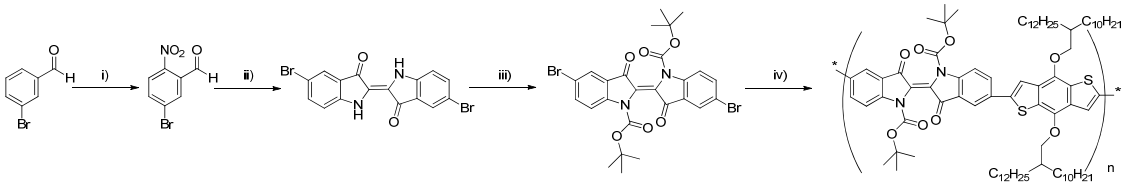

6 **7** **8** **P4**

Scheme 4-1 Synthetic route to **P4**. Reagents and conditions: i) $HNO_3/H_2SO_4/0$ °C to r.t.; ii) NaOH/acetone/r.t.; iii) 4-dimethylaminopyridine/di-*tert*-butyldicarbonate/DMF/0 °C to r.t.; iv) (4,8-bis((2-decyltetradecyl)oxy)benzo[1,2-*b*:4,5-*b'*]dithiophene-2,6-diyl)bis(trimethylstannane)/Pd_2dba_3/ P(*o*-tolyl)$_3$/110 °C.

P4 was synthesized according to **Scheme 4-1**. Compound **6** was readily prepared in 76% yield by using a literature method. [136] Compound **7** (5,5'-dibromoindigo) was then synthesized in 75% yield by stirring **6** in acetone in the presence of aq. NaOH at room temperature. Substitution of **7** with *t*-Boc groups using di-*tert*-butyl 3,3'-dioxo-[2,2'-biindolinylidene]-1,1'-dicarboxylate yielded compound **8** (83%). Finally polymer **P4** was obtained by the Stille coupling polymerization between **8** and **5** with tris(dibenzylideneacetone)-dipalladium (Pd_2dba_3)/tri(*o*-tolyl)phosphine (P(*o*-tolyl)$_3$) as a catalyst in chlorobenzene at 110 °C for 60 h. The obtained crude polymer was subjected to consecutive Soxhlet extraction with acetone, hexane, and chloroform. The yield of the polymer extracted with chloroform was 39%. The molecular weight of **P4** was determined by gel-permeation chromatography (GPC) with chlorobenzene as an eluent and polystyrene as standards at a column temperature of 40 °C. The number average molecular weight (M_n) of **P4** (extracted with chloroform) was 32.6 kDa with a polydispersity index (PDI) of 2.53.

The purpose of using the thermocleavable *t*-Boc groups in **P4** was to retrieve the highly coplanar geometry of the ID units for improved the *intra*-molecular charge transport after thermal annealing. [82] TGA showed that **P4** started to lose weight at ~170 °C and reached a flat region with a weight loss of ~14 % at ~240 °C (Figure 4-5). The weight loss agrees with the calculated amount of the *t*-Boc groups (~15%) in the polymer, indicating a complete removal of the *t*-Boc groups in this region. The second abrupt weight loss started at ~280 °C was caused by further decomposition of the polymer. The thermal decomposition behavior of **P4** is very similar to that of its regioisomer, **P3**.[82]

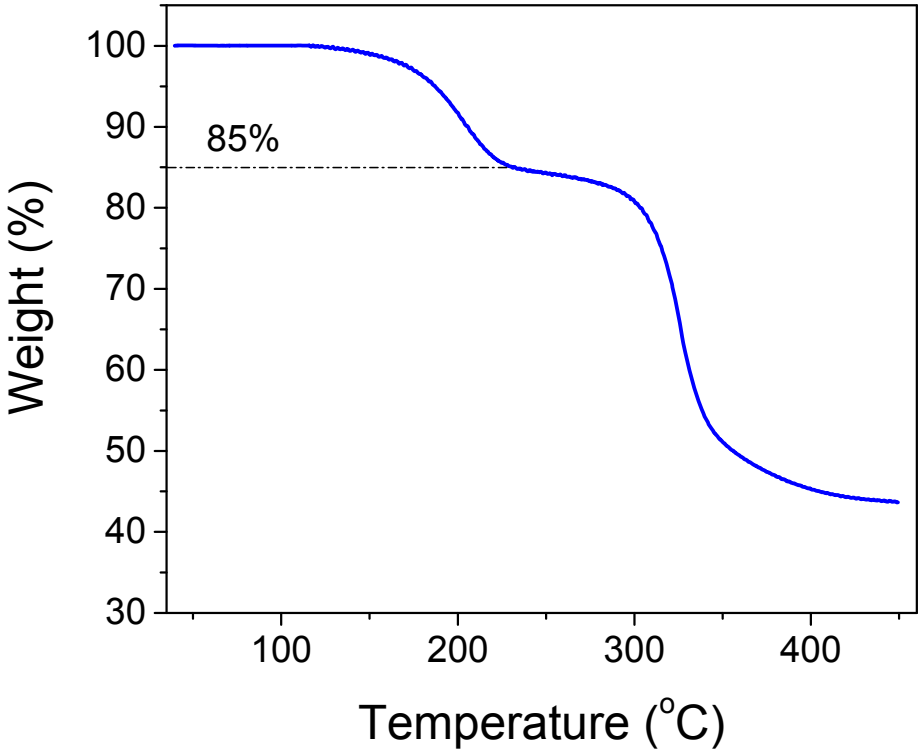

Figure 4-5 TGA curves of **P4** at a heating rate of 10 °C min^{-1} under nitrogen.

Compounds **7** and **8** were dissolved in dilute 1,1,2,2-tetrachloroethane (TCE) to obtain their UV-vis absorption spectra (Figure 4-6a). Compound **7** showed a wavelength of the maximum absorption (λ_{max}) at 621 nm, while compound **8** showed a ~60 nm blue shift in λ_{max} due to the twisting of this molecule caused by the *t*-Boc groups. A dilute solution of **P4** in 1,2,4-trichlorobenzene showed a λ_{max} at ~630 nm (Figure 4-6b). After heated at 200 °C for 1 h and cooled down to room temperature, the measured λ_{max} red shifted to ~665 nm, indicating the more coplanar geometry of the polymer main chains after thermal removal of the *t*-Boc groups. Figure 4-6c showed the spectral changes of the **P4** polymer thin films on glass substrates after annealing at 200 °C for 1 h. Compared to the non-annealed film, the λ_{max} of the 200 °C-annealed film red shifted from 642 nm to 669 nm, similar to the phenomenon observed for the heated

solution. Cyclic voltammetry (CV) was used to determine the energy levels of **P4** thin films spin coated on conductive indium tin oxide (ITO) substrates (Figure 4-7). The non-annealed polymer thin film has HOMO and LUMO levels of -5.6 eV and -3.6 eV, respectively, with ferrocene as the reference (-4.8 eV). [120] After annealing at 200 °C for 1 h, the LUMO level of the polymer film remained at ~-3.6 eV, while the HOMO level increased to -5.3 eV. In comparison to the 200 °C-annealed **P3**, which showed HOMO and LUMO levels of -5.8 eV and -4.2 eV, [82] the 200 °C-annealed **P4** has significantly higher HOMO and LUMO levels, which would favor hole transport over electron transport.

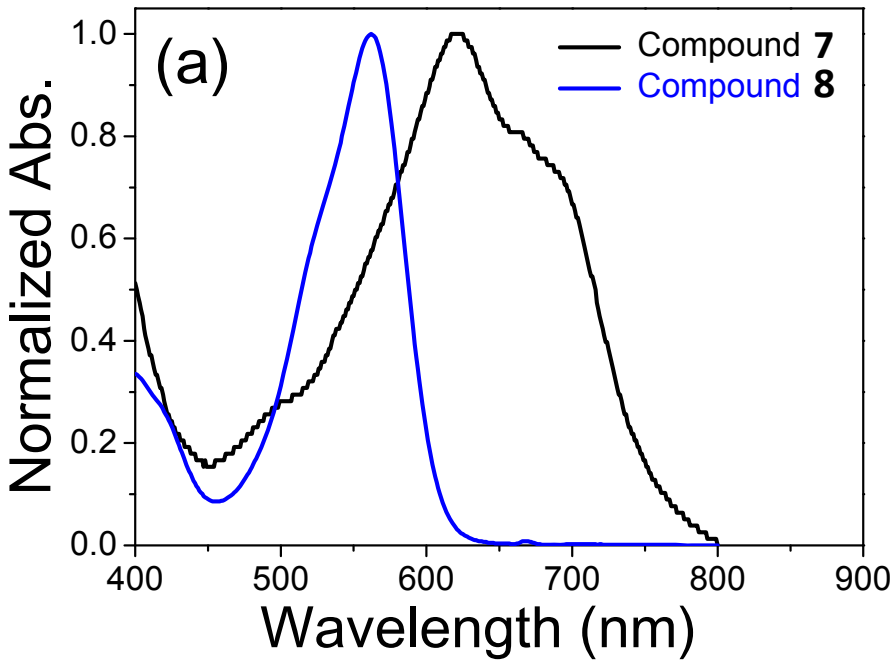
(a)
Compound 7
Compound 8
Normalized Abs.
Wavelength (nm)
1.0
0.8
0.6
0.4
0.2
0.0
400
500
600
700
800
900

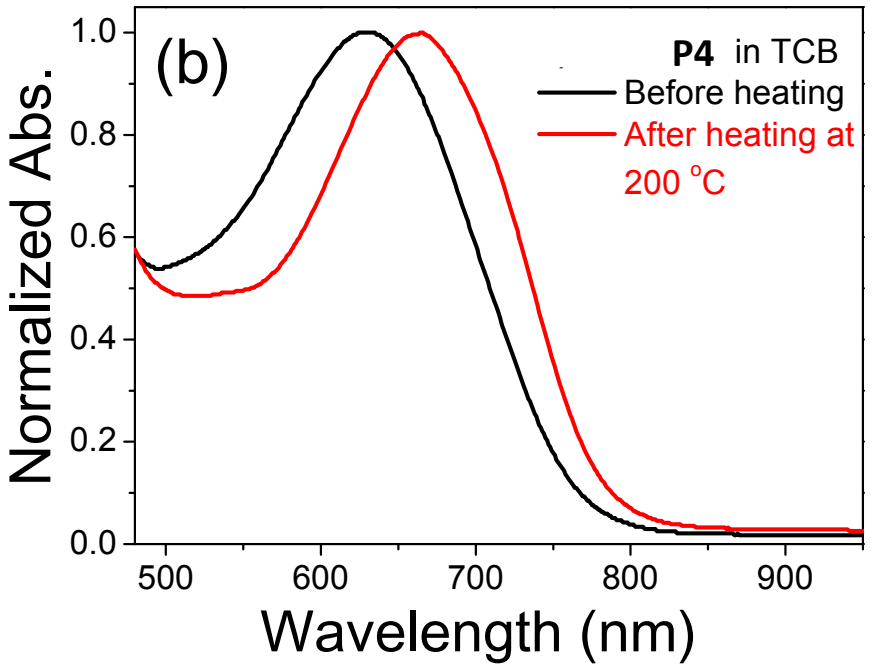
(b)
P4 in TCB
Before heating
After heating at
200 °C
Normalized Abs.
Wavelength (nm)
1.0
0.8
0.6
0.4
0.2
0.0
500
600
700
800
900

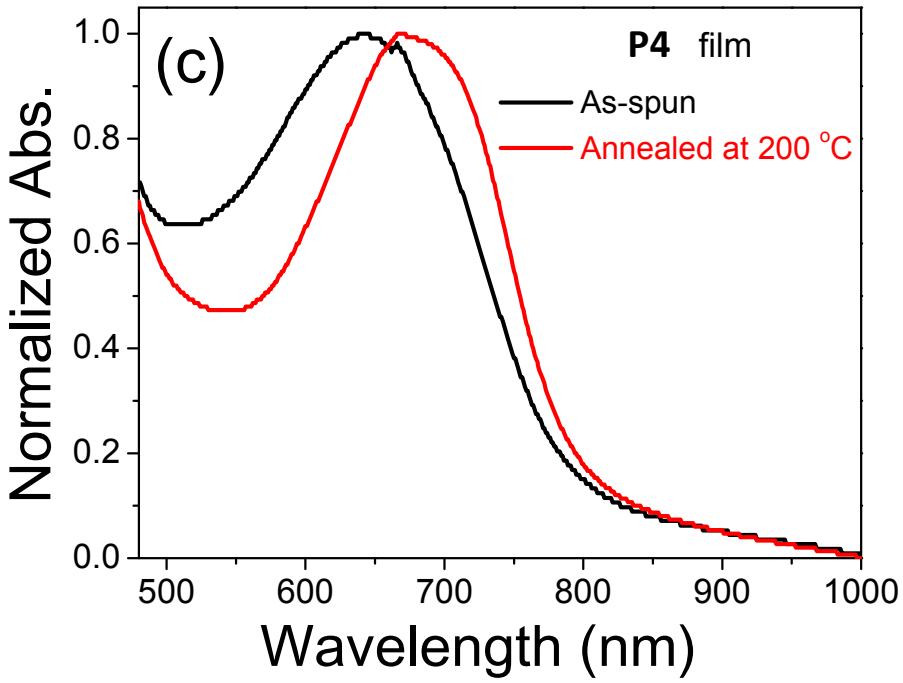

Figure **4-6** UV-vis absorption spectra of (a) compounds **7** and **8** in TCE solutions, (b) a solution of **P4** in 1,2,4-trichlorobenzene (TCB) before and after heating at 200 °C for 1 h, and (c) a **P4** film spin coated on a glass substrate before (as-spun) and after annealing at 200 °C for 1 h.

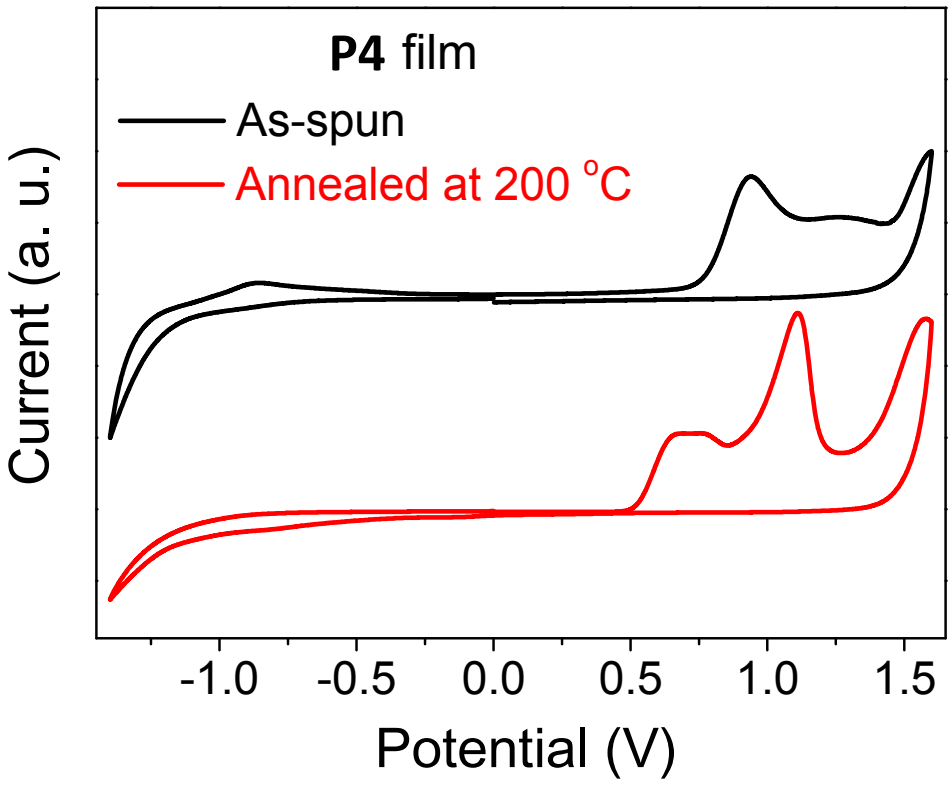

Figure 4-7 Cyclic voltammograms of an as-spun and 200 °C-annealed **P4** thin film measured in anhydrous CH_3CN solution using Bu_4NPF_6 as the electrolyte.

A top-gate, bottom-contact OTFT device configuration was used to evaluate **P4** as a channel semiconductor. A solution of **P4** (10 mg mL^{-1}) in a mixture of chloroform/1,2-dichlorobenzene (v/v = 9/1) was spin coated on n-doped Si/SiO_2 wafer patterned with gold source and drain electrode pairs to form a thin film (~40 nm). After thermal annealing at 100 °C, 150 °C, 200°C or 250 °C for 1 h on a hot plate, a CYTOP layer (~570 nm) was spin coated to form the gate dielectric. Finally an Al layer (~70 nm) was thermally evaporated as the gate electrode. The devices were characterized in air in the absence of light. While the 100 °C- and 150 °C-annealed polymer films showed no field effect behavior, the devices annealed at 200 °C exhibited typical p-type hole transport characteristics with mobility as high as 2.5×10^{-4} cm^2 V^{-1} s^{-1} (current on-to-off ratios of ~10^3) (Figure 4-8). The appearance of field effect performance for the films annealed at 200 °C is due to the backbone coplanarization by thermal removal of the *t*-Boc groups, which

allowed extended π-electron delocalization along the polymer main chains to facilitate *intra*-molecular charge transport. A similar phenomenon was observed for **P3**, [82] which showed the charge transport performance only after the *t*-Boc groups were removed at 200 °C. However, **P3** showed the opposite n-type electron transport performance. The results fully supported our prediction on the charge transport polarity for **P4** based on the DFT calculations. The mobility of **P4** is lower compared to that of **P3**, which might be due to its poor crystallinity verified by the X-ray diffractometry (XRD) measurement (Figure 4-9) and AFM (Figure 4-10). The devices annealed at 250 °C did not show field effect performance, which might be due to the decomposition of the polymer.

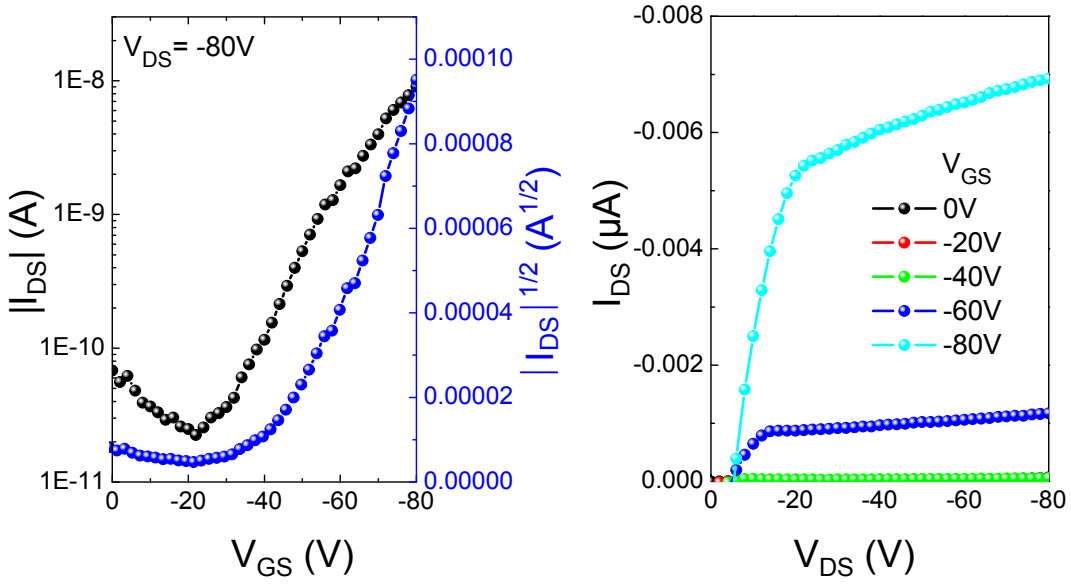

Figure 4-8 Transfer (left) and output curves (right) of an OTFT devices with a **P4** thin film annealed at 200 ºC for 1 h. Device dimensions: channel width (*W*) = 1 mm; channel length (*L*) = 30 µm.

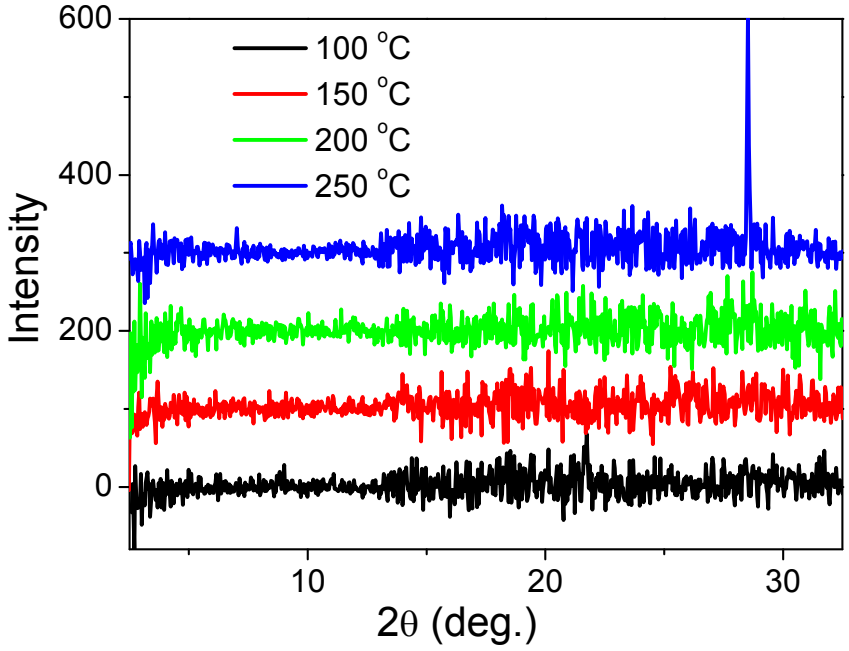

Figure 4-9 XRD diagrams obtained from spin-coating **P4** thin film on SiO_2/Si substrates annealed at 100 °C, 150 °C, 200 °C and 250 °C. Note: The peak at 2θ = ~28 ° for the 250 °C-annealed sample is the (111) peak of the Si substrate.

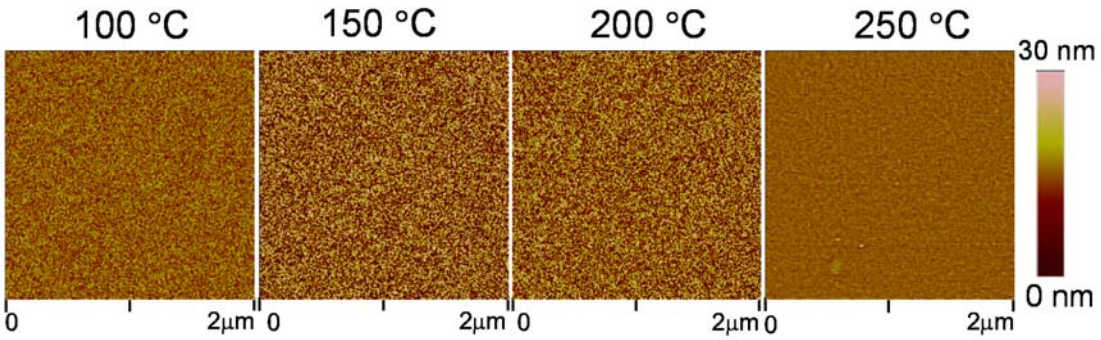

Figure 4-10 AFM images (2 μm × 2 μm) of **P4** thin films on SiO_2/Si substrates annealed at 100 °C, 150 °C, 200 °C and 250 °C.

4.3 Conclusion

The HOMO and LUMO wave functions of the indigo (ID) unit obtained by DFT calculations

showed that electrons were differently (oppositely) distributed on the 6,6'-positions and the 5,5'-positions. While the simulation results could explain the n-type electron transport behaviour of **P3** containing 6,6'-ID units, they also led us to predict that the regioisomeric polymer **P4**, which contains 5,5'-ID units, would favour p-type hole transport performance. To prove our assumption, we synthesized **P4**, which was found to have higher HOMO and LUMO energy levels compared to **P3**, after thermal removal of the *t*-Boc groups. As expected, this polymer showed p-type hole transport behaviour in OTFT devices, which is opposite to that of its regioisomer **P3**. This work inspired by a serendipitous finding demonstrated a new way to predict and control the polarity of a polymer semiconductor by examining the HOMO and LUMO wave functions using computer simulations.

Chapter 5 Synthesis of Bisthienyl Diketopyrrolopyrrole-Bithiazole Copolymers via Direct (Hetero)arylation Polymerization

(This chapter is partially quoted from a manuscript submitted to Polymer Chemistry (2015), Guo, C.; Sun, B.; Quinn, J.; Li, Y..)

5.1 Introduction

To enhance charge carrier mobility, electron-donating and electron-accepting building blocks can be combined in the repeat units to form donor-acceptor (D-A) polymers to shorten the π-stacking distance for more efficient charge hopping.[21,41,54] Diketopyrrolopyrrole (DPP) has been widely used as an electron-acceptor building block for the development of high-performance polymeric semiconductors for OTFTs and OPVs.[31,41–45,47,48] The majority of the DPP-based polymers reported in the literature were synthesized using either Suzuki or Stille coupling polymerization, which requires tedious steps to synthesize the organoboron or organotin monomers. Many organotin compounds are known to be highly toxic and are environmental hazards. Recently, a new alternative method, direct (hetero)arylation polymerization (DHAP),[66,137–139] has been explored to construct conjugated polymers for organic electronics.[65,67,69–71] Since DHAP involves the C-C bond formation through a coupling reaction between a C–H bond in one conjugated monomer (an arene or heteroarene) and a C–X bond (X is usually a halide of Br or I) in another, this new method is much more environmentally friendly and cost effective than the Suzuki and Stille coupling methods.

In this chapter, we describe the synthesis of 1,4-DPP-bithiazole copolymers by DHAP method. Compared to thiophene, which is a commonly used electron donor building block, thiazole is a weak acceptor[140] and has been utilized to promote the electron transport performance of polymer semiconductors.[69,141,142] Previously, DPP-quaterthiophene based conjugating polymers

(**PDQT**)[43,63,143] were reported to show p-type hole transport performance with high mobility up to 6.9 $cm^2V^{-1}s^{-1}$.[143] If a bithiophene unit in **PDQT** is replaced by a 2,2'-bithiazole or 5,5'-bithiazole unit (Figure 5-1), the resulting polymer **PDBTz** or **PDBTz'** is expected to show electron transport behaviour. Very recently, a **PDBTz** polymer, **PDBTz-27** (R = 5-decylheptadecyl) synthesized by the Stille coupling polymerization was reported by Reichmanis and coworkers,[144] which showed high electron mobility up to 0.3 $cm^2V^{-1}s^{-1}$ in OTFT devices. In this study, we used the DHAP method through two different routes to prepare two **PDBTz** polymers, **P5** and **P6** (R = 2-decyltetradecyl). The syntheses of these polymers reported here involved fewer steps than the Stille coupling method. It was found that 2,2'-bithiazole as a monomer showed good regioselectivity in DHAP, producing a polymer with higher electron mobility up to 0.53 $cm^2V^{-1}s^{-1}$ in OTFT devices.

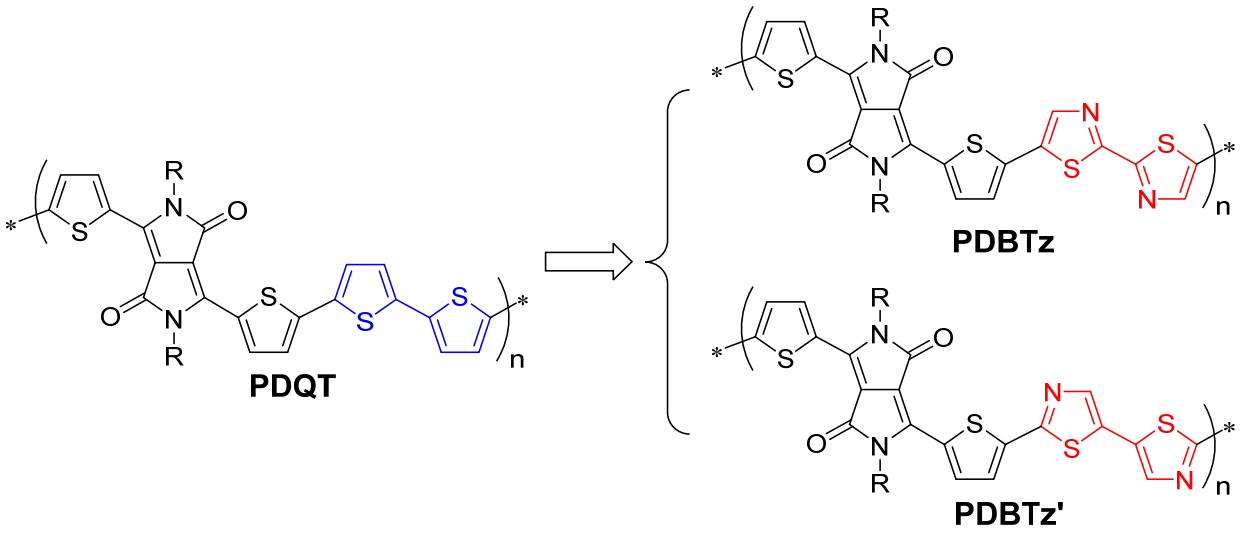

Figure 5-1 Structures of 1,4-DPP-thiophene based polymer **PDQT** and 1,4-DPP-thiazole based polymers **PDBTz** and **PDBTz'**. R is an alkyl chain.

5.2 Results & Discussion

The synthetic routes to **PDBTz** polymers are outlined in Scheme 5-1. Stannylation of 2-bromothiazole resulted in compound **9**, which was coupled with 2-bromothiazole to afford

compound **10** in 78% yield. Compound **10** was then brominated at the 5,5'-positions using *N*-bromosuccinimide (NBS) to form compound **11** in 98% yield. The bithiazole compounds **10** and **11** are comonomers for the following DHAP polymerization reactions. The DPP-containing comonomers, compounds **12** and **13**, were prepared according to the literature methods.[143] The target polymer **PDBTz** could be synthesized via DHAP through two routes by (A) coupling between **11** and **12** to afford **P5** and (B) coupling between **10** and **13** to afford **P6**.

The α C-H bond (at the C2 or C5 position) of thiophene is known to have higher activity toward a C-X (Br or I) bond through DHAP than a β C-H bond (at the C3 or C4 position), allowing for synthesis of soluble polymers with minimal cross-linked structural defects under certain controlled conditions.[70,145–149] Monomer **12** in Route A has 2 α C-H bonds and 4 β C-H bonds on two thiophenes. If DHAP occurs predominantly at the desired α C-H bonds, a linear polymer **P5** could be obtained. The regioselectivity of an α C-H bond (at C2 or C5) over the β C-H bond (at C4) in thiazole has also been reported to be very high in DHA reactions of small molecule compounds.[150–159] A bithiazole compound with the C4 positions substituted (blocked) with nonyl side chains was used for DHAP to make a soluble conjugated polymer without observable cross-linking side reactions.[160] However, to the best of our knowledge, the use of a thiazole compound having both α and β C-H bonds as a monomer for DHAP has not been demonstrated yet. Therefore it is interesting to explore if the use of a β non-substituted bithiazole compound **10** as a comonomer in Route B can form a soluble target polymer **PDBTz-B**.

Two polymerization reactions were conducted under identical conditions, in the presence of a catalyst system containing *trans*-bis(acetato)bis[*o*-(di-*o*-tolylphosphino)benzyl]dipalladium(II) (Herrmann-Beller's catalyst), tris(*o*-methoxyphenyl)phosphine, cesium carbonate and pivalic acid under reflux in toluene for 16 h, which were successfully used for the preparation of other conjugated polymers through DHAP.[67,69–71,161] Both crude polymers were purified by Soxhlet extraction using acetone, hexane, chloroform and 1,1,2,2-tetrachloroethane (TCE) sequentially.

Negligible amounts of polymers were dissolved by acetone and hexane. For **P5**, 9% was dissolved by chloroform and 53% by TCE. The remaining (~38%) solid was almost insoluble in any solvent. **P6** showed improved solubility with 66% dissolved in chloroform and 10% dissolved in TCE, but ~24% of this polymer still remained insoluble (Scheme 5-1). High temperature gel permeation chromatography (HT-GPC) with 1,2,4-trichlorobenzene as an eluent and polystyrene as standards at a column temperature of 140 °C was used to determine the molecular weights of **P5** and **P6** due to the strong chain aggregation tendency at room temperature. The number-average molecular weight (M_n)/polydispersity index (PDI) of **P5** are 17 kDa/6.9 for the chloroform extracted fraction and 11 kDa/5.9 for the TCE extracted fraction. M_n/PDI of **P6** are 18 kDa/3.8 for the chloroform extracted fraction and 23 kDa/3.9 for the TCE extracted fraction (Scheme 5-1).

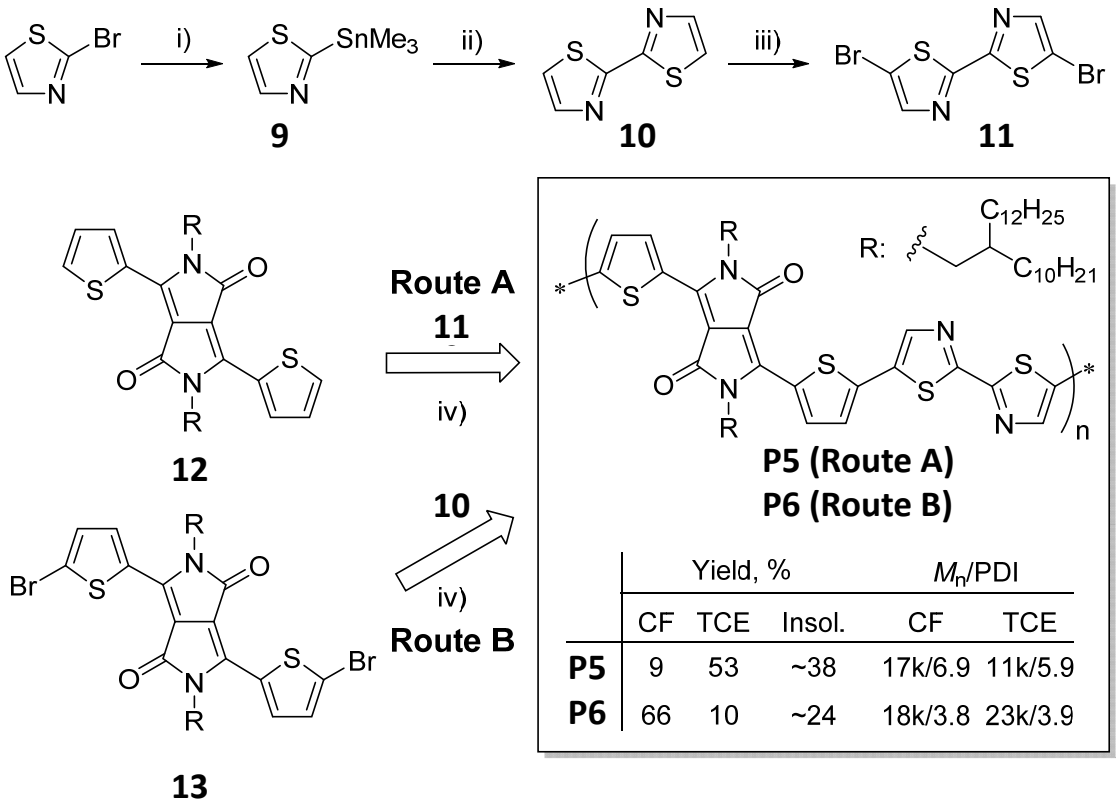

Scheme 5-1 Synthetic route to the polymer **P5** and **P6** : a) *n*-butyllithium/trimethyltin chloride/ether/-78 °C; ii) Pd $(PPh_3)_4$ /toluene/reflux; iii) NBS/DMF/60 °C; iv) K_2CO_3/DMF/130 °C; v) NBS/DMF/50 °C; vi) Herrmann-Beller's catalyst/tris(*o*-methoxyphenyl)phosphine/cesium carbonate/pivalic acid/toluene/reflux.

One challenging issue associated with DHAP is that side reactions of C-X (X = Br or I) groups with the undesirable (hetero)aromatic C-H groups, such as the β C-H at the C3 or C4 position in thiophene,[162] might occur, leading to formation of cross-linked, insoluble polymers and low molecular weight soluble fractions.[71,145,160,163,164] Therefore it is reasonable to think that the presence of a significant amount of insoluble fractions for both polymers (**P5**: ~38%; **P6**: ~24%) are most likely due to the formation of cross-linked structures via the side reactions between the α C-Br and the β C-H bonds on thiophene and/or thiazole units. **P6** showed much better solubility and narrower molecular weight distributions for its soluble fractions in chloroform and TCE compared with **P5**, indicating that less α−β coupling side reactions occurred

in Route B. The mechanism for the mismatched coupling side reactions for DHAP is still not well understood yet and requires further investigation.[145,160,163,164] For the current two DHAP reactions, it is possible that the terminal α' (or α) C-Br groups and the β (or β') C-H groups on the polymer main chains (or monomers) react to form α'–β or α–β' coupling defects in Route A and Route B, respectively (Scheme 5-2). The α C-H and α' C-H groups embedded on the polymer main chain would be prone to further couple with C-Br groups, forming branched and cross-linked polymer structures. The dramatically different solubilities observed for **P5** and **P6** could be explained by the different regioselectivities between thiophene and thiazole. It was reported that DHA reactions on the β C-H (C4) of thiazole is very difficult.[150–159,165] Computer simulations have also shown that while the Gibbs free energies of activation for the cleavage of the β C-H bond in thiazole (C4) and thiophene (C3 or C4) are similar (29.7 kcal mol^{-1} vs. 29.9 kcal mol^{-1}), the value for the α C-H at C5 in thiazole is much smaller than that of thiophene (23.7 kcal mol^{-1} vs. 25.6 kcal mol^{-1}).[166] Therefore the regioselectivity of α C-H (C5) over β C-H (C4) for the bithiazole monomer **10** might be much higher than that for the thiophenes in monomer **12**, which could account for the lesser degree of cross-linking observed in Route B. The abnormally lower number-average molecular weight of the TCE-extracted fraction than that of the chloroform-extracted fraction obtained for **P5** might be indicative of the presence of more branched or lightly cross-linked structures, which have smaller hydrodynamic sizes than the linear polymer chains, leading to its lower apparent molecular weight. The presence of α–β coupling defects in **PDBTz** would disrupt the main chain conjugation. The existence of branched or cross-linked structures would also cause a twisting of the polymer backbone. As a result, the optical band gap of the polymer with more α–β coupling defects would be larger, which is confirmed by the UV-Vis absorption spectra of these two polymers, whereas **P5** showed a blue shift in the absorption profile compared to **P6** (to be discussed later).

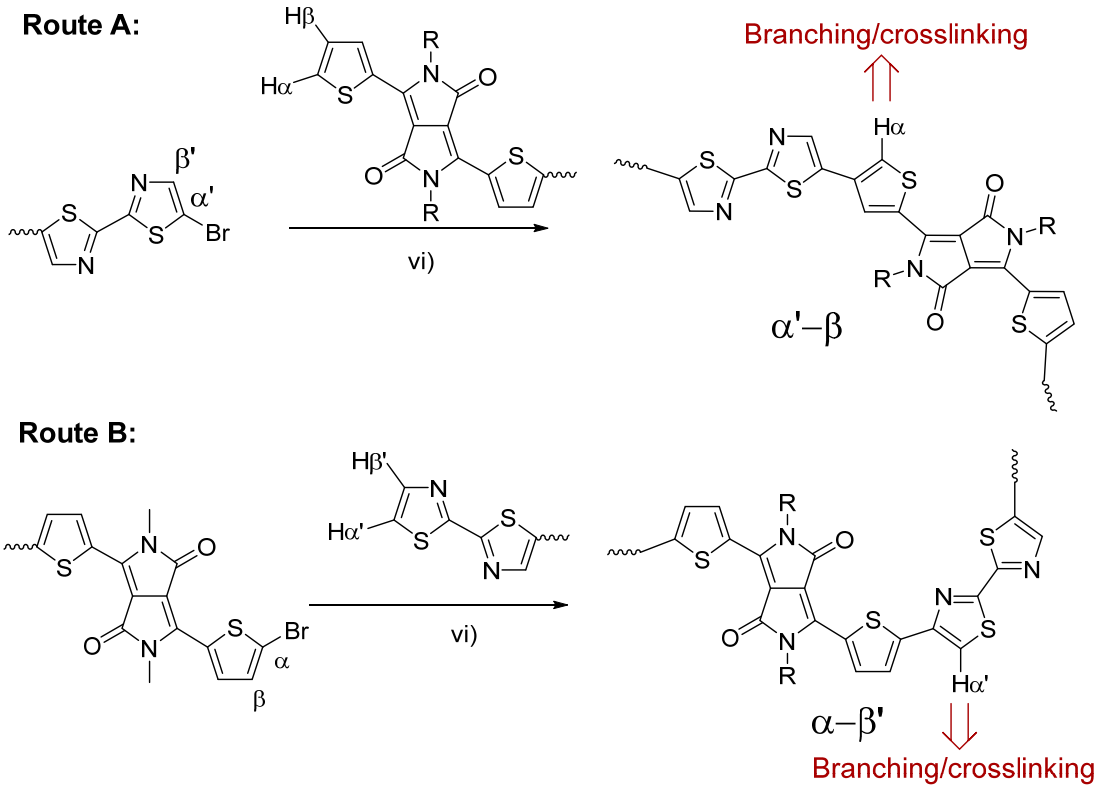

Scheme 5-2 Possible α'-β and α-β' coupling side reactions in Route A and Route B, respectively, between a C-Br in a terminal thiazole (α') or thiophene (α) unit of a polymer chain or monomer and a β C-H in a thiophene (β) or thiazole (β') unit of a polymer chain or monomer, where C-Hα in the α'-β defect and C-Hα' in the α-β' defect have much higher reactivity than that of other β C-H groups on the polymer backbone, resulting in branched and cross-linked structures.

To further shed light on the structural defect formation, **P5** and **P6** were subjected to NMR analysis. Due to the strong aggregation tendency of these polymers in solution, which have been observed for other DPP-based polymers,[63] ^{1}H NMR spectra of these polymers measured at room temperature showed weak and broad peaks in the aromatic region and could not reveal the presence of the structural defects formed by the side reactions (Figure 5-2). Hence, the polymer samples were measured at an elevated temperature of 125 °C to improve the resolution of the NMR spectra. As can be seen in Figure 5-3, two polymers showed dramatically different NMR patterns in the aromatic regions, indicating their different polymer structures. However, the NMR spectra for both polymers are too complicated to identify the α–β defect structures. It is expected

that the amount of defects in the TCE fractions to be larger than in the chloroform fractions, but no obvious differences in the relative intensities of peaks were observed between the chloroform and TCE fractions. Because a trace amount of α−β coupling structures would cause formation of cross-linked insoluble polymers, NMR spectra of the soluble polymer fractions may be unable to show these defect structures. Therefore the integrals of some peaks seem too large and thus the very complicated NMR patterns observed for both polymers may not originate from the α−β coupling defect structures. One possible reason for the appearance of more than expected aromatic peaks might be due to relatively low molecular weights of these polymers (with a number of repeat unit = ~10-20). Another possible reason is that the homocoupling structures due to the C-H/C-H and C-Br/C-Br coupling reactions, which were reported to be present in other polymers prepared by the DHAP method.[146,148,167,168] Significant homocoupling side reactions were also observed recently for Pd catalyzed Suzuki and Stille polymerizations.[63,169] Because the TCE-extracted fractions showed lower solubility at room temperature and poorer film formation property, only the chloroform-extracted fractions of **P5** and **P6** were used for characterizing the properties of these two polymers.

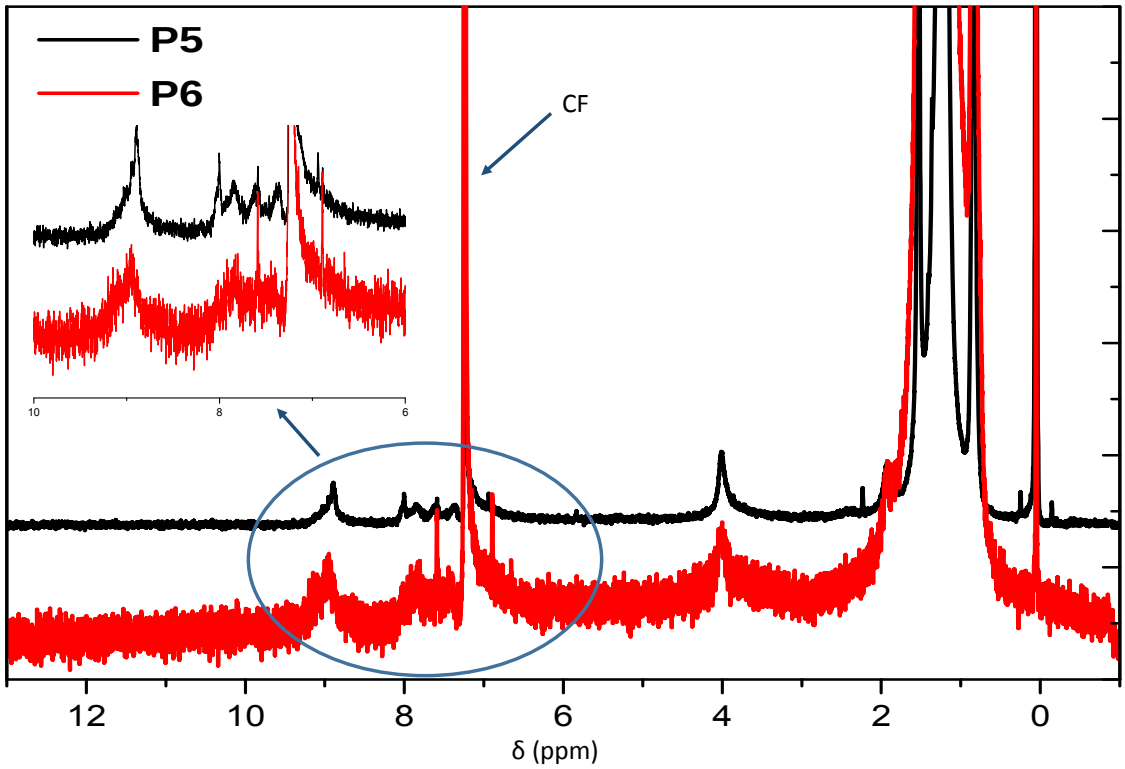

Figure 5-2 The 300 MHz ^{1}H NMR spectra of **P5** and **P6** (chloroform extracted fractions) measured at room temperature in $CDCl_3$.

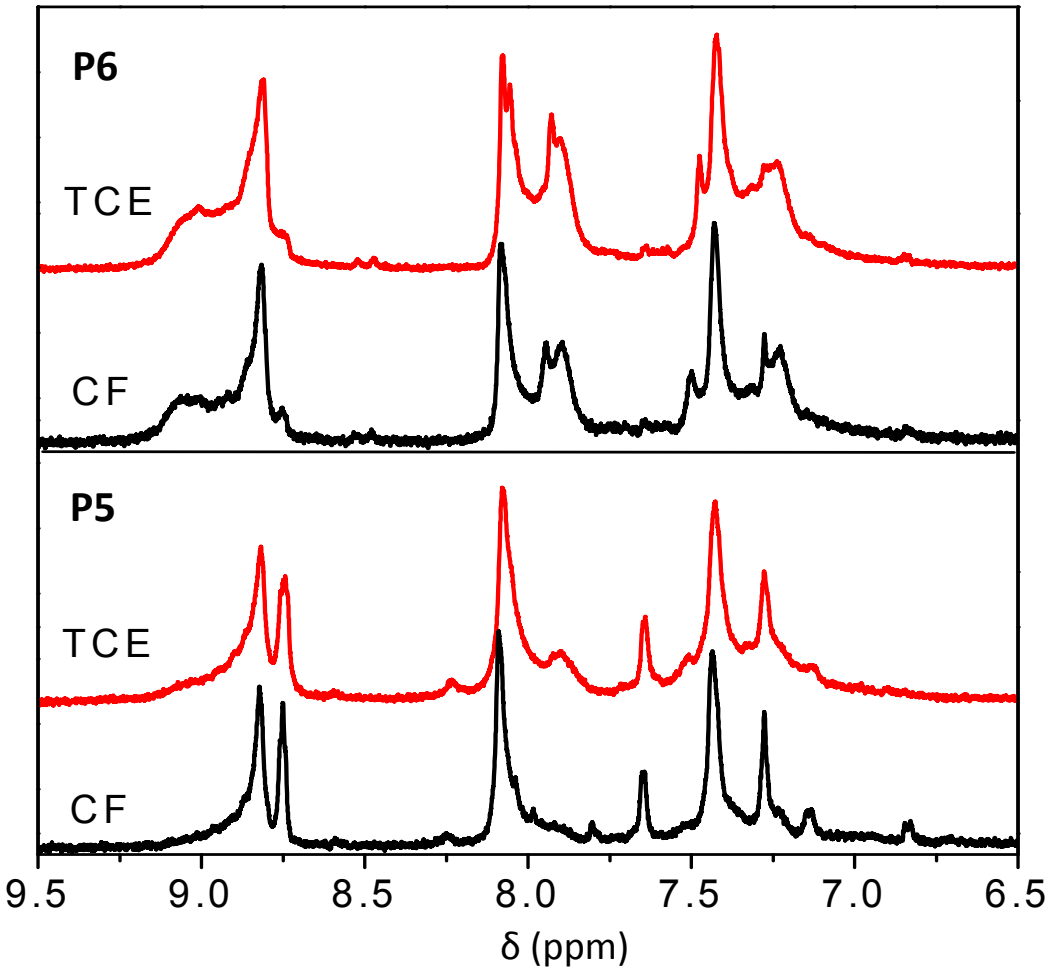

Figure 5-3 500 MHz ^{1}H NMR spectra of **P5** and **P6** fractioned extracted with chloroform (CF) and 1,1,2,2-tetrachloroethane (TCE) measured in TCE-d_2 at 120 °C.

The UV-Vis absorption characteristics of **P5** and **P6** were obtained in their dilute chloroform solutions and thin films (Figure 5-4a). The wavelength of maximum absorbance (λ_{max}) of **P5** was observed at 660 nm in solution and 746 nm in the thin film. **P6** showed a longer λ_{max} at 677 nm in solution. The as-cast film of **P6** exhibited a λ_{max} at 737 nm, which is shorter than that of the **P5** film. However, the right side of the absorption spectrum of the **P6** film extends farther into the near infrared region than the **P5** film. As a result, the optical band gap of **P6** (1.42 eV) is narrower than that of **P5** (1.49 eV) calculated using the onset absorption wavelengths of their

films. The larger optical band gap of **P5** suggests its shorter effective conjugation length than that of **P6**. Because the M_n's of **P5** and **P6** extracted with chloroform are very similar (17 kDa vs. 18 kDa) and the weight-average molecular weight (M_w) of **P5** (117 kDa) is much larger than that of **P6** (70 kDa), the effective conjugation length of **P5** should be similar or larger than that of **P6** if both polymers have linear main chain structures. The disagreement of the UV-Vis data with the molecular weights of these two polymers seems to support that **P5** contains more α–β coupling defects in the main chain as discussed previously. In addition, the presence of branched (or lightly cross-linked) structures would also cause twisting of the polymer backbone, resulting in a blue-shift of the absorption spectrum of **P5**.

Cyclic voltammetry (CV) was used to determine the energy levels of **P5** and **P6** films (Figure 5-4b). By using the onset oxidative/reductive potentials, the HOMO/LUMO levels are calculated to be -5.55 eV/-3.61 eV for **P5**, and -5.56 eV/-3.63 eV for **P6**, respectively. The energy levels of **P5** and **P6** are similar to those of the DPP-bithiazole copolymer **PDBTz-27** (R = 5-decylheptadecyl) obtained by Stille coupling (E_{HOMO}/E_{LUMO} = -5.54 eV/-3.75 eV).[144] The HOMO levels of **P5** and **P6** are lower compared to their thiophene analogue **PDQT-24** (-5.33 eV) [143] due to the presence of the electron-deficient bithiazole units.[140]

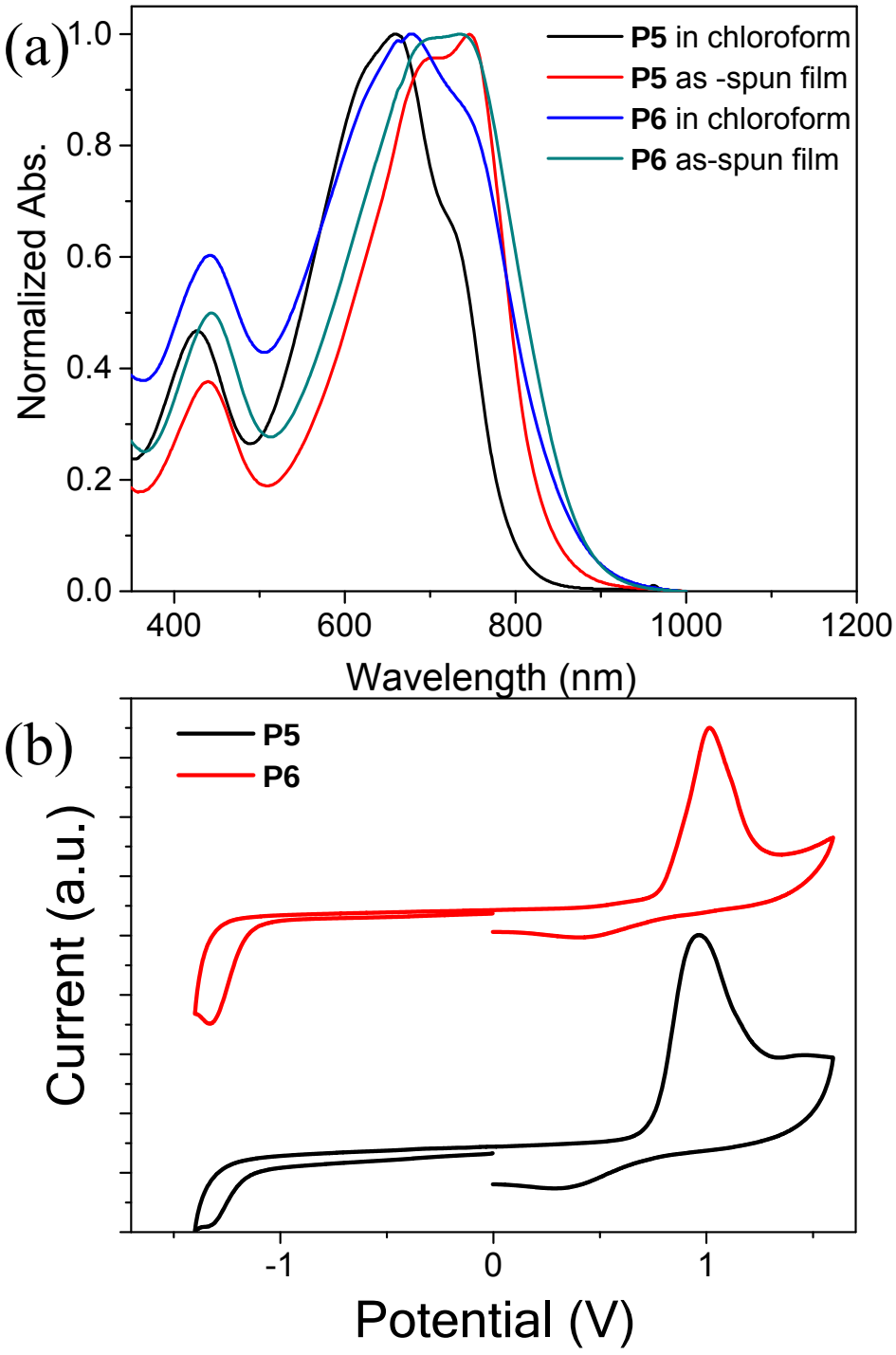

Figure 5-4 (a) UV-Vis absorption spectra of **P5** and **P6** in chloroform solutions and in thin films; (b) Cyclic voltammograms of as-cast **P5** and **P6** films measured in anhydrous CH_3CN solution using Bu_4NPF_6 as the electrolyte.

The atomic force microscopy (AFM) images (Figure 5-5) of **P5** and **P6** showed that all the polymer thin films are very smooth and did not undergo dramatic morphological changes at thermal annealing temperatures ranging from 100 °C to 250 °C. The crystallinity of the polymer thin films was investigated by reflection X-ray diffractometry (XRD). The **P5** film annealed at 100 °C showed no obvious diffraction peaks, indicating its very poor crystallinity (Figure 5-6a). When the annealing temperature was increased to 150 °C, a weak primary (100) peak appeared at 2θ = 3.85°, which corresponds to a *d*-spacing distance of 2.29 nm. By increasing the annealing temperature to 200 °C, the crystallinity of the **P5** film improved notably, as evidenced by the much intensified peak at 2θ = 3.94° (*d*-spacing = 2.24 nm). Further increasing the annealing temperature to 250 °C, the intensity of the primary peak and the *d*-spacing remained almost the same. As shown in Figure 5-6b, the reflection XRD pattern of the **P6** thin film annealed at 100 °C exhibited a small peak at 2θ = 3.69°, which corresponds to a *d*-spacing of 2.39 nm. As the annealing temperature increased to 150 °C, the primary peak intensified significantly and the peak shifted slightly to 2θ = 3.93°, which corresponds to a much shorter *d*-spacing distance of 2.25 nm. Upon annealing at higher temperatures of 200 and 250 °C, a continued incensement in the intensity of the primary peak as well as a shift of this peak to 2θ = 3.99° (*d*-spacing = 2.21 nm) and 4.05° (*d*-spacing = 2.18 nm) were observed. A noticeable secondary peak also appeared at 2θ = 7.87°. This manifests that the polymer chains were packed much more orderly and compactly with the aid of thermal annealing at high temperatures. The significantly higher crystallinity of the **P6** films than that of the **P5** films annealed at the same temperatures most likely resulted from the presence of less branched and lightly-cross-linked structural defects in the former as discussed previously. Since no (010) peaks can be seen, the polymer chains of **P5** and **P6** in the spin-coated thin film samples presumably adopted a layer-by-layer lamellar packing motif with an edge-on orientation, which has been observed for other crystalline conjugated polymers.[20,84] To elucidate the in-plane chain packing motif, we measured the 250 °C-annealed **P5** and **P6** flakes using

transmission XRD (Figure 5-6c). Both polymers showed a broad peak around 2θ = ~20° (*d*-spacing = 0.44 nm), which represents the typical van der Waals distance for an amorphous polymer phase. The 250 °C-annealed **P6** flakes showed a distinct (010) peak at 24.6°, which corresponds to a π-π stacking distance of 0.36 nm. **P5**, on the other hand, exhibited a small hump at the similar position, suggesting that the polymer main chains are much less orderly packed along the π-π stacking direction in this polymer. Again, the presence of more α-β coupling linkages and branched (and lightly cross-linked) structural defects in **P5** would sterically encumber the π-π stacking of the polymer main chains. It is noticed that the π-π stacking distance of these polymers is smaller than that of **PDQT-24** (0.39 nm)[143], indicating the stronger intermolecular interaction in **PDBTz** polymers.

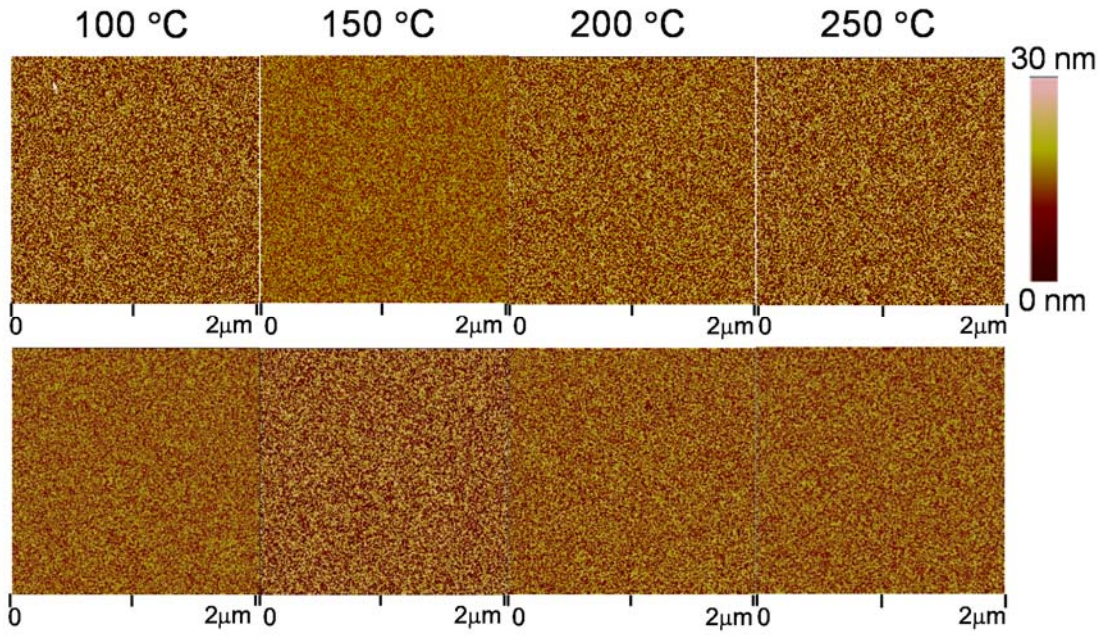

Figure 5-5 AFM images (2 μm × 2 μm) of **P5** (top) and **P6** (bottom) thin films (~40 nm) on silicon dioxide substrates annealed at 100, 150, 200 and 250°C

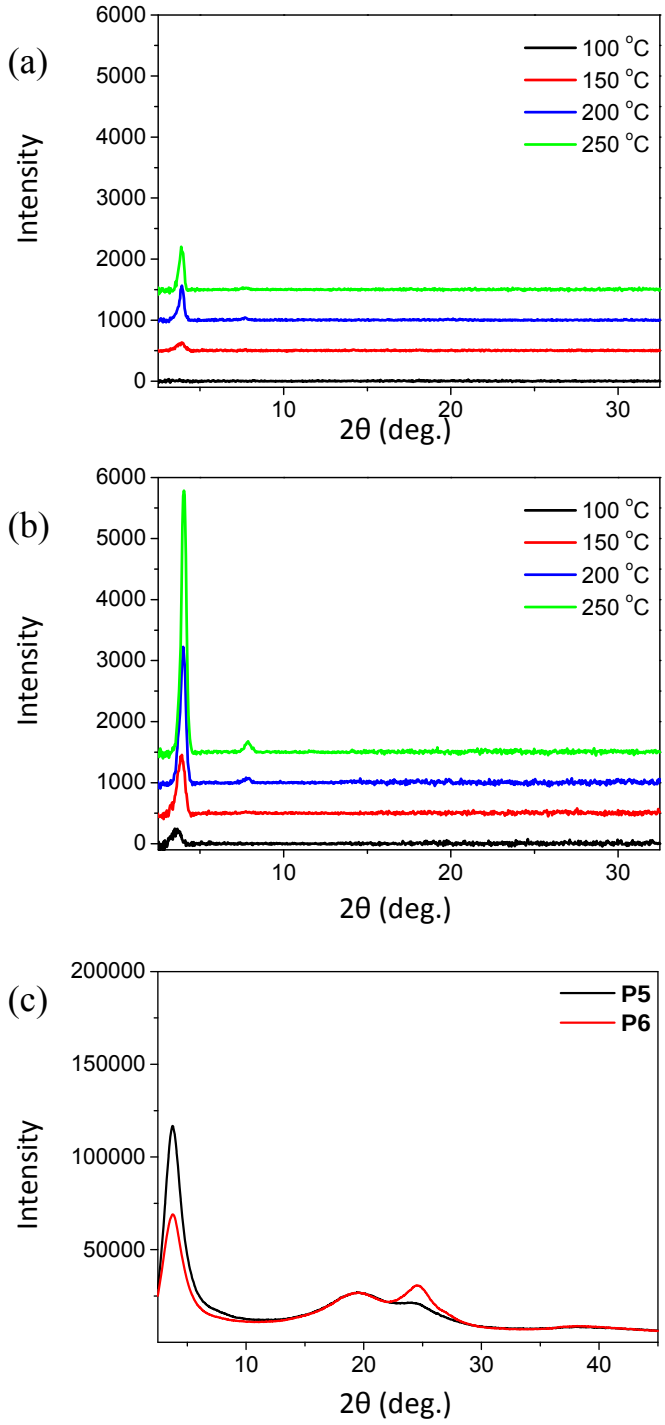

Figure 5-6 XRD diagrams obtained from spin-coating **P5** (a) and **P6** (b) thin films (~40 nm) on SiO_2/Si substrates, and transmission diagram (c) of 250 °C-annealed **P5** and **P6** flakes.

To evaluate the charge transport performance of **P5** and **P6**, we used these two polymers as channel semiconductors in top-gate, bottom-contact OTFT devices. The Au source and drain electrodes were deposited on a SiO_2/Si wafer substrate by a common photolithography method. A solution of **P5** or **P6** in chloroform (10 mg mL^{-1}) was spin-coated on the substrate to obtain a polymer thin film (~40 nm), which was annealed at 100 °C, 150 °C, 200 °C or 250 °C for 15 min on a hotplate in nitrogen. Then the gate dielectric layer (~570 nm) was formed by spin-coating a Cytop (a fluoropolymer) solution at 2000 rpm. After baking on a hotplate at 100 °C for 1 hr in nitrogen, a ~70 nm Al layer was deposited by thermal evaporation as the gate electrode. The devices were characterized in air in the absence of light. In contrast with **PDQT** that showed unipolar hole transport performance,[43,63,143] all devices of **P5** and **P6** exhibited ambipolar charge transport behavior with more pronounced electron transport over hole transport (Table 5-1), which is a result of the presence of electron-deficient bithiazole units. In the n-channel operation mode, devices based on the **P5** thin films showed electron mobility up to 3.7×10^{-3} $cm^2V^{-1}s^{-1}$ for the 100 °C-annealed films. The mobility improved as the annealing temperature increased. The highest electron mobility of 2.4×10^{-2} $cm^2V^{-1}s^{-1}$ was achieved for a 250 °C-annealed film. On the other hand, **P6** showed much superior electron transport performance. The average electron mobility increased from 1.6×10^{-2} $cm^2 V^{-1} s^{-1}$ for the 100 °C-annealed films to 0.42 $cm^2 V^{-1} s^{-1}$ for the 250 °C-annealed films. A maximum electron mobility of ~0.53 $cm^2 V^{-1} s^{-1}$ was achieved for a 250 °C-annealed **P6** film (Figure 5-7). In the p-channel operation mode, both polymers showed hole transport characteristics, but their hole mobilities are about one order of magnitude lower than their respective electron mobilities at the same annealing temperatures. The best hole mobilties are 2.4×10^{-3} $cm^2 V^{-1} s^{-1}$ for **P5** and 5.9×10^{-2} $cm^2 V^{-1} s^{-1}$ for **P6**, both achieved for the films annealed at 250 °C. The significantly lower charge transport performance shown by **P5** is considered primarily due to the presence of a larger amount of irregular α-β coupling linkages and branched (and lightly cross-linked) structures, which reduced the main chain conjugation

length and resulted in disordered chain ordering as revealed by the UV-Vis and XRD data. Polymer thin films annealed at a higher temperature of 300 °C were also tested, but the mobility values dropped. Because both **P5** and **P6** showed very good thermal stability with a 5% weight loss at 395 °C and 384 °C, respectively (Figure 5-8), the drop in mobility for the 300 °C-annealed polymer films is presumably due to the deteriorated semiconductor/dielectric or semiconductor/electrode interface.

Table 5-1 Performance of OTFT devices using **P5** and **P6** annealed at different temperatures

Polymer	Annealing temperature (°C)	Average electron mobility (standard deviation) ($cm^2V^{-1}s^{-1}$)	Maximum electron mobility ($cm^2V^{-1}s^{-1}$)	Average hole mobility (standard deviation) ($cm^2V^{-1}s^{-1}$)	Maximum hole mobility ($cm^2V^{-1}s^{-1}$)
P5	100	3.3×10^{-3} (6.7×10^{-4})	3.7×10^{-3}	5.7×10^{-4} (1.3×10^{-4})	7.2×10^{-4}
	150	1.3×10^{-2} (5.8×10^{-4})	1.3×10^{-2}	3.0×10^{-4} (1.1×10^{-4})	3.0×10^{-4}
	200	2.3×10^{-2} (1.1×10^{-2})	3.9×10^{-2}	3.8×10^{-4} (1.9×10^{-4})	5.5×10^{-4}
	250	2.4×10^{-2} (9.2×10^{-3})	3.9×10^{-2}	2.0×10^{-3} (2.6×10^{-4})	2.4×10^{-3}
P6	100	1.6×10^{-2} (1.2×10^{-3})	1.7×10^{-2}	7.0×10^{-3} (1.7×10^{-3})	8.9×10^{-3}
	150	7.9×10^{-2} (1.1×10^{-2})	9.2×10^{-2}	7.0×10^{-3} (3.5×10^{-3})	1.1×10^{-2}
	200	7.9×10^{-2} (2.3×10^{-2})	0.11	7.0×10^{-3} (1.1×10^{-3})	8.2×10^{-3}
	250	0.42 (0.11)	0.53	4.8×10^{-2} (1.1×10^{-2})	5.9×10^{-2}

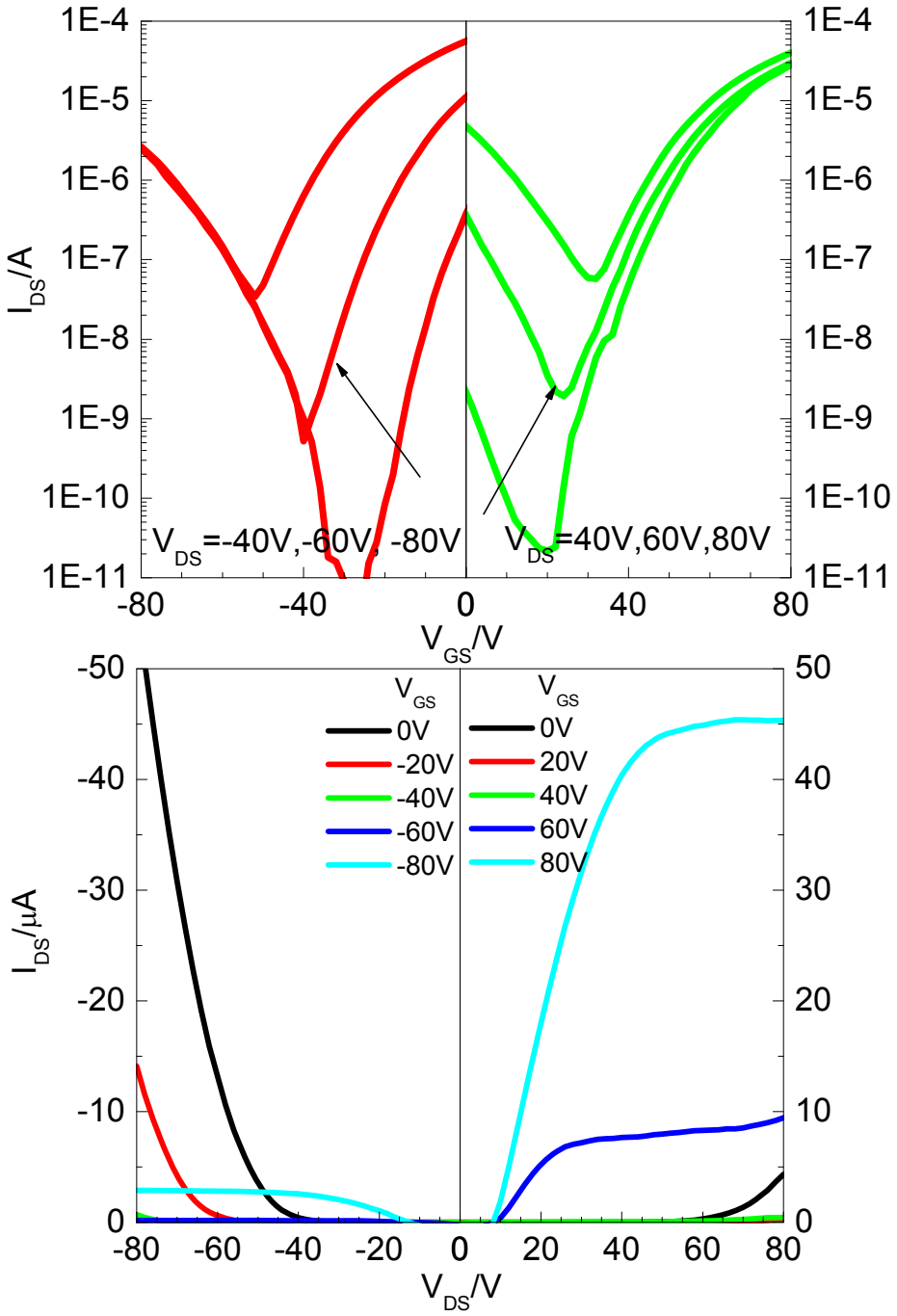

Figure 5-7 Transfer (a) and output curves (b) of OTFT devices with **P6** thin films annealed at 250 °C for 15 min. Device dimensions: channel width (W) = 1 mm; channel length (L) = 30 μm.

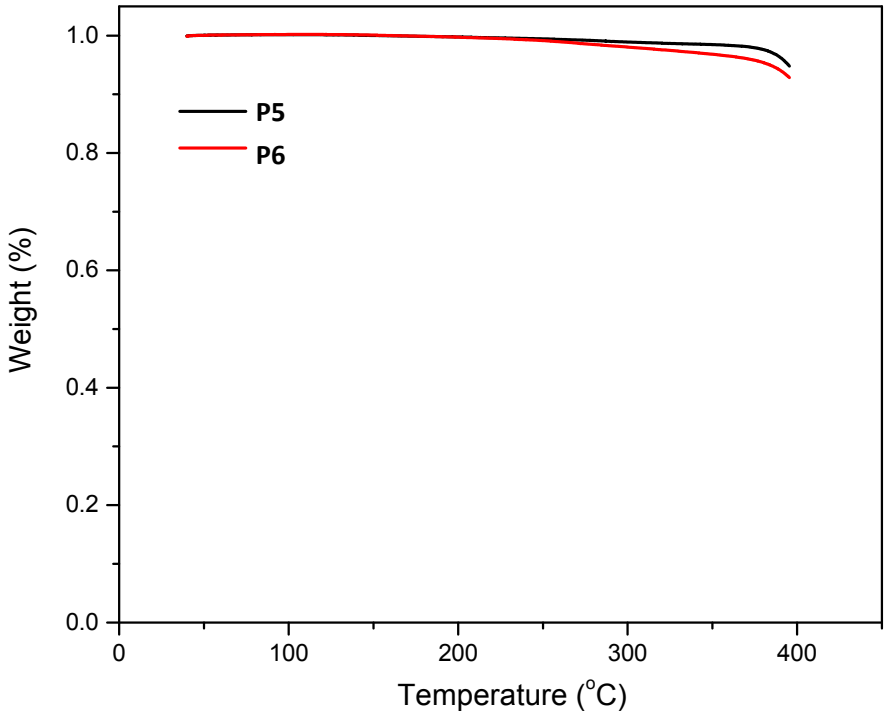

Figure 5-8 TGA curves of **P5** and **P6** at a heating rate of 10 °C min^{-1} under nitrogen.

5.3 Conclusion

Two DPP-bithiazole copolymers **P5** and **P6** were synthesized using the DHAP method via two routes. **P5** was synthesized by reacting 5,5'-dibromo-2,2'-bithiazole and the DPP monomer, while **P6** was synthesized by reacting the dibromo DPP monomer and 2,2'-bithiazole. It was found that **P5** showed a larger band gap, much poorer solubility and lower degree of crystallinity compared to **P6**, which were considered to be due to the presence of a larger amount of α-β coupling linkages and branched (and lightly cross-linked) structures in the former. **P6**, which has less structural defects, achieved very high ambipolar charge transport performance with electron/hole mobility up to 0.53 $cm^2V^{-1}s^{-1}$ and 5.9 × 10^{-2} $cm^2V^{-1}s^{-1}$, respectively, in OTFT devices. In contrast, **P5** showed one order of magnitude lower mobilities. Our results

demonstrated that placing the bromo groups on different monomers could significantly influence the occurrence of α–β coupling side reactions, which led to the formation of polymers with dramatically different properties. This work for the first time demonstrated that 2,2'-bithiazole is a suitable monomer with good regioselectivity for the construction of regular conjugated polymers with promoted electron transport performance via DHAP. The synthesis of **PDBTz'** (Figure 5-1), an isomer of **PDBTz**, by DHAP between 5,5'-bithiazole (or 2,2'-dibromo-5,5'-bithiazole) and the DPP-containing monomer **12** (or **13**) is under way. Changing the positions of the nitrogen atoms in the bithiazole units may have an impact on the side reactions and the charge transport performance of the resulting polymers.

Chapter 6 Novel Pyrrolo[3,4-*c*]pyrrole-1,3-dione (1,3-DPP) Based High Crystallinity Conjugated Polymers

(This chapter is partially published in Polymer Chemistry (2014), Guo, C.; Sun, B.; Li, Y., **5**: 5247-5254.)

6.1 Introduction

As indicated in the last chapter, diketopyrrolopyrrole (DPP), or more precisely, pyrrolo[3,4-*c*]pyrrole-1,4(2*H*,5*H*)dione (1,4-DPP as shown in Figure 6-1), has been extensively investigated for the development of high-performance small molecules and polymeric semiconductors for OTFTs and OPVs.[31,41–45,47,48,68,170–172] Another diketopyrrolopyrrole isomer, pyrrolo[3,2-*b*]pyrrole-2,5(1*H*,4*H*)-dione (2,5-DPP in Figure 6-1), was recently investigated, which showed promising mobility up to 0.03 $cm^2V^{-1}s^{-1}$ in OTFTs and power conversion efficiency up to 5.1 % in OPVs.[73] The third DPP isomer, pyrrolo[3,4-*c*]pyrrole-1,3(2*H*,5*H*)-dione (1,3-DPP in Figure 6-1), was recently used as a building block for polymers for OPVs.[173] In this chapter, we designed and synthesized two copolymers comprising this 1,3-DPP building block and quaterthiophene for OTFTs. We found that these polymers showed dramatic differences in their optoelectronic properties from the ones based on the 1,4-DPP isomer. In OTFT devices, both new polymers showed characteristic p-type charge transport behavior with hole mobility in the order of 10^{-2} $cm^2V^{-1}s^{-1}$.

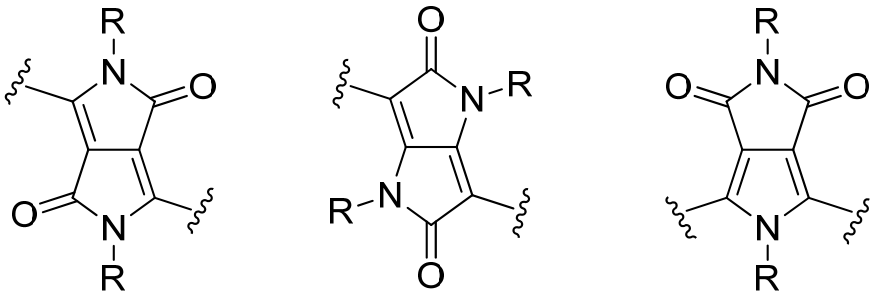

Figure 6-1 Chemical structures of 1,4-DPP, 2,5-DPP, and pyrrolo[3,4-*c*]pyrrole-1,3(2*H*,5*H*)-dione (1,3-DPP).

6.2 Results & Discussion

Scheme 6-1 outlines the synthesis of 1,3-DPP monomer and its corresponding copolymers. Diethyl 1*H*-pyrrole-3,4-dicarboxylate (**14**) and 1*H*-pyrrole-3,4-dicarboxylic acid (**15**) were prepared in 55% and 87% yields, respectively, according to the literature methods.[46] Branched 2-octyldodecan-1-amine was then reacted with compound **15** to obtain 4-((2-octyldodecyl)carbamoyl)-1*H*-pyrrole-3-carboxylic acid (**16**) (90% yield), which was ring-closed in refluxing thionyl chloride to form (2-(2-octyldodecyl)pyrrolo[3,4-*c*]pyrrole-1,3(2*H*,5*H*)-dione (**17**) (62% yield). Two types of side chains, 2-octyldodecyl and dodecyl, were incorporated at the 5-position of **9** using the respective alkylbromide. The resultant 2,5-disubstituted **18a** and **18b** were then brominated at the 4,6-positions to form compound **19a** and **19b** using *N*-bromosuccimide (NBS). Stille coupling reaction of **20a** and **20b** with 2-tributylstannylthiophene produced compounds **20a** and **20b**, which were further brominated with NBS to afford the monomers **21a** and **21b**, respectively. The target polymers **P7** and **P8** were synthesized via Stille coupling polymerization with 5,5'-bis(trimethylstannyl)-2,2'-bithiophene. The crude polymers were purified by Soxhlet extraction using acetone to remove oligomers. **P7** showed excellent solubility and could be dissolved completely with refluxing hexane with 98.7 % yield. **P8** with one branched

2-octyldodecyl side chain and one shorter straight dodecyl side chain is insoluble in hexane, but could be easily dissolved in chloroform with 94.3 % yield. Gel permeation chromatography (GPC) with chloroform as an eluent and polystyrene as standards at a column temperature of 50 °C was used to determine the molecular weights of both polymers. The number average molecular weight (M_n) / the polydispersity index (PDI) are 37.8 kDa / 2.13 for **P7** and 40.7 kDa / 2.05 for **P8**. Both polymers showed very good thermal stability with a 5% weight loss at 412 °C for **P7** and 415 °C for **P8**, as determined by TGA (Figure 6-2).

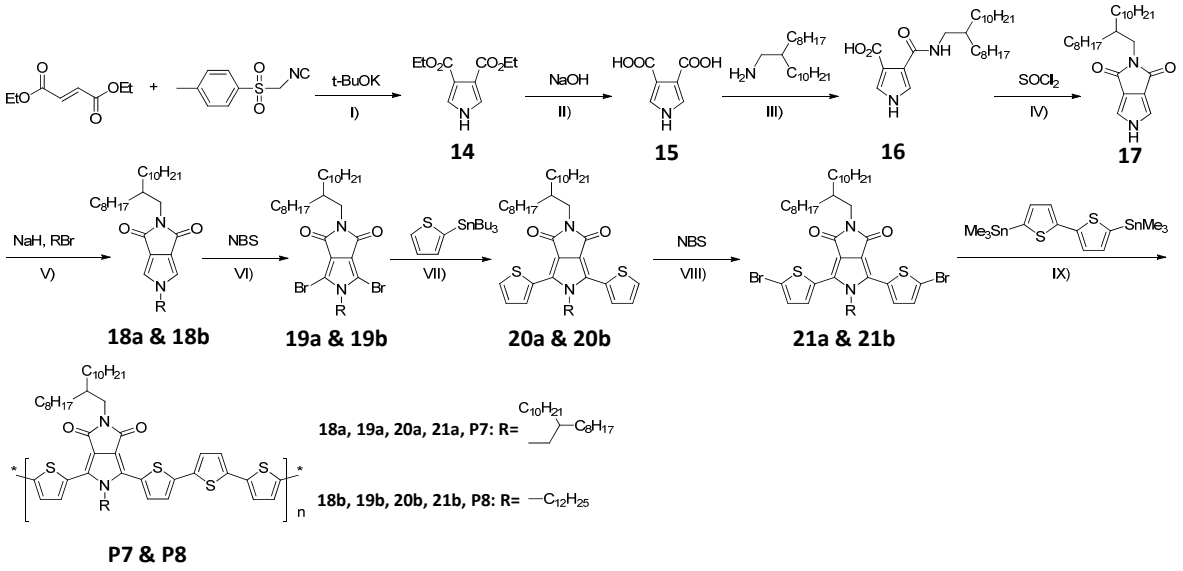

Scheme 6-1 Synthetic route to 1,3-DPP monomers and polymers **P7** and **P8**: i) THF/r.t.; ii) ethanol/H_2O/reflux; iii) THF/reflux to r.t.; iv) DMF/r.t.; v) DMF/r.t.; vi) DMF/r.t.; vii) toluene/$Pd_2(dba)_3$/P(*o*-tolyl)$_3$/110 ˚C; vii) DMF/r.t.; ix) chlorobenzene/$Pd_2(dba)_3$/P(*o*-tolyl)$_3$/130 ˚C.

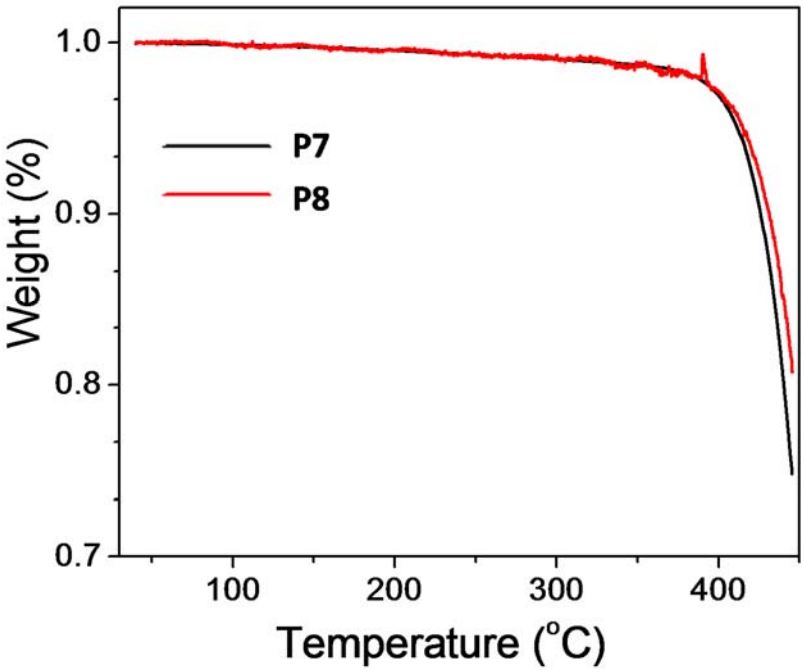

Figure 6-2 TGA curves of **P7&P8** with a heating rate of 10 °C·min^{-1} under N_2.

In solution, both polymers have an identical structure. In solid state, however, the lay direction of thiophenes adjacent to 1,3-DPP core would have strong influence on backbone coplanarity and molecular geometry. Between two rotamers (Figure 6-3), it is hard to tell which is preferred since interactions between S (thionyl)…O (carbonyl) could exist in T-OS structure, while T-NS structure possess intramolecular hydrogen bonding. Therefore, we conducted a computer simulation on a simple 1,3-DPP-Me core with two thiophene units to compare two rotamers, by performing density functional theory (DFT) calculations using Gaussian 09W (the B3LYP hybrid functional with the 6-31G basis set).[116,117] Based on the calculation and side views, the dihedral angle between 1,3-DPP-Me core and thiophene of T-OS is about 32°, much larger than that of T-NS (17°). Besides, the distance between S (thienyl)…O (carbonyl) of T-OS is 3.31 Å, which is almost equal to the sum of S and O van der Waals radii (3.32 Å), and larger than the hydrogen bonding distance (2.23 Å). All the results indicate the intramolecular interaction of

hydrogen bonding surpass that between S (thienyl)…O (carbonyl), and T-NS would be preferred in the solid state.

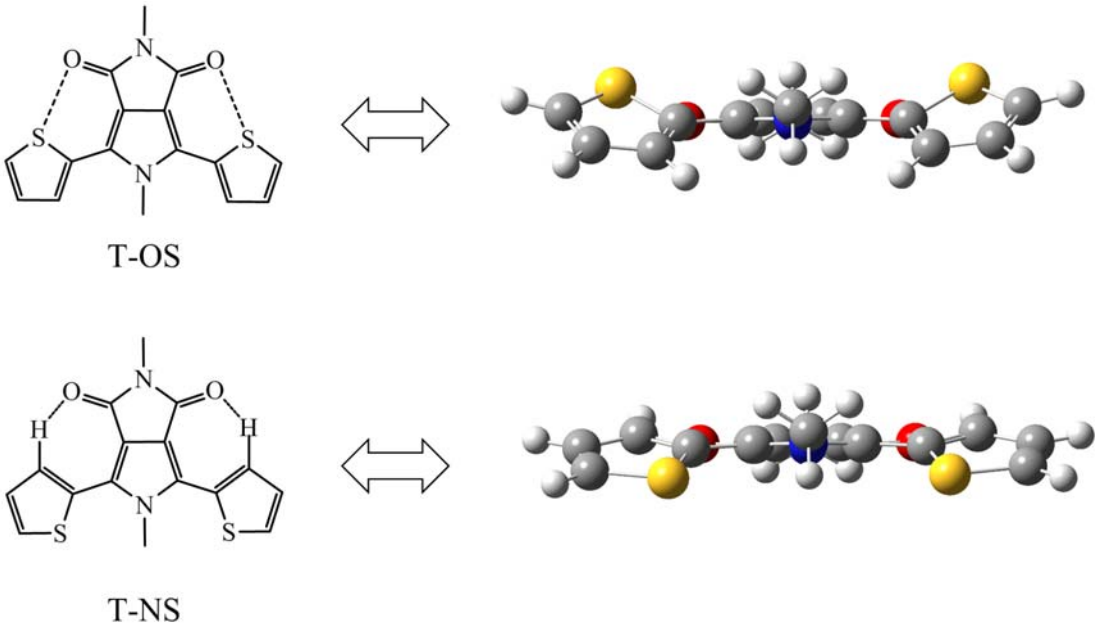

Figure 6-3 The structures of two rotamers (T-OS and T-NS) and their simulated side view.

To reveal absorption profiles, **P7** and **P8** were measured in dilute chloroform solutions, showing the wavelength of maximum absorption (λ_{max}) at 473 nm and 497 nm, respectively (Figure 6-4a). The red-shift (~24 nm) in λ_{max} in solution for **P8** with respect to **P7** most likely resulted from the more coplanar backbone of **P8** due to the less steric effect of its straight dodecyl substituent on the neighboring thiophenes than that of the bulkier 2-octyldodecyl in **P7**. In the solid state, the λ_{max} of **P7** and **P8** red-shifted to 483 and 526nm, respectively. Notice that a small shoulder appeared in the absorption curve of the **P8** film. The large red-shift in λ_{max} from solution to film for **P8** (29 nm) than that for **P7** (10 nm) as well as the appearance of a shoulder in **P8** suggest that the polymer chains in **P8** are more ordered due to the reduced steric effect of the straight side chain in **P8**. As a result, the optical band gap of **P8** (1.92 eV) is narrower than that of **P7** (2.02 eV), calculated from the absorption onset of the as-spun films. The observation of reversible oxidative cycles obtained by cyclic voltammetry (CV) suggests that both polymers are

stable in the oxidation processes. The reductive processes are also reversible, but the currents are much weaker relative to those in the oxidative processes. By using the onset oxidative potentials, the highest occupied molecular orbital (HOMO) levels were calculated to be -5.54 eV and -5.40 eV for **P7** and **P8**, respectively. The lowest unoccupied molecular orbital (LUMO) levels were estimated using the HOMO levels by CV and the optical bandgaps by UV to be -3.52 eV and -3.48 eV, respectively. The UV-vis absorption and the electrochemical properties of **P7** and **P8** dramatically differ from those of their analogous polymers based on 1,4-DPP and quarterthiophene (λ_{max} = 777 nm in solution) and 790 nm in film; E_{HOMO} / E_{LUMO} = -5.2 eV / - 4.0 eV).[43] Although data of the exact analogous polymer based on 2,5-DPP and quaterthiophene are unavailable due to its poor solubility, other 2,5-DPP polymers showed similar UV and CV properties to those of **P8**.[73] Therefore the 1,3-DPP building block seems more resembling the 2,5-DPP isomer, and thus a weaker electron acceptor than the 1,4-DPP isomer.

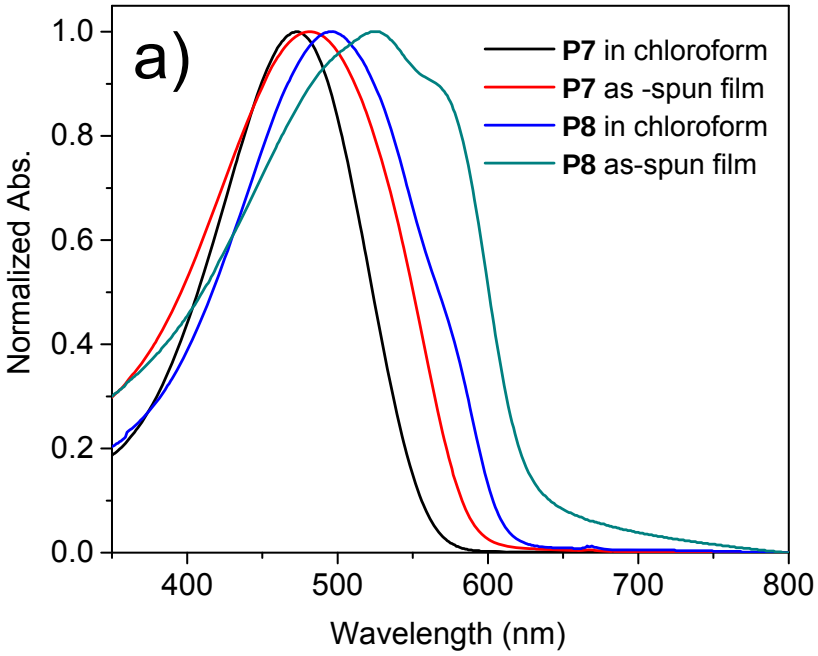

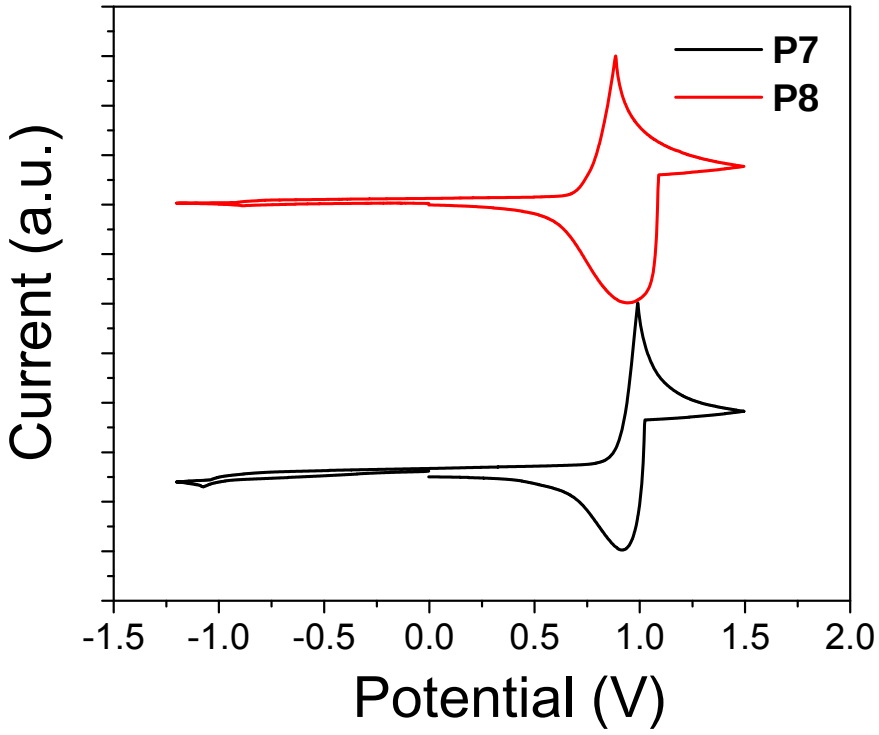

Figure 6-4 UV-vis absorption spectra of (a) **P7** and **P8** in chloroform solutions and in thin films; (b) Cyclic voltammograms of as-spun **P7** and **P8** thin films measured in anhydrous CH_3CN solution using Bu_4NPF_6 as the electrolyte.

Owing to their excellent solubility in common organic solvents, both polymers showed very good film formation property as shown in the atomic force microscopy (AFM) images in Figure 6-5. All **P7** thin films are very smooth and didn't change markedly by thermal annealing. In contrast, small grains are observed for the **P8** thin film annealed at 100 °C. At an annealing temperature of 150 °C, the grains have grown notably and all grains are well interconnected. The 200 °C-annealed **P8** thin film, however, showed more isolated grains with larger grain boundaries. To study the chain ordering of these polymers, we used both reflection and transmission X-ray diffractometry (XRD) techniques. As shown in Figure 6-6, the reflection XRD of the **P7** thin films showed no peaks at the annealing temperatures of 100, 150, and 200 °C, indicating that all these **P7** films are amorphous. This is due to the two bulky branched side chains on the 1,3-DPP

unit, which impede the ordering of the polymer backbone. The **P8** film annealed at 100 °C exhibited a peak at 2θ = 4.23°, which corresponds to a *d*-spacing of 2.1 nm. Since there are no other diffraction peaks, the polymer chains presumably adopted a layer-by-layer lamellar packing motif, which has been frequently observed for other crystalline conjugated polymers.[20,84] As the annealing temperature increased to 150 °C, the primary peak intensified significantly and the peak shifted slightly to 2θ = 4.35°, which corresponds to a *d*-spacing distance of 2.03 nm. A small secondary peak also appeared at 2θ = 8.63°. This manifests that the polymer chains are packed much more orderly with the aid of thermal annealing at this temperature. Upon further increasing the annealing temperature to 200 °C, a precipitous drop in the intensity of the primary peak was observed, indicating the reduced crystallinity and the chain ordering of the polymer film. To elucidate the in-plane chain packing, we measured the 150 °C-annealed polymer thin films using transmission XRD (Figure 6-7). As expected, **P7** showed a broad peak around 2θ = ~20° (*d* = 0.44 nm), which represents the typical van der Walls distance for an amorphous polymer. On the other hand, the 150 °C-annealed **P8** thin film showed a distinct peak at 23.68°, corresponding to a π-π stacking distance of 0.376 nm. The XRD data fully agrees with the AFM images observed for the polymer thin films annealed at different temperatures.

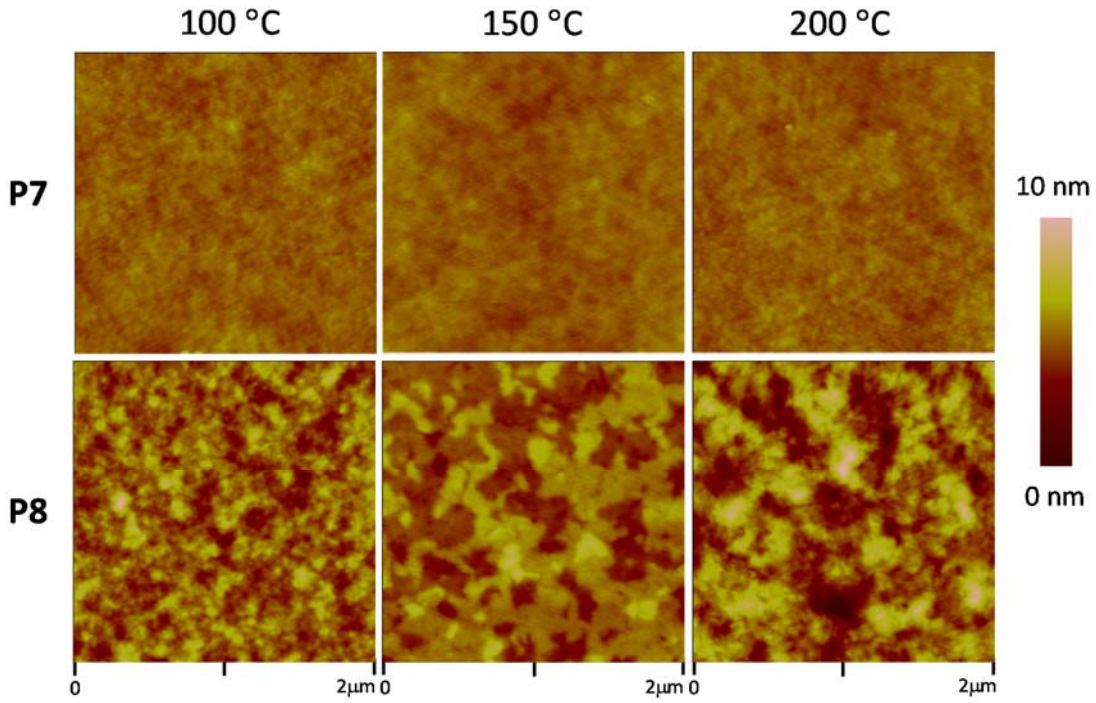

Figure 6-5 AFM images (2 μm × 2 μm) of **P7** and **P8** thin films (~50-60 nm) spin coated on silicon substrates annealed at 100, 150 and 200 °C under nitrogen.

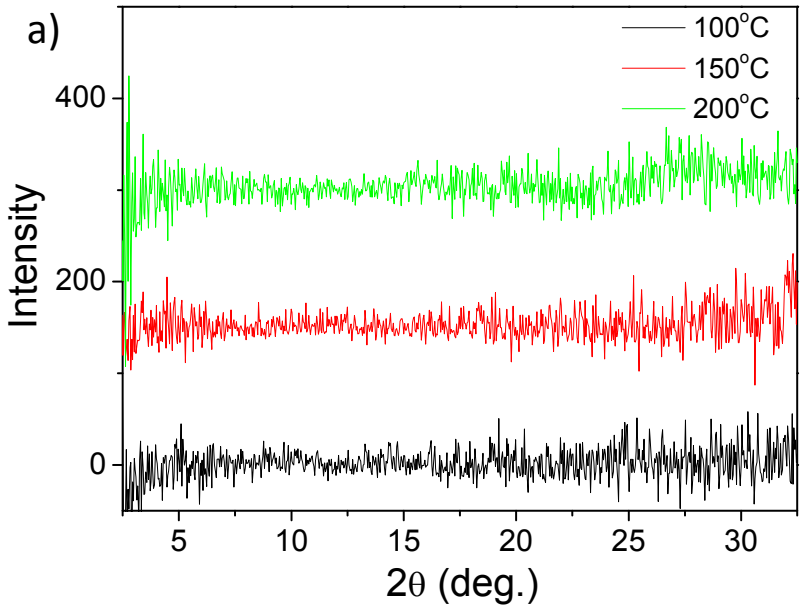

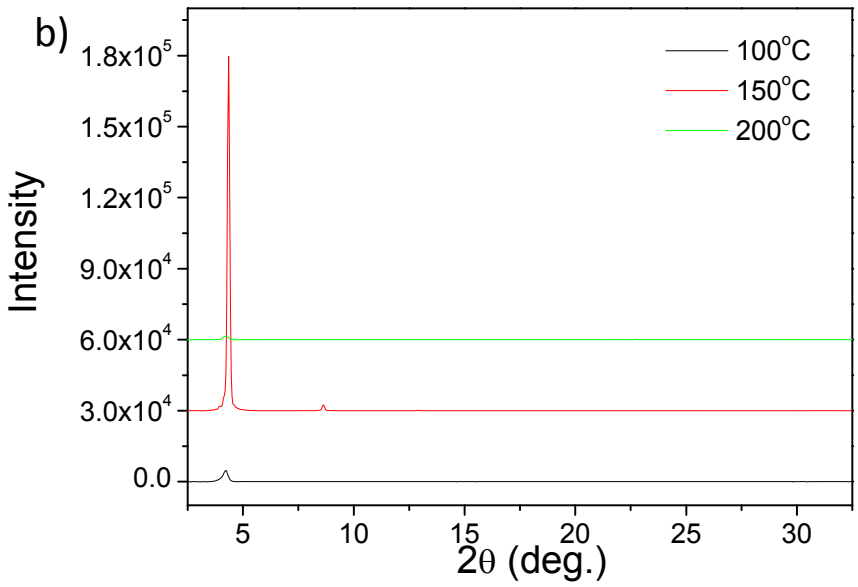

Figure 6-6 XRD diagrams obtained from spin-coating **P7** (a) and **P8** (b) thin film on silicon substrates annealed at 100, 150 and 200 °C.

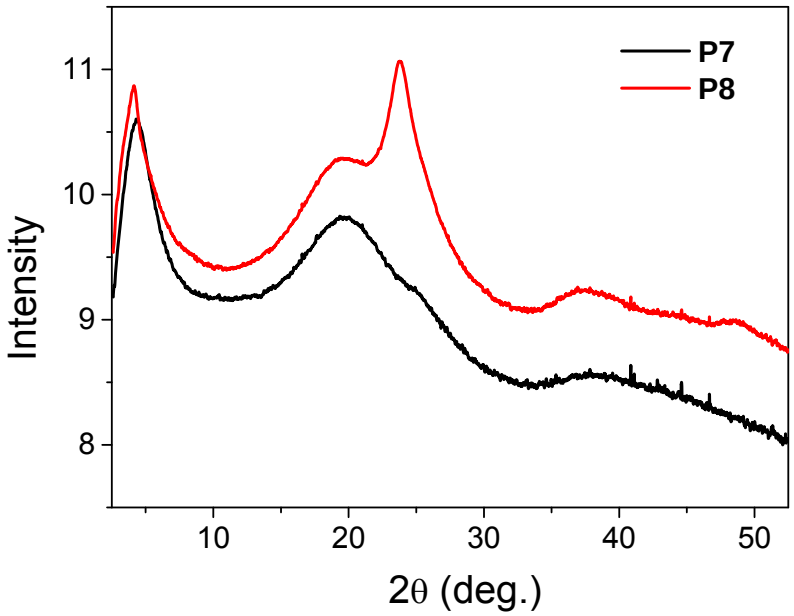

Figure 6-7 2D-XRD diagrams obtained from spin-coating **P7** and **P8** thin film on silicon substrates annealed at 150 °C.

To evaluate their charge transport performance, we used these two polymers as channel semiconductors in bottom-gate, bottom-contact OTFT devices. Gold source and drain electrode pairs (with a channel length of 30 μm and a channel width of 1 mm) were deposited on heavily n-doped Si wafer (as the gate) with a 300 nm-thick top SiO_2 insulating layer (as the dielectric), using a conventional photolithography technique. Prior to use, the SiO_2 surface in the channel region was passivized with dodecyltrichlorosilane (DDTS). Then a polymer thin film (~30-50 nm) was deposited by spin-coating a polymer solution in chloroform, followed by thermal annealing at different temperatures on a hot plate in a glove box. After cooling to room temperature, the devices were analyzed in the same glove box in the absence of light. Devices based on the **P7** thin films annealed at 100, 150, and 200 °C showed almost the same hole transport characteristics with mobility up to 3.2×10^{-4} $cm^2V^{-1}s^{-1}$ (current on-to-off ratios of $\sim10^3$) (Figure 6-8a, b). Devices based on the **P8** thin films were investigated in more detail with finer annealing temperature intervals at 100, 130, 140, 150, 160, 180, and 200 °C, since the crystallinity and morphology of **P8** were found to be very sensitive to the annealing temperature, particularly around 150 °C, as discussed previously. As can be clearly seen in Figure 6-9, the average mobility increases from 3.9×10^{-3} $cm^2V^{-1}s^{-1}$ for the 100 °C -annealed film to 1.2×10^{-2} $cm^2V^{-1}s^{-1}$ for the 150 °C-annealed film, then decreases as the annealing temperature is beyond 150 °C. This trend is in agreement with the change in crystallinity revealed by the XRD and AFM results. The maximum mobility is 1.3×10^{-2} $cm^2V^{-1}s^{-1}$ (on-to-off ratios of $\sim5\times10^4$) for a device with a 150 °C-annealed **P8** film (Figure 6-8c, d). The mobility values are similar to those achieved for the 2,5-DPP based polymers.[73] The dramatic difference in mobility between **P7** and **P8** suggests that the side chains have a significant impact on the charge transport performance of these 1,3-DPP polymers, that is, the incorporation of a straight side chain at the 5-position of 1,3-DPP helps increasing the chain ordering and thus the charge transport of the resultant polymer. If the side chains could be

optimized and other donor building blocks are applied, the chain ordering and the charge transport performance of this class of polymers are expected to improve.

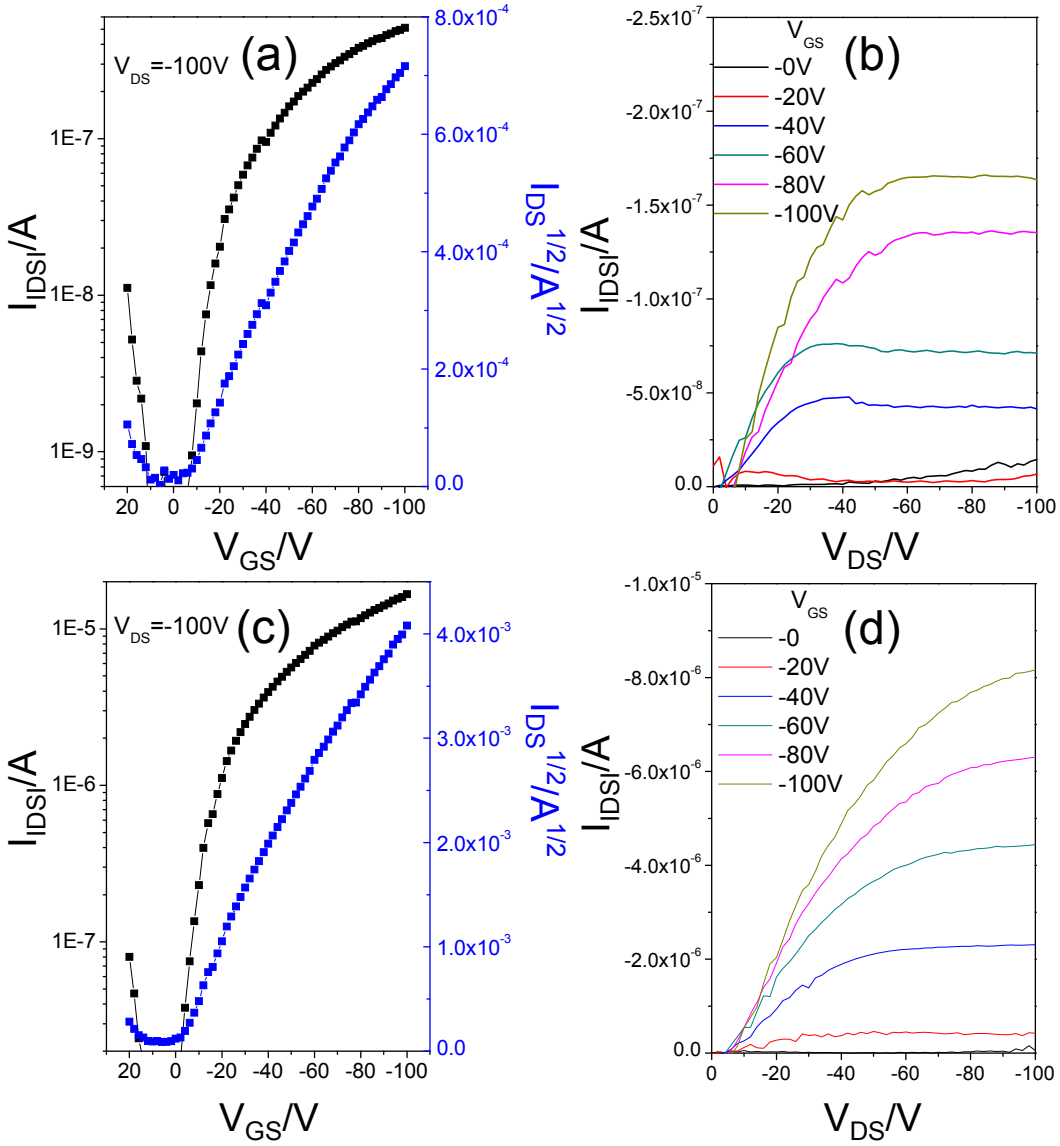

Figure 6-8 Transfer and output curves of OTFT devices with **P7** (a and b) and **P8** (c and d) thin films.

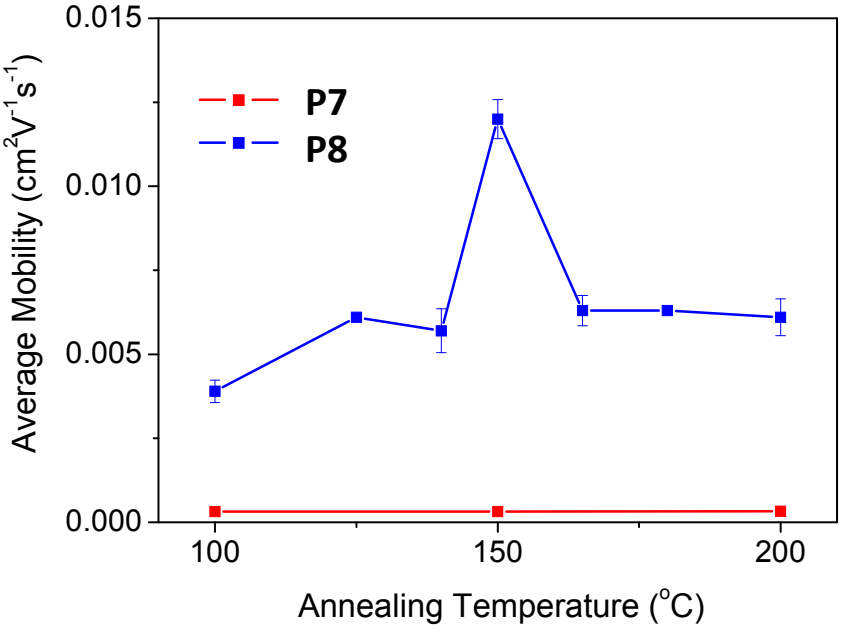

Figure 6-9 Mobility variation vs annealing temperature of OTFTs based on **P7** and **P8** thin film.

6.3 Conclusion

In summary, we reported the use of a DPP isomer, pyrrolo[3,4-*c*]pyrrole-1,3-dione (1,3-DPP), as a building block to construct π-conjugated polymers as channel semiconductors for OTFTs. Two copolymers based on 1,3-DPP and quaterthiophene units with different side chain combinations were obtained, which showed dramatically different optoelectronic properties and molecular packing from those of the polymers based on the 1,4-DPP isomer. Charge transport performance of these polymers was evaluated in OTFTs and hole mobility as high as 0.013 $cm^2V^{-1}s^{-1}$ was obtained. Our preliminary results indicate 1,3-DPP is a promising building block for constructing polymer semiconductors for printed electronics.

Chapter 7 Conclusions and Future Direction

This thesis consists of two parts: I) development of novel acceptor building block indigo in D-A conjugated polymers for OTFTs (Chapters 2-4) (

Figure **7-1**); II) development of new DPP based polymers (Chapters 5 and 6) (Figure 7-2).

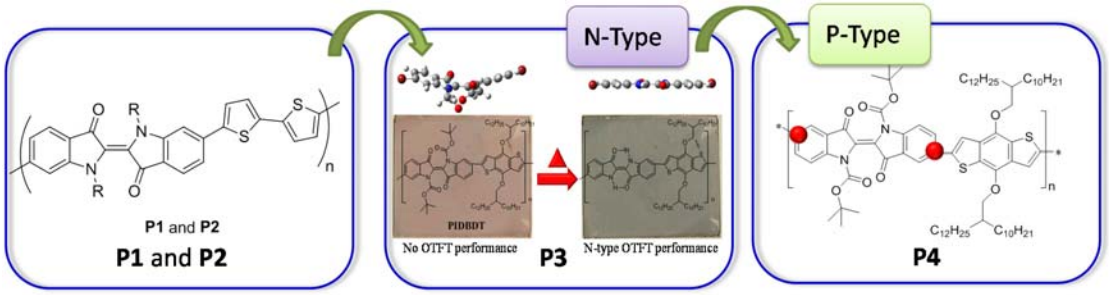

Figure 7-1 Research work in Chapters 2-4.

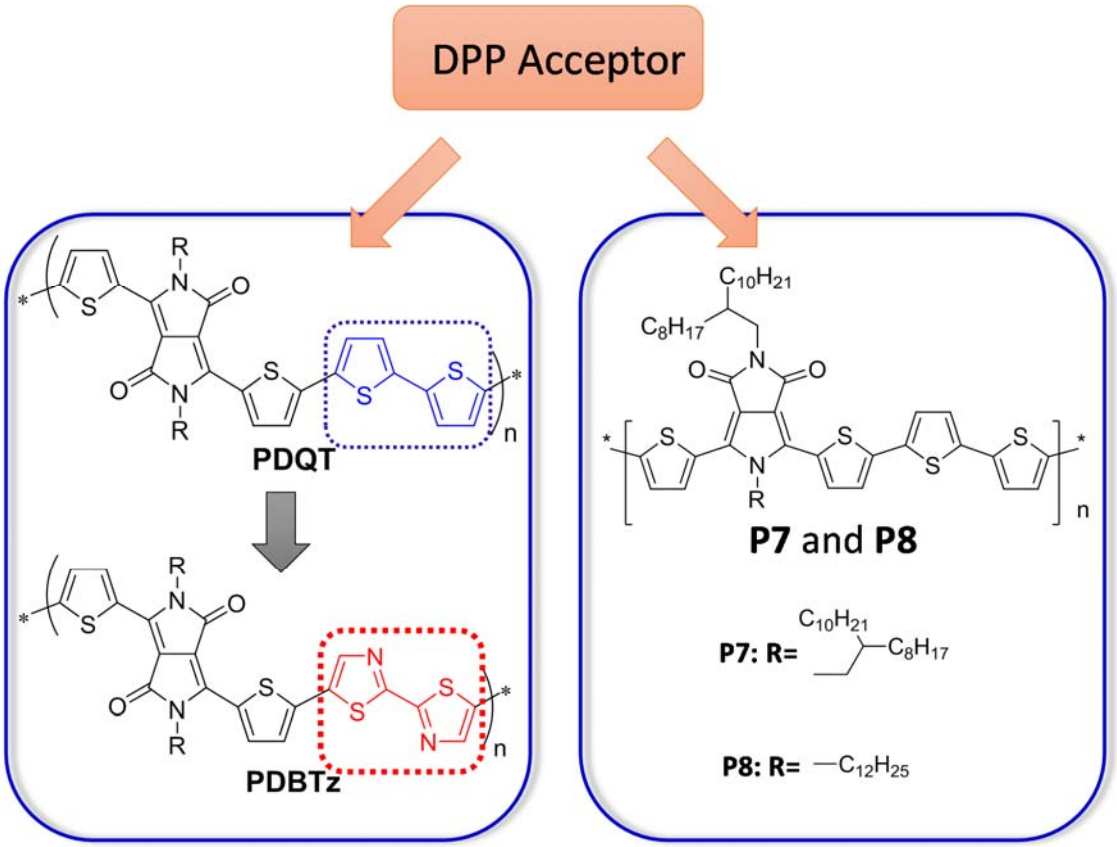

Figure 7-2 Research work in Chapters 5-6

In Chapter 2, a natural dye, Tyrian Purple (6,6'-dibromoindigo), was successfully used as a novel acceptor building block in D-A conjugated polymers. The non-substituted indigo has been reported as the small molecular organic semiconductor in OTFTs and showed good electrical performane.[95–98] However this compound could not be used to construct D-A polymers since its poor solubility is a big challenge for purification and polymerization. After numerous attempts, it was found that 6,6'-dibromoindigo could be solubilized by substitution with acyle side chains, allowing for the synthesis of soluble indigo-based polymers. The resulting 6,6'-indigo based D-A polymers showed p-type hole transport performance in organic semiconductors in OTFTs, which are the first indigo-based polymers that have been demonstrated as active layers in OTFTs.

To increase the mobility of indigo based polymers, backbone coplanarity was achieved using a post-deposition thermal annealing of novel functional indigo polymers (Chapter 3). Tyrian purple was substituted with *tert*-butoxy carbonyl (*t*-Boc), which is a thermally labile protection group, and then copolymerized with another monomer unit, BDT that bears bulky alkoxy side chains as a donor. Upon thermal removal of the *t*-Boc groups, the indigo units of the resulting polymer become highly coplanar, affording improved electron transport performance in OTFTs with a 5-fold increase in electron mobility compared to that of the indigo-based polymers reported in Chapter 2. These results confirmed that the backbone coplanarity plays a key role in determining the charge transport performance and that the use of *t*-Boc as a substituent is a feasible approach to achieving both good solubility and high coplanarity of indigo-based polymers.

A new way to control the charge transport polarity of a polymer semiconductor was demonstrated in Chapter 4. We found that all the polymers reported in Chapter 2 and 3, which contains 6,6'-indigo units, showed n-type electron transport behavior. Electron distributions in the LUMO and HOMO of the indigo unit calculated by DFT could explain the electron transport behavior since electrons can be delocalized along the polymer backbone through the LUMO rather than the HOMO along the backbone through the 6- and 6'-positions. Serendipitously, we

found that the 5- and 5'-positions of the indigo unit are occupied by electrons in the HOMO but empty in the LUMO, opposite to the 6 and 6' positions. This suggests that the corresponding polymer containing the 5,5'-indigo units, a regioisomer of **P3** reported in Chapter 3, may exhibit the opposite p-type charge transport behavior. To prove our assumption, we synthesized **P4** and found that this polymer indeed showed p-type semiconductor behavior. This is the first demonstration that the type of charge the carrier (hole or electron) can be readily controlled by simply changing the regiochemcial position of a building block in the polymer.

Chapter 5 introduced direct (hetero)arylation polymerization (DHAP) to synthesize bisthienyl diketopyrrolopyrrole-bithiazole copolymers. Compared to other polymerization methods such as Suzuki and Stille coupling reactions, DHAP involves less synthetic steps and is environmentally friendlier. Side reactions at the undesirable C-H bonds have been frequently reported for DHAP, which result in irregular cross-linked structures and fail to obtain high molecular weight soluble polymer products. Thiophene derivatives and several other types of compounds have been used successfully to prepare soluble high performance polymer semiconductors for printed electronics under controlled polymerization conditions. However, thiazole compounds containing both α and β C-H bonds have not been used as monomers for DHAP. This work for the first time demonstrated that a thiazole compound, 2,2'-bithiazole, is a suitable monomer with good regioselectivity for the construction of regular conjugated polymers with promoted electron transport performance via DHAP. We also found that the polymer synthesized by DHAP showed much higher electron mobility than that of similar polymer synthesized by the Stille coupling polymerization.

In Chapter 6, the isomer of 1,4-DPP, 1,3-DPP was used as a building block to construct copolymers with a quaterthiophene unit. The resulting conjugated polymers showed rather high LUMO (the lowest unoccupied molecular orbital) levels of ca. -3.5 eV, compared to the polymers based on the well-known 1,4-DPP isomeric structure. We found the type of alkyl side chain (straight or branched) has a great impact on the molecular ordering and the charge transport

performance of the resulting polymers. With a combination of a straight side chain and a branched side chain on 1,3-DPP, the polymer showed good solubility, high crystallinity, and promising p-channel charge transport performance with hole mobility up to 0.013 $cm^2V^{-1}s^{-1}$ in organic thin films transistors.

In conclusion, this work developed novel conjugated building blocks, systematically studied the properties of novel D-A polymers, and provided insights into DHAP using a thiazole-based monomer. The findings made in this work may lead to the discovery of the next generation high mobility polymer semiconductors.

Future research following this work may be directed to:

1) Explore other types of appropriate donors to improve the charge transport performance of indigo-based polymers. Upon thermal removal of the *t*-Boc groups, the indigo units of **P3** become highly coplanar. However, the donors also determine the coplanarity and conjugation of the polymer. For **P3** and **P4**, the dihedral angles between indigo units (acceptor) and benzodithiophene units (donor) are around 26º according to the DFT simulation results. The twisting could also disrupt the electron delocalization along the polymer backbone, and resulted in low mobility. An appropriate donor that has small dihedral angle with the indigo unit should improve the charge transport performance of the resulting polymer.
2) Explore other conjugated building blocks which have similar electron distribution to that of the indigo unit. Computer simulations can be utilized to predict the electron distribution and suitable building blocks will be synthesized and incorporated into polymers to further demonstrate that the strategy to control the electron or hole charge transport polarity is also applicable to some other building blocks besides indigo.
3) Study the side reaction mechanisms in DHAP of bithiazole monomers. Our preliminary results have indicated the poor solubility and low performance of **P5** might be due to the cross-linking in polymerization. However the proposed mechanism need to be supported

by further experiments, which is important for the synthesis of other novel polymers by DHAP. In addition, the synthesis and property of **PDBTz'** (Figure 5-1), an isomer of **P5** and **P6**, by DHAP between 5,5'-bithiazole (or 2,2'-dibromo-5,5'-bithiazole) and the DPP-containing monomer **12** (or **13**) would be interesting. Changing the positions of the nitrogen atoms in the bithiazole units may have an impact on the side reactions and the charge transport performance of the resulting polymers.

4) Achieve high coplanarity of the 1,3-DPP based polymers by using sterically less demanding comonomers to improve the charge transport performance. As part of the research in Chapter 6, we found the dihedral angles between 1,3-DPP monomer and neighboring thiophenes is quite large (~17^{o}), indicating that the repeat unit is twisted, which would reduce the effective conjugation length of the polymer backbone. It may explain the fact that **P8** showed relatively low carrier mobility even through this polymer showed a high degree of crystallinity. To reduce the steric effect of the neighboring units on the 1,3-DPP core, sterically less demanding furan and 3-thiazole instead of thiophene may be used in the future. We conducted computer simulations on 1,3-DPP-bifuran and 1,3-DPP-bithiazole. As expected, the dihedral angles of these two monomer units are only 2.9^{o} and 8.5 ^{o}, respectively. Therefore, the charge carrier mobility of corresponding polymers based on 1,3-DPP-bifuran and 1,3-DPP-bithiazole may be improved compared with the polymers based on 1,3-DPP-bithiophene.

Appendix: Experimental Methods

In this chapter, instrumentation, detailed synthesis of materials, and device fabrication and characterization are provided.

Materials and Characterization

Chemicals were purchased from commercial sources and used without further purification. NMR spectra were recorded on a Bruker DPX 300MHz spectrometer with chemical shifts relative to tetramethylsilane (TMS, 0 ppm). Thermo Scientific GENESYS20 Spectrophotometer was used to collect UV-Vis spectra. With ferrocene as a reference which has a highest occupied molecular orbital (HOMO) of -4.8 eV,[43] cyclic voltammetry (CV) data were obtained with a electrochemical analyser CHI600E using an Ag/AgCl reference electrode, a Pt wire counter electrode, and a Pt foil working electrode in 0.1 M tetrabutylammonium hexafluorophosphate in dry acetonitrile at a scan rate of 50 mVs^{-1}. Low temperature gel-permeation chromatography (GPC) measurements were performed on a Waters SEC with chlorobenzene as the eluent at 40 °C. High temperature GPC measurements were performed on a Malvern HT-GPC using 1,2,4-trichlorobenzene as the eluent and polystyrene as standards for conventional calibration at 140 °C. AFM profiles were recorded on polymer thin films on dodecyltrichlorosilane (DDTS) - modified SiO_2 / Si substrates using a Dimension 3100 scanning probe microscope. The same samples were scanned by a Bruker D8 Advance powder diffractometer with standard Bragg-Bretano geometry using Cu Kα radiation (λ = 1.5406 Å). The thermogravimetry analysis (TGA) was conducted using a TGA Q500 (TA Instruments) at a heating rate of 10 $°Cmin^{-1}$ under nitrogen. Elemental analysis (EA) was performed on Elementar Vario EL Cube elemental analyzer.

Computer Simulations of Model Compounds

Geometry optimization of model compounds was performed based on the density functional theory (DFT) using the B3LYP hybrid function[174,175] and the 6-31G* basis set and the Gaussian

09W package[116,117] on the Shared Hierarchical Academic Research Computer Network (SHARCNET) of Canada.

The route used for all calculations was the following:

opt=tight freq b3lyp/6-31g(d) guess=save geom=connectivity int=ultrafine

Synthesis

Part 1: Synthesis of Compounds in Chapter 2

6,6'-Dibromo-[2,2'-biindolinylidene]-3,3'-dione (1)[111]

4-Bromo-2-nitrobenzaldehyde (2 g, 8.7 mmol) was dissolved in acetone (90 mL) and water (100 mL) was added slowly. 2N aqueous NaOH solution was added dropwise to adjust the pH to 10. The suspension was then stirred overnight. Filtration gave a dark purple solid, which was washed with excess acetone and water. The resulting solid was dried in vacuo to give product. Yield: 1.32 g (72.1%).

6,6'-Dibromo-1,1'-bis(2-hexyldecanoyl)-[2,2'-biindolinylidene]-3,3'-dione (2a)

Compound **1** （0.672 g, 1.6 mmol） was dissolved in anhydrous *N*-methyl-2-pyrrolidone (NMP) (20 mL) at room temperature. Then sodium hydride (0.154 g, 6.4 mmol) was added and the mixture was stirred for 2 h. 2-Hexyldecanoyl chloride (1.319 g, 4.8 mmol) was added into the reaction mixture. After stirring for 24 h at room temperature, the reaction mixture was poured into deionized (DI) water, and extracted with ethyl acetate three times. The organic layer was washed with brine and DI water to remove NMP. The combined organic layer was dried over anhydrous sodium sulfate and filtered. After evaporating the solvent, the residue was purified by column chromatography on silica gel with toluene as the eluent to give the title compound as a dark purple solid. Yield: 0.491 g (34.2%). ^{1}H NMR (300 MHz, $CDCl_3$) δ 8.43 (s, 2H), 7.60 (d, J = 8.1 Hz, 2H), 7.39 (dd, J = 8.1, 1.3 Hz, 2H), 3.10 – 2.97 (m, 2H), 0.84 (t, J = 6.9 Hz, 12H).^{13}C NMR

(75 MHz, $CDCl_3$) δ 182.64, 150.03, 132.39, 128.26, 125.17, 119.80, 43.85, 31.79, 29.77, 29.41, 22.62, 14.06, 13.96.

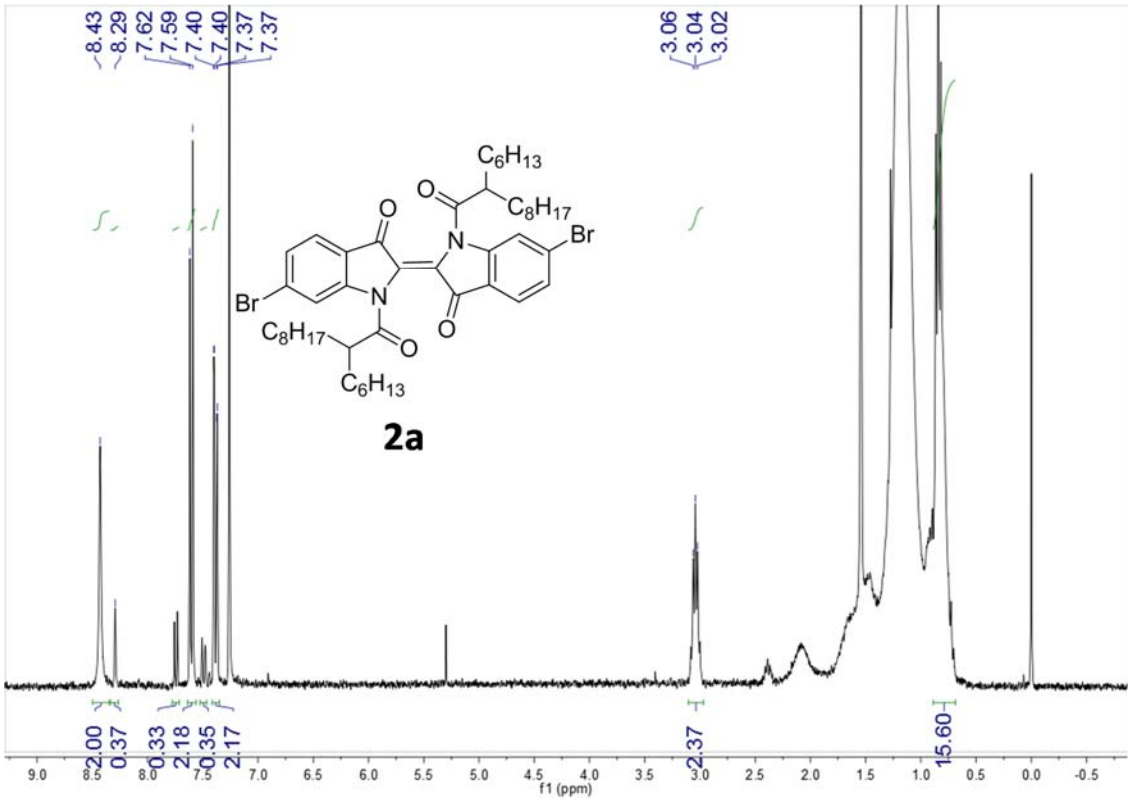

Figure S1 The 300 MHz ^{1}H NMR spectrum of 6,6'-dibromo-1,1'-bis(2-hexyldecanoyl)-[2,2'-biindolinylidene]-3,3'-dione (**2a**) measured in $CDCl_3$.

6,6'-Dibromo-1,1'-bis(2-octyldodecanoyl)-[2,2'-biindolinylidene]-3,3'-dione (2b)

Compound **2b** was synthesized following a similar procedure for the synthesis of **2a**, except of using 2-octyldodecanoyl chloride instead of 2-hexyldecanoyl chloride. Yield: 0.984g (39.0 %). ^{1}H NMR (300 MHz, $CDCl_3$) δ 8.43 (s, 2H), 7.60 (d, *J* = 8.1 Hz, 2H), 7.38 (dd, *J* = 8.1, 1.4 Hz, 2H), 3.11 – 2.96 (m, 2H), 0.87 (t, *J* = 7.5 Hz, 12H). ^{13}C NMR (75 MHz, $CDCl_3$) δ ^{13}C NMR (75 MHz, $CDCl_3$) δ 182.53, 149.93, 132.30, 128.18, 125.10, 119.70, 43.72, 31.78, 29.67, 29.47, 29.22, 22.56, 22.51, 13.98, 13.94.

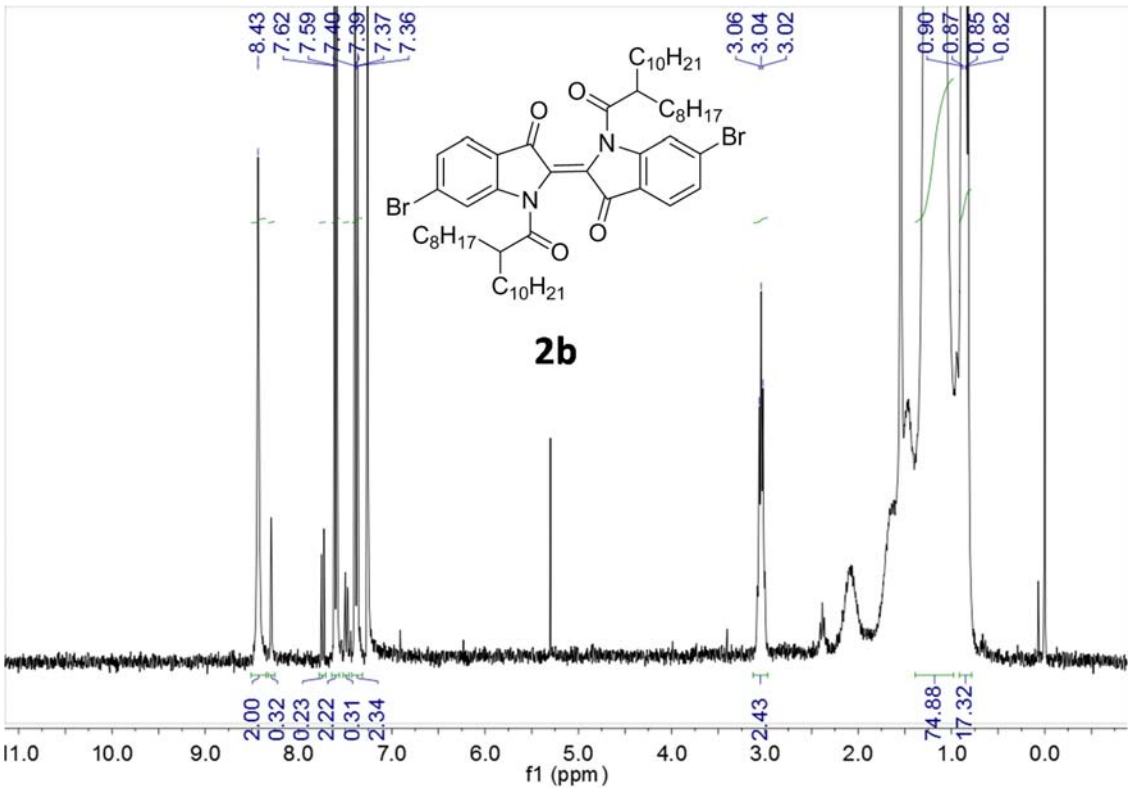

Figure S2 The 300 MHz ^{1}H NMR spectrum of 6,6'-dibromo-1,1'-bis(2-octyldodecanoyl)-[2,2'-biindolinylidene]-3,3'-dione (**2b**) measured in $CDCl_3$.

Synthesis of P1

To a 25 mL dry flask was added **2a** (0.360 g, 0.401 mmol), 5,5'-bis(trimethylstannyl)bithiophene (0.197 g, 0.401 mmol) and tri(*o*-tolyl)phosphine (9.8 mg, 0.0321 mmol). After degassing and refilling argon for 3 times, anhydrous chlorobenzene (8 mL) and tris(dibenzylideneacetone)-dipalladium (7.3 mg, 0.008 mmol) were added under an argon atmosphere. The mixture was stirred for 60 h at 90 °C. After being cooled to room temperature, the reaction mixture was poured into methanol and stirred for 0.5 h. The precipitated solid was collected by filtration and subjected to Soxhlet extraction with acetone, hexane, chloroform, and then the remaining polymer was heated in TCE at 130 °C and filtered after cooling. Very little polymer was dissolved in chloroform. The yield of the polymer dissolved by TCE is 52.4 mg (15.0%). The remaining polymer was insoluble.

Syntehsis of P2

P2 was synthesized using **2b** (0.352 g, 0.349 mmol) and 5,5'-bis(trimethylstannyl)bithiophene (0.172 g, 0.349 mmol), following the similar procedure for the synthesis of **P1**. Yield: 49.1 mg (12.6 %) with the chloroform extraction, 228.2mg (58.7%) with the TCE extraction. The remaining polymer is insoluble.

Part 2: Synthesis of Compounds in Chapter 3

Di-*tert*-butyl 6,6'-dibromo-3,3'-dioxo-[2,2'-biindolinylidene]-1,1'-dicarboxylate (3)[126]

To a suspension of compound **1** (0.842 g, 2.0 mmol) and 4-dimethylaminopyridine (0.147 g, 1.2 mmol) in *N*,*N*-dimethylformamide (DMF) (5 mL) was added di-*tert*-butyldicarbonate (2.31 g, 10.6 mmol) in two portions at 0 °C. Then the mixture was stirred for 20 h at room temperature, during which time the color of the suspension changed from dark red to bright red. The product was isolated by filtration and the residue was washed with DMF and DI water, and dried. Recrystallization of the solid from a mixture of chloroform/isopropanol gave a bright red powder (1.03 g, 82.7 %). ^{1}H NMR (300 MHz, $CDCl_3$) δ 8.26 (s, 2H), 7.61 (d, J = 8.1 Hz, 2H), 7.37 (dd, J = 8.1, 1.5 Hz, 2H), 1.61 (s, 18H).

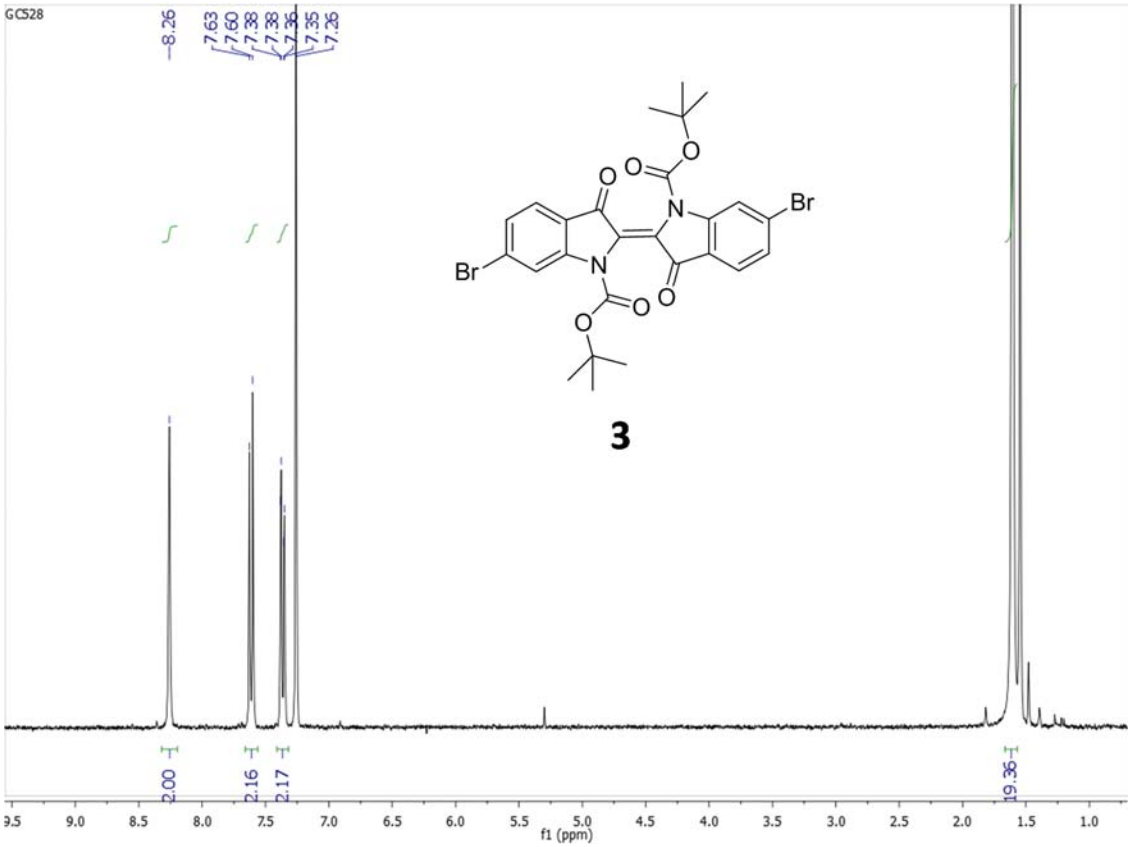

Figure S3 The 300 MHz ^{1}H NMR spectrum of di-*tert*-butyl 6,6'-dibromo-3,3'-dioxo-[2,2'-biindolinylidene]-1,1'-dicarboxylate (**3**) measured in $CDCl_3$.

4,8-Bis((2-decyltetradecyl)oxy)benzo[1,2-*b*:4,5-*b'*]dithiophene (4)[129]

NaOH (0.6 g, 15.0 mmol) was added into a mixture of 4,8-dihydrobenzo[1,2-*b*:4,5-*b'*]dithiophen-4,8-dione (0.22 g, 1.0 mmol), zinc powder (0.143 g, 2.2 mmol), and water (5 mL) at room temperature. The mixture was refluxed for 1 h and then 11-(bromomethyl)tricosane (1.3 g, 3.0 mmol) and tetrabutylammonium bromide (49 mg, 0.15 mmol) were added. After refluxing for an additional 8 h, the reaction mixture was cooled to room temperature and quenched with cold water. The mixture was extracted with diethyl ether (100 mL × 2) and the ether layer was separated and dried over anhydrous sodium sulphate. After the solvent was removed, the residue was purified by column chromatography on silica gel with

hexane to afford a yellow oil (0.627 g, 70.0 %). ^{1}H NMR (300 MHz, $CDCl_3$) δ 7.47 (d, *J* = 5.6 Hz, 2H), 7.35 (d, *J* = 5.5 Hz, 2H), 4.16 (d, *J* = 5.3 Hz, 4H), 0.88 (t, *J* = 6.6 Hz, 12H).

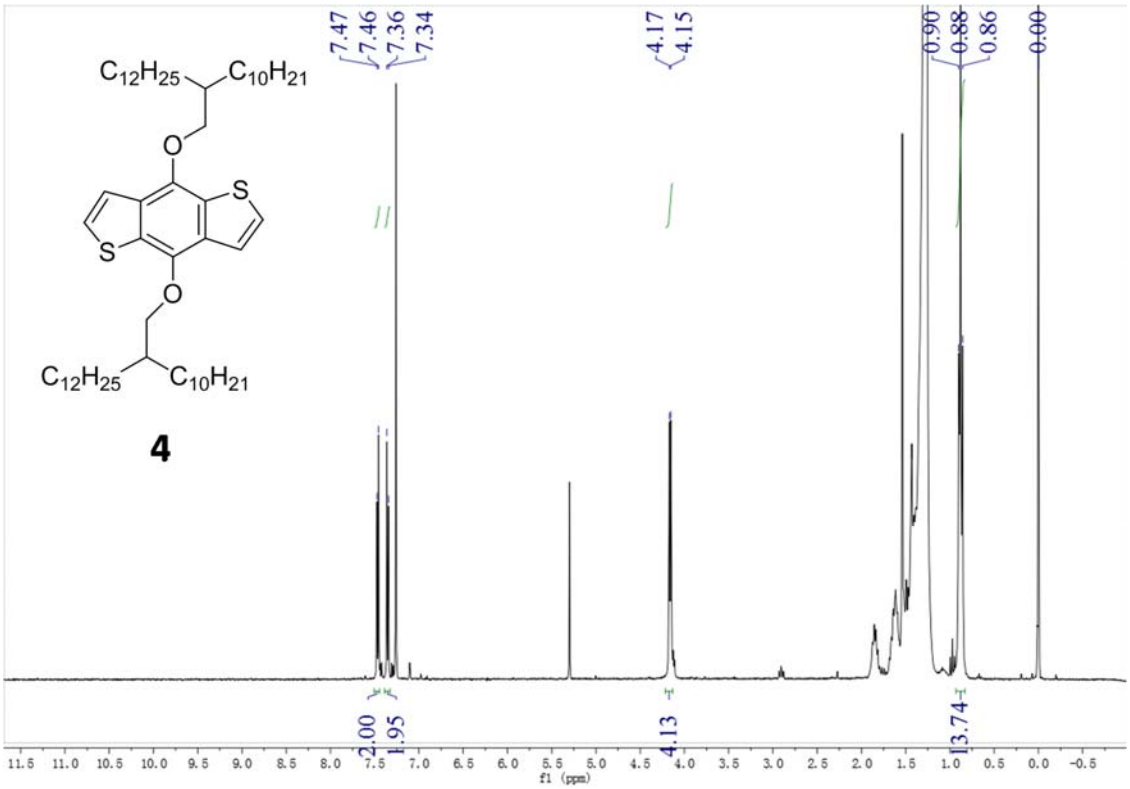

Figure S4 The 300 MHz ^{1}H NMR spectrum of 4,8-bis((2-decyltetradecyl)oxy)benzo[1,2-*b*:4,5-*b'*]dithiophene (**4**) measured in $CDCl_3$.

(4,8-Bis((2-decyltetradecyl)oxy)benzo[1,2-*b*:4,5-*b'*]dithiophene-2,6-diyl)bis(trimethylstannane) (5)[129]

Compound **4** (0.448 g, 0.5 mmol) was dissolved in dry tetrahydrofuran (THF) (7 mL) under argon. The solution was cooled to -78 °C and *n*-butyllithium (0.7 mL, 1.8 mmol, 2.5 M in hexane) was added drop-wise. After the mixture was stirred at room temperature for 1 h, trimethyltin chloride (0.239 g, 1.2 mmol) was added in one portion. The mixture was stirred at room temperature for 2 h and poured into water (200 mL). The mixture was extracted with diethyl ether and the organic layer was separated and dried over anhydrous sodium sulphate. After the solvent was removed, the residue was recrystallized from acetone twice to give a white solid (0.434 g,

71.0 %). ^{1}H NMR (300 MHz, DMSO-d_6) δ7.50 (s, 2H), 4.17 (d, J = 5.3 Hz, 4H), 0.88 (t, J = 6.6 Hz, 12H).

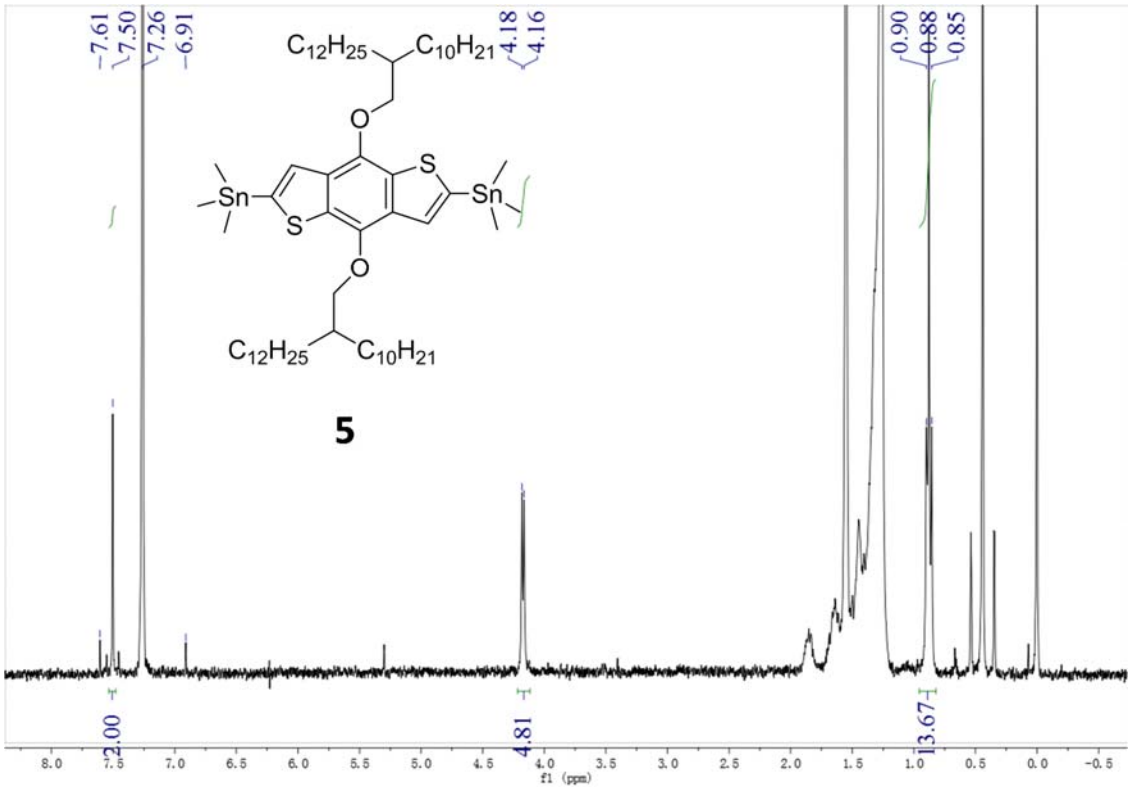

Figure S5 The 300 MHz ^{1}H NMR spectrum of (4,8-bis((2-decyltetradecyl)oxy)benzo[1,2-*b*:4,5-*b*′]dithiophene-2,6-diyl)bis(trimethylstannane) (**5**) measured in $CDCl_3$.

Synthesis of P3

To a 25 mL dry Schlenk flask was added **3** (0.0941 g, 0.15 mmol), **5** (0.185 g, 0.15 mmol) and tri(*o*-totyl)phosphine (P(*o*-tolyl)$_3$) (3 mg, 0.012 mmol). After degassing and refilling argon 3 times, anhydrous chlorobenzene (5 mL) and tris(dibenzylideneacetone)-dipalladium (Pd_2dba_3) (2.8 mg, 0.003 mmol) were added under an argon atmosphere. The mixture was stirred for 60 h at 110 °C under argon and then cooled to room temperature. After bromobenzene (0.5 mL) was added, the mixture was heated to 110 °C again and stirred for an additional 2 h. The cooled mixture was poured into methanol, and the precipitate was collected by filtration and subjected to

Soxhlet extraction sequentially with acetone, hexane and chloroform. Yield: 63.1 mg (30 %) from the hexane extract and 129.3 mg (63 %) from the chloroform extract.

Part 3: Synthesis of Compounds in Chapter 4

5-bromo-2-nitrobenzaldehyde (6) [136]

At 0 °C, 3-bromobenzaldehyde (4.12g, 22.3 mmol) was added in small portions into a mixture of HNO_3 (60-70% solution in H_2O, 5 mL) and H_2SO_4 (96%, 10 mL) over a period of 30 min. The resulting yellow suspension was then stirred at room temperature for another 45 min. The mixture was slowly poured with stirring into saturated $NaHCO_3$ solution (60 mL) maintained at 0 °C with and then extracted with ethyl acetate. The combined organic layers were washed with saturated $NaHCO_3$ solution until the pH of the aqueous phase was ~8-9. The organic phase was dried over Na_2SO_4 and filtered. After evaporation of the solvent, the crude product was purified by column chromatography (hexane/DCM = 2:1) to give a dark-orange solid. Yield: 3.90 g (76 %). ^{1}H NMR (300 MHz, $CDCl_3$) δ 10.42 (s, 1H), 8.07 (d, J = 2.2 Hz, 1H), 8.03 (d, J = 8.6 Hz, 1H), 7.88 (dd, J = 8.7, 2.2 Hz, 1H).

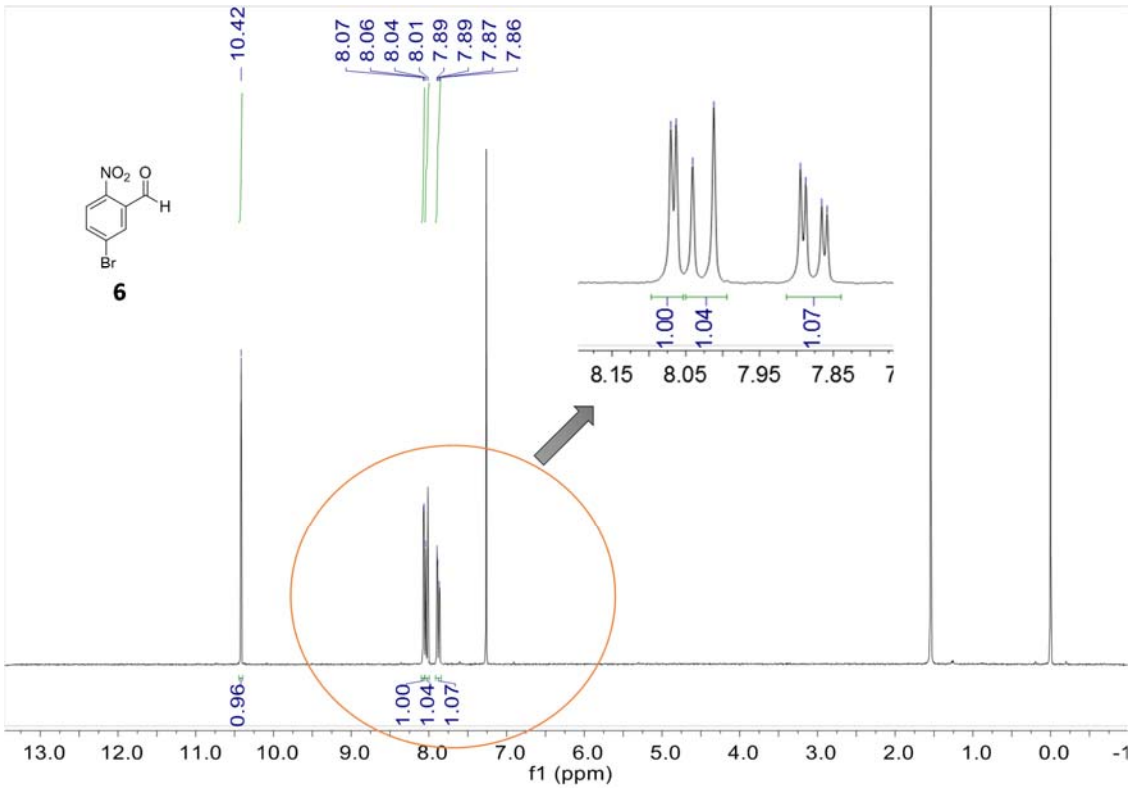

Figure S6 The 300 MHz ^{1}H NMR spectrum of 5-bromo-2-nitrobenzaldehyde (**6**) measured in $CDCl_3$.

5,5'-dibromo-[2,2'-biindolinylidene]-3,3'-dione (7)

Compound **7** was synthesized following a similar procedure for the synthesis of 6,6'-dibromo-[2,2'-biindolinylidene]-3,3'-dione.[82] Compound **6** (1 g, 4.4 mmol) was dissolved in acetone (45 mL), followed by slow addition of water (50 mL). Then a 2 N aqueous NaOH solution was added drop-wise at room temperature to adjust the pH to 10. The mixture was stirred overnight at room temperature and filtered. The solid was washed with excess acetone and de-ionized (DI) water, and dried in vacuo to give a blue powder. Yield: 0.69 g (75 %). This product has poor solubility in organic solvents and was used for the next step reaction without further purification. Synthesis of compound **2** was reported previously using a different procedure.[131]

Di-*tert*-butyl 5,5'-dibromo-3,3'-dioxo-[2,2'-biindolinylidene]-1,1'-dicarboxylate (8)

Compound **8** was synthesized following the similar procedure for the synthesis of di-*tert*-butyl 6,6'-dibromo-3,3'-dioxo-[2,2'-biindolinylidene]-1,1'-dicarboxylate.[82] To a suspension of compound **7** (0.336 g, 0.8 mmol) and 4-dimethylaminopyridine (57 mg, 0.46 mmol) in *N*,*N*-dimethylformamide (DMF) (3 mL) was added di-*tert*-butyldicarbonate (0.922 g, 4.22 mmol) in two portions at 0 °C. Then the mixture was stirred for 20 h at room temperature, during which time the color of the suspension changed from dark red to bright red. The product was isolated by filtration and the residue was washed with DMF and de-ionized (DI) water, and dried. Recrystallization of the solid from a mixture of chloroform/isopropanol gave a dark red powder. Yield: 0.265 g (53 %). ^{1}H NMR (300 MHz, $CDCl_3$) δ 7.92 (*d*, *J* = 8.7 Hz, 2H), 7.87 (*d*, *J* = 2.0 Hz, 2H), 7.70 (*dd*, J_1 = 8.8 Hz, J_2 =2.0 Hz, 2H), 1.60 (*s*, 18H). HRMS $(M+H)^+$ Calc. for $C_{26}H_{23}Br_2N_2O_6^+$: 618.9902; found: 619.0067.

Synthesis of compound **8** was reported previously using a different procedure. [176]

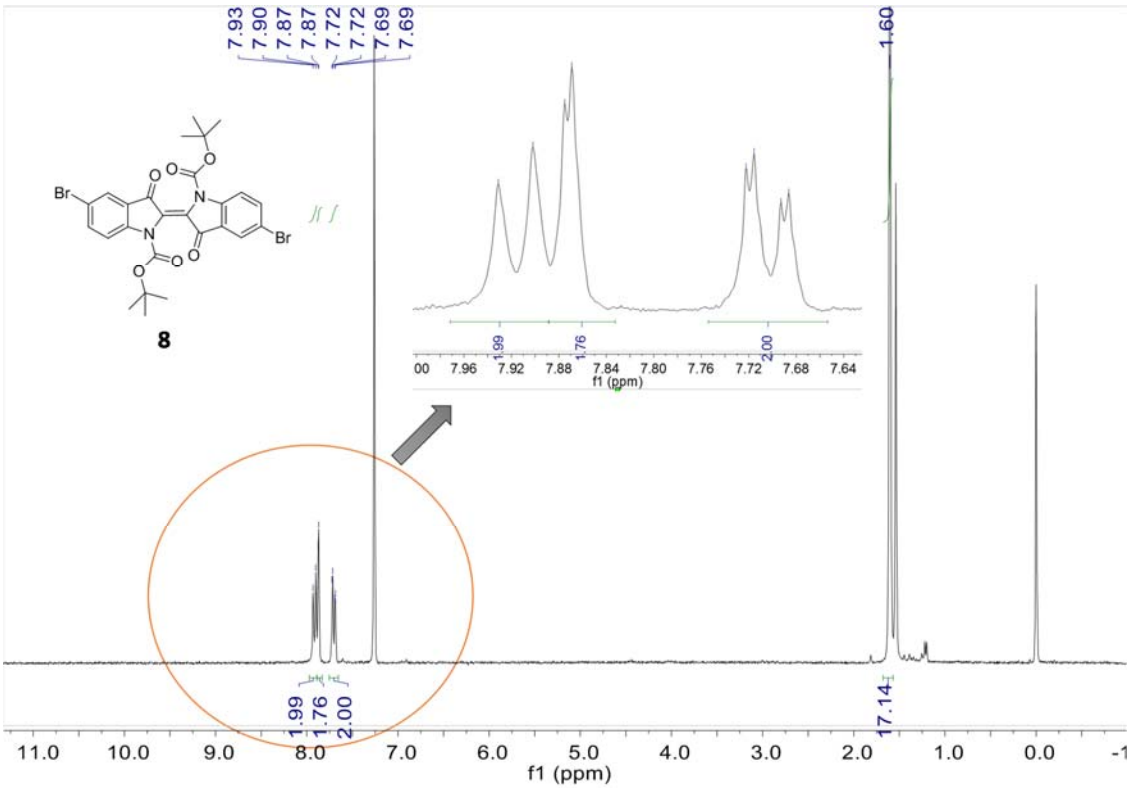

Figure S7 The 300 MHz ^{1}H NMR spectrum of di-*tert*-butyl 5,5'-dibromo-3,3'-dioxo-[2,2'-biindolinylidene]-1,1'-dicarboxylate (**8**) measured in $CDCl_3$.

Synthesis of P4

To a 25 mL dry Schlenk flask was added **8** (0.0557 g, 0.09 mmol), **5** (0.110 g, 0.09 mmol) and tri(*o*-totyl)phosphine (P(*o*-tolyl)$_3$) (2 mg, 0.007 mmol). After degassing and refilling argon 3 times, anhydrous chlorobenzene (3 mL) and tris(dibenzylideneacetone)-dipalladium (Pd_2dba_3) (1.6 mg, 0.002 mmol) were added under an argon atmosphere. The mixture was stirred for 60 h at 110 °C under argon before cooling to room temperature. After bromobenzene (0.5 mL) was added, the mixture was heated to 110 °C again and stirred for an additional 2 h. The cooled mixture was poured into methanol, and the precipitate was collected by filtration and subjected to Soxhlet extraction sequentially with acetone, hexane and chloroform. Yield of the chloroform extracted fraction: 47 mg (39 %). GPC data: Number average molecular weight (M_n) = 32.6 kDa; Polydispersity index (PDI) = 2.53.

Part 4: Synthesis of Compounds in Chapter 5

2-(Trimethylstannyl)thiazole (9)

A solution of 2-bromothiazole (1.64 g, 10 mmol) in 25 mL diethyl ether was slowly added into a stirred solution of *n*-butyllithium (4.4 mL, 2.5M in hexane) in 40 mL diethyl ether at -78 °C. The mixture was stirred for 1 h, then a solution of trimethyltin chloride (11 mL, 1.0 M in hexane) is added dropwise in 15 min. After an additional 1h at -78 °C, the reaction mixture was washed with 15 mL saturated aqueous sodium hydrogen carbonate and extracted with diethyl ether. The organic layer was dried with sodium sulfate and the solvent is removed under vacuum. The resultant yellow liquid was directly used in the next step without further purification. Yield: 2.51 g (~ 100 %). ^{1}H NMR (300 MHz, $CDCl_3$) δ 8.15 (d, J = 2.5 Hz, 1H), 7.56 (d, J = 2.7 Hz, 1H), 0.47 (s, 9H).

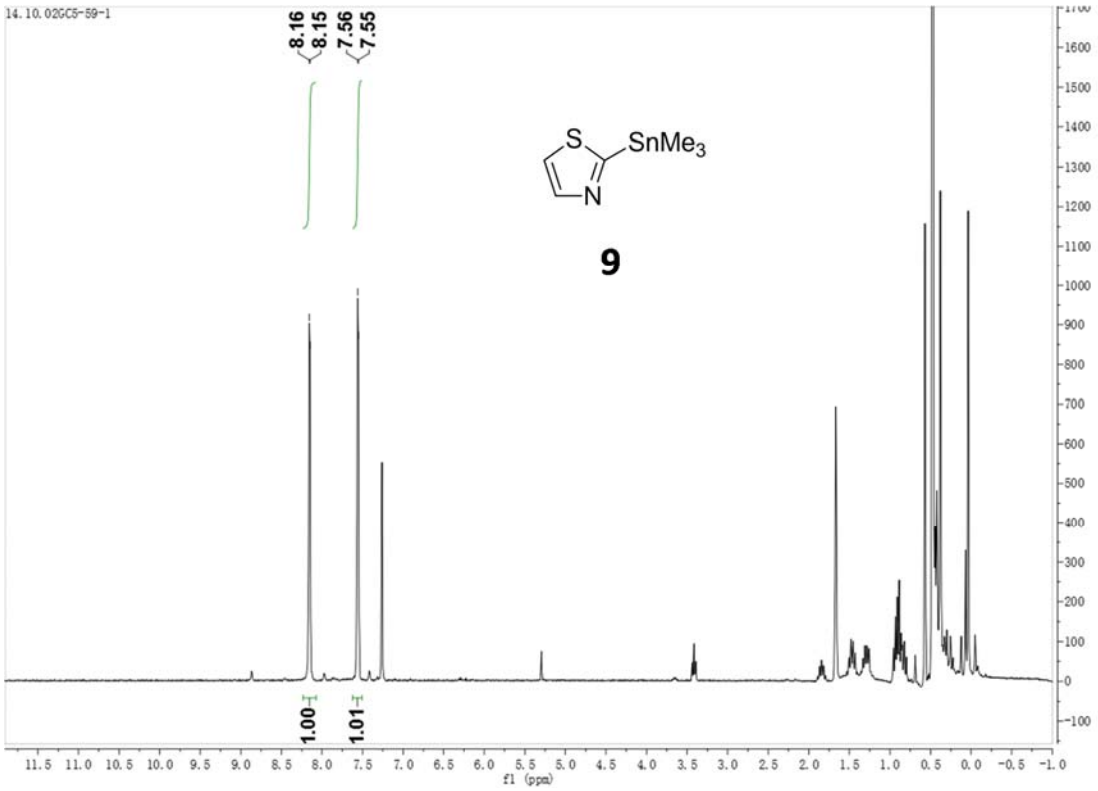

Figure S8 The 300 MHz ^{1}H NMR spectrum of 2-(trimethylstannyl)thiazole (**9**) measured in $CDCl_3$.

2,2'-Bithiazole (10)

A solution of **9** (0.694 g, 2.8 mmol), 2-bromothiazole (0.328 g, 2 mmol) and terakis(triphenylphosphine)palladium(0) (Pd (PPh_3)$_4$) (46 mg, 0.05 mmol) in toluene was refluxed for 24 h under a nitrogen atmosphere. The reaction mixture was allowed to cool down to room temperature, then the solvent was removed under vacuum and the crude reaction mixture purified by column chromatography on silica gel with hexane/ethyl acetate (volume ratio = 7:3) as an eluent to give the compound **10** as a white crystal. Yield: 0.263g (78.1%). ^{1}H NMR (300 MHz, $CDCl_3$) δ 7.90 (d, J = 3.1 Hz, 2H), 7.44 (d, J = 3.2 Hz, 2H).

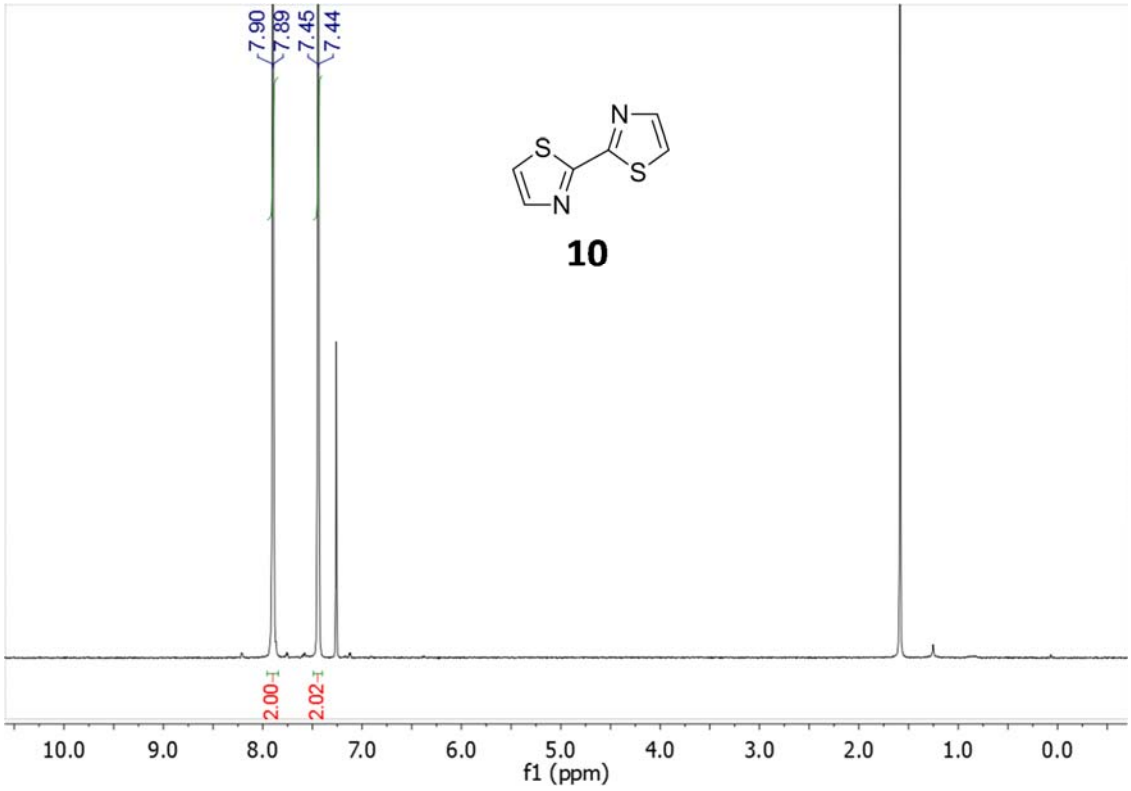

Figure S9 The 300 MHz ^{1}H NMR spectrum of 2,2'-bithiazole (**10**) measured in $CDCl_3$.

5,5'-Dibromo-2,2'-bithiazole (11)

NBS (0.872 g, 4.9 mmol) was slowly added to the a of **10** (0.206 g, 1.2 mmol) in 10 mL dimethylformamide (DMF). The reaction mixture was the stirred at 60 °C for 5h. The mixture was poured into 200 mL water and extracted with dichloromethane and dried over anhydrous magnesium sulfate. The crude product was purified by column chromatography on silica gel with hexane/ethyl acetate (volume ratio = 3:1) as an eluent to give the compound **11** as yellow crystals. Yield: 0.390 g (98.0 %). ^{1}H NMR (300 MHz, $CDCl_3$) δ7.75 (s, 2H).

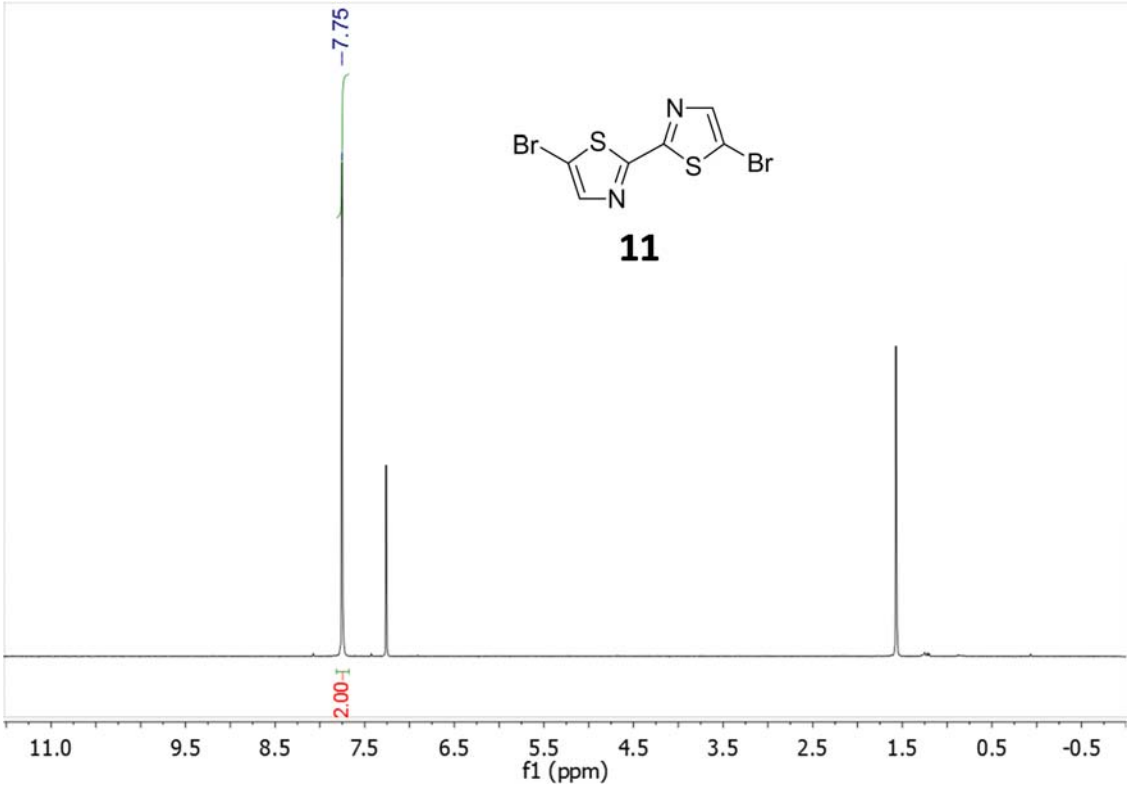

Figure S10 The 300 MHz ^{1}H NMR spectrum of 5,5'-dibromo-2,2'-bithiazole (**11**) measured in $CDCl_3$.

Synthesis of P5

To a 25 mL Schlenk flask were added compound **11** (24.5 mg, 0.075 mmol), **12** (73.0 mg, 0.075 mmol) and Herrmann-Beller's catalyst (1.4 mg, 2 % mol)/ tris(2-methoxyphenyl)phosphine (2.1 mg, 8% mol)/cesium carbonate (56.2mg, 0.29 mmol)/pivalic acid (2.3 mg, 30 % mol). After degassing and refilling argon 3 times, 3 mL anhydrous toluene was added under argon. The flask was sealed and the mixture was refluxed for 16 h. After cooling down to room temperature, the reaction mixture was poured into methanol (100 ml). The precipitated product was collected by filtration and subjected to Soxhlet extraction with acetone, hexane, chloroform and TCE. Yield: 7.7 mg (9.0 %) from the chloroform extract, and 45.4 mg (53.2 %) from TCE extract.

Synthesis of P6

P6 was synthesized using compound **10** (12.6 mg, 0.075 mmol) and **13** (84.9 mg, 0.075 mmol), following the similar procedure for **P5**. The precipitated product was collected by filtration and subjected to Soxhlet extraction with acetone, hexane, and chloroform. Yield: 56.5 mg (66.2 %) from the chloroform extract, and 8.2 mg (9.6%) from TCE extract.

Part 5: Synthesis of Compounds in Chapter 6

Diethyl 1*H*-pyrrole-3,4-dicarboxylate (14)[177]

A solution of *p*-toluenesulfonylmethyl isocyanide (20.0 g, 102 mmol) and diethyl fumarate (17.6 g, 102 mmol) in anhydrous THF (100 mL) was added dropwise into a suspension of potassium *t*-butoxide (23.0 g, 205 mmol) in anhydrous THF (200 mL) under argon atmosphere at room temperature. The mixture was then stirred for overnight. Saturated aqueous NaCl (100 mL) and THF (100 mL) were added into the mixture. The organic layer was separated, dried over Na_2SO_4 and filtrated. After removal of solvent from the filtrate, a dark red residue was obtained, which was then dissolved in methanol again. With slow addition of water, a white precipitate formed. The solid was washed with excess water and then dried to give the product. Yield: 11.6 g (53.6%). ^{1}H NMR (300 MHz, $CDCl_3$) δ 8.63 (s, 1H), 7.35 (d, J = 2.5 Hz, 2H), 4.31 (q, J = 7.1 Hz, 4H), 1.34 (t, J = 7.1 Hz, 6H).

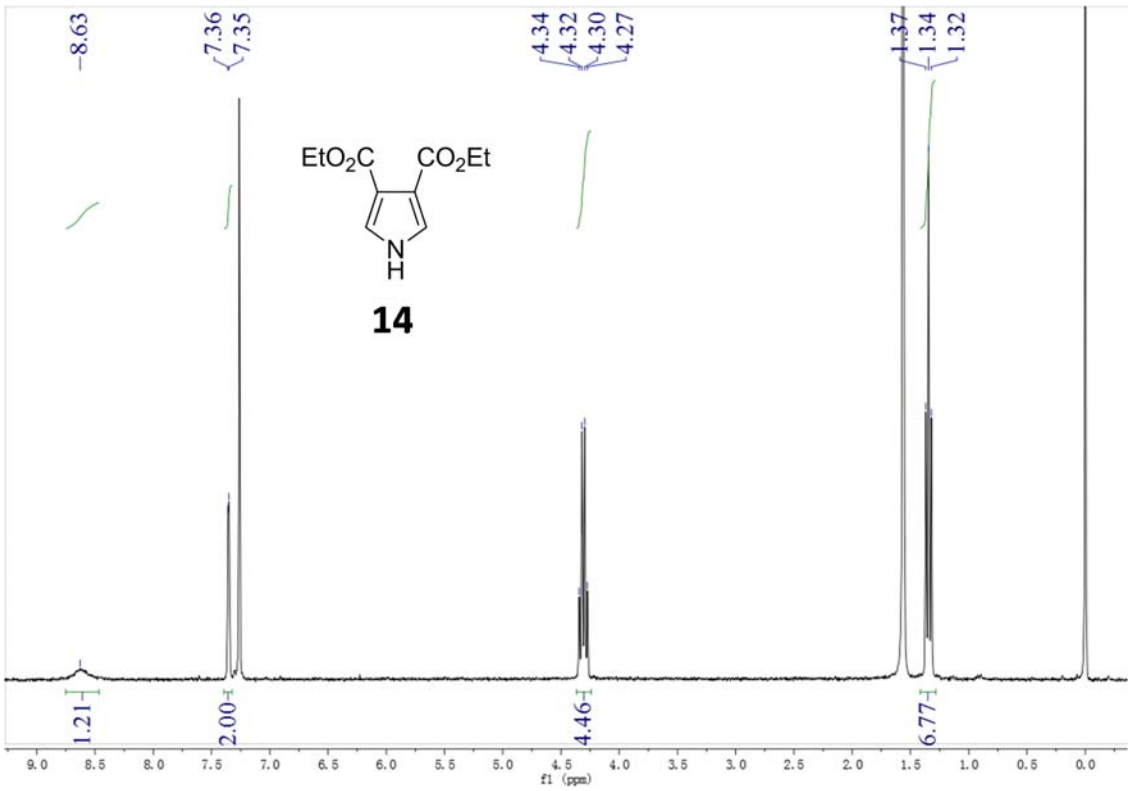

Figure S11 The 300 MHz ^{1}H NMR spectrum of diethyl 1*H*-pyrrole-3,4-dicarboxylate (**14**) measured in $CDCl_3$.

1*H*-pyrrole-3,4-dicarboxylic acid (15)[177]

To a solution of NaOH (4.69 g, 118 mmol) in 50 v % aqueous ethanol (47 mL) was added compound **14** (3.17 g, 15.0 mmol), which was then heated to reflux for 2 h. Before cooling down, the mixture was added to water and then acidified with 10% HCl solution to pH 4~5. The white precipitate was filtrated, washed with water and dried to give a white solid. Yield: 2.02 g (86.9%). ^{1}H NMR (300 MHz, DMSO-d_6) δ 12.21 (s, 2H), 7.65 (d, J = 2.9 Hz, 2H).

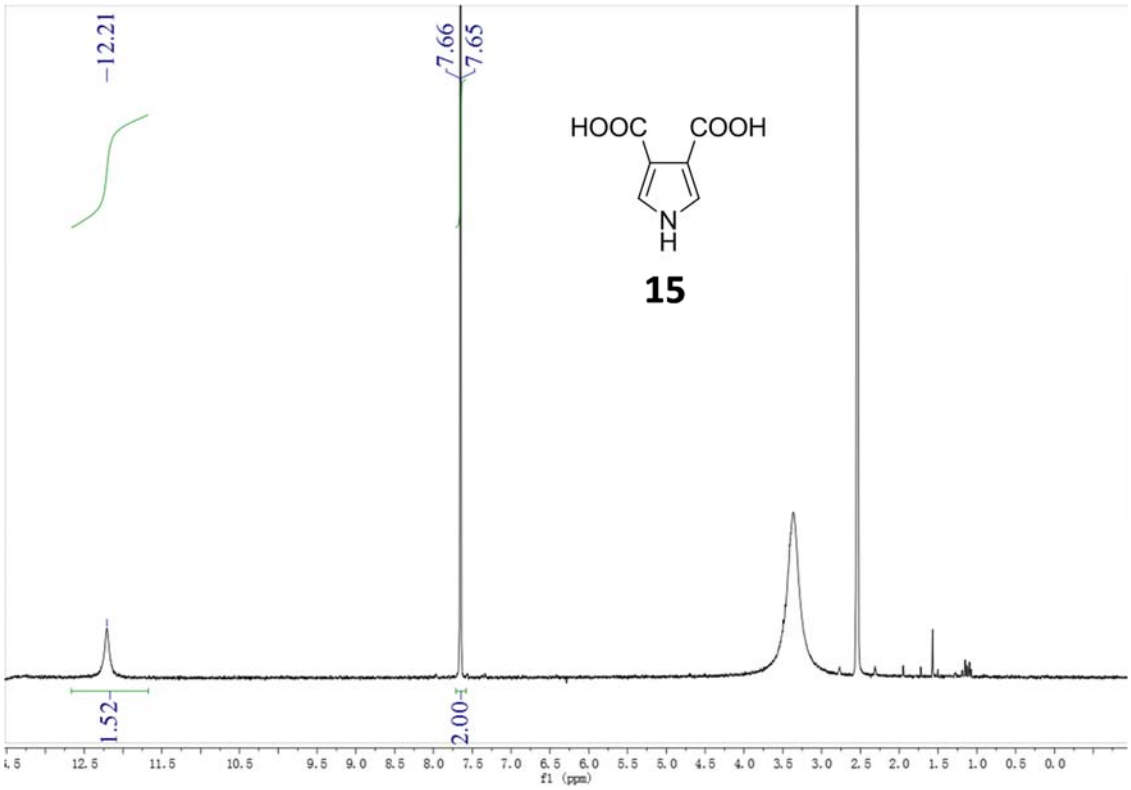

Figure S12 The 300 MHz ^{1}H NMR spectrum of 1*H*-pyrrole-3,4-dicarboxylic acid (**15**) measured in DMSO.

4-((2-Octyldodecyl)carbamoyl)-1*H*-pyrrole-3-carboxylic acid (16)

Compound **15** (0.944 g, 6.08 mmol) and *N*,*N*'-dicyolohexylcarbodiimide (1.51 g, 7.30 mmol) was dissolved in anhydrous THF (15 mL) under argon atmosphere. The mixture was refluxed with stirring for 2 h before cooling down to room temperature. The precipitate (*N*,*N*'-dicyclohexylurea) was filtered off and washed with THF. Under argon atmosphere, 2-octyldodecan-1-amine was added dropwise into the filtrate with stirring. The reaction mixture was stirred overnight at room temperature, poured into DI water and extracted with ethyl acetate three times. The combined organic layer was dried over Na_2SO_4 and filtered. After evaporating the solvent, the resulting solid was washed with dilute HCl and dried. This solid was used in the next step reaction without further purification. Yield: 2.61 g (98.7%). ^{1}H NMR (300 MHz, DMSO-d_6) δ 11.87 (s, 1H), 8.96 (s, 1H), 7.64 (s, 1H), 7.48 (s, 1H), 1.19 (s, 30H), 0.81 (d, J = 2.0

Hz, 7H). ^{13}C NMR (75 MHz, DMSO-d_6) δ 165.90, 165.39, 128.37, 124.59, 116.12, 115.65, 31.59, 31.51, 29.58, 29.55, 29.29, 29.26, 29.18, 28.99, 28.95, 26.22, 22.39, 14.23.

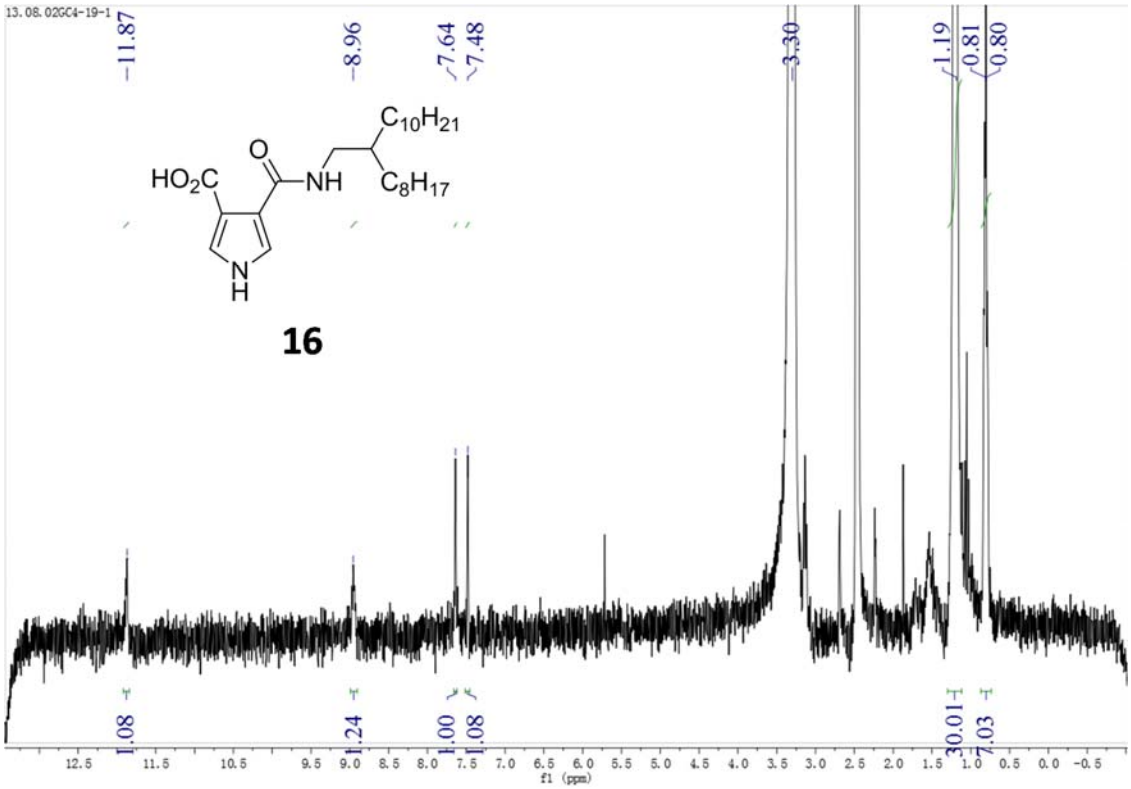

Figure S13 The 300 MHz ^{1}H NMR spectrum of 4-((2-octyldodecyl)carbamoyl)-1*H*-pyrrole-3-carboxylic acid (**16**) measured in DMSO.

2-(2-Octyldodecyl)pyrrolo[3,4-*c*]pyrrole-1,3(2*H*,5*H*)-dione (17)

To a solution of compound (**16**) (1.78 g, 4.08 mmol) in anhydrous *N*,*N*-dimethylformamide (DMF) (5 mL) was added thionyl chloride (0.9 mL) at 0 °C under argon atmosphere. After stirring overnight at room temperature, the solution was poured into an ice / water mixture and extracted with ethyl acetate three times. The organic layers were combined and dried over Na_2SO_4. After evaporating the solvent, the residue was purified by column chromatography on silica gel with a mixture of ethyl acetate and hexane (1 : 2, v : v) as an eluent to give a yellow solid. Yield: 1.05 g (62.0%). ^{1}H NMR (300 MHz, $CDCl_3$) δ 8.80 (s, 1H), 7.10 (d, J = 2.5 Hz, 2H), 3.45 (d, J = 7.3 Hz, 2H), 0.87 (dd, J = 6.7, 4.7 Hz, 6H). ^{13}C NMR (75 MHz, $CDCl_3$) δ 165.04,

121.27, 115.71, 42.23, 36.90, 31.81, 31.79, 31.34, 29.92, 29.54, 29.52, 29.46, 29.24, 29.20, 26.20, 22.57, 22.56, 14.01. HRMS $(M+H)^+$ Calc. for $C_{26}H_{45}N_2O_2^+$: 417.3481; found: 417.3485. Elemental analysis: Calc. for $C_{26}H_{44}N_2O_2$: C 74.95, H 10.64, N 6.72%; found: C 75.01, H 10.40, N 6.66%.

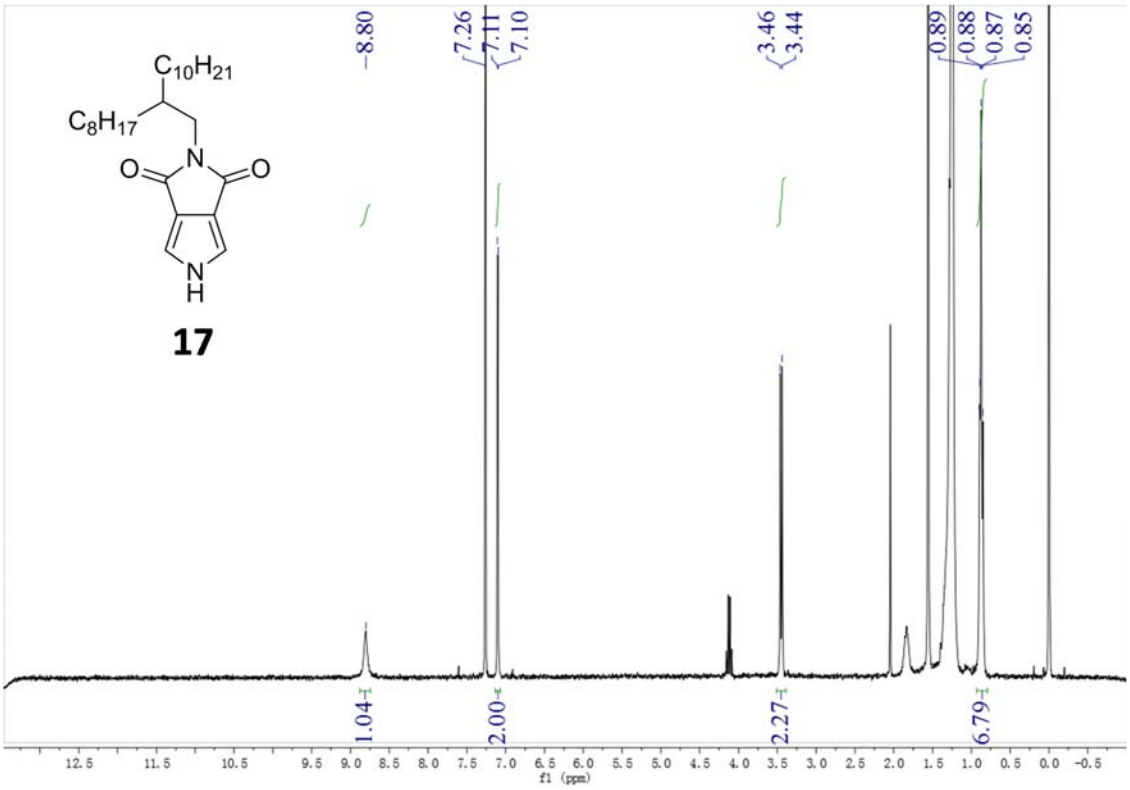

Figure S14 The 300 MHz ^{1}H NMR spectrum of 2-(2-octyldodecyl)pyrrolo[3,4-*c*]pyrrole-1,3(2*H*,5*H*)-dione (**17**) measured in $CDCl_3$.

2,5-Bis(2-octyldodecyl)pyrrolo[3,4-*c*]pyrrole-1,3(2*H*,5*H*)-dione (18a)

Sodium hydride (67.2 mg, 2.80 mmol) was added to a solution of compound **17** (1.05 g, 2.53 mmol) in anhydrous DMF (10 mL) and the mixture was stirred at room temperature for 2 h. To this mixture was added 9-(bromomethyl)nonadecane (1.10 g, 3.04 mmol) and the solution was stirred overnight at room temperature. After removing the solvent, the product was purified using chromatography on silica gel (hexane : dichloromethane (DCM) = 1 : 1, v : v) to give a yellow oil. Yield: 1.21 g (69.3%). ^{1}H NMR (300 MHz, $CDCl_3$) δ 6.88 (s, 2H), 3.81 (d, J = 6.7 Hz, 2H), 3.42

(d, J = 7.2 Hz, 2H), 1.78 (d, J = 23.4 Hz, 2H), 0.87 (d, J = 6.4 Hz, 12H). ^{13}C NMR (75 MHz, $CDCl_3$) δ 164.91, 121.15, 118.53, 54.46, 42.11, 39.67, 36.92, 31.77, 31.71, 31.40, 31.08, 29.92, 29.69, 29.51, 29.45, 29.41, 29.36, 29.21, 29.18, 29.10, 26.23, 22.53, 22.51, 13.95. HRMS $(M+H)^+$ Calc. for $C_{46}H_{85}N_2O_2^+$: 697.6611; found: 697.6611. Elemental analysis: Calc. for $C_{46}H_{84}N_2O_2$: C 79.25, H 12.14, N 4.02%; found: C 79.64, H 12.30, N 3.89%.

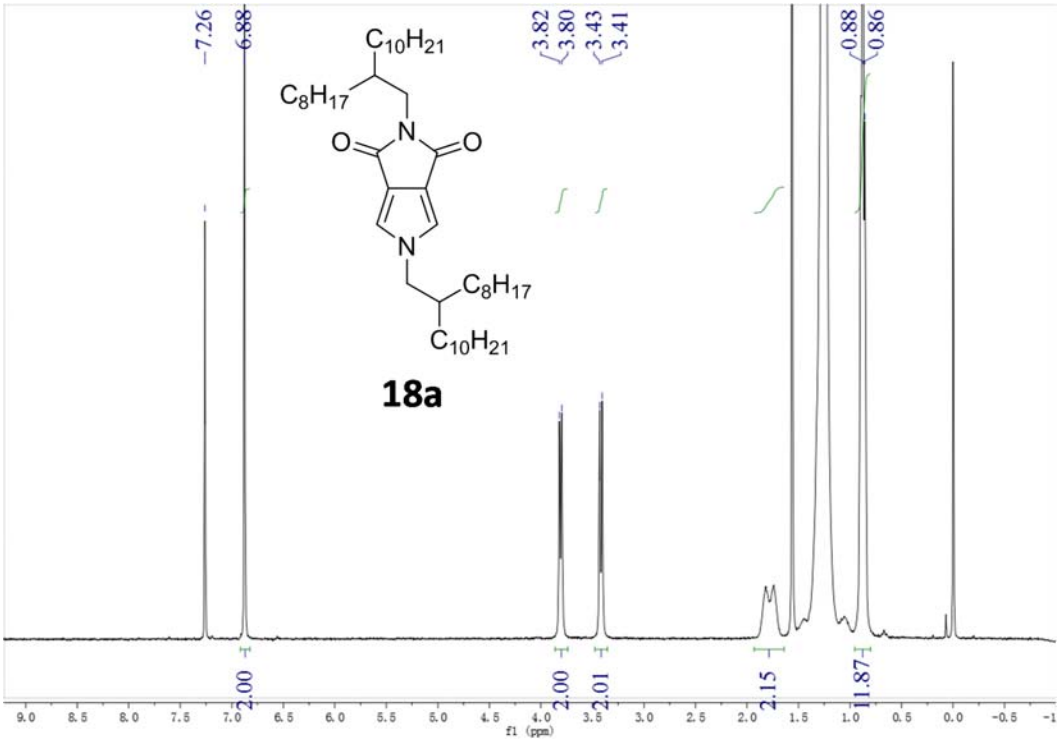

Figure S15 The 300 MHz ^{1}H NMR spectrum of 2,5-bis(2-octyldodecyl)pyrrolo[3,4-*c*]pyrrole-1,3(2*H*,5*H*)-dione (**18a**) measured in $CDCl_3$.

5-Dodecyl-2-(2-octyldodecyl)pyrrolo[3,4-*c*]pyrrole-1,3(2*H*,5*H*)-dione (18b)

Compound **18b** was synthesized following the similar procedure for compound **18a** using 1-bromododecane instead of 9-(bromomethyl)nonadecane. Yield: 0.840 g (73.6%). ^{1}H NMR (300 MHz, $CDCl_3$) δ 6.92 (s, 2H), 3.92 (t, *J* = 7.1 Hz, 2H), 3.42 (d, *J* = 7.3 Hz, 2H), 0.87 (dd, *J* = 6.7, 4.3 Hz, 9H). ^{13}C NMR (75 MHz, $CDCl_3$) δ 164.82, 121.24, 117.98, 50.58, 42.04, 36.90, 31.78, 31.75, 31.39, 31.07, 29.89, 29.49, 29.43, 29.37, 29.26, 29.20, 29.16, 28.91, 26.34, 26.21, 22.52,

13.93. HRMS $(M+H)^+$ Calc. for $C_{38}H_{69}N_2O_2^+$: 585.5359; found: 585.5374. Elemental analysis: Calc. for $C_{38}H_{68}N_2O_2$: C 78.02, H 11.72, N 4.79%; found: C 78.62, H 11.68, N 4.83%.

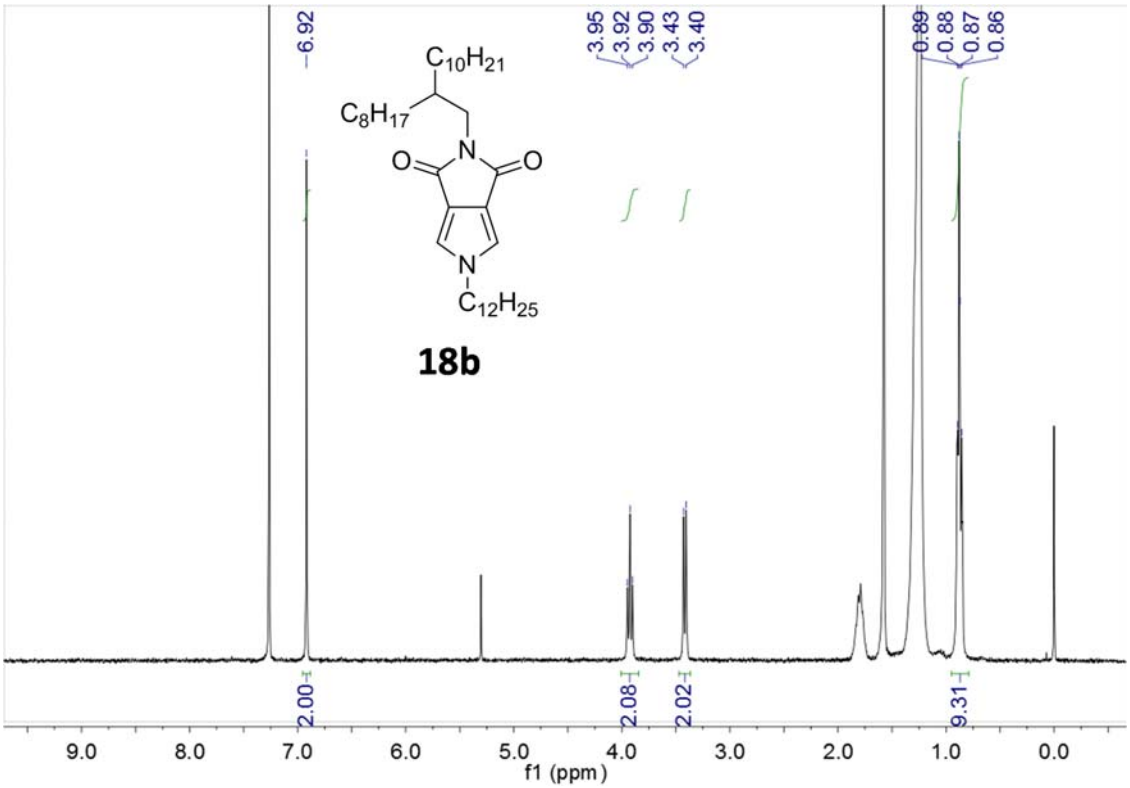

Figure S16 The 300 MHz ^{1}H NMR spectrum of 5-dodecyl-2-(2-octyldodecyl)pyrrolo[3,4-*c*]pyrrole-1,3(2*H*,5*H*)-dione (**18b**) measured in $CDCl_3$.

4,6-Dibromo-2,5-bis(2-octyldodecyl)pyrrolo[3,4-*c*]pyrrole-1,3(2*H*,5*H*)-dione (19a)

To a solution of compound **18a (**1.20 g, 1.72 mmol) in DMF (10 mL) was added *N*-bromosuccinimide (NBS) (0.705 g, 3.96 mmol) in absence of light. After stirring at room temperature overnight, the mixture was poured into water (200 mL), extracted with DCM, dried over Na_2SO_4, and filtered. After removing the solvent, the residual was purified using silica-gel column chromatography (hexane : ethyl acetate = 3 : 1, v : v) to give the product as a liquid. Yield: 1.21 g (88.0%). ^{1}H NMR (300 MHz, $CDCl_3$) δ 3.93 (d, J = 7.5 Hz, 2H), 3.42 (d, J = 7.1 Hz, 2H), 0.88 (t, J = 6.0 Hz, 12H). ^{13}C NMR (75 MHz, $CDCl_3$) δ 162.51, 121.43, 101.28, 51.60, 42.44, 38.34, 36.99, 31.93, 31.92, 31.91, 31.89, 31.84, 31.83, 31.81, 31.81, 31.50, 31.22, 29.95,

29.80, 29.79, 29.65, 29.63, 29.61, 29.59, 29.58, 29.56, 29.54, 29.53, 29.51, 29.49, 29.47, 29.46, 29.44, 29.33, 29.30, 29.28, 29.22, 26.36, 22.66, 22.65, 22.62, 14.08, 14.05, 0.98. HRMS $(M+H)^+$ Calc. for $C_{46}H_{83}Br_2N_2O_2^+$: 855.4801; found: 855.4821. Elemental analysis: Calc. for $C_{46}H_{82}Br_2N_2O_2$: C 64.62, H 9.67, N 3.28%; found: C 64.80, H 9.68, N 3.20%.

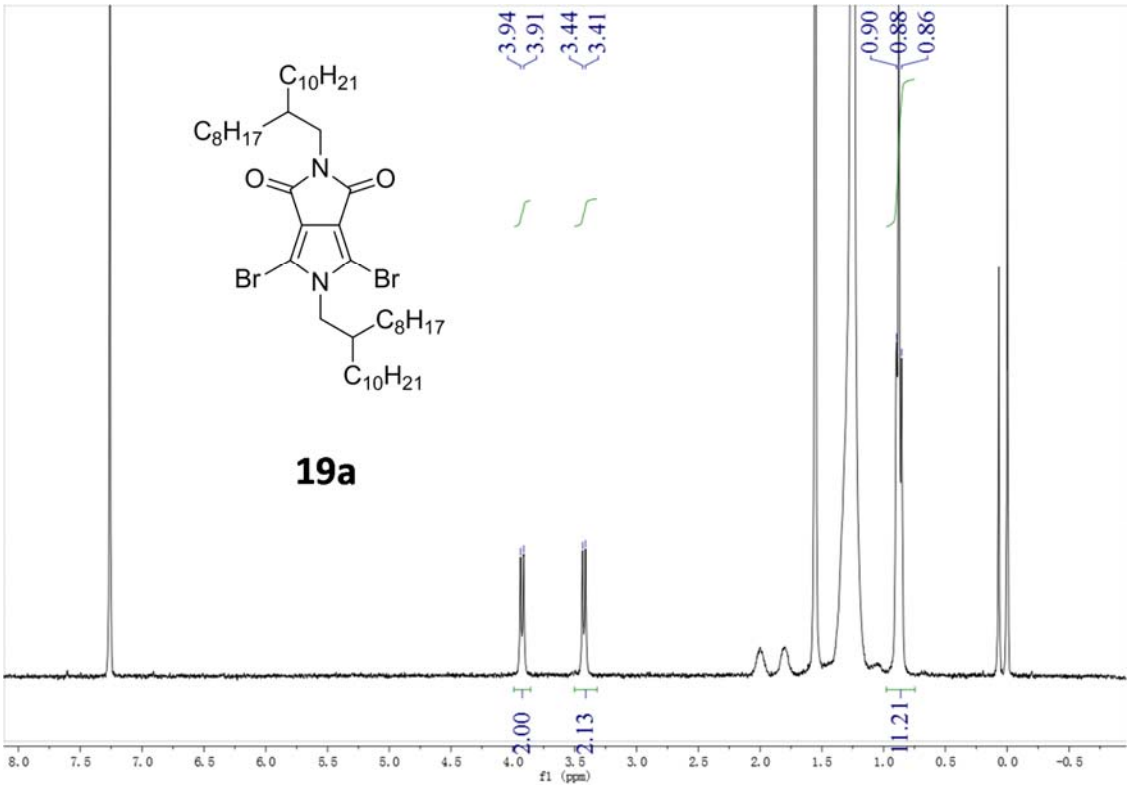

Figure S17 The 300 MHz ^{1}H NMR spectrum of 4,6-dibromo-2,5-bis(2-octyldodecyl)pyrrolo[3,4-*c*]pyrrole-1,3(2*H*,5*H*)-dione (**19a**) measured in $CDCl_3$.

4,6-Dibromo-5-dodecyl-2-(2-octyldodecyl)pyrrolo[3,4-*c*]pyrrole-1,3(2*H*,5*H*)-dione (19b)

Compound **19b** was synthesized following the similar procedure for compound **19a** using compound **18b** (0.704 g, 1.20 mmol) instead of compound **18a**. Yield: 0.782 g (87.7%). ^{1}H NMR (300 MHz, $CDCl_3$) δ 4.11 – 3.97 (m, 2H), 3.42 (d, J = 7.2 Hz, 2H), 0.88 (t, J = 5.8 Hz, 9H). ^{13}C NMR (75 MHz, $CDCl_3$) δ 162.35, 121.30, 100.41, 47.33, 42.28, 36.86, 31.76, 31.38, 29.82, 29.69, 29.50, 29.48, 29.45, 29.35, 29.25, 29.20, 29.17, 29.16, 28.92, 26.28, 26.22, 22.53, 13.93. HRMS

$(M+H)^+$ Calc. for $C_{38}H_{67}Br_2N_2O_2^+$: 743.3549; found: 743.3542. Elemental analysis: Calc. for $C_{38}H_{66}Br_2N_2O_2$: C 61.45, H 8.96, N 3.77%; found: C 61.13, H 8.96, N 3.76%.

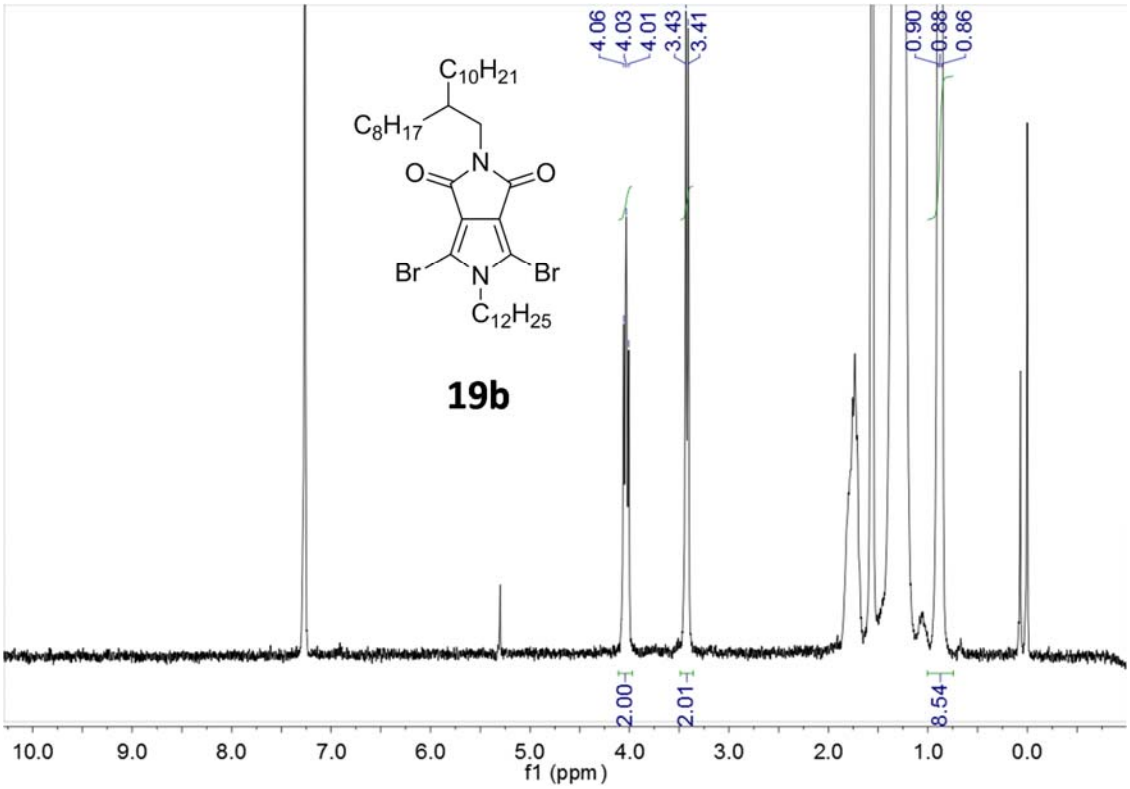

Figure S18 The 300 MHz ^{1}H NMR spectrum of 4,6-dibromo-5-dodecyl-2-(2-octyldodecyl)pyrrolo[3,4-*c*]pyrrole-1,3(2*H*,5*H*)-dione (**19b**) measured in $CDCl_3$.

2,5-Bis(2-octyldodecyl)-4,6-di(thiophen-2-yl)pyrrolo[3,4-*c*]pyrrole-1,3(2*H*,5*H*)-dione (20a)

Compound **19a** (1.11 g, 1.29 mmol) and 2-(tributylstannyl)thiophene (1.06 g, 2.85 mmol) were charged to a 25 mL flask. After degassing and refilling argon for 3 times, toluene (8 mL) and $Pd_2(dba)_3$ (32 mg, 0.104 mmol) were added and the reaction mixture was heated to 110 °C and stirred overnight. After cooling down to room temperature, solvent was removed. The liquid was dissolved in hexane and purified by column chromatography on silica gel (hexane : DCM =

2 : 1, v : v) to give a light yellow solid. Yield: 1.08 g (96.8%). ^{1}H NMR (300 MHz, $CDCl_3$) δ 7.58 (dd, *J* = 3.6, 1.1 Hz, 2H), 7.45 (dd, *J* = 5.1, 1.1 Hz, 2H), 7.14 (dd, *J* = 5.1, 3.7 Hz, 2H), 4.30 (d, *J* = 7.5 Hz, 2H), 3.42 (d, *J* = 7.2 Hz, 2H), 0.85 (dt, *J* = 7.0, 3.6 Hz, 12H). ^{13}C NMR (75 MHz, $CDCl_3$) δ 164.25, 130.06, 129.64, 127.62, 127.53, 127.47, 118.71, 50.90, 42.33, 37.83, 37.02, 31.78, 31.72, 31.54, 30.69, 29.89, 29.56, 29.51, 29.47, 29.44, 29.32, 29.26, 29.21, 29.17, 29.08, 28.15, 26.63, 26.34, 25.71, 22.55, 17.17, 13.96, 13.43. HRMS $(M+H)^+$ Calc. for $C_{54}H_{89}N_2O_2S_2^+$: 861.6365; found: 861.6366. Elemental analysis: Calc. for $C_{54}H_{88}N_2O_2S_2$: C 75.29, H 10.30, N 3.25%; found: C 74.77, H 10.08, N 3.09%.

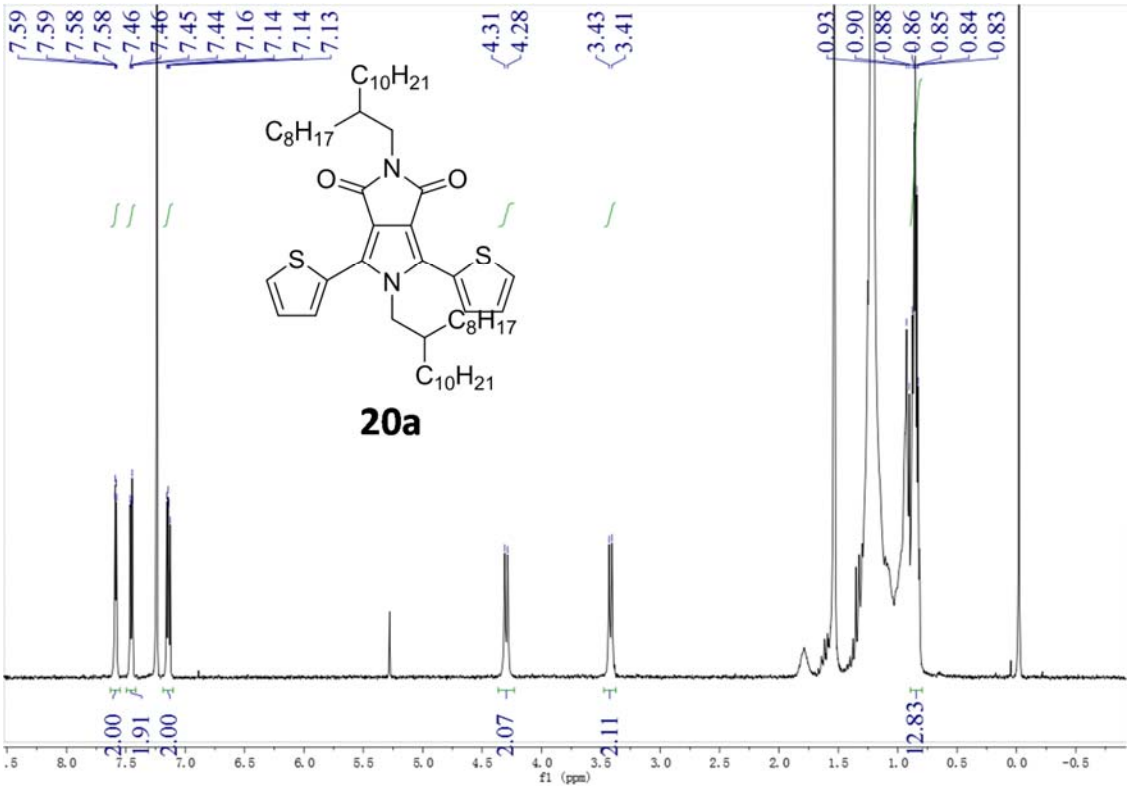

Figure S19 The 300 MHz ^{1}H NMR spectrum of 2,5-bis(2-octyldodecyl)-4,6-di(thiophen-2-yl)pyrrolo[3,4-*c*]pyrrole-1,3(2*H*,5*H*)-dione (**20a**) measured in $CDCl_3$.

5-Dodecyl-2-(2-octyldodecyl)-4,6-di(thiophen-2-yl)pyrrolo[3,4-*c*]pyrrole-1,3(2*H*,5*H*)-dione (20b)

Compound **20b** was synthesized following the similar procedure for compound **20a** using compound **19b** (0.642 g, 0.865 mmol) instead of compound **19a**. Yield: 0.464 g (71.7%). ^{1}H NMR (300 MHz, $CDCl_3$) δ 7.77 (d, *J* = 2.9 Hz, 2H), 7.48 (d, *J* = 4.4 Hz, 2H), 7.19 (dd, *J* = 4.9, 3.9 Hz, 2H), 4.40 – 4.25 (m, 2H), 3.45 (d, *J* = 7.2 Hz, 2H), 0.88 (dt, *J* = 6.7, 5.3 Hz, 9H). ^{13}C NMR (75 MHz, $CDCl_3$) δ 164.27, 130.45, 129.20, 127.63, 127.35, 126.81, 118.47, 46.39, 42.31, 37.03, 31.78, 31.54, 30.81, 29.90, 29.51, 29.46, 29.32, 29.21, 29.19, 28.72, 28.15, 26.63, 26.35, 26.13, 22.55, 17.16, 13.97, 13.44. HRMS $(M+H)^+$ Calc. for $C_{46}H_{73}N_2O_2S_2^+$: 749.5113; found: 749.5109. Elemental analysis: Calc. for $C_{46}H_{72}N_2O_2S_2$: C 73.74, H 9.69, N 3.74%; found: C 72.66, H 9.65, N 3.50%.

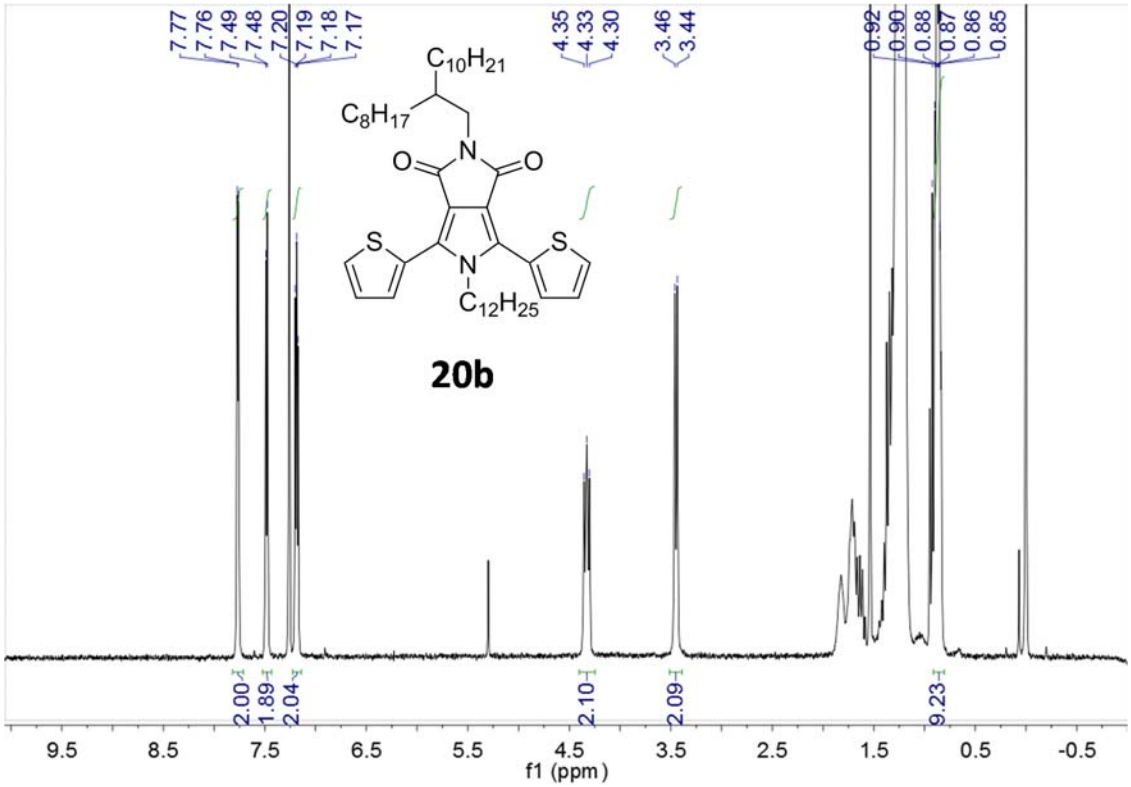

Figure S20 The 300 MHz ^{1}H NMR spectrum of 5-dodecyl-2-(2-octyldodecyl)-4,6-di(thiophen-2-yl)pyrrolo[3,4-*c*]pyrrole-1,3(2*H*,5*H*)-dione (**20b**) measured in $CDCl_3$.

4,6-Bis(5-bromothiophen-2-yl)-2,5-bis(2-octyldodecyl)pyrrolo[3,4-*c*]pyrrole-1,3(2*H*,5*H*)-dione (21a)

To a solution of compound **20a** (0.964 g, 1.12 mmol) in DMF (10 mL) was added NBS (0.459 g, 2.58 mmol). The reaction mixture was stirred at room temperature overnight and then poured into water (100 mL). After extraction with DCM, the combined organic phase was dried over Na_2SO_4 and filtered. After removing the solvent, the residual was purified using column chromatography on silica gel (hexane : ethyl acetate = 3 : 1, v : v) to give the product as a liquid. Yield: 1.05 g (91.8%). ^{1}H NMR (300 MHz, $CDCl_3$) δ 7.34 (d, *J* = 3.9 Hz, 2H), 7.12 (d, *J* = 3.9 Hz, 2H), 4.20 (d, *J* = 7.5 Hz, 2H), 3.43 (d, *J* = 7.2 Hz, 2H), 0.93 – 0.80 (m, 12H). ^{13}C NMR (75 MHz, $CDCl_3$) δ 163.92, 130.83, 130.45, 130.25, 126.60, 119.00, 114.86, 31.79, 31.74, 29.50, 29.22,

29.17, 29.12, 22.56, 22.54, 14.00. HRMS $(M+H)^+$ Calc. for $C_{54}H_{87}Br_2N_2O_2S_2^+$: 1019.4555; found: 1019.4539. Elemental analysis: Calc. for $C_{54}H_{86}Br_2N_2O_2S_2$: C 63.64, H 8.50, N 2.75%; found: C 63.94, H 8.47, N 2.78%.

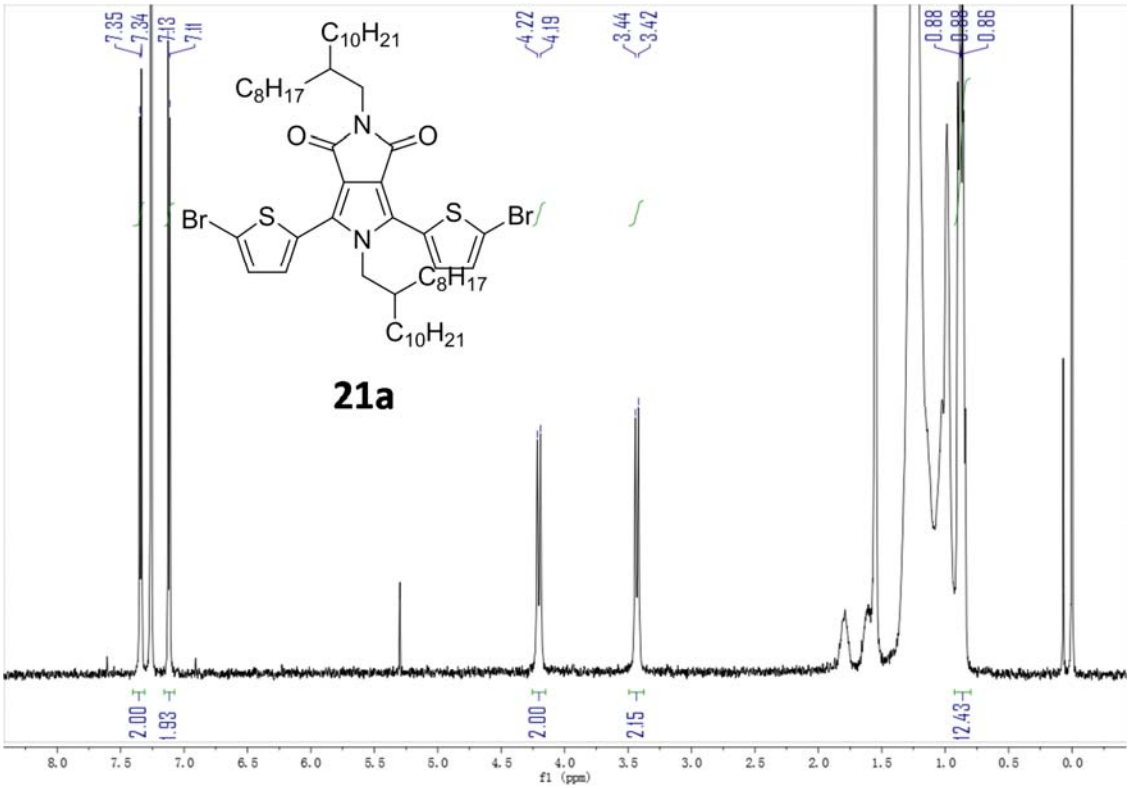

Figure S21 The 300 MHz ^{1}H NMR spectrum of 4,6-bis(5-bromothiophen-2-yl)-2,5-bis(2-octyldodecyl)pyrrolo[3,4-*c*]pyrrole-1,3(2*H*,5*H*)-dione (**21a**) measured in $CDCl_3$.

4,6-Bis(5-bromothiophen-2-yl)-5-dodecyl-2-(2-octyldodecyl)pyrrolo[3,4-*c*]pyrrole-1,3(2*H*,5*H*)-dione (21b)

Compound **21b** was synthesized following the similar procedure for compound **21a** using compound **20b** (0.377 g, 0.500 mmol) instead of compound **20a**. Yield: 0.410 g (90.5%). ^{1}H NMR (300 MHz, $CDCl_3$) δ 7.50 (d, J = 3.9 Hz, 2H), 7.14 (d, J = 3.9 Hz, 2H), 4.31 – 4.15 (m, 2H), 3.44 (d, J = 7.2 Hz, 2H), 0.95 – 0.79 (m, 9H). ^{13}C NMR (75 MHz, $CDCl_3$) δ 164.09, 130.83,

130.73, 130.54, 126.01, 118.91, 114.90, 46.63, 42.49, 37.14, 31.94, 31.60, 30.99, 30.03, 29.65, 29.60, 29.51, 29.37, 29.33, 28.82, 26.45, 26.20, 22.72, 14.16. HRMS $(M+H)^+$ Calc. for $C_{46}H_{71}Br_2N_2O_2S_2^+$: 907.3303; found: 907.3293. Elemental analysis: Calc. for $C_{46}H_{70}Br_2N_2O_2S_2$: C 60.91, H 7.78, N 3.09%; found: C 61.17, H 7.74, N 3.03%.

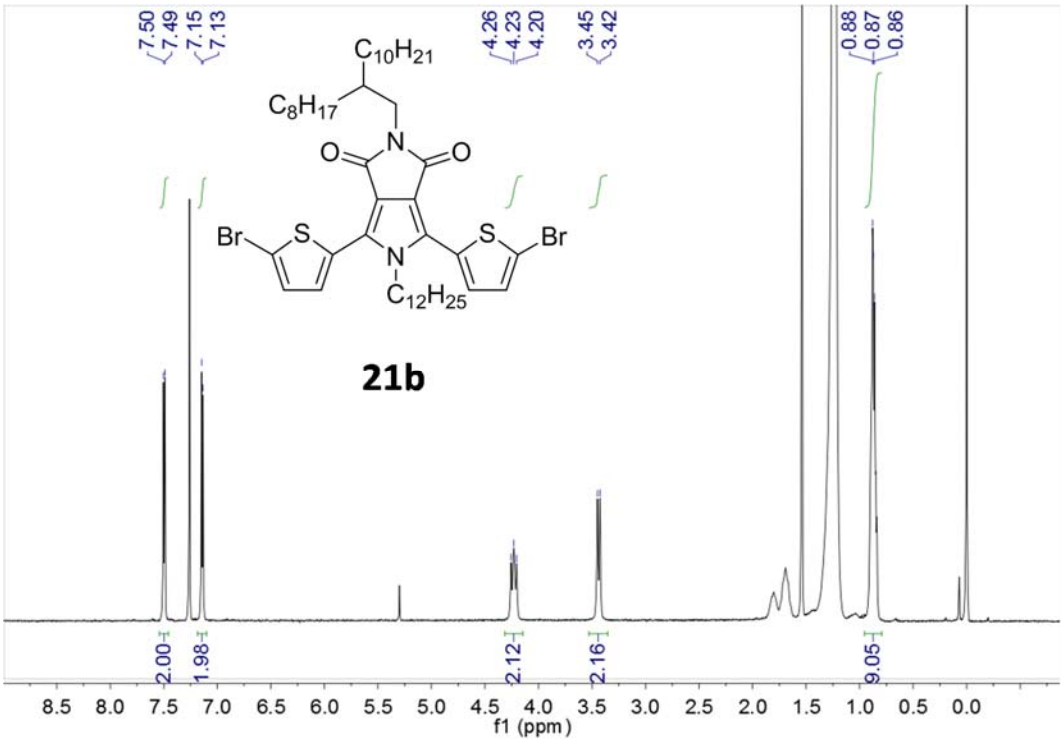

Figure S22 The 300 MHz ^{1}H NMR spectrum of 4,6-bis(5-bromothiophen-2-yl)-5-dodecyl-2-(2-octyldodecyl)pyrrolo[3,4-*c*]pyrrole-1,3(2*H*,5*H*)-dione (**21b**) measured in $CDCl_3$.

Synthesis of P7

To a 25 mL Schlenk flask were added compound **21a** (0.231 g, 0.227 mmol), 5,5'-bis(trimethylstannyl)-2,2'-bithiophene (0.112 g, 0.227 mmol) and tri(*o*-totyl)phosphine (5.5 mg, 0.018 mmol). After degassing and refilling argon for 3 times, anhydrous chlorobenzene (5 mL) and tris(dibenzylideneacetone)-dipalladium (4.2 mg, 0.00454 mmol) were added under argon. The flask was sealed and stirred for 60 h at 130 °C. After cooling down to room temperature, the

reaction mixture was poured into methanol (100 ml). The precipitated product was collected by filtration and subjected to Soxhlet extraction with acetone and hexane. Yield: 229.4 mg (98.7%) from the hexane extract.

Synthesis of P8

P8 was synthesized using compound **21b** (0.186 g, 0.205 mmol) and 5,5'-bis(trimethylstannyl)-2,2'-bithiophene (0.101 g, 0.205 mmol), following the similar procedure for **P7**. The precipitated product was collected by filtration and subjected to Soxhlet extraction with acetone, hexane, and chloroform. Yield: 176.2 mg (94.3%) from the chloroform extract.

Device Fabrication

Two configurations (bottom contact bottom gate (BCBG) or bottom contact top gate (BCTG)) are applied in this proposal to characterize the device performance, depending on the solubility and stability of the polymer, as well as the film quality.

All BCBG devices were characterized in nitrogen atmosphere in the absence of light using an Agilent B2900A Semiconductor Analyzer.

All BCTG devices were characterized in air in the absence of light using an Agilent 4155C Semiconductor Analyzer.

Part 1: Bottom Gate, Bottom Contact OTFTs

Heavily n-doped Si / SiO_2 wafer was used as the substrate and dielectric. The source / drain electrode pairs were deposited using the conventional photolithography to obtain the defined device dimensions with a channel length (L) of 30 μm and a channel width (W) of 1 mm. The substrate was cleaned using an ultrasonic bath with de-ionized (DI) water, rinsed with acetone

and isopropanol and then modified by dodecyltrichlorosilane (DDTS). The polymer films with thickness ~30 to 50 nm were deposited on the substrate by spin-coating a polymer solution (5 mg / mL in chloroform, 10 mg / mL in other solvents, depends on the solubility) at 3000 rpm for 50 s subsequently annealed at 100, 150 or 200 °C for 20 min.

Part 2: Top Gate, Bottom Contact OTFTs

The substrate, electrodes deposition and polymer film coating are the same as bottom gate, bottom contact OTFTs, while a CYTOP layer (~570 nm) were spin-coated above the polymer film as the gate dielectric. After being dried at 100 °C on a hotplate for 30 min, Al gate electrode (~70 nm) was deposited through thermal evaporation as gate electrode. *C*i (the capacitance per unit area) of the CYTOP layer (570 nm) is determined from a metal-insulator-metal structure as 3.2 $nF \cdot cm^{-2}$.

Bibliography

(1) Dimitrakopoulos, C. D. *Science (80).* **1999**, *283* (5403), 822–824.

(2) Schön, J. H. *Synth. Met.* **2001**, *122* (1), 157–160.

(3) Dimitrakopoulos, C. D.; Malenfant, P. R. L. *Adv. Mater.* **2002**, *14* (2), 99–117.

(4) Vivek, S. In *Organic Field-Effect Transistors*; CRC Press, 2007; pp 489–505.

(5) Luisa, T.; Tanese, M.; Brian, C.; Ananth, D.; Liang, W. In *Organic Field-Effect Transistors*; CRC Press, 2007; pp 507–528.

(6) Wang, L.; Fine, D.; Sharma, D.; Torsi, L.; Dodabalapur, A. *Anal. Bioanal. Chem.* **2006**, *384* (2), 310–321.

(7) Lin, P.; Yan, F. *Adv. Mater.* **2012**, *24* (1), 34–51.

(8) Knopfmacher, O.; Hammock, M. L.; Appleton, A. L.; Schwartz, G.; Mei, J.; Lei, T.; Pei, J.; Bao, Z. *Nat Commun* **2014**, *5*.

(9) Liu, X.; Guo, Y.; Ma, Y.; Chen, H.; Mao, Z.; Wang, H.; Yu, G.; Liu, Y. *Adv. Mater.* **2014**, *26* (22), 3631–3636.

(10) Chandar Shekar, B.; Lee, J.; Rhee, S.-W. *Korean J. Chem. Eng.* **2004**, *21* (1), 267–285.

(11) Katz, H. E.; Bao, Z.; Gilat, S. L. *Acc. Chem. Res.* **2001**, *34* (5), 359–369.

(12) Allard, S.; Forster, M.; Souharce, B.; Thiem, H.; Scherf, U. *Angew. Chemie-International Ed.* **2008**, *47* (22), 4070–4098.

(13) Leong, W. L.; Mathews, N.; Tan, B.; Vaidyanathan, S.; Dotz, F.; Mhaisalkar, S. *J. Mater. Chem.* **2011**, *21* (14), 5203–5214.

(14) Klauk, H. *Chem. Soc. Rev.* **2010**, *39* (7), 2643–2666.

(15) Arias, A. C.; MacKenzie, J. D.; McCulloch, I.; Rivnay, J.; Salleo, A. *Chem. Rev.* **2010**, *110* (1), 3–24.

(16) Facchetti, A. *Chem. Mater.* **2011**, *23* (3), 733–758.

(17) Guo, C.; Hong, W.; Aziz, H.; Li, Y. *Rev. Adv. Sci. Eng.* **2012**, *1* (3), 200–224.

(18) Facchetti, A. *Mater. Today* **2013**, *16* (4), 123–132.

(19) He, Y.; Hong, W.; Li, Y. *J. Mater. Chem. C* **2014**, *2*, 8651–8661.

(20) Ong, B. S.; Wu, Y.; Li, Y.; Liu, P.; Pan, H. *Chem. A Eur. J.* **2008**, *14* (16), 4766–4778.

(21) Nielsen, C. B.; Turbiez, M.; McCulloch, I. *Adv. Mater.* **2012**, *25* (13), 1859–1880.

(22) Edgar, L. J. Google Patents 1930.

(23) McGinness, J. E. *Sci.* **1972**, *177* (4052), 896–897.

(24) McGinness, J.; Corry, P.; Proctor, P. *Sci.* **1974**, *183* (4127), 853–855.

(25) Tsumura, A.; Koezuka, H.; Ando, T. *Appl. Phys. Lett.* **1986**, *49* (18), 1210–1212.

(26) Ong, B. S.; Wu, Y.; Liu, P.; Gardner, S. *J. Am. Chem. Soc.* **2004**, *126* (11), 3378–3379.

(27) Street, R. A.; Northrup, J. E.; Salleo, A. *Phys. Rev. B* **2005**, *71* (16), 165202.

(28) Jones, B. A.; Facchetti, A.; Wasielewski, M. R.; Marks, T. J. *J. Am. Chem. Soc.* **2007**, *129* (49), 15259–15278.

(29) Yan, H.; Chen, Z.; Zheng, Y.; Newman, C.; Quinn, J. R.; Dotz, F.; Kastler, M.; Facchetti, A. *Nature* **2009**, *457* (7230), 679–686.

(30) Yuen, J. D.; Wudl, F. *Energy Environ. Sci.* **2013**, *6* (2), 392–406.

(31) Li, Y.; Sonar, P.; Murphy, L.; Hong, W. *Energy Environ. Sci.* **2013**, *6* (6), 1684–1710.

(32) Sirringhaus, H. *Adv. Mater.* **2014**, *26* (9), 1319–1335.

(33) Bundgaard, E.; Krebs, F. C. *Sol. Energy Mater. Sol. Cells* **2007**, *91* (11), 954–985.

(34) Kroon, R.; Lenes, M.; Hummelen, J. C.; Blom, P. W. M.; de Boer, B. *Polym. Rev.* **2008**, *48* (3), 531–582.

(35) Cheng, Y. J.; Yang, S. H.; Hsu, C. S. *Chem. Rev.* **2009**, *109* (11), 5868–5923.

(36) McGinness, J. E. *Sci.* **1972**, *177* (4052), 896–897.

(37) McGinness, J.; Corry, P.; Proctor, P. *Sci.* **1974**, *183* (4127), 853–855.

(38) De Leeuw, D. M.; Simenon, M. M. J.; Brown, A. R.; Einerhand, R. E. F. *Synth. Met.* **1997**, *87* (1), 53–59.

(39) Yan, Z.; Sun, B.; Li, Y. *Chem. Commun.* **2013**, *49* (36), 3790–3792.

(40) Wang, L.; Zhang, X.; Tian, H.; Lu, Y.; Geng, Y.; Wang, F. *Chem. Commun.* **2013**, *49* (96), 11272–11274.

(41) Li, Y.; Singh, S. P.; Sonar, P. *Adv. Mater.* **2010**, *22*, 4862–4866.

(42) Li, Y.; Sonar, P.; Singh, S. P.; Soh, M. S.; Van, M. M.; Tan, J. *Polym. Prepr.* **2011**, *52*, 941–942.

(43) Li, Y.; Sonar, P.; Singh, S. P.; Soh, M. S.; Van, M. M.; Tan, J. *J. Am. Chem. Soc.* **2011**, *133*, 2198–2204.

(44) Li, Y.; Sonar, P.; Singh, S. P.; Zeng, W.; Soh, M. S. *J. Mater. Chem.* **2011**, *21*, 10829–10835.

(45) Sonar, P.; Singh, S. P.; Li, Y.; Ooi, Z.; Ha, T.; Wong, I.; Soh, M. S.; Dodabalapur, A. *Energy Environ. Sci.* **2011**, *4* (6), 2288–2296.

(46) Li, J.; Zhao, Y.; Tan, H. S.; Guo, Y.; Di, C.-A.; Yu, G.; Liu, Y.; Lin, M.; Lim, S. H.; Zhou, Y.; Su, H.; Ong, B. S. *Sci. Rep.* **2012**, *2*.

(47) Meager, I.; Ashraf, R. S.; Rossbauer, S.; Bronstein, H.; Donaghey, J. E.; Marshall, J.; Schroeder, B. C.; Heeney, M.; Anthopoulos, T. D.; McCulloch, I. *Macromolecules* **2013**, 5961–5967.

(48) Tang, A.; Li, L.; Lu, Z.; Huang, J.; Jia, H.; Zhan, C.; Tan, Z.; Li, Y.; Yao, J. *J. Mater. Chem. A* **2013**, *1* (18), 5747–5757.

(49) Sun, B.; Hong, W.; Yan, Z.; Aziz, H.; Li, Y. *Adv. Mater.* **2014**, *26* (17), 2636–2642.

(50) Sun, B.; Hong, W.; Aziz, H.; Li, Y. *Polym. Chem.* **2015**, *6* (6), 938–945.

(51) He, Y.; Guo, C.; Sun, B.; Quinn, J.; Li, Y. *Chem. Commun.* **2015**, *51* (38), 8093–8096.

(52) McCulloch, I.; Heeney, M.; Bailey, C.; Genevicius, K.; Macdonald, I.; Shkunov, M.; Sparrowe, D.; Tierney, S.; Wagner, R.; Zhang, W.; Chabinyc, M. L.; Kline, R. J.; McGehee, M. D.; Toney, M. F. *Nat. Mater.* **2006**, *5* (4), 328–333.

(53) Pan, H.; Li, Y.; Wu, Y.; Liu, P.; Ong, B. S.; Zhu, S.; Xu, G. *J. Am. Chem. Soc.* **2007**, *129* (14), 4112–4113.

(54) Osaka, I.; Sauve, G.; Zhang, R.; Kowalewski, T.; McCullough, R. D. *Adv. Mater.* **2007**, *19* (23), 4160–4165.

(55) Zhu, Y.; Champion, R. D.; Jenekhe, S. A. *Macromolecules* **2006**, *39* (25), 8712–8719.

(56) Lei, T.; Cao, Y.; Fan, Y.; Liu, C.-J.; Yuan, S.-C.; Pei, J. *J. Am. Chem. Soc.* **2011**, *133* (16), 6099–6101.

(57) Mei, J.; Kim, D. H.; Ayzner, A. L.; Toney, M. F.; Bao, Z. *J. Am. Chem. Soc.* **2011**, *133* (50), 20130–20133.

(58) Lei, T.; Dou, J.-H.; Ma, Z.-J.; Yao, C.-H.; Liu, C.-J.; Wang, J.-Y.; Pei, J. *J. Am. Chem. Soc.* **2012**, *134* (49), 20025–20028.

(59) Lei, T.; Dou, J.-H.; Pei, J. *Adv. Mater.* **2012**, *24* (48), 6457–6461.

(60) Kim, G.; Kang, S.-J.; Dutta, G. K.; Han, Y.-K.; Shin, T. J.; Noh, Y.-Y.; Yang, C. *J. Am. Chem. Soc.* **2014**, *136* (26), 9477–9483.

(61) Lei, T.; Dou, J.-H.; Cao, X.-Y.; Wang, J.-Y.; Pei, J. *Adv. Mater.* **2013**, *25* (45), 6589–6593.

(62) Kang, I.; Yun, H.-J.; Chung, D. S.; Kwon, S.-K.; Kim, Y.-H. *J. Am. Chem. Soc.* **2013**, *135* (40), 14896–14899.

(63) Hong, W.; Chen, S.; Sun, B.; Arnould, M. A.; Meng, Y.; Li, Y. *Chem. Sci.* **2015**, *6* (5), 3225–3235.

(64) Najari, A.; Berrouard, P.; Ottone, C.; Boivin, M.; Zou, Y.; Gendron, D.; Caron, W.-O.; Legros, P.; Allen, C. N.; Sadki, S.; Leclerc, M. *Macromolecules* **2012**, *45* (4), 1833–1838.

(65) Burke, D. J.; Lipomi, D. J. *Energy Environ. Sci.* **2013**, *6* (7), 2053–2066.

(66) Ouattara, M. P.; Lenfant, S.; Vuillaume, D.; Pézolet, M.; Rioux-Dubé, J.-F.; Brisson, J.; Leclerc, M. *Macromolecules* **2013**, *46* (16), 6408–6418.

(67) Wang, D. H.; Pron, A.; Leclerc, M.; Heeger, A. J. *Adv. Funct. Mater.* **2013**, *23* (10), 1297–1304.

(68) Shiyong, L.; Weifei, F.; Jingqi, X.; Congcheng, F.; Hao, J.; Minmin, S.; Hanying, L.; Junwu, C.; Yong, C.; Hongzheng, C. *Nanotechnology* **2014**, *25* (1), 14006.

(69) Kuramochi, M.; Kuwabara, J.; Lu, W.; Kanbara, T. *Macromolecules* **2014**, *47* (21), 7378–7385.

(70) Pouliot, J.-R.; Sun, B.; Leduc, M.; Najari, A.; Li, Y.; Leclerc, M. *Polym. Chem.* **2015**, *6* (2), 278–282.

(71) Luzio, A.; Fazzi, D.; Nübling, F.; Matsidik, R.; Straub, A.; Komber, H.; Giussani, E.; Watkins, S. E.; Barbatti, M.; Thiel, W.; Gann, E.; Thomsen, L.; McNeill, C. R.; Caironi, M.; Sommer, M. *Chem. Mater.* **2014**, *26* (21), 6233–6240.

(72) Sonar, P.; Foong, T. R. B.; Dodabalapur, A. *Phys. Chem. Chem. Phys.* **2014**, *16*, 4275–4283.

(73) Lu, S.; Drees, M.; Yao, Y.; Boudinet, D.; Yan, H.; Pan, H.; Wang, J.; Li, Y.; Usta, H.; Facchetti, A. *Macromolecules* **2013**, *46* (10), 3895–3906.

(74) Cui, W.; Yuen, J.; Wudl, F. *Macromolecules* **2011**, *44* (20), 7869–7873.

(75) Hong, W.; Guo, C.; Li, Y.; Zheng, Y.; Huang, C.; Lu, S.; Facchetti, A. *J. Mater. Chem.* **2012**, *22* (41), 22282–22289.

(76) Rumer, J. W.; Levick, M.; Dai, S.-Y.; Rossbauer, S.; Huang, Z.; Biniek, L.; Anthopoulos, T. D.; Durrant, J. R.; Procter, D. J.; McCulloch, I. *Chem. Commun.* **2013**.

(77) Hong, W.; Sun, B.; Guo, C.; Yuen, J.; Li, Y.; Lu, S.; Huang, C.; Facchetti, A. *Chem. Commun.* **2013**, *49* (5), 484–486.

(78) Shirakawa, H.; Louis, E. J.; MacDiarmid, A. G.; Chiang, C. K.; Heeger, A. J. *J. Chem. Soc. Chem. Commun.* **1977**, No. 16, 578–580.

(79) Farchioni, R.; Grosso, G. *Organic Electronic Materials: Conjugted Polymers and Low Molecular Weight Electronic Solids*; Springer Berlin Heidelberg, 2001.

(80) Chen, M. S.; Niskala, J. R.; Unruh, D. A.; Chu, C. K.; Lee, O. P.; Fréchet, J. M. J. *Chem. Mater.* **2013**, *25* (20), 4088–4096.

(81) Cai, Z.; Luo, H.; Qi, P.; Wang, J.; Zhang, G.; Liu, Z.; Zhang, D. *Macromolecules* **2014**, *47* (9), 2899–2906.

(82) Guo, C.; Quinn, J.; Sun, B.; Li, Y. *J. Mater. Chem. C* **2015**, *3*, 5226–5232.

(83) Street, R. A.; Northrup, J. E.; Salleo, A. *Phys. Rev. B* **2005**, *71* (16), 165202.

(84) Sirringhaus, H.; Brown, P. J.; Friend, R. H.; Nielsen, M. M.; Bechgaard, K.; Langeveld-Voss, B. M. W.; Spiering, A. J. H.; Janssen, R. A. J.; Meijer, E. W.; Herwig, P.; de Leeuw, D. M. *Nature* **1999**, *401* (6754), 685–688.

(85) Wu, Y.; Liu, P.; Ong, B. S.; Srikumar, T.; Zhao, N.; Botton, G.; Zhu, S. *Appl. Phys. Lett.* **2005**, *86* (14), 142102/1–142102/3.

(86) Umeda, T.; Kumaki, D.; Tokito, S. *J. Appl. Phys.* **2009**, *105* (2), 24515–24516.

(87) *American Heritage Dictionary*. 3rd Ed. Boston: Houghton Mifflin 1992.

(88) W. Heywang, K. H. Z. *Silicon: evolution and future of a technology* ; P. Siffert, E. F. K., Ed.; Springer, 2004.

(89) Ebisawa, F.; Kurokawa, T.; Nara, S. *J. Appl. Phys.* **1983**, *54* (6), 3255–3259.

(90) Facchetti, A. *Mater. Today* **2007**, *10* (3), 28–37.

(91) Takayasu, S.; Tsuyoshi, S.; Takao, S. In *Organic Field-Effect Transistors*; CRC Press, 2007; pp 529–550.

(92) Jia, H.; Pant, G. K.; Gross, E. K.; Wallace, R. M.; Gnade, B. E. *Org. Electron.* **2006**, *7* (1), 16–21.

(93) Sandberg, G. *Indigo Textiles: Technique and History*; A & C Black;Lark Books: London;Asheville, 1989.

(94) McGovern, P. E.; Michel, R. H. *Acc. Chem. Res.* **1990**, *23* (5), 152–158.

(95) Robinson, R. *J. Soc. Dye. Colour.* **1921**, *37* (3), 77–81.

(96) Weinstein, J.; Wyman, G. M. *J. Am. Chem. Soc.* **1956**, *78* (11), 2387–2390.

(97) Lüttke, W.; Klessinger, M. *Chem. Ber.* **1964**, *97* (8), 2342–2357.

(98) Klessinger, M.; Lüttke, W. *Chem. Ber.* **1966**, *99* (7), 2136–2145.

(99) Yasarawan, N.; van Duijneveldt, J. S. *Langmuir* **2008**, *24* (14), 7184–7192.

(100) Sousa, M. M.; Miguel, C.; Rodrigues, I.; Parola, A. J.; Pina, F.; Seixas de Melo, J. S.; Melo, M. J. *Photochem. Photobiol. Sci.* **2008**, *7* (11), 1353–1359.

(101) Sadler, P. W. *Spectrochim. Acta* **1960**, *16* (9), 1094–1099.

(102) Haucke, G. P. R. *Photophysikalische Chemie indigoider Farbstoffe*; Deutsche Akademie d. Naturforscher Leopoldina ; Barth Halle (Saale); Leipzig, 1978.

(103) Wille, E.; Lüttke, W. *Chem. Ber.* **1973**, *106* (10), 3240–3257.

(104) Perpète, E. A.; Preat, J.; André, J.-M.; Jacquemin, D. *J. Phys. Chem. A* **2006**, *110* (17), 5629–5635.

(105) Glowacki, E. D.; Leonat, L.; Voss, G.; Bodea, M.-A.; Bozkurt, Z.; Ramil, A. M.; Irimia-Vladu, M.; Bauer, S.; Sariciftci, N. S. *AIP Adv.* **2011**, *1* (4), 42132–42136.

(106) Głowacki, E. D.; Voss, G.; Leonat, L.; Irimia-Vladu, M.; Bauer, S.; Sariciftci, N. S. *Isr. J. Chem.* **2012**, *52* (6), 540–551.

(107) Irimia-Vladu, M.; Głowacki, E. D.; Troshin, P. A.; Schwabegger, G.; Leonat, L.; Susarova, D. K.; Krystal, O.; Ullah, M.; Kanbur, Y.; Bodea, M. A.; Razumov, V. F.; Sitter, H.; Bauer, S.; Sariciftci, N. S. *Adv. Mater.* **2012**, *24* (3), 375–380.

(108) Kanbur, Y.; Irimia-Vladu, M.; Głowacki, E. D.; Voss, G.; Baumgartner, M.; Schwabegger, G.; Leonat, L.; Ullah, M.; Sarica, H.; Erten-Ela, S.; Schwödiauer, R.; Sitter, H.; Küçükyavuz, Z.; Bauer, S.; Sariciftci, N. S. *Org. Electron.* **2012**, *13* (5), 919–924.

(109) Kojima, H.; Mori, T. *Chem. Lett.* **2013**, *42* (1), 68–70.

(110) Marcus, R. A. *Rev. Mod. Phys.* **1993**, *65* (3), 599–610.

(111) Imming, P.; Imhof, I.; Zentgraf, M. *Synth. Commun.* **2001**, *31* (23), 3721–3727.

(112) Urano, K.; Ohno, T.; Tomono, K.; Miyamura, K. *Bull. Chem. Soc. Jpn.* **2013**, *86* (1), 159–165.

(113) Sun, B.; Hong, W.; Aziz, H.; Li, Y. *J. Mater. Chem.* **2012**, *22* (36), 18950–18955.

(114) Setsune, J.; Wakemoto, H.; Matsueda, T.; Matsuura, T.; Tajima, H.; Kitao, T.; Ishihara, S.; Yamamoto, R. *J. Chem. Soc. Perkin Trans. 1* **1984**, 2305.

(115) Seely, G. R.; Shaw, E. R. *J. Photochem.* **1984**, *24* (4), 383–393.

(116) Frisch, M. J. *Gaussian 09 Programmer's Reference*; Gaussian, 2009.

(117) Frisch, M. J.; Trucks, G. W.; Schlegel, H. B.; Scuseria, G. E.; Robb, M. A.; Al., E.; Cheeseman, J. R.; Scalmani, G.; Barone, V.; Mennucci, B.; Petersson, G. A.; Nakatsuji, H.; Caricato, M.; Li, X.; Hratchian, H. P.; Izmaylov, A. F.; Bloino, J.; Zheng, G.; Sonnenberg, J. L.; Hada, M.; Ehara, M.; Toyota, K.; Fukuda, R.; Hasegawa, J.; Ishida, M.; Nakajima, T.; Honda, Y.; Kitao, O.; Nakai, H.; Vreven, T.; Montgomery, J. A.; Peralta, J. E.; Ogliaro, F.; Bearpark, M.; Heyd, J. J.; Brothers, E.; Kudin, K. N.; Staroverov, V. N.; Kobayashi, R.; Normand, J.; Raghavachari, K.; Rendell, A.; Burant, J. C.; Iyengar, S. S.; Tomasi, J.; Cossi, M.; Rega, N.; Millam, J. M.; Klene, M.; Knox, J. E.; Cross, J. B.; Bakken, V.; Adamo, C.; Jaramillo, J.; Gomperts, R.; Stratmann, R. E.; Yazyev, O.; Austin, A. J.; Cammi, R.; Pomelli, C.; Ochterski, J. W.; Martin, R. L.; Morokuma, K.; Zakrzewski, V. G.; Voth, G. A.; Salvador, P.; Dannenberg, J. J.; Dapprich, S.; Daniels, A. D.; Farkas; Foresman, J. B.; Ortiz, J. V; Cioslowski, J.; Fox, D. J. Wallingford CT 2009.

(118) Braun, S.; Salaneck, W. R.; Fahlman, M. *Adv. Mater.* **2009**, *21* (14-15), 1450–1472.

(119) Wan, A.; Hwang, J.; Amy, F.; Kahn, A. *Org. Electron.* **2005**, *6* (1), 47–54.

(120) D'Andrade, B. W.; Datta, S.; Forrest, S. R.; Djurovich, P.; Polikarpov, E.; Thompson, M. E. *Org. Electron.* **2005**, *6* (1), 11–20.

(121) Oh, Y.; Pyo, S.; Yi, M. H.; Kwon, S.-K. *Org. Electron.* **2006**, *7* (2), 77–84.

(122) Guo, C.; Sun, B.; Quinn, J.; Yan, Z.; Li, Y. *J. Mater. Chem. C* **2014**, *2* (21), 4289–4296.

(123) Głowacki, E. D.; Apaydin, D. H.; Bozkurt, Z.; Monkowius, U.; Demirak, K.; Tordin, E.; Himmelsbach, M.; Schwarzinger, C.; Burian, M.; Lechner, R. T.; Demitri, N.; Voss, G.; Sariciftci, N. S. *J. Mater. Chem. C* **2014**, *2* (38), 8089–8097.

(124) Pitayatanakul, O.; Higashino, T.; Kadoya, T.; Tanaka, M.; Kojima, H.; Ashizawa, M.; Kawamoto, T.; Matsumoto, H.; Ishikawa, K.; Mori, T. *J. Mater. Chem. C* **2014**, *2* (43), 9311–9317.

(125) Lee, J.; Han, A. R.; Hong, J.; Seo, J. H.; Oh, J. H.; Yang, C. *Adv. Funct. Mater.* **2012**, *22* (19), 4128–4138.

(126) Ichimura, K.; Arimitsu, K.; Tahara, M. *J. Mater. Chem.* **2004**, *14* (7), 1164–1172.

(127) Hunger, K.; Hamprecht, R.; Miederer, P.; Heid, C.; Engel, A.; Kunde, K.; Mennicke, W.; Griffiths, J. In *Industrial Dyes*; Wiley-VCH Verlag GmbH & Co. KGaA, 2004; pp 113–338.

(128) Zou, Y.; Najari, A.; Berrouard, P.; Beaupré, S.; Réda Aïch, B.; Tao, Y.; Leclerc, M. *J. Am. Chem. Soc.* **2010**, *132* (15), 5330–5331.

(129) Shi, Q.; Fan, H.; Liu, Y.; Chen, J.; Ma, L.; Hu, W.; Shuai, Z.; Li, Y.; Zhan, X. *Macromolecules* **2011**, *44* (11), 4230–4240.

(130) Yuan, J.; Huang, X.; Zhang, F.; Lu, J.; Zhai, Z.; Di, C.; Jiang, Z.; Ma, W. *J. Mater. Chem.* **2012**, *22* (42), 22734.

(131) Friedländer, P.; Bruckner, S.; Deutsch, G. *Justus Liebigs Ann. Chem.* **1912**, *388* (1), 23–49.

(132) Cornil, J.; Beljonne, D.; Calbert, J.-P.; Brédas, J.-L. *Adv. Mater.* **2001**, *13* (14), 1053–1067.

(133) Brédas, J. L.; Calbert, J. P.; da Silva Filho, D. A.; Cornil, J. *Proc. Natl. Acad. Sci.* **2002**, *99* (9), 5804–5809.

(134) Cheng, X.; Noh, Y.-Y.; Wang, J.; Tello, M.; Frisch, J.; Blum, R.-P.; Vollmer, A.; Rabe, J. P.; Koch, N.; Sirringhaus, H. *Adv. Funct. Mater.* **2009**, *19* (15), 2407–2415.

(135) Sun, B.; Hong, W.; Thibau, E.; Aziz, H.; Lu, Z.-H.; Li, Y. *Org. Electron.* **2014**, *15* (12), 3787–3794.

(136) Peters, M.; Trobe, M.; Tan, H.; Kleineweischede, R.; Breinbauer, R. *Chem. – A Eur. J.* **2013**, *19* (7), 2442–2449.

(137) Se´vignon, M.; Papillon, J.; Schulz, E.; Lemaire, M. *Tetrahedron Lett.* **1999**, *40* (32), 5873–5876.

(138) Wang, Q.; Takita, R.; Kikuzaki, Y.; Ozawa, F. *J. Am. Chem. Soc.* **2010**, *132* (33), 11420–11421.

(139) Mercier, L. G.; Leclerc, M. *Acc. Chem. Res.* **2013**, *46* (7), 1597–1605.

(140) Blouin, N.; Michaud, A.; Gendron, D.; Wakim, S.; Blair, E.; Neagu-Plesu, R.; Belletête, M.; Durocher, G.; Tao, Y.; Leclerc, M. *J. Am. Chem. Soc.* **2008**, *130* (2), 732–742.

(141) Osaka, I.; Zhang, R.; Sauve, G.; Smilgies, D.-M.; Kowalewski, T.; McCullough, R. D. *J. Am. Chem. Soc.* **2009**, *131* (7), 2521–2529.

(142) Guo, X.; Quinn, J.; Chen, Z.; Usta, H.; Zheng, Y.; Xia, Y.; Hennek, J. W.; Ortiz, R. P.; Marks, T. J.; Facchetti, A. *J. Am. Chem. Soc.* **2013**, *135* (5), 1986–1996.

(143) Chen, S.; Sun, B.; Hong, W.; Aziz, H.; Meng, Y.; Li, Y. *J. Mater. Chem. C* **2014**, *2* (12), 2183–2190.

(144) Fu, B.; Wang, C.-Y.; Rose, B. D.; Jiang, Y.; Chang, M.; Chu, P.-H.; Yuan, Z.; Fuentes-Hernandez, C.; Kippelen, B.; Brédas, J.-L.; Collard, D. M.; Reichmanis, E. *Chem. Mater.* **2015**, *27* (8), 2928–2937.

(145) Rudenko, A. E.; Wiley, C. A.; Stone, S. M.; Tannaci, J. F.; Thompson, B. C. *J. Polym. Sci. Part A Polym. Chem.* **2012**, *50* (18), 3691–3697.

(146) Guo, Q.; Dong, J.; Wan, D.; Wu, D.; You, J. *Macromol. Rapid Commun.* **2013**, *34* (6), 522–527.

(147) Rudenko, A. E.; Wiley, C. a.; Tannaci, J. F.; Thompson, B. C. *J. Polym. Sci. Part A Polym. Chem.* **2013**, *51* (12), 2660–2668.

(148) Lombeck, F.; Komber, H.; Gorelsky, S. I.; Sommer, M. *ACS Macro Lett.* **2014**, *3* (8), 819–823.

(149) Matsidik, R.; Komber, H.; Luzio, A.; Caironi, M.; Sommer, M. *J. Am. Chem. Soc.* **2015**, *137* (20), 6705–6711.

(150) Pivsa-Art, S.; Satoh, T.; Kawamura, Y.; Miura, M.; Nomura, M. *Bulletin of the Chemical Society of Japan*. 1998, 467–473.

(151) Mori, A.; Sekiguchi, A.; Masui, K.; Shimada, T.; Horie, M.; Osakada, K.; Kawamoto, M.; Ikeda, T. *J. Am. Chem. Soc.* **2003**, *125* (7), 1700–1701.

(152) DERRIDJ, F.; GOTTUMUKKALA, A. L.; DJEBBAR, S.; DOUCET, H. *Eur. J. Inorg. Chem.* **2008**, No. 16, 2550–2559.

(153) Roger, J.; Požgan, F.; Doucet, H. *J. Org. Chem.* **2009**, *74* (3), 1179–1186.

(154) Shibahara, F.; Yamaguchi, E.; Murai, T. *J. Org. Chem.* **2011**, *76* (8), 2680–2693.

(155) Liu, X. W.; Shi, J. L.; Yan, J. X.; Wei, J. B.; Peng, K.; Dai, L.; Li, C. G.; Wang, B. Q.; Shi, Z. J. *Org. Lett.* **2013**, *15* (22), 5774–5777.

(156) Chen, L.; Bruneau, C.; Dixneuf, P. H.; Doucet, H. *ChemCatChem* **2013**, *5* (7), 1956–1963.

(157) Tani, S.; Uehara, T. N.; Yamaguchi, J.; Itami, K. *Chem. Sci.* **2014**, *5* (1), 123.

(158) Chávez, P.; Ngov, C.; Frémont, P. de; Lévêque, P.; Leclerc, N. *J. Org. Chem.* **2014**, *79* (21), 10179–10188.

(159) Karaca, E. Ö.; Gürbüz, N.; Özdemir, İ.; Doucet, H.; Şahin, O.; Büyükgüngör, O.; Çetinkaya, B. *Organometallics* **2015**, *34* (11), 2487–2493.

(160) Lu, W.; Kuwabara, J.; Kanbara, T. *Polym. Chem.* **2012**, *3* (12), 3217.

(161) Wang, Q.; Wakioka, M.; Ozawa, F. *Macromol. Rapid Commun.* **2012**, *33*, 1203–1207.

(162) Fujinami, Y.; Kuwabara, J.; Lu, W.; Hayashi, H.; Kanbara, T. *ACS Macro Lett.* **2012**, *1* (1), 67–70.

(163) Lu, W.; Kuwabara, J.; Kanbara, T. *Macromolecules* **2011**, *44* (6), 1252–1255.

(164) Fujinami, Y.; Kuwabara, J.; Lu, W.; Hayashi, H.; Kanbara, T. *ACS Macro Lett.* **2012**, *1* (1), 67–70.

(165) Turner, G. L.; Morris, J. a.; Greaney, M. F. *Angew. Chemie - Int. Ed.* **2007**, *46* (42), 7996–8000.

(166) Gorelsky, S. I. *Coord. Chem. Rev.* **2013**, *257* (1), 153–164.

(167) Lu, W.; Kuwabara, J.; Iijima, T.; Higashimura, H.; Hayashi, H.; Kanbara, T. *Macromolecules* **2012**, *45* (10), 4128–4133.

(168) Chang, S. W.; Waters, H.; Kettle, J.; Kuo, Z. R.; Li, C. H.; Yu, C. Y.; Horie, M. *Macromol. Rapid Commun.* **2012**, *33* (22), 1927–1932.

(169) Hendriks, K. H.; Li, W.; Heintges, G. H. L.; van Pruissen, G. W. P.; Wienk, M. M.; Janssen, R. A. J. *J. Am. Chem. Soc.* **2014**, *136* (31), 11128–11133.

(170) Sun, B.; Hong, W.; Aziz, H.; Abukhdeir, N. M.; Li, Y. *J. Mater. Chem. C* **2013**, *1* (29), 4423–4426.

(171) Huang, J.; Zhan, C.; Zhang, X.; Zhao, Y.; Lu, Z.; Jia, H.; Jiang, B.; Ye, J.; Zhang, S.; Tang, A.; Liu, Y.; Pei, Q.; Yao, J. *ACS Appl. Mater. Interfaces* **2013**, *5* (6), 2033–2039.

(172) Kim, Y.; Song, C. E.; Cho, A.; Kim, J.; Eom, Y.; Ahn, J.; Moon, S.; Lim, E. *Mater. Chem. Phys.* **2014**, *143* (2), 825–829.

(173) Tamilavan, V.; Song, M.; Agneeswari, R.; Kang, J.-W.; Hwang, D.-H.; Hyun, M. H. *Polymer (Guildf).* **2013**, *54* (22), 6125–6132.

(174) Becke, A. D. *Phys. Rev. A* **1988**, *38* (6), 3098–3100.

(175) Lee, C.; Yang, W.; Parr, R. G. *Phys. Rev. B* **1988**, *37* (2), 785–789.

(176) Glowacki, E. D.; Voss, G.; Demirak, K.; Havlicek, M.; Sunger, N.; Okur, A. C.; Monkowius, U.; Gasiorowski, J.; Leonat, L.; Sariciftci, N. S. *Chem. Commun.* **2013**, *49* (54), 6063–6065.

(177) Pollack, S. K.; Hijji, Y. M.; Kgobane, B. *Macromolecules* **1997**, *30* (21), 6709–6711.